Doctoral Dissertation

Si Photonics Microring Modulator Array for Radio over Fiber Applications and Its Optical Control

（光無線応用のための Si フォトニクス

マイクロリング変調器アレイとその光制御）

Liucun Li

（李 鎦村）

Yokohama National University

Department of Mathematics, Physics, Electrical Engineering and Computer Science

March 2024

Abstract

In recent years, the rapid development of the 5th generation mobile communication system (5G) has been transformative. 5G, with its key features of high speed (up to 20 Gbps), low latency (less than 1 ms), and wide connectivity, spanning various technologies such as the Internet of Things (IoT), has become pervasive in all aspects of people's lives. The wavebands of 5G can be categorized into the Sub 6 GHz bands and the millimeter wave bands. In Japan, the Sub 6 GHz band mainly includes the 3.7 GHz band and the 4.5 GHz band, while the millimeter wave band mainly includes the 28 GHz band. For 5G devices capable of multi-band communication, like smartphones, the presence of antennas in multiple bands adds complexity to the design and evaluation of the antenna. In the production line of such 5G products, visualizing the intensity and distribution of the 5G antenna radiation becomes crucial. Traditional electromagnetic (EM) wave imaging systems, implemented using large antenna arrays, face significant propagation losses, especially for high-frequency signals. Achieving remote electromagnetic wave imaging that maintains low power consumption is challenging. Some electromagnetic wave imaging modalities using E/O sensors face obstacles due to the acquisition of sensor crystals and their unsuitability for 5G signals.

However, Radio over Fiber (RoF) systems based on silicon photonics offer a superior solution for such applications. The fundamental concept of RoF involves converting a high-frequency electrical signal into an optical signal through an electro-optical modulator. This optical signal is then transmitted along an optical fiber to a remote location and ultimately converted back to an electrical signal. This approach facilitates the transmission of high-frequency electrical signals due to the low loss in optical fibers (~0.2 dB/km). Moreover, the insensitivity of fiber optic communication to electromagnetic noise makes it an excellent solution for visualizing weak electromagnetic waves. The silicon photonics platform provides a compact solution for electro-optical modulation in RoF systems. In this study, a microring modulator (MRM) is employed as the basic device for electro-optical modulation. The size of an MRM is typically only a few tens of micrometers, and its resonator structure allows for high modulation efficiency without requiring a lengthy physical size. Electro-optic modulation using the free carrier dispersion effect enables MRMs to handle data rates up to tens or even hundreds of GHz. In this specific investigation, MRMs are designed and fabricated for modulating Sub 6 GHz band signals in the 5G band. The integrated MRM array is connected to an RF probe for detecting Sub 6 GHz EM signals. Through the utilization of thermo-optic tuning by an integrated Titanium Nitride (TiN) heater, we successfully achieved high-density, wide-range near-field EM imaging consistent with simulation results.

In electromagnetic wave imaging, we currently employ thermo-optic tuning controlled by an electrical heater to select the modulator. However, this method necessitates a considerable number of external DC power supplies and electrical connections. As we look toward visualizing electromagnetic waves in higher frequency bands in the future, the abundance of electrical elements poses a challenge to further compacting the system. Moreover, specific situations, such as environments with explosives or flammable gases or those sensitive to electromagnetic noise, require optical control rather than electrical. In the conventional silicon photonics heating methods, direct heating of a silicon waveguide or slab proves more efficient (at the several nm/mW level) and faster (less than 1 μs) than indirect heating via an electrical heater integrated above the waveguide device. Indirect optical heating methods encompass techniques such as irradiation and metal absorption. On the other hand, direct optical heating methods have been less explored, with studies limited, for instance, to free-carrier absorption in microring resonators. An urgently needed development involves creating a convenient, simple, versatile, and efficient method for optical direct heating. A novel optical direct heating method is proposed here, utilizing a high concentration of doping to absorb and exothermally generate heat from the incoming control light. This heat is then diffused to the adjacent waveguide with the assistance of a highly thermally conductive silicon slab, enabling the tuning of the phase of the signal light in the adjacent

waveguide. This approach eliminates the need for any electrical devices and holds broad applications. Through careful design, we have realized an optical heating method that surpasses the efficiency of the electrical heating method while maintaining the same temporal response speed. Subsequently, we integrated this optical heater into an MRM array and verified the modulation selection of the MRM array using the optical control method. This integrated design opens up possibilities for visualizing 5G electromagnetic wave signals in higher frequency bands in the future.

In Chapter 2, we present an overview of the silicon optical foundry and the processes involved in fabricating silicon devices using Multi Project Wafer (MPW). The selected foundry for this study is the National Institute of Advanced Industrial Science and Technology (AIST) in Japan, utilizing 300 mm wafers and employing the ArF excimer laser immersion exposure process on Si waveguides to achieve a minimum linewidth of 80 nm. The Computer-Aided Design (CAD) layout in this study are generated through scripts, and the resulting gds layout files undergo Design Rule Check (DRC) before being taped out to the foundry. Additionally, we provide an overview of the common Si photonics components employed in this study, encompassing spot size converter (SSC), strip waveguide, rib waveguide, bending, directional coupler, p-n junction, microring resonator (MRR), microring modulator (MRM), electrical heater, and optical heater. For waveguide design, we calculated the width ensuring single-mode propagation using the Lumerical Finite-Difference Eigenmode (FDE) solver. The waveguide widths for strip waveguide and rib waveguide are 0.45 μm and 0.5 μm, respectively. A low-loss bending radius of 5 μm is employed for the waveguide bending part. Additionally, the coupling length and coupling spacing of the directional coupler were determined using the Lumerical Finite-Difference Time-Domain (FDTD) solver to meet specific coupling efficiencies for subsequent MRMs. The capacitance of the p-n junction, optical losses, depletion profiles, and optical modes were calculated using the Lumerical CHARGE solver and the FDE solver to achieve specific optical losses in the MRM. For MRR and MRM, our focus was on realizing critical coupling conditions and calculating the optical bandwidth. Regarding the electrical/optical heaters, their infrastructure is described, with a detailed comparison presented in Chapter V.

In Chapter 3, we presented the MRM, a vital electro-optical device of silicon photonics and the core of our investigation. Specifically, we designed and fabricated MRMs with a 10 μm radius and a Q-factor of around 4000, enabling adjustment of the resonant wavelength through an integrated TiN electrical heater. To optimize modulation, our aim was to maintain the MRM close to the critical coupling state. This involved establishing a specific correlation between the microring and bus waveguide coupling ratio and the in-ring losses from doping within the microring. The achieved device closely adheres to the intended specifications. The integrated TiN electrical heater demonstrates a heating efficiency of 0.17 nm/mW, ensuring flexibility in tuning the resonant wavelength. The MRM achieves a resonance depth of 17 dB, and the in-ring losses and coupling coefficients to the bus waveguide, assessed through parametric fitting, are in close agreement. This implies that the MRM is near the critical coupling state, resulting in a modulation extinction ratio exceeding 5 dB. The carrier depletion effect under reverse bias is harnessed in this study to attain a modulation efficiency of 9.94 pm/V, with a low $V_\pi L$ of 2.42 Vcm. Additionally, the MRM's optoelectronic bandwidth is approximately 30 GHz at wavelength of peak modulation efficiency, extending to over 40 GHz with the aid of the peaking effect (limited by the experimental equipment bandwidth). Modulating pseudo-random binary sequence (PRBS) signals up to 32 Gbps with the MRM produces clear eye patterns and extinction ratios exceeding 5 dB. Importantly, this high-performance modulation remains unimpacted by the self-heating of the MRM induced by the high-power optical input.

In Chapter 4, we organized the MRMs with high-performance design and electrically linked them to an RF probe equipped with non-resonant slot antennas from Arai Lab., forming an electromagnetic wave imaging system. Transmitting a 3.5 GHz sine wave signal from the source through a dipole antenna, we utilized the RF probe to receive the signal. Each antenna within the RF probe was connected to an individual MRM in the MRM array. Through a LabVIEW automation program, we modulated the electrical signals received by each MRM, outputting them sequentially. This process facilitated the

acquisition of the spatial intensity distribution of the electromagnetic waves emitted by the dipole antenna. The obtained results closely mirrored the simulation results, successfully imaging EM wave signals with different polarization directions. The study encompassed 441 imaging points, covering a total area of 3515 mm², achieved a dynamic range of imaging exceeding 20 dB and a cross-polarization discrimination surpassing 10 dB. Further optimization of the measurement environment holds the potential to enhance these metrics. Consequently, successful visualization of the signal strength of EM waves in the Sub 6 GHz band within the 5G spectrum was accomplished, opening avenues for potential visualization of EM waves in higher bands in the future.

In Chapter 5, we propose an all-optical control mechanism that eliminates the need for electrical components, with the primary goal of minimizing the system size. We introduce an optical heater employing a light absorption and exothermic approach. The control light is directed into a waveguide doped with a high concentration, where it is absorbed, emitting heat. This heat is then diffused from the silicon slab with high thermal conductivity to the adjacent waveguide, inducing a change in the effective refractive index and, consequently, altering the phase of the signaling light it transmits. The design incorporates optimized parameters such as the shape of the high concentration of doping, the length of the waveguide slab, waveguide spacing, and more. This optical heater is integrated into MZI-type and MRR-type optical switches, replacing the conventional electrical heater. The use of a 30 μm long triangular doped shape ensures gradual light absorption and uniform heat emission. Subsequent experiments revealed that for the MZI-type optical switch with the optical heater, only 17 mW of power was required for tuning to achieve the π-phase change, compared to 22.5 mW for the usual electrical heater. In the case of the MRR-type optical switch, both the optical heater and the electrical heater exhibited heating efficiencies measured at 0.19 nm/mW. These results demonstrate that the heating efficiency of the optical heater can surpass that of typical electrical heaters, ensuring a minimum switching response time of 12 μs, comparable to the usual electrical heating method.

In Chapter 6, our conclusion centered on validating the independent optical control of individual MRMs within an MRM array, demonstrating its suitability for integration into an electromagnetic wave imaging system. This accomplishment involved incorporating optical heaters into a 4-channel MRM array. In this configuration, all four MRMs share the same modulator design but feature distinct optical heater designs, allowing the selective influence of the input control light on each MRM. With an increase in control light power, the resonance wavelengths of the MRMs gradually separate and sequentially pass through the wavelength of the laser light source, facilitating the sequential modulation of electrical signals. In practical measurements, we achieved an MRM with a modulation efficiency of 8.6 pm/V and $V_{\pi}L = 2.37$ Vcm, confirming a tuning efficiency of up to 0.07 nm/mW. Optical selection of the four MRMs was accomplished by setting the wavelength of the laser light source at the appropriate position. Each MRM in the array can be independently selected and modulated, maintaining low interchannel crosstalk. This successful utilization of light to control the resonance tuning of individual MRMs within the array lays the foundation for realizing a more compact MRM imaging system in the 5G band.

Contents

Chapter 1
Introduction

1.1 Si Photonics

1.1.1 Overview

Silicon (Si) is one of the abundant elements in the Earth's crust, readily available, and relatively low in cost. Its stable physical and chemical properties enable it to exhibit excellent performance and long-term durability in various environments. As a common semiconductor material, Si is frequently used in large-scale integrated circuits (LIC) for its outstanding high-speed, low-power electronic signal processing capabilities. Si photonics is an integrated optoelectronics technology that enables the integration of optical and electrical components onto Silicon on Insulator (SOI) wafers for high-rate, high-density, low-loss signal processing. It is fully compatible with the Complementary Metal-Oxide-Semiconductor (CMOS) platform used in semiconductor integrated circuits (IC) manufacturing, which is one of the main reasons for its rapid development since its emergence. Figure 1-1 shows a 300 mm SOI wafer, a Si chip and optical devices.

Si photonics originated in the mid-1980s when Soref *et al.* proposed photonic integration by employing Si waveguide devices on a chip, leading to ongoing studies in this field[1-1]. The most important optical component in Si photonics is the optical waveguide. When Si is used as an optical waveguide in silica (SiO_2) cladding with a properly designed size, it exhibits a significant refractive index difference between the core and cladding. For light with a wavelength of 1550 nm, the refractive indices of Si and SiO_2 are approximately 3.45 and 1.45, resulting in an index difference of 40%. This high index contrast allows for efficient light confinement within the waveguide, enabling low-loss bending over several micrometers [1-2]. Meanwhile, other common passive components like intersection[1-3], splitter[1-4], arrayed waveguide grating (AWG)[1-5], directional coupler[1-6], multi/demultiplexer[1-7], etc. further enhance the richness and usefulness of Si photonics. Active devices such as Mach-Zehnder modulator (MZM)[1-8], microring modulator (MRM)[1-9], photodetector[1-10], etc. introduce electronics into Si photonics, making possible high-speed modulation and detection of optoelectronic signals.

Si based photonic integrated circuits (PICs) were also introduced in late 1980s [1-11]. With low-loss waveguides being first proposed in 1992 [1-12, 13], Si photonics has evolved from the era of small-scale integration with only tens of components in a single PIC to the era of large-scale integration with over 10^4 components integrated on the same PIC. This enables numerous important applications such as biological applications[1-14, 15], sensors[1-16, 17], optical interconnects[1-18, 19], photonics integration[1-20, 21], etc. These also include many applications that were previously difficult to realize with electronics alone, such as light detection and ranging (LiDAR)[1-21–23], high-speed optical computing [1-24–28], quantum computing, etc. The implementation of high density photonic integrated circuits by means of CMOS process technology enabling complex optical functionality on a compact chip at a low cost[1-29, 30].

The commercialization of Si-based integrated photonics platforms is seriously hampered by the fact that effective light sources cannot be achieved by relying on Si alone since Si is an indirect bandgap crystal. Although Raman lasing using Si photonics can be a solution[1-31, 32], the lasing efficiency is still a problem compared to active materials. Therefore, on-chip light source integration realized by adapting heterogeneous integration with III-V materials is an excellent candidate [1-33, 34]. On the

other hand, the Si photonics technology based on silicon nitride (SiN), which has become increasingly mature in recent years, has also increased the maximum input optical power supported on-chip, achieved lower light propagation and coupling loss[1-35], enabled waveguides with enhanced phase control in interferometric devices[1-36], and introduced good useful nonlinear characteristics [1-37]. The next generation of photonics large-scale integration technology allows Si photonics to grow to a new and unprecedented level by using more sophisticated and complex co-packaging techniques with electronics[1-38–40].

1.1.2 Applications

A.Optical Interconnect in data centers

With the recent boom in big data, cloud computing, Internet of Things (IoT), and machine learning (ML), artificial intelligence (AI), especially the explosion of conversational AI technologies such as ChatGPT, there is a growing demand for high-speed and high quality signal processing. This requires significant link capacity for high-speed data interconnections in data centers. Currently, data centers commonly use spine-leaf structures with a large number of connections and short distances between nodes, while the rapid growth in traffic has led to a rapid technological update of optical modules. Therefore, data centers are suitable for a large number of cost-sensitive but not demanding performance modules (Fig. 1-2). And all of these characteristics are met by Si photonics. Si photonics modules outperform traditional copper wires, and fiber optic connections are better suited for large-scale board-to-board interconnections. On the other hand, Si materials are more cost-effective than III-V materials, which is an advantage in data center applications.

The growing demand for data processing making chips run faster and faster, but optical signals must still be converted to electrical signals to communicate with chips on circuit boards located deep within data centers. Si photonics, however, can be co-packaged with other networking, storage, and computing application-specific integrated circuits (ASICs) using heterogeneous integration (co-packaging optics, CPO) to enable semiconductor optical I/O directly from the Si chip itself. As bandwidth to server nodes continues to expand and copper transmission distances shorten, there will be use cases for optical I/O from network interface cards (NICs) or directly from the server itself. As shown in Fig. 1-3, with a step-by-step process of moving the end of the fiber inside the PCB board, or even moving the optical I/O inside the Si-based chip through on-chip integration of the laser, we can maximize optoelectronic integration and significantly reduce data center power consumption and cost after mass production.

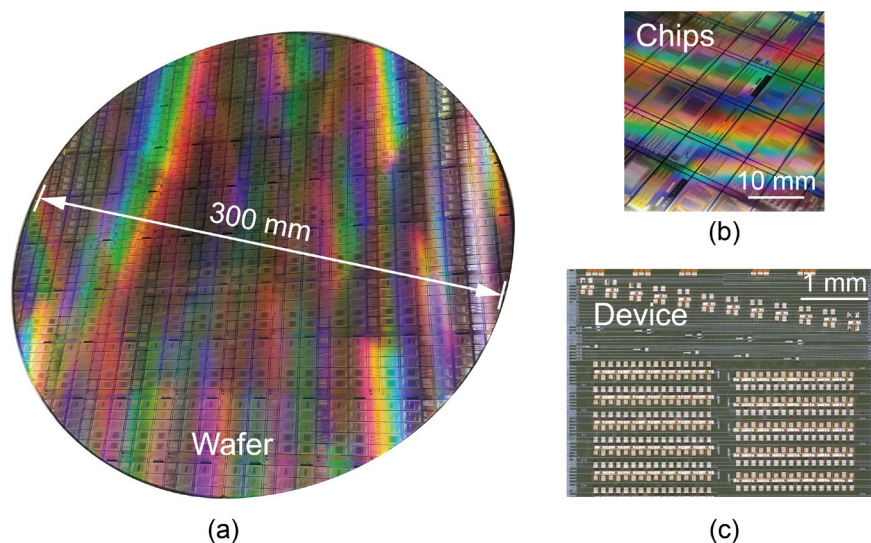Heat dissipation and power consumption in data centers have always been the focus of the industry.

Figure 1-1 (a) A 300 mm wafer fabricated by CMOS process on SOI wafer. (b) A photonic chip after dicing. (c) Si photonics devices.

In traditional technology, the optical signal first passes through the transceiver for photoelectric signal conversion, and then goes through the digital signal processing process to transmit the electrical signal into the chip. However, since the Si photonics technology uses chip-based optical transmission, removing a large number of traditional technologies in the cumbersome photoelectric conversion and processing, its overall power consumption will be significantly reduced. For data centers, a significant reduction in power consumption of IT equipment is the maximum efficient energy saving for the overall server room.

B.Sensing

With its excellent optical properties, Si photonics is also commonly used in biological and chemical sensing[1-41, 42]. Si photonics provides a biosensor solution that can be a good replacement for existing expensive, bulky, non-real-time traditional methods of molecular detection and analysis. For biosensing, Si photonics based optical sensors often use the evanescent field detection method [1-43–45]. When the concentration of biomolecules in the environment surrounding the sensor changes, the refractive index of the waveguide-based sensor will also change significantly. Through specified optical structures, such as Mach-Zehnder interferometers[1-46, 47], microring resonators[1-48, 49], micro-disk resonators[1-50, 51], photonic crystal waveguides[1-52, 53], photonic crystal lasers[1-54], etc., the change in local refractive index will ultimately be read out as a change in the intensity or phase of the output light. This enables sensitive, real-time, fast, label-free detection of biomolecules [1-55, 56]. Meanwhile, CMOS-based Si optical chip mass production technology allows such biosensors to be produced in large, compact quantities[1-57]. This also makes individual biosensors cheap and even disposable [1-54]. Furthermore, similar approaches can be applied to chemical sensing, with particular interest in gas sensing. It will help us to detect low concentrations of hazardous or combustible gases and also monitor the impact of changes in air quality on public health. Most of the gas sensors also monitor changes in gas concentration by indirectly measuring changes in the effective refractive index of the optical mode effected by environmental changes. Such changes can be the absorption of the infrared light evanescent field by gases such as carbon dioxide, methane, etc. [1-58–60], or the chemical reaction between ammonia, carbon dioxide, hydrogen, etc. with the Si waveguide coating [1-61–63]. Si photonics makes such bio/chemical sensors efficient, real-time, and inexpensive, providing a solution for public health and safety, hazardous environment monitoring, environmental health protection, and more.
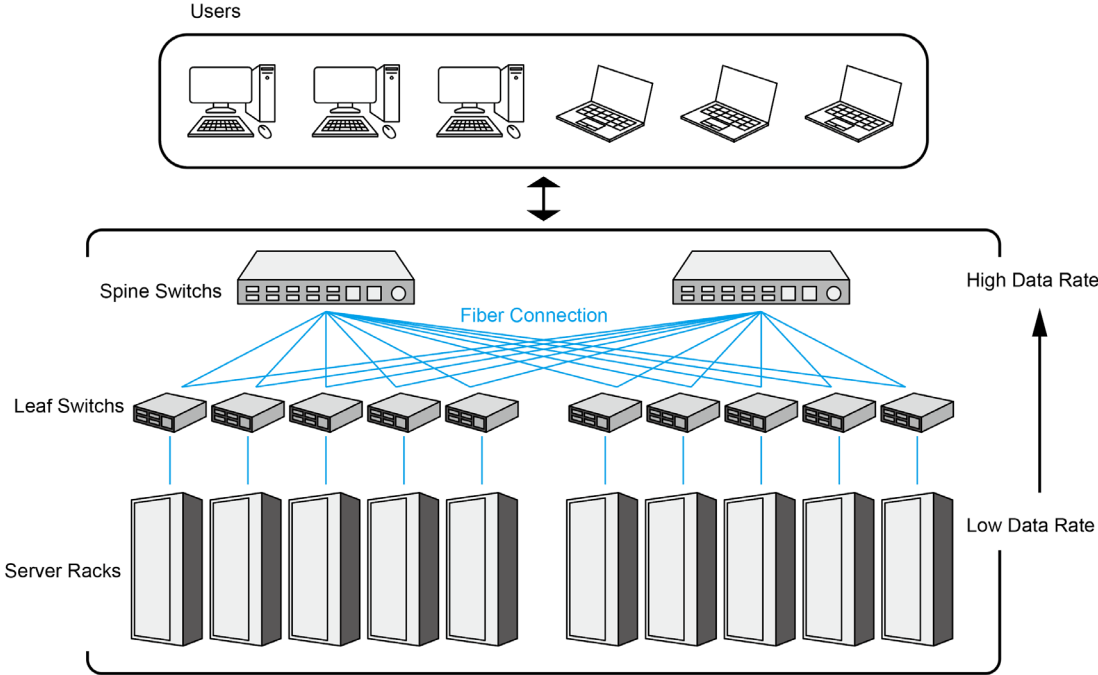

Figure 1-2 Spine-leaf configuration in data center with optical connection.
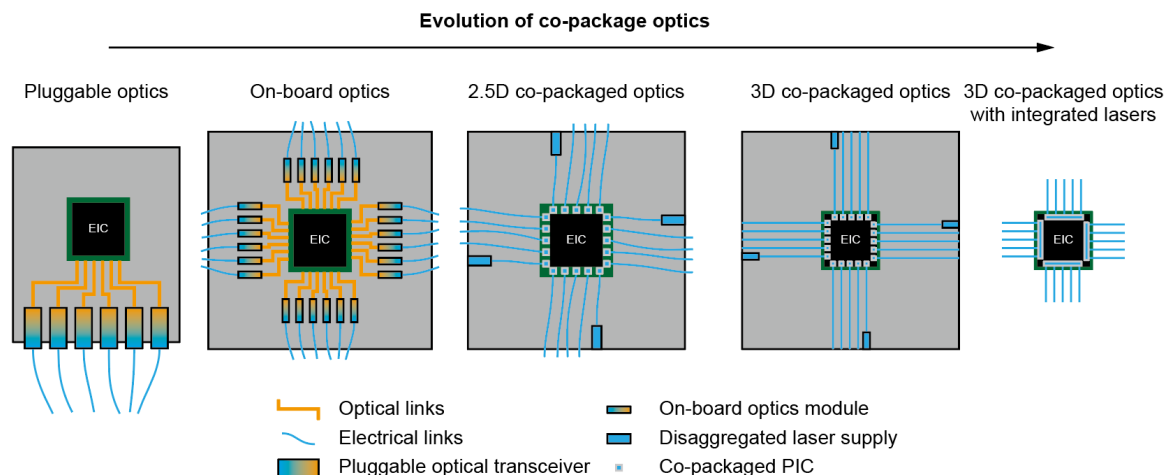
Figure 1-3 Evolution of co-package optics.

1.2   Si Microring Devices

To address the growing demand for data interconnections, we need to build larger scale optical interconnect networks on a single chip. As mentioned earlier, CMOS-based Si photonics enables large-scale optoelectronic integration while realizing optical interconnect networks with lower loss, higher speed, and higher quality. However, increasingly stringent requirements have been placed on the size of optical devices. Optical microrings have become a popular choice for optical devices due to their small footprint, high quality factor, and low reflection. Si-based microrings can be used as optical filters[1-64, 65] or optoelectronic modulators[1-66–68] after doping, or even as microring lasers and microring photodetectors by introducing optical gain or absorption mechanisms [1-69, 70]. These optical components cover almost all critical applications in optical interconnects.

1.2.1   Microring Resonator (MRR)

A. Overview

A microring resonator is a ring-type resonator with a radius typically ranging from a few microns to tens of microns. Based on the shape of the microring, there are circular[1-71], racetrack[1-72], and triangular[1-73] types. Compared to other photonic devices such as Mach-Zehnder interferometers, grating resonators, photonic crystal cavities, and couplers, microring resonators have simpler and more compact dimensions. On the other hand, Si-based microrings have a larger refractive index contrast than microring resonators made of other materials. This also enables the Si-based microring to have a smaller radius compared to other materials, while still maintaining lower bending losses. The relationship between the typical radius of the optical microring and the refractive index difference of the core/cladding layer using polymer[1-74–82], SiN[1-83–91], Lithium Niobate (LN)[1-92–101] and Si[1-71, 102–110] as the core material and silica as the cladding material is shown in Fig. 1-4. The refractive index difference between the core layer and the cladding layer Δn is calculated from Eq. 1-1.

$$\Delta n = \frac{n_1^2 - n_2^2}{2n_1^2} \tag{1-1}$$

Here, n_1 is the refractive index of the core material, and n_2 is the refractive index of the cladding material. The refractive indices of polymer, SiN, LN, and Si are approximately 1.57, 1.90, 2.20, and 3.45 here, respectively, and the refractive index of silica is 1.45. From Fig. 1-4, it can be observed that the larger the refractive index difference Δn, the smaller the minimum radius that can be achieved. Additionally, the bending loss of the waveguide is also influenced by the bend's design. For instance, bending loss can be further reduced by introducing a radial offset to the bending section[1-111, 112] or by using other kinds of curves instead of circular arcs[1-113].

Similar to microdiscs and microspheres, a microring resonator operates by allowing light entering the cavity to circulate multiple times through the same structure, leading to cumulative effects such as thermal light and electrical light. Figure 1-5 illustrated all-pass typed microring resonator and add-drop typed microring resonator. Typically, one (all-pass type) or two (add-drop type) bus waveguides are positioned alongside the rings to couple incoming and outgoing light. When the optical path length of the microring is an integer multiple of the wavelength of the input light, the input light will resonate within the ring and will appear in the transmission spectrum as a deep resonance. Consequently, multiple resonant modes appear in the transmission spectrum of the microring resonator. The wavelength difference between two adjacent resonant modes is known as the free spectral range (FSR). The FSR can be calculated using Eq. 1-2.

$$FSR = \frac{\lambda^2}{n_g L} \tag{1-2}$$

where λ is the wavelength of light, n_g is the group refractive index, and L is the ring circumference. Microring resonators can also operate at different wavelengths of light by simultaneously integrating more than one. Therefore, microring resonators are common optical devices in WDM, which we will discuss later. For such applications, a sufficiently large FSR is required to accommodate multiple wavelengths of signaling light, which also necessitates the microring resonator to be generally small in size.

B.WDM

Wavelength Division Multiplexing (WDM) is an optical communication technology that enables the transmission of multiple optical signals over a single optical fiber, each at a different wavelength (or frequency). The main principle of this technology is to leverage the fact that optical signals of different wavelengths can be transmitted simultaneously without interfering with each other. This increases the bandwidth and capacity of fiber optic transmission while reducing the complexity of the communication system. A typical WDM system is depicted in Fig. 1-6. At the input of WDM, optical signals of different wavelengths emitted by multiple lasers are simultaneously fed into an optical multiplexer (Mux). The optical multiplexer combines the optical signals of multiple wavelengths onto a single fiber. At the receiving part, the optical DeMultiplexer (DeMux) separates the multiplexed signals in the optical fiber into individual signals and routes them to the photodetector (PD) for reception through different paths. To accommodate optical signals of different wavelengths as efficiently as possible, it's necessary to minimize the spacing between adjacent wavelengths. However, this also increases the complexity of laser wavelength control and splitter filtering control simultaneously. Therefore, the International
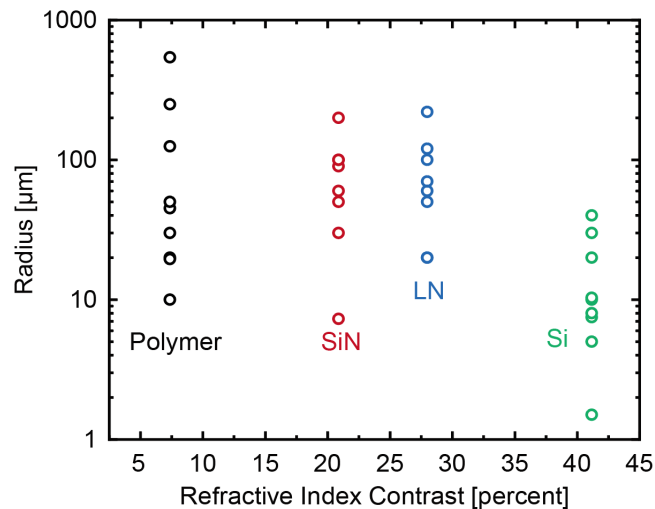

Figure 1-4 Relationships between radius and refractive index contrast in microrings made from different materials.

5

Telecommunication Union Telecommunication Standardization Sector (ITU-T) has proposed Coarse Wavelength Division Multiplexing (CWDM) and Dense Wavelength Division Multiplexing (DWDM) based on practical applications. Here, CWDM is used in low-data capacity scenarios, typically over distances of 50 to 80 km. It offers 18 wavelength channels at 20 nm intervals, starting from 1271 nm and ending at 1611 nm, covering five major optical communication bands from the O-band to the L-band. DWDM, on the other hand, is mainly applied to long-distance optical transmission and relies on optical amplifiers as a prerequisite. It has a much higher channel density with a channel spacing of 100 GHz (approximately 0.8 nm in wavelength). This poses a significant challenge to WDM system components, especially optical multiplexers and splitters. In practice, there are several ways to implement MUX and DeMUX. The thin-film filter type device can be customized easily based on the filtering parameters required by the system, but its optical loss tends to increase significantly with the number of signal light channels [1-114]. Grating-typed (De)MUX disperses or combines light of different wavelengths at different angles, but the spatial dimensions are often on the millimeter scale [1-115]. Array wavelength grating (AWG) disperses and combines optical signals of different wavelengths through the grating effect. It comprises an input waveguide, a grating structure, and an output waveguide, enabling the simultaneous processing of multiple wavelengths. But its relatively large size makes it unsuitable for miniaturized or portable applications[1-116, 117]. Although Si photonics allows for AWGs with a footprint of just a few micrometers[1-118], precise temperature control remains challenging [1-119]. Another approach involves using ultra-compact microring resonators, which will be introduced as follows.

In silicon photonics, to implement a WDM system, we can integrate optical splitters and optical multiplexers onto a Si optical chip, thus combining multiple input signals into a single waveguide or fiber, or separating signals of different wavelengths into multiple outputs[1-67]. This integration enhances fiber utilization and reduces system size and complexity. For direct modulated signal transmission (directly loading the transmitted electrical signal onto the laser carrier), we can use cascaded add-drop type microring resonators (microring resonator array) to achieve optical multiplexing of multiple directly modulated lights. In fact, for a multiplexer, an all-pass typed microring modulator array is more commonly used instead of a microring resonator to externally modulate the electrical signals loaded into the microring onto the optical carrier, as we will discuss in the next section. At this point, the realization of optical multiplexing can be achieved using devices such as diffraction gratings [1-120]. As shown in Fig. 1-7, we can also utilize a comb laser or microcomb ring to generate comb light at multiple wavelengths simultaneously, further reducing system complexity [1-121–123]. On the output side, we can employ an array of add-drop type microring resonators to extract multiple optical signals from the fiber to each branch and receive them using photodetectors. At this stage, the microring resonator serves as an optical filter. To filter out one of the many channels (wavelengths) of the signal without affecting the transmission of other signals, we must design the microring with a sufficiently high Q value to enhance its wavelength selectivity. The Q value is calculated by dividing the average energy stored inside the ring by the energy lost internally or coupled externally in each optical cycle. It can be obtained by dividing the resonant wavelength, λ_{res}, by the full width at half maximum (FWHM), as given in Eq. 1-3.

$$Q = \frac{\lambda_{res}}{FWHM} \tag{1-3}$$

For microring resonators, the Q value is limited by internal losses. In the case of Si-based microrings with radii lager than 5 μm, the bending loss of the microring is negligible. Since the microring resonator is not additionally doped, most of the internal losses arise from radiation losses caused by side-wall roughness. This roughness also induces the counterpropagating mode of the resonant light.

To use the microring resonator array for high-density WDM systems like DWDM, we need to consider the roll-off characteristics of the transmission spectrum, or the Lorentz function, of a single microring. When we aim for -3 dB crosstalk between the transmission spectra of two neighboring

microrings in a DWDM system with a channel spacing of approximately 0.8 nm, the FWHM of the microring's transmission spectrum should be 1.6 nm. According to Eq. 1-3, we can determine that the Q factor of a single microring only needs to be greater than 969. However, in practice, -3 dB of channel crosstalk is typically intolerable. To achieve the highest possible channel isolation and the smallest possible channel crosstalk, we need a larger Q value. However, considering the bandwidth of the transmitted signal, we also aim for the filter's passband ripple to be as small as possible, while the roll-off and stop band attenuation to be as large as possible. Accomplishing these adjustments can be challenging to achieve with a single microring, so higher-order microring is often used to create optical filters [73, 124, 125]. As the order of the microring increases, meaning the number of microrings becomes larger, its filtering characteristics become more box-like.
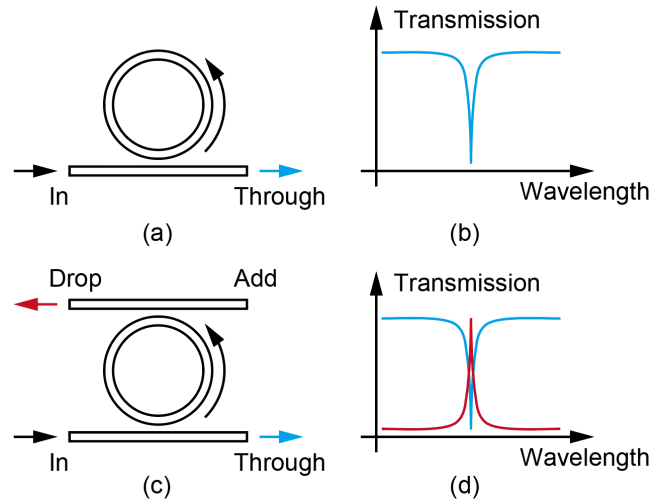

Figure 1-5 (a) All-pass type microring resonator and (b) optical transmission spectrum of through port. (c) Add-drop type microring resonator and (d) optical transmission spectrum from through and drop port.
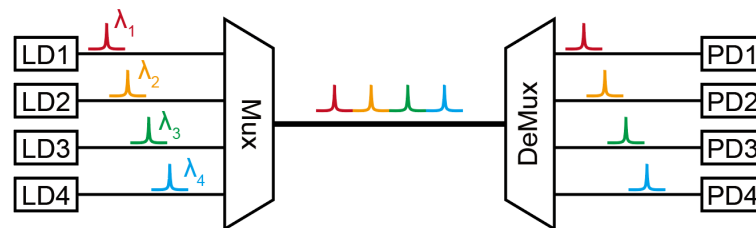

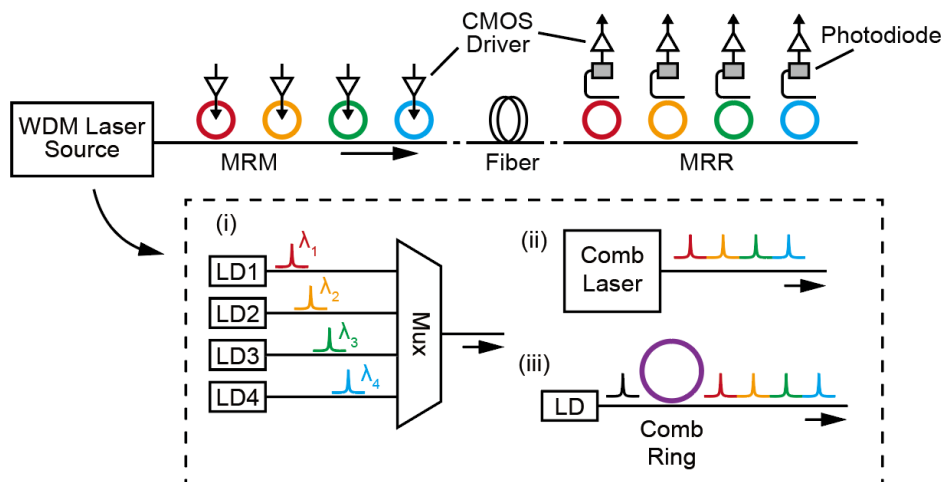Figure 1-6 Configuration of typical optical WDM system.

Figure 1-7 WDM system using Si microring devices.

1.2.2 Microring Modulator (MRM)

A.Overview

Based on the selective effect of the microring resonator on the wavelength of light, when the effective refractive index of the microring is modulated by some mechanism, the transmittance of the input light near the resonance wavelength changes significantly. Such mechanisms can be based on the thermo-optic effect, free carrier plasma effect, photovoltaic effect [1-70], quantum-confined Stark effect (QCSE) [1-126], pockels effect[1-127], etc. [1-1, 128]. For the thermo-optic effect, a change in the waveguide temperature can induce a change in the effective refractive index. Si exhibits a significant thermo-optic coefficient near 300 K (approximately 1.86×10^{-4} K^{-1}), making thermo-optic modulation an option for Si-based microrings [1-129]. However, the bandwidth of thermo-optic modulation is typically limited to the MHz level, which is highly dependent on the microring's structure, material, and heat capacity. As a result, the thermo-optic effect is often used in scenarios where high-speed modulation is not required. Examples include thermal tuning in WDM systems [1-130] and thermal feedback for electro-optical modulation of microring modulators [1-131, 132]. The most commonly used modulation method in Si microring modulators nowadays is electro-optical modulation based on the free carrier plasma effect [1-1]. Varying the concentration of free carriers in the ring leads to changes in both the real and imaginary parts of the material refractive index of Si. These changes are reflected in alterations of optical phase and optical amplitude (loss), respectively. Research on this topic dates back to the early days of Si photonics [1-1]. Soref and Bennett examined the quantitative relationship between changes in refractive index and absorption coefficient induced by carrier concentration at different wavelengths. Eqs. 1-4, 5 depict the empirical relationship between the refractive index change Δn of the waveguide and the associated loss as a function of carrier concentration in 1550 nm[1-1].

$$\Delta n = \Delta n_e + \Delta n_h = -8.8 \times 10^{-22} \times \Delta N_e - 8.5 \times 10^{-18} \times (\Delta N_h)^{0.8} \tag{1-4}$$

$$\Delta \alpha = \Delta \alpha_e + \Delta \alpha_h = 8.5 \times 10^{-18} \times \Delta N_e + 6.0 \times 10^{-18} \times \Delta N_h \tag{1-5}$$

where ΔN_h is the change of free hole concentration, ΔN_e is the change of free electron concentration. It revealed the principle of refractive index change due to the free carrier dispersion effect and noted that electro-optical modulation based on this effect would also introduce some inevitable light intensity attenuation.

A typical construction of a Si-based microring modulator and its static modulation characteristics are depicted in Fig. 1-8. It's important to note that this modulator is based on a microring resonator but differs from a typical microring resonator. To achieve carrier concentration modulation in the ring via applied voltage, both p-type and n-type doping are applied to the microring. Additionally, to direct carriers into or out of the Si waveguide, electrodes are connected to the waveguide using a Si slab. Consequently, ridge waveguides are used in all microring modulators.

Depending on whether doping is applied directly to the microring, we can categorize microring modulators as carrier depletion or carrier injection modulators, utilizing the carrier depletion effect and carrier injection effect, respectively [1-133, 134]. In addition to these, some microring modulators also utilize carrier accumulation effects [1-135], which we won't delve into further at this time. These junctions are also widely used in other types of electro-optical modulators, such as Mach-Zehnder modulators (MZM), for example.
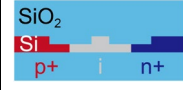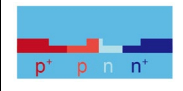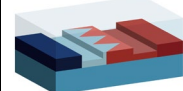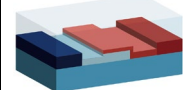
The structure of a carrier injection type microring modulator is illustrated in Fig. 1-8(a). In this type of microring modulator, we typically use forward bias to inject carriers into a Si waveguide, causing a change in the refractive index of the waveguide. Therefore, this microring waveguide is electrically equivalent to a PIN diode operating under forward bias. The highly doped region is positioned away from the waveguide, with the undoped Si waveguide in the middle, referred to as the intrinsic region. This type of microring modulators is known for its high modulation efficiency and low optical losses. However, its modulation bandwidth is limited by the forward diffusion capacitance, which usually has a bandwidth of only a few hundred MHz. This limitation can be addressed by employing a pre-emphasis

drive signal [1-68] or by incorporating an equalizer circuit [1-136, 137].

As for the carrier depletion microring modulator, its structure is shown in Fig. 1-8(b). Its waveguide is doped with p-type and n-type dopants, and the slab plateau for electrode contact are highly doped with p+ and n+ dopants. This type of microring is typically operated at the reverse bias voltage, where the waveguide can be electrically equated to a PN junction operating under reverse bias. When microring is zero-biased, there is a certain concentration of carriers inside the waveguide. When reverse bias is applied, the width of the depletion region enlarges, the carrier concentration in the waveguide region decreases, and the effective refractive index of the waveguide increases, resulting in reduced losses. Usually, the higher the pn doping concentration, the larger the refractive index change under the same bias [1-138], but it also introduces higher optical losses. To minimize the optical loss due to doping, the typical doping concentration is around 1×10^{17}~1×10^{18} cm^{-3}. The small junction capacitance of the reverse-biased pn junction, approximately 0.2~0.8 pF/mm, results in a low modulation efficiency of the depletion-type microring modulator. However, this also enables the microring modulator to have a smaller RC time constant and a larger electrical bandwidth. Non-return-to-zero (NRZ) modulation at more than 100 Gbps is now achievable[1-139–141]. Therefore, depletion-type modulators are often used in high-speed Si optical modules [1-102]. Additionally, to further enhance the modulation efficiency of depletion-type microrings, some microring modulator studies offset the center of the PN junction from the center of the waveguide[1-142, 143]. This adjustment is based on the fact that the refractive index change caused by a variation in hole concentration is greater than that caused by a change in electron concentration [1-1].

To enhance the modulation efficiency of depletion modulators, researchers often concentrate on optimizing the shape of the pn junction. As illustrated in Table 1-1, Li *et al.* employed the interleaved junction [1-144], where p-type doping and n-type doping alternate in the direction of optical mode propagation. This arrangement increases the overlap between the depletion region and the optical modes, consequently boosting modulator modulation efficiency [1-108, 109, 145–147]. This can also be understood as having multiple junction capacitances in parallel, enhancing charge storage and thereby increasing modulation efficiency. Similar to interleaved junctions, zig-zag type junctions have been proposed by Xiao *et al.*, further improving modulation efficiency [1-106, 148]. However, the larger junction capacitance leads to a reduction in the modulation rate. Moreover, this type of junction demands higher doping accuracy. Another common configuration includes L-shaped [139, 1-149] or U-shaped junctions [1-149], in which pn junctions are created vertically within the optical waveguide using particular ion implantation. This results in a larger overlap of the depletion region with the optical modes, leading to increased modulation efficiency. Among these, the U-shaped junction provides an even larger junction capacitance facing area, achieving a greater overlap of optical modes and the depletion region, thereby increasing the modulation efficiency. However, the fabrication of this pn junction involves two stages of ion implantations with different energies, making the process more complex [1-150].

Table1-1 Comparison of modulator using carrier injection and carrier depletion.

Method	Junction Model	Ref. (Year)	R [μm]	Q	Modulation Efficiency [pm/V]	$V_\pi L$ [Vcm]	Speed [Gbps]	V_{pp} [V]
Carrier Injection (pin diode)		[1-66] (2005)	6	39350	139[*]	-	1.5	6.9
		[1-68] (2007)	5	20000	50[*]	-	12.5	16[#]
		[1-151] (2007)	12	12000	-	-	18	8[#]
		[1-152] (2010)	2.5	3000	-	-	1	0.15
		[1-137] (2014)	5	9000	104.7[*]	-	9	2
Carrier Depletion (pn diode)		[1-143] (2009)	15	14500	18	1.5	10	2
		[1-153] (2010)	5	9000	16.5	-	12.5	3
		[1-103] (2011)	7.5	8000	22	-	25	1
		[1-147] (2012)	48[^]	7500	29.4[*]	0.76	40	1.6
		[1-106] (2012)	10	8015	16	1.7	44	3
		[1-109] (2012)	30	29400	40	0.68	25	2
		[1-102] (2017)	5	9900	30.1	1.39	-	-
				2200	45.1	1.39	56	1
		[1-139] (2019)	10	5000	26.9	0.52	128	2.4
		[1-154] (2022)	10	2740	62.1	0.85	50	4.5

[*]Estimate by author
[#]After pre-emphasis
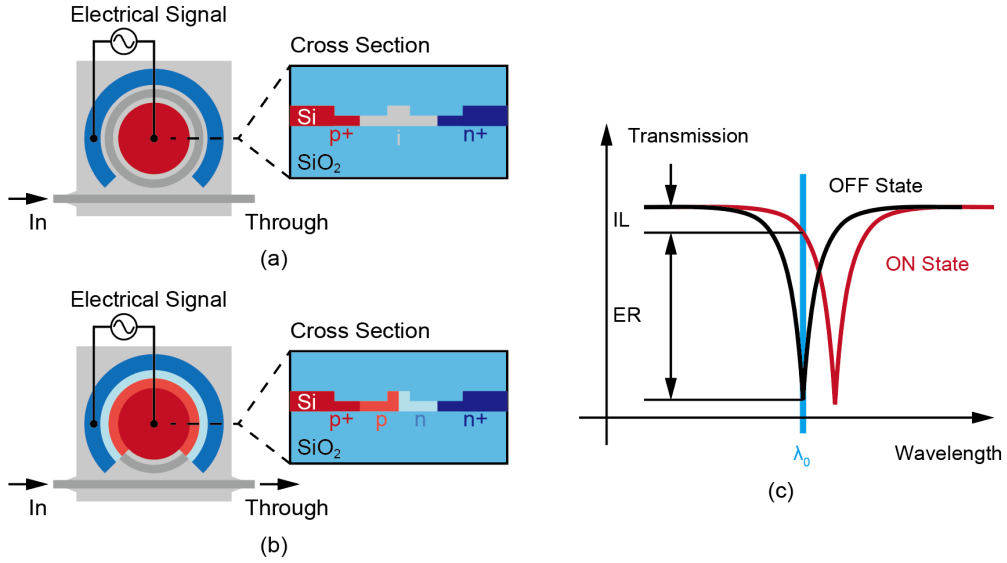[^]Equivalent radius of racetrack ring

Figure 1-8 Typical configuration and cross section of (a) carrier injection type MRM and (b) carrier depletion type MRM. (c) Electro-optic modulation by shifting resonance of MRM.

B. High-quality Electro-optical Modulation

To achieve high-speed, high-efficiency, low-power, low-footprint electro-optic modulation, it's essential to analyze and optimize each parameter of the microring. For electro-optical modulation using a microring modulator, the key parameters include microring modulator footprint (or microring radius), FSR, Q factor, extinction ratio, insertion loss, modulation efficiency, $V_\pi L$, optical/electrical bandwidth, electro-optical bandwidth, and the tuning efficiency of the heater used for thermal tuning.

A larger microring radius corresponds to a smaller FSR. Typically, for a Si-based microring modulator with a radius of 10 μm, its FSR is approximately 9 nm. In WDM communications, a wider FSR allows for more channels, but it also necessitates a smaller radius. This reduces the device's footprint while increasing design complexity and the precision required for the fabrication process. Smaller microrings result in shorter phase modulator lengths and larger $V_\pi L$. As seen in Table 1-1, typical microring modulator radii are around 10 μm. The Q factor indicates the sharpness of the resonance peak of the microring, affecting the extinction ratio ER of the modulation in the microring modulator's performance. Achieving high extinction ratio modulation, which alters the refractive index or internal loss of the microring, involves ensuring that the microring is in the critical coupling condition as much as possible (i.e., the internal loss matches the energy coupled in from the bus waveguide). Additionally, it requires a sufficiently large Q value and high modulation efficiency to make the transmittance spectrum of the microring vary significantly with the applied voltage at specific wavelengths. Therefore, modulation at specific wavelengths near resonance (typically around −3 dB transmittance) results in a large modulation extinction ratio. The position of these specific wavelengths (operating points) also impacts the insertion loss IL of the microring.

The relationship between ER and IL is depicted in Fig. 1-8(c). On the other hand, modulation efficiency describes the change in refractive index or the resonance shift that occurs per unit voltage caused by carrier dispersion effects. $V_\pi L$ denotes the value of voltage required to induce a change in phase of π, multiplied by the length of the phase shifter portion of device. As the length of the phase shifter increases, it moderates the V_π requirement, making $V_\pi L$ a parameter that integrates this trade-off relationship with a unit of Vcm. The typical $V_\pi L$ for a carrier depletion modulator is 1.5 Vcm, while for the carrier injection type, it is 0.02 Vcm, which is two orders of magnitude smaller than that of the carrier depletion modulator. Eq. 1-6 shows the electro-optical modulation bandwidth f_{3dB} of the microring modulator in relation to the optical bandwidth f_Q and the electrical bandwidth f_{RC} [1-143, 147, 155]. The optical bandwidth f_Q is determined by the photon lifetime τ (Eq. 1-7), and its relationship with the Q factor is shown in Eq. 1-8. The smaller the Q factor, the shorter the time photons are confined in the

11

microring, resulting in a shorter photon lifetime in the microring and a larger optical bandwidth. On the other hand, the electrical bandwidth f_{RC} is determined by the electrical characteristics of the microring, as shown in Eq. 1-9. Both the reduction of the microring junction resistance and the junction capacitance increase the electrical bandwidth. Additionally, other electrically connected parts of the microring also affect the overall electrical bandwidth. Therefore, conducting an overall equivalent circuit analysis of the microring modulator is an important step in understanding its modulation performance. Numerous studies have been conducted to fully analyze and optimize the equivalent circuit of microring modulator [1-102, 103, 106, 108–110, 145, 156, 157]. Furthermore, slightly shifting the laser wavelength from the resonant wavelength of the microring, known as the peaking effect [1-104, 107], can also extend the modulation bandwidth, although at the cost of reduced modulation efficiency.

$$\frac{1}{f_{3dB}^2} = \frac{1}{f_Q^2} + \frac{1}{f_{RC}^2} \tag{1-6}$$

$$f_Q = \frac{1}{2\pi\tau} \tag{1-7}$$

$$\tau = \frac{Q\lambda}{2\pi c} \tag{1-8}$$

$$f_{RC} = \frac{1}{2\pi RC} \tag{1-9}$$

In some systems, such as WDM applications involving MRM/MRR or its arrays, alignment of the microring's resonance becomes necessary due to inevitable fabrication errors [1-102, 158, 159]. To achieve a wide range of tuning in such cases, a thermo-optic heater is generally required. The tuning efficiency of the heater is defined as the shift of the resonant wavelength achieved per unit power and is closely related to the heater's design. To reduce the power consumption of the heater, many studies have optimized the heating method of the heater. Commonly used thermo-optic heaters, as shown in Table 1-2, are typically constructed from materials like Ti, TiN, W, etc., and are placed in the SiO_2 clad above the microring. While this design is simple and straightforward to fabricate, it comes with the potential drawback that the electrodes and wiring of the heater may interfere with those of the modulator. Moreover, the thermo-optic coefficient of silica, which serves as the cladding, is two orders of magnitude lower than that of silicon (8.5×10^{-6} K^{-1}) [1-160, 161]. This means that the heat generated by the heater may not be efficiently conducted to the Si microring waveguide. Therefore, an alternative approach is to integrate the heater directly into the Si waveguide, benefiting from Si's better thermal conductivity[1-139, 162–164]. To make the waveguide or a part of the Si slab a thermo-optic heater, partial doping is required. However, high-concentration doping may introduce unwanted optical losses, so the heater should be placed away from the waveguide that propagates the signal light. Nevertheless, this will reduce heating efficiency. Designers must consider the trade-off relationship between them. Furthermore, the method that heats the waveguide directly by adapting bias current via a conventional modulation electrode is also attractive[1-165, 166]. However, the available range of temperature change is limited. Another strategy to reduce unwanted thermal diffusion and increase thermal tuning efficiency is to introduce air trenches or substrate isolation [1-167], although this may decrease the heating speed of the microheater[1-168].

On the other hand, the high-temperature coefficient of Si also makes the microring extremely sensitive to unintentional ambient temperature changes. The variation of the microring resonance wavelength with respect to temperature is expressed by Eq. 1-10 [1-169, 170].

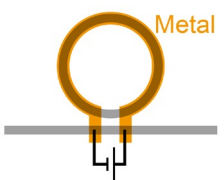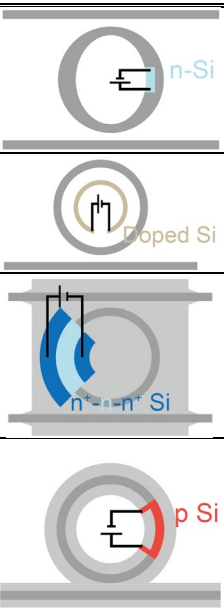$$\frac{d\lambda}{dT} = \frac{\partial n_{eff}}{\partial T} \frac{\lambda_0}{n_g} \tag{1-10}$$

where λ_0 is resonant wavelength, n_g is group index. In typical designs, temperature changes greater than 1 K can prevent the microring from functioning properly [1-171]. Therefore, to achieve stable electro-optical modulation, we can either reduce the temperature dependence of the device through athermal

design or by calibrating and locking the wavelength with the help of thermo-optic feedback tuning. Athermal design includes using negative thermo-optic materials [1-172, 173] or implementing interferometric structures to counteract thermal interference [1-174, 175]. Another common method using thermal feedback is to change the voltage of the thermo-optic heater of the microring by employing an on-chip integrated photodiode or an off-chip photodiode to monitor changes in light intensity from the drop port [1-131, 162, 176]. For on-chip integrated photodetectors, the photodiode can be integrated inside the ring with the help of an in-resonator defect-state-absorption (DSA)-based photodetector [1-164, 177]. Some studies have directly monitored the microring resonance state with an infrared camera to regulate the heater [1-178]. Others have eliminated the effect of ambient temperature on the modulator using balanced homodyne locking [1-179]. Some have directly monitored the output light intensity of the through port to regulate the resonance of multiple microrings [1-180].

On the other hand, whether the material is a metal or a semiconductor, electrical heaters remain the primary method for controlling signals through the thermo-optic effect in most research [1-169]. However, in specific environments or situations, using electrical heaters or other electrical devices may not be the optimal solution. In the case of large-scale integrated optical circuits, such as large-scale optical switch arrays [1-181–183], the inclusion of thousands of thermo-optic micro-heaters can significantly complicate the design, wiring, and place extreme demands on electrical drivers. Moreover, the heating efficiency and switching speed of microheaters placed in the cladding are often insufficient, resulting in increased overall power consumption and delayed response times in large-scale switching systems. Furthermore, in extreme environments, like optical signal processing at cryogenic temperatures, electrical devices and even electrical wiring generate significantly more heat compared to optical connections such as optical fibers. It can negatively impact heat dissipation capabilities, as seen in applications like cryocoolers [1-184] and superconducting systems such as superconducting quantum circuits [1-185] operating under cryogenic conditions [1-186]. Additionally, gas sensors in environments with explosive gases often prefer optical methods other than electrical connections [1-187].

There have been many important, novel studies on all optic control. For example, optically heating microspheres to tune the resonance of whisper gallery mode (WGM) or to realize specific wavelength filtering[1-188–190], Si plasmon waveguide heaters using surface plasmon polaritons (SPPs) [1-191–193], and so on. However, there is potential to improve their efficiency, simplicity, and ease of fabrication. In Si microrings, the use of FSR spaced pump and signal light to control the resonance of the microring resonator suggested a new on-chip all-optical control method [1-194]. However, this kind of resonance controlling restricts its application in non-resonant cavities. Therefore, we require a universal, simple, and efficient all-optical control method that is CMOS-compatible, scalable, and convenient for remote control. In this study, we propose a similar approach that uses the doped waveguide as a heater, but unlike these studies, we do not need to use any electrical components for thermo-optic controlling. This will be described in detail in Chapter 5.

Method	Junction Model	Ref. (Year)	Material	Thermal Tuning Efficiency [pm/mW]	Power for FSR tuning [mW]	Tuning Speed [µs]
Traditional Heater		[1-195] (2007)	Ti	285.7	42	14
		[1-196] (2008)	Metal	250	35	-
		[1-197] (2009)	Ti	161.6	21	10
		[1-198] (2010)	Ti	424	46	-
		[1-168] (2010)	Ti[*]	4800 (4 µm radius)	2.4	170
		[1-168] (2010)	Ti[*]	2700 (10 µm radius)	2.4	170
		[1-167] (2010)	Ti[*]	909.1	21	9
		[1-167] (2010)	Ti	704.2	27	-
		[1-153] (2010)	Ti	417	46.8	-
		[1-199] (2010)	Ti	87	46	-
		[1-154] (2022)	TiN	150	111.7	-
Slab/Waveguide Heating		[1-200] (2009)	Doped Si	2250	20	1
		[1-163] (2013)	Doped Si	1600	10.6	-
		[1-162] (2015)	Doped Si	250	50	-
		[1-201] (2019)	Doped Si	252.1	48	0.9
		[1-139] (2019)	Doped Si	188.6	39	-

[*]With air trench

14

1.3 Radio over Fiber (RoF)

1.3.1 Overview

Nowadays, mobile communication has become an essential part of people's lives. However, RF-based mobile communication has dead zones in specific places such as train tunnels, underground shopping malls, upper floors of high-rise buildings, and remote mountainous areas. Although adding new base transceiver stations is effective, other methods need consideration when setup area or budget constraints exist. Remote transmission of RF signals using coaxial cables may seem feasible, but coaxial cables have high RF bandwidth signal losses. On the other hand, optical signal transmission through fiber optics can extend over thousands of meters, suffering just a fraction of the loss of coaxial cables. Additionally, optical communication boasts a high bandwidth of up to 100 GHz per channel, hundreds of times greater than wireless communication with a bandwidth of only a few GHz, making it possible to dramatically increase communication speeds. Therefore, using optical fiber to transmit RF signals has become a proven solution. Radio over Fiber (RoF), which propagates radio signals over optical fiber, has been widely studied and applied. It combines optical and microwave communication technology to leverage the freedom of wireless communication and the characteristics of optical communication: low loss, low delay, high bandwidth. This enhances the bandwidth of wireless access networks and provides users with "anywhere, anytime, anything" services. Using optical fiber for signal transmission can overcome geographical and cost limitations, making it an effective solution to address mobile communication dead zones, extend transmission distances, enhance communication bandwidth, and reduce communication costs.

The basic realization of an RoF system involves modulating the baseband signal with a radio frequency (RF) wave, and then transmitting it using an optical link. At the receiving end, the RF signal is recovered, transmitted through the antenna to receive the RF signal, and then demodulated at the mobile or fixed terminal to obtain the baseband signal (see Fig. 1-9). Simultaneously, the mobile terminal can make service requests to the service provider through the RoF system, enabling two-way interactive communication. RoF systems offer several advantages:

1. Long transmission distance and low transmission loss: Microwave signals experience increased loss due to absorption and reflection as the frequency rises, making it necessary for high-frequency RF signals to have expensive regeneration equipment for long-distance distribution. In contrast, single-mode fiber (SMF) used in optical communication has lower losses in the O-band and C-band, which are much lower than those of other communication lines. Therefore, optical fibers enable much longer communication relay distances.

2. Large transmission capacity: Optical fiber communications in the O-band and C-band can accommodate a total bandwidth of more than 20 THz. Using WDM configurations, different signals with different wavelengths of light can be loaded into the same fiber for transmission, with sufficient intervals between wavelengths to prevent interference.

3. Anti-electromagnetic interference: RoF communications are immune to electromagnetic interference since the signal transmission medium is optical fiber, which does not generate electromagnetic induction like coaxial cables. This characteristic ensures that RoF systems are secure and private, free from electromagnetic noise in the communication link.

While early RoF systems were initially developed to address spectral congestion issues in millimeter
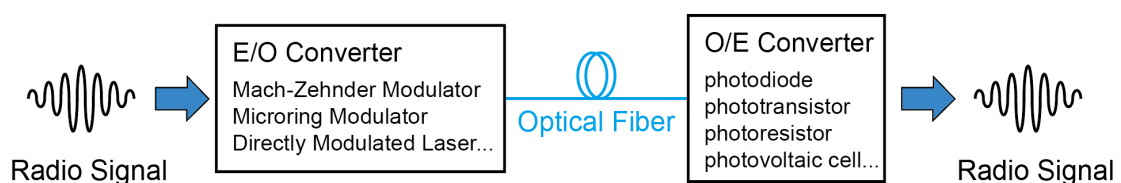

Figure 1-9 Concept of RoF system.

wave communication, they are now poised to play a crucial role in ultra-high-speed wireless transmission strategies, especially with the widespread deployment of fiber optic networks and the popularity of smart mobile devices[1-202, 203]. The emergence of the fifth generation of mobile communications (5G) has further emphasized the significance of RoF technology, particularly the analog signal transmission scheme (A-RoF), in mobile front-end communication systems. RoF-based mobile communications can greatly contribute to the development of centralized radio access networks (CRANs). Figure 1-10 provide an overview of the infrastructure of a mobile front-end communication system employing RoF. In this setup, a centralized baseband unit (BBU) generates RF signals and transmits them over optical fibers. The remote radio head (RRH) at the cell site demodulates the RF signals from the received optical signals and sends them to mobile devices via antennas. This transmission direction is referred to as the Downlink. Similarly, communication requests from users in the opposite direction can be handled by the RoF system, which constitutes the Uplink. The portion of the network from the BBU to the RRH is known as the fronthaul, as it is closer to the end-users. The segment from the core network to the BBU is termed the backhaul.

RoF technology extends beyond its primary application for signal processing and transmission between BBUs and RRHs. Its architecture makes it suitable for various situations requiring remote control, monitoring, or signal distribution/collection, where issues like power fading and high costs associated with long coaxial lines or airborne propagation are not acceptable. For instance, RoF systems find utility in critical applications such as remote Foreign Object Debris (FOD) detection near airport runways, enhancing security measures[1-204]. They can also facilitate zoned communication to high-speed mobile terminals, reducing delays and energy consumption associated with cross-zone switching. One notable example is the use of RoF and a distributed antenna system (DAS) for mobile communication on high-speed trains, distributing millimeter waves via the RoF system to each train compartment, enabling large-capacity and stable communication[1-205]. Furthermore, RoF technology can be applied in various fields, including ultra-wideband vertical-cavity surface-emitting laser (VCSEL) radar systems[1-206], high-resolution radar imaging systems in the Ka-band[1-207], beamformers for 5G millimeter wave beam self-steering[1-208], and reconfigurable RoF systems for Ubiquitous Power Internet of Things (IoT) [1-209] and so on.

1.3.2 RoF with Si Photonics

In RoF systems, the conversion of optoelectronic signals and the efficient transmission of signals are critical. These functions can be effectively achieved using Si photonics technology. Moreover, RoF systems employing Si optical technology can be designed to be more compact and energy-efficient. Si photonics technology is typically deployed at the BBUs and RRHs to process incoming microwave or millimeter wave signals.

Si optical modulators can be used as generators and transceivers of RoF signals. For downlink signal generation, Tong *et al*. implemented a remote radio front (RRF) for a millimeter wave analog RoF system using Si-based MZM and MRM cascade configurations to achieve 40 GHz millimeter wave Orthogonal frequency-division multiplexing (OFDM) signal generation [1-210], while employing single-sideband (SSB) modulation to increase the system's tolerance to fiber dispersion. Van Gasse *et al*. used GeSi Electro Absorption Modulators (EAMs) with MZI structures to achieve 64- quadrature
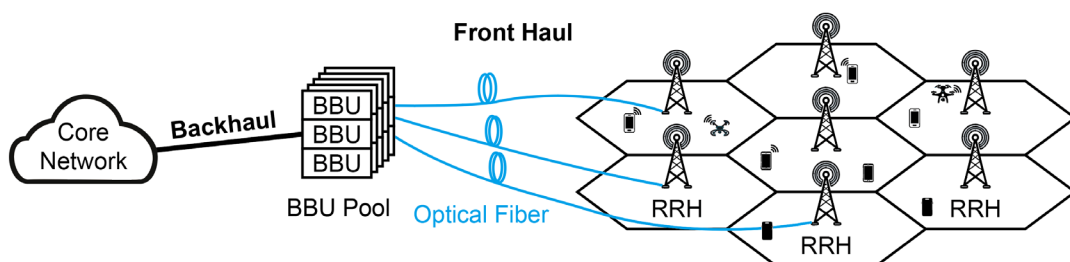

Figure 1-10 Configuration of CRAN with RoF.

amplitude modulation (QAM) data upconversion of 1.5 GHz intermediate frequency (IF) signals to any carrier frequency from 7 to 26 GHz, validating the high degree of integration of RoF up/downconverters and transceivers using Si photonics [1-211]. The carrier suppression approach ensures that the photodiode is not saturated by optical carriers that do not contribute to the signal. In the uplink direction, high-speed optical receivers have also been realized on Si platforms. For example, Bogaert *et al*. presented a 36 Gbps high-speed optical receiver for RRH based on a Si photodetector and a co-designed GaAs low-noise amplifier [1-212]. Ko *et al*. presented Si-based avalanche photodiode (APD) photonic-wireless interface (PWI) integrated circuits (ICs) realizing 5 GHz RoF and 60 GHz baseband over fiber [1-213].

In addition, Si photonics-based WDM systems are often used to increase data capacity, save carrier resources, and enable high-speed switching. For example, a large-scale 4.781 Tbps-class high-capacity Si-based RRH for massive multiple-input-multiple-output (MIMO) was realized, utilizing a 24-wavelength WDM system [1-214]. Furthermore, a 5G RoF service to a passive optical network (PON) by reusing carriers was achieved using Si-based microring devices [1-215]. Additionally, WDM operation of an A-RoF platform based on a 4×4 switch array of Si microring resonators was realized [1-216].

On the other hand, with the advent of 5G communication, mobile communication is progressing toward high-speed and high-capacity capabilities. To achieve high-speed and high-quality communication, mobile device antennas have become increasingly complex. Therefore, quality inspection of mobile device antennas has become essential. In manufacturing plants and similar environments, there's a need for large-scale, fast, real-time remote imaging of the electromagnetic (EM) fields emitted by fabricated antennas. Traditional electromagnetic imaging systems are bulky, experience high signal loss when used for remote monitoring via electrical cables, and require electrical amplification for weak EM signals, especially high-frequency ones (such as millimeter waves) [1-217, 218]. This amplification leads to increased energy consumption. Hence, using RoF systems for imaging electromagnetic field imaging is a novel option. To achieve large-scale, high-precision imaging of electromagnetic wave signals, array-type components are necessary to provide scanning functionality. To achieving compact device footprints, microring modulators are suitable, as previously mentioned. While most RoF systems using microring devices use a WDM configuration for efficient channel utilization and spectrum enhancement, simpler configurations can be applied for tasks like EM wave imaging, as shown in Fig. 1-11(a).

For electromagnetic wave detection, dedicated antenna arrays can be integrated into a PCB or Si optical chip. In this study, given the imaging object is the Sub 6 GHz band signal of the 5G specification, corresponding to a centimeter-level antenna size, the antenna probes must be integrated on an external PCB, and the received EM wave signal is transmitted to the modulator via suitable electrical connections. For electromagnetic wave imaging in the millimeter wave band, millimeter-level antenna arrays can be directly integrated onto Si chips and connected to the modulator closely and directly through methods like wire bonding or transfer printing. In the modulation configuration, a single laser light source can be used. Thermo-optic tuning allows each microring to actively adjust to the light source's wavelength and modulate and transmit the signal. The design of each microring modulator in the array remains consistent to ensure their resonant wavelengths are essentially the same (as shown in Fig. 1-11(b)), although this consistency may be compromised somewhat by fabrication errors. When the RF antenna array is exposed to electromagnetic wave signals of the corresponding frequency band, the signals detected by each RF antenna at different locations are loaded onto the microring modulators connected to them. When the microring modulator's wavelength is tuned to a fixed laser wavelength via a thermal optical heater, the RF signals received by the microring modulator are loaded onto the optical carrier and transmitted through an optical fiber to a remote photodiode (PD). The photodiode recovers the RF signal from the modulated light, and its intensity is displayed as a pixel point in the visualization map, as shown in the Fig. 1-11(a). Compared to a typical WDM system, this approach requires only one laser light source, reducing the system's cost. Additionally, even when using multiple microrings with different

designs to implement WDM, resonance wavelengths are likely to shift due to fabrication errors, necessitating multiple heaters to work simultaneously to maintain a uniform resonance distribution and spacing in wavelength. This not only consumes extra power but also increases control complexity. Thus, we propose a method to achieve electromagnetic wave imaging by employing a fixed wavelength and switching each microring through thermal tuning for transmitting received electromagnetic wave signals. This approach can accommodate more channels, which is crucial for the imaging system's maximum resolution. Essentially, the entire RoF system functions as an RF signal selector switch. In this study, we present an electromagnetic wave imaging system realized using a RoF system based on a microring modulator. Moreover, we integrate the optical heater, mentioned earlier, without any electrical components into this system, opening up the possibility of remote and all-optic operation for electromagnetic wave imaging.

1.4 Objective

1.4.1 High Quality Signal Transmission

Although very high-quality modulation can already be achieved using modulators with such as MZM structures, we still need MRMs to meet the requirements for overall device size and integration. Therefore, to realize the RoF system proposed in this study, the most fundamental component, the MRM, needs to be well-designed. This requires the microring modulator to have the following attributes:1. A small footprint. 2. High modulation efficiency. 3. High tuning efficiency. 4. Wide bandwidth. 5. High linearity, etc. For the footprint, since we use MRMs, the overall size will be in the tens of micrometers. While MRMs come in various typical radii, as shown in Figs. 1-4, an excessively large radius will result in too small of an FSR. For our proposed non-WDM system, the FSR doesn't need to be large enough to accommodate a sufficient number of channels, but an FSR that is too small will make the microring selection equally difficult. Regarding modulation efficiency, as mentioned earlier, carrier injection type MRMs have higher modulation efficiency than carrier depletion type. However, we also need to achieve a modulation bandwidth of at least the Sub 6 GHz band. The modulation bandwidth of carrier-injected MRMs is typically low, only a few MHz. Therefore, we use a carrier-depleted microring modulator. Modulation efficiency can be optimized by adjusting the phase shifter length and the position of high concentration doping. To simplify the design and moderate the doping resolution requirement, we use a typical pn junction shape consistent with the waveguide direction. For thermo-optic tuning efficiency, since we only need to achieve a tuning distance of half the FSR length, we can use the well-established TiN electrical heater integrated into the cladding above the microring. Additionally, we can integrate the optical heater mentioned in the previous section near the microring to achieve high-efficiency all-optical control as well. As for the bandwidth of the modulator, we need to ensure that the total bandwidth combined by the electrical bandwidth and optical bandwidth is larger than the Sub 6 GHz band. The electrical bandwidth is mainly determined by the RC characteristics of the pn junction, while the optical bandwidth is primarily determined by the Q value of the microring. The smaller the Q value of the microring, the larger the optical bandwidth. We refer to the design of MRM with low Q in [1-102] and set the target Q value to around 4000 to achieve an optical bandwidth of around 40 GHz. In addition, we need to ensure that the microring has small nonlinear characteristics when transmitting RF signals to facilitate the demodulation of RF signals at the receiving end. This is related to the electrical characteristics of the microring as well as the setting of the optical operation point. In this study, we optimize these design parameters to meet the requirements for high-quality signal transmission.
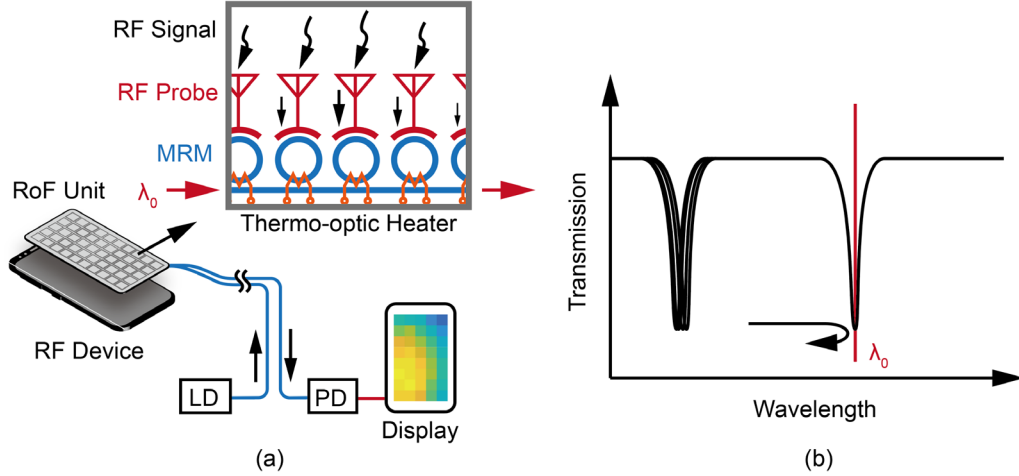
Figure 1-11 (a) Proposed electromagnetic wave imaging system using RoF configuration. (b) Each resonance of MRM array can be thermally tuned to the laser wavelength.

1.4.2 Signal Switching

In order to visualize the electromagnetic wave or say, scan the electromagnetic wave intensity at different locations, we need to rapidly switch the RF signal received by each RF probe. For a microring modulator array integrated with multiple microring modulators, we need to sequentially tune the resonant wavelength of each microring to the laser wavelength in sequence, as shown in Fig. 1-11(b), to enable the transmission of RF signals. To achieve the signal switching function, we require the following: 1. High thermal tuning efficiency. 2. Low thermal crosstalk. 3. Enough thermal tuning speed. First, for thermal tuning efficiency, as mentioned before, we can use TiN electrical heaters with mature technology to achieve efficient thermal tuning. In this study, the thermal tuning power required to achieve a thermal tuning length of half FSR is approximately 25 mW. Second, we need to minimize thermal crosstalk to ensure that when thermally selecting a particular microring, neighboring microrings are not disturbed or misoperated. To achieve low thermal crosstalk, we can either increase the spacing between the microrings or introduce adiabatic cladding between them. Finally, the heater structure and the method of externally controlling the heater's power supply determine the tuning speed of the microring array and the scanning speed of the visualized image. Electrical heaters formed from the cladding layers have switching response times on the order of 10 μs, while heaters that directly heat a Si slab or waveguide can achieve response times on the order of 1 μs, as Table 1-2 shown. We will explore both types of heating. As for the control of the heater power supply, different communication methods and integration levels introduce varying communication delays. In this study, our requirement for signal switching speed is not very high because we are conducting a proof-of-concept (POC) experiment. For higher-quality, more practical electromagnetic wave imaging, a dedicated well-designed driver can be used to drive the microring modulator array, and a high-speed thermo-optic heater with smaller thermal capacity can be employed for thermal tuning.

1.4.3 Electromagnetic Wave Imaging using RoF System

For a general electromagnetic wave imaging system, as mentioned earlier, it typically has a large size and high energy consumption. To make it more compact, efficient, and remotely controllable, we utilize a RoF system based on a Si-based microring modulator array. To the best of the authors' knowledge, there has been no prior application of a RoF system in an electromagnetic wave imaging system. To implement electromagnetic wave imaging using the proposed RoF system, we must first effectively detect electromagnetic waves. This entails using a high-gain antenna probe designed for the Sub 6 GHz band, which is connected to the microring modulator array via low-loss electrical wiring. Another RF antenna is required to transmit the EM wave signals for testing. Additionally, the relative position

19

between the two antennas must be alterable to measure and image the strength of the EM wave signals at different locations. Furthermore, by utilizing the EM wave imaging results obtained at adjacent positions, we can achieve a larger area of EM wave imaging through calibration. For the rapid alignment of microring resonance wavelengths, specific algorithms are needed to achieve this. When each microring is periodically tuned to the optimal modulation point, the output modulated light will periodically carry information about the EM wave signal strength at each position. By using a PD to convert the RF signal and reading it using a power meter, we can display the EM wave signal strength at each antenna probe in real-time. Using the antenna probe's cross-polarization discrimination, we can also assess variations in electromagnetic wave intensity across different polarization directions.

1.4.4 High Efficiency All-Optic Control

For applications where electrical connections cannot be used, or where electrical connections would significantly increase system complexity, as mentioned earlier, optical controls are needed in place of electrical controls. One of the most commonly used devices for optical tuning and correction is the heater. Traditional heaters typically rely on electrical control due to their simplicity, straightforwardness, and ease of fabrication. However, as the number of optical devices requiring control increases, integrating electrical heaters becomes progressively more challenging, and the space allocated for electrical heaters constitutes a growing proportion of the effective chip area. This undoubtedly hinders the miniaturization of Si-based optical devices. An excellent alternative is to replace electrical heaters with optical heaters. However, some existing optical control methods involve external optical fiber connections, specialized metallic material deposition, or are suitable only for specific structural optical heating. To achieve a simple, compact, and versatile optical heating method, this study introduces an innovative approach based on optical absorption generated by doping. It simply requires directing the control light into the doped control waveguide adjacent to the signal waveguide to heat the signal optical waveguide and indirectly adjust the phase of the signal light. This method can be applied to many optical switches or resonant structures to facilitate the adjustment of optical signal intensity or phase.

1.4.5 MRM Array Controlled All-optically

As mentioned earlier, the electrical wiring required for electro-optical heaters can be quite cumbersome, particularly for large optical switching arrays. Similarly, electrical heaters used in EM wave imaging systems with RoF, especially when dealing with a large number of channels, demand careful design to ensure efficient signal switching operations. However, for remote EM wave imaging, an excessive number of electrical connections can also increase system complexity and power consumption. Therefore, we've integrated optical heaters using light into our RoF system, relying on just two optical fibers for carrier input, signal readout, and resonance alignment for all microrings. This integration significantly reduces the effective area of the device, as there's no longer a need to allocate space for electrical heaters, wirings and contact pads. Additionally, the use of optical heaters enhances the tuning speed of the microrings. For higher data rate electromagnetic signals, we can even integrate the antenna probe and the modulator array into the same chip, requiring only two optical fibers for all external connections. This minimizes system complexity and ensures higher-quality EM wave imaging.

1.5 Outline of This Dissertation

Figure 1-12 illustrate the structure of this dissertation. Chapter 2 provides a general overview of Si photonics and outlines the fundamental design methodology for Si photonics devices. This chapter introduces the Si optical foundry, its necessary design rules, CAD layout creation methods, conversion processes to meet the foundry's requirements, and design rule check (DRC). Additionally, it covers the design and fabrication of various Si photonics components. Chapter 3 is dedicated to explaining the design and evaluation of MRM. It delves into the basic theory, simulation design of individual components, and the practical measurement of fabricated MRMs. This chapter encompasses optical

characterizations, parameter extraction, static and dynamic modulation studies, and an exploration of the modulation efficiency, optical bandwidth, electrical bandwidth, and other relevant microring characteristics. It also includes experiments related to thermal tuning and addresses the phenomenon of self-heating observed when input optical power exceeded specified limits. Chapter 4 outlines the implementation of electromagnetic wave imaging using an array of microring modulators. A non-resonant slot antenna probe is employed for real-time electromagnetic wave imaging over an area of $3515\,\text{mm}^2$. It also examines the differences in imaging results for electromagnetic waves with orthogonal polarization directions. Chapter 5 covers the design and optimization of an optical heater for all-optical control, demonstrating its application in MZI-type and MRR-type optical switches. The heating efficiency of these optical heaters is measured and compared with traditional electrical heaters, with a conclusion that optical heaters offer higher heating efficiency. In Chapter 6, we integrate a RoF system using a microring modulator array with optical heater and validate the modulator's modulation function and the optical heater's tuning capabilities. By controlling the light's power for heating, we achieve optical switching in a 4-channel all-optical controlled modulator array. Chapter 7 provides a comprehensive summary of the entire dissertation.
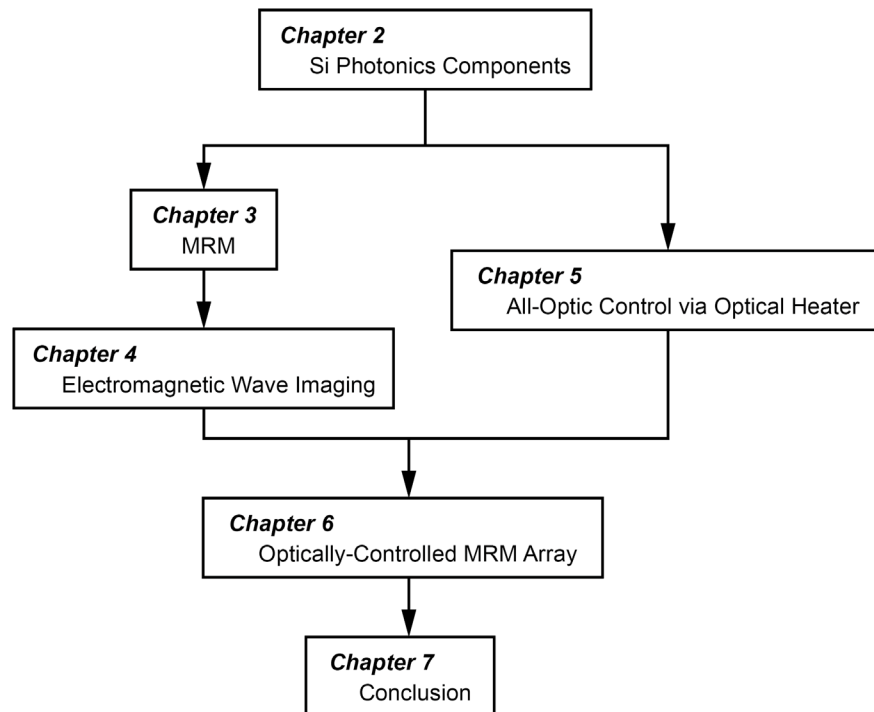

Figure 1-12 Structure of this dissertation.

Reference

[1-1]   R. Soref and B. Bennett, "Electrooptical effects in silicon," *IEEE J. Quantum Electron.*, vol. 23, no. 1, pp. 123–129, 1987, doi: 10.1109/JQE.1987.1073206.

[1-2]   A. S. A. Sakai, G. H. G. Hara, and T. B. T. Baba, "Propagation Characteristics of Ultrahigh-Δ Optical Waveguide on Silicon-on-Insulator Substrate," *Jpn. J. Appl. Phys.*, vol. 40, no. 4B, p. L383, Apr. 2001, doi: 10.1143/JJAP.40.L383.

[1-3]   T. Fukazawa, T. Hirano, F. Ohno, and T. Baba, "Low Loss Intersection of Si Photonic Wire Waveguides," *Jpn. J. Appl. Phys.*, vol. 43, no. 2R, p. 646, Feb. 2004, doi: 10.1143/JJAP.43.646.

[1-4]   A. Sakai, T. Fukazawa, and T. Baba, "Low Loss Ultra-Small Branches in a Silicon Photonic Wire Waveguide," *IEICE TRANS ELECTRON*, 2002.

[1-5]   T. Fukazawa, F. Ohno, and T. Baba, "Very Compact Arrayed-Waveguide-Grating Demultiplexer Using Si Photonic Wire Waveguides," *Jpn. J. Appl. Phys.*, vol. 43, no. 5B, p. L673, Apr. 2004, doi: 10.1143/JJAP.43.L673.

[1-6]   P. D. Trinh, S. Yegnanarayanan, and B. Jalali, "Integrated optical directional couplers in silicon-on-insulator," *Electron. Lett.*, vol. 31, no. 24, pp. 2097-2098(1), Nov. 1995.

[1-7]   P. D. Trinh, S. Yegnanarayanan, F. Coppinger, and B. Jalali, "Silicon-on-insulator (SOI) phased-array wavelength multi/demultiplexer with extremely low-polarization sensitivity," *IEEE Photonics Technol. Lett.*, vol. 9, no. 7, pp. 940–942, 1997, doi: 10.1109/68.593358.

[1-8]   L. Liao, D. Samara-Rubio, M. Morse, A. Liu, D. Hodge, D. Rubin, U. D. Keil, and T. Franck, "High speed silicon Mach-Zehnder modulator," *Opt Express*, vol. 13, no. 8, pp. 3129–3135, Apr. 2005, doi: 10.1364/OPEX.13.003129.

[1-9]   C. K. Tang and G. T. Reed, "Highly efficient optical phase modulator in SOI waveguides," *Electron. Lett.*, vol. 31, no. 6, pp. 451-452(1), Mar. 1995.

[1-10] J. Michel, J. Liu, and L. C. Kimerling, "High-performance Ge-on-Si photodetectors," *Nat. Photonics*, vol. 4, no. 8, pp. 527–534, Aug. 2010, doi: 10.1038/nphoton.2010.157.

[1-11] R. A. Soref and J. P. Lorenzo, "Single-crystal silicon: a new material for 1.3 and 1.6 μm integrated-optical components," *Electron. Lett.*, vol. 21, no. 21, p. 953, 1985, doi: 10.1049/el:19850673.

[1-12] J. Schmidtchen, A. Splett, B. Schüppert, K. Petermann, and G. Burbach, "Low loss singlemode optical waveguides with large cross-section in silicon-on-insulator," *Electron. Lett.*, vol. 27, no. 16, pp. 1486-1488(2), Aug. 1991.

[1-13] B. L. Weiss, G. T. Reed, S. K. Toh, R. A. Soref, and F. Namavar, "Optical waveguides in SIMOX structures," *IEEE Photonics Technol. Lett.*, vol. 3, no. 1, pp. 19–21, 1991, doi: 10.1109/68.68035.

[1-14] K. Aoki, H. T. Miyazaki, H. Hirayama, K. Inoshita, T. Baba, K. Sakoda, N. Shinya, and Y. Aoyagi, "Microassembly of semiconductor three-dimensional photonic crystals," *Nat. Mater.*, vol. 2, no. 2, pp. 117–121, Feb. 2003, doi: 10.1038/nmat802.

[1-15] W.-C. Lai, S. Chakravarty, Y. Zou, and R. T. Chen, "Silicon nano-membrane based photonic crystal microcavities for high sensitivity bio-sensing," *Opt Lett*, vol. 37, no. 7, pp. 1208–1210, Apr. 2012, doi: 10.1364/OL.37.001208.

[1-16] W. J. Westerveld, Md. Mahmud-Ul-Hasan, R. Shnaiderman, V. Ntziachristos, X. Rottenberg, S. Severi, and V. Rochus, "Sensitive, small, broadband and scalable optomechanical ultrasound sensor in silicon photonics," *Nat. Photonics*, vol. 15, no. 5, pp. 341–345, May 2021, doi: 10.1038/s41566-021-00776-0.

[1-17] C. Rogers, A. Y. Piggott, D. J. Thomson, R. F. Wiser, I. E. Opris, S. A. Fortune, A. J. Compston, A. Gondarenko, F. Meng, X. Chen, G. T. Reed, and R. Nicolaescu, "A universal 3D imaging sensor on a silicon photonics platform," *Nature*, vol. 590, no. 7845, pp. 256–261, Feb. 2021, doi:

10.1038/s41586-021-03259-y.

[1-18] G. Roelkens, L. Liu, D. Liang, R. Jones, A. Fang, B. Koch, and J. Bowers, "III-V/silicon photonics for on-chip and intra-chip optical interconnects," *Laser Photonics Rev.*, vol. 4, no. 6, pp. 751–779, 2010, doi: https://doi.org/10.1002/lpor.200900033.

[1-19] A. V. Krishnamoorthy, R. Ho, X. Zheng, H. Schwetman, J. Lexau, P. Koka, G. Li, I. Shubin, and J. E. Cunningham, "Computer Systems Based on Silicon Photonic Interconnects," *Proc. IEEE*, vol. 97, no. 7, pp. 1337–1361, 2009, doi: 10.1109/JPROC.2009.2020712.

[1-20] M. Streshinsky, R. Ding, Y. Liu, A. Novack, C. Galland, A. E.-J. Lim, P. G.-Q. Lo, T. Baehr-Jones, and M. Hochberg, "The Road to Affordable, Large-Scale Silicon Photonics," *Opt Photon News*, vol. 24, no. 9, pp. 32–39, Sep. 2013, doi: 10.1364/OPN.24.9.000032.

[1-21] X. Zhang, K. Kwon, J. Henriksson, J. Luo, and M. C. Wu, "A large-scale microelectromechanical-systems-based silicon photonics LiDAR," *Nature*, vol. 603, no. 7900, pp. 253–258, Mar. 2022, doi: 10.1038/s41586-022-04415-8.

[1-22] T. Baba, T. Tamanuki, H. Ito, M. Kamata, R. Tetsuya, S. Suyama, H. Abe, and R. Kurahashi, "Silicon Photonics FMCW LiDAR Chip With a Slow-Light Grating Beam Scanner," *IEEE J. Sel. Top. Quantum Electron.*, vol. 28, no. 5: Lidars and Photonic Radars, pp. 1–8, 2022, doi: 10.1109/JSTQE.2022.3157824.

[1-23] C. V. Poulton, A. Yaacobi, D. B. Cole, M. J. Byrd, M. Raval, D. Vermeulen, and M. R. Watts, "Coherent solid-state LIDAR with silicon photonic optical phased arrays," *Opt Lett*, vol. 42, no. 20, pp. 4091–4094, Oct. 2017, doi: 10.1364/OL.42.004091.

[1-24] C. Ramey, "Silicon Photonics for Artificial Intelligence Acceleration : HotChips 32," in *2020 IEEE Hot Chips 32 Symposium (HCS)*, Los Alamitos, CA, USA: IEEE Computer Society, Aug. 2020, pp. 1–26. doi: 10.1109/HCS49909.2020.9220525.

[1-25] C. Huang, S. Fujisawa, T. F. de Lima, A. N. Tait, E. C. Blow, Y. Tian, S. Bilodeau, A. Jha, F. Yaman, H.-T. Peng, H. G. Batshon, B. J. Shastri, Y. Inada, T. Wang, and P. R. Prucnal, "A silicon photonic–electronic neural network for fibre nonlinearity compensation," *Nat. Electron.*, vol. 4, no. 11, pp. 837–844, Nov. 2021, doi: 10.1038/s41928-021-00661-2.

[1-26] B. J. Shastri, A. N. Tait, T. Ferreira de Lima, W. H. P. Pernice, H. Bhaskaran, C. D. Wright, and P. R. Prucnal, "Photonics for artificial intelligence and neuromorphic computing," *Nat. Photonics*, vol. 15, no. 2, pp. 102–114, Feb. 2021, doi: 10.1038/s41566-020-00754-y.

[1-27] S. Bandyopadhyay, A. Sludds, S. Krastanov, R. Hamerly, N. Harris, D. Bunandar, M. Streshinsky, M. Hochberg, and D. Englund, "Single chip photonic deep neural network with accelerated training." 2022.

[1-28] F. Ashtiani, A. J. Geers, and F. Aflatouni, "An on-chip photonic deep neural network for image classification," *Nature*, vol. 606, no. 7914, pp. 501–506, Jun. 2022, doi: 10.1038/s41586-022-04714-0.

[1-29] B. Jalali and S. Fathpour, "Silicon Photonics," *J. Light. Technol.*, vol. 24, no. 12, pp. 4600–4615, 2006, doi: 10.1109/JLT.2006.885782.

[1-30] D. Thomson, A. Zilkie, J. E. Bowers, T. Komljenovic, G. T. Reed, L. Vivien, D. Marris-Morini, E. Cassan, L. Virot, J.-M. Fédéli, J.-M. Hartmann, J. H. Schmid, D.-X. Xu, F. Boeuf, P. O'Brien, G. Z. Mashanovich, and M. Nedeljkovic, "Roadmap on silicon photonics," *J. Opt.*, vol. 18, no. 7, p. 073003, Jun. 2016, doi: 10.1088/2040-8978/18/7/073003.

[1-31] H. Rong, S. Xu, Y.-H. Kuo, V. Sih, O. Cohen, O. Raday, and M. Paniccia, "Low-threshold continuous-wave Raman silicon laser," *Nat. Photonics*, vol. 1, no. 4, pp. 232–237, Apr. 2007, doi: 10.1038/nphoton.2007.29.

[1-32] Y. Takahashi, Y. Inui, M. Chihara, T. Asano, R. Terawaki, and S. Noda, "A micrometre-scale

Raman silicon laser with a microwatt threshold," *Nature*, vol. 498, no. 7455, pp. 470–474, Jun. 2013, doi: 10.1038/nature12237.

[1-33] A. W. Fang, H. Park, O. Cohen, R. Jones, M. J. Paniccia, and J. E. Bowers, "Electrically pumped hybrid AlGaInAs-silicon evanescent laser," *Opt Express*, vol. 14, no. 20, pp. 9203–9210, Oct. 2006, doi: 10.1364/OE.14.009203.

[1-34] Baets, Roel and Roelkens, Günther and Kuyken, Bart, "Heterogeneous integration in silicon photonics," in *Heterogeneous Integration Global Summit 2021 at Semicon Taiwan, Abstracts*, Taipei, Taiwan (virtual conference), 2021. [Online]. Available: {https://www.semicontaiwan.org/en/programs/HI-global-summit}

[1-35] Y. Maegami, M. Okano, G. Cong, M. Ohno, and K. Yamada, "Completely CMOS compatible SiN-waveguide-based fiber coupling structure for Si wire waveguides," *Opt Express*, vol. 24, no. 15, pp. 16856–16865, Jul. 2016, doi: 10.1364/OE.24.016856.

[1-36] J. F. Bauters, M. L. Davenport, M. J. R. Heck, J. K. Doylend, A. Chen, A. W. Fang, and J. E. Bowers, "Silicon on ultra-low-loss waveguide photonic integration platform," *Opt Express*, vol. 21, no. 1, pp. 544–555, Jan. 2013, doi: 10.1364/OE.21.000544.

[1-37] D. J. Blumenthal, "Photonic integration for UV to IR applications," *APL Photonics*, vol. 5, no. 2, p. 020903, Feb. 2020, doi: 10.1063/1.5131683.

[1-38] N. Margalit, C. Xiang, S. M. Bowers, A. Bjorlin, R. Blum, and J. E. Bowers, "Perspective on the future of silicon photonics and electronics," *Appl. Phys. Lett.*, vol. 118, no. 22, p. 220501, Jun. 2021, doi: 10.1063/5.0050117.

[1-39] V. Stojanović, R. J. Ram, M. Popović, S. Lin, S. Moazeni, M. Wade, C. Sun, L. Alloatti, A. Atabaki, F. Pavanello, N. Mehta, and P. Bhargava, "Monolithic silicon-photonic platforms in state-of-the-art CMOS SOI processes," *Opt Express*, vol. 26, no. 10, pp. 13106–13121, May 2018, doi: 10.1364/OE.26.013106.

[1-40] W. Bogaerts and L. Chrostowski, "Silicon Photonics Circuit Design: Methods, Tools and Challenges," *Laser Photonics Rev.*, vol. 12, no. 4, p. 1700237, 2018, doi: https://doi.org/10.1002/lpor.201700237.

[1-41] A. V. Tsarev, "Overview of Integrated Optical Sensors Based on Silicon: Forecasts and Results of the Decade [Invited Article]," *Optoelectron. Instrum. Data Process.*, vol. 56, no. 4, pp. 412–430, Jul. 2020, doi: 10.3103/S8756699020040123.

[1-42] L. Pavesi, "Thirty Years in Silicon Photonics: A Personal View," *Front. Phys.*, vol. 9, 2021, doi: 10.3389/fphy.2021.786028.

[1-43] L. M. Lechuga, "Chapter 5 Optical biosensors," in *Biosensors and Modern Biospecific Analytical Techniques*, vol. 44, in Comprehensive Analytical Chemistry, vol. 44. , Elsevier, 2005, pp. 209–250. doi: https://doi.org/10.1016/S0166-526X(05)44005-2.

[1-44] G. Ajoy and T. K., "Introduction to fiber optics," 1998, doi: 10.1017/cbo9781139174770.

[1-45] K. OKAMOTO, "Fundamentals of Optical Waveguides, 2nd ed," *Chap 9 Sec 931*, 2006, [Online]. Available: https://cir.nii.ac.jp/crid/1574231875521546752

[1-46] E. F. Schipper, A. M. Brugman, C. Dominguez, L. M. Lechuga, R. P. H. Kooyman, and J. Greve, "The realization of an integrated Mach-Zehnder waveguide immunosensor in silicon technology," *Sens. Actuators B Chem.*, vol. 40, no. 2, pp. 147–153, 1997, doi: https://doi.org/10.1016/S0925-4005(97)80254-7.

[1-47] A. Densmore, D.-X. Xu, S. Janz, P. Waldron, T. Mischki, G. Lopinski, A. Delâge, J. Lapointe, P. Cheben, B. Lamontagne, and J. H. Schmid, "Spiral-path high-sensitivity silicon photonic wire molecular sensor with temperature-independent response," *Opt Lett*, vol. 33, no. 6, pp. 596–598, Mar. 2008, doi: 10.1364/OL.33.000596.

[1-48] K. D. Vos, I. Bartolozzi, E. Schacht, P. Bienstman, and R. Baets, "Silicon-on-Insulator microring resonator for sensitive and label-free biosensing," *Opt Express*, vol. 15, no. 12, pp. 7610–7615, Jun. 2007, doi: 10.1364/OE.15.007610.

[1-49] S. TalebiFard, S. Schmidt, W. Shi, W. Wu, N. A. F. Jaeger, E. Kwok, D. M. Ratner, and L. Chrostowski, "Optimized sensitivity of Silicon-on-Insulator (SOI) strip waveguide resonator sensor," *Biomed Opt Express*, vol. 8, no. 2, pp. 500–511, Feb. 2017, doi: 10.1364/BOE.8.000500.

[1-50] A. M. Armani, R. P. Kulkarni, S. E. Fraser, R. C. Flagan, and K. J. Vahala, "Label-Free, Single-Molecule Detection with Optical Microcavities," *Science*, vol. 317, no. 5839, pp. 783–787, 2007, doi: 10.1126/science.1145002.

[1-51] S. M. Grist, S. A. Schmidt, J. Flueckiger, V. Donzella, W. Shi, S. T. Fard, J. T. Kirk, D. M. Ratner, K. C. Cheung, and L. Chrostowski, "Silicon photonic micro-disk resonators for label-free biosensing," *Opt Express*, vol. 21, no. 7, pp. 7994–8006, Apr. 2013, doi: 10.1364/OE.21.007994.

[1-52] S. Mandal, X. Serey, and D. Erickson, "Nanomanipulation Using Silicon Photonic Crystal Resonators," *Nano Lett.*, vol. 10, no. 1, pp. 99–104, Jan. 2010, doi: 10.1021/nl9029225.

[1-53] M. Lee and P. M. Fauchet, "Two-dimensional silicon photonic crystal based biosensing platform for protein detection," *Opt Express*, vol. 15, no. 8, pp. 4530–4535, Apr. 2007, doi: 10.1364/OE.15.004530.

[1-54] T. Baba, "Photonic and Iontronic Sensing in GaInAsP Semiconductor Photonic Crystal Nanolasers," *Photonics*, vol. 6, no. 2, 2019, doi: 10.3390/photonics6020065.

[1-55] A. L. Washburn, L. C. Gunn, and R. C. Bailey, "Label-Free Quantitation of a Cancer Biomarker in Complex Media Using Silicon Photonic Microring Resonators," *Anal. Chem.*, vol. 81, no. 22, pp. 9499–9506, Nov. 2009, doi: 10.1021/ac902006p.

[1-56] E. Luan, H. Shoman, D. M. Ratner, K. C. Cheung, and L. Chrostowski, "Silicon Photonic Biosensors Using Label-Free Detection," *Sensors*, vol. 18, no. 10, 2018, doi: 10.3390/s18103519.

[1-57] R. Soref, "The Past, Present, and Future of Silicon Photonics," *IEEE J. Sel. Top. Quantum Electron.*, vol. 12, no. 6, pp. 1678–1687, 2006, doi: 10.1109/JSTQE.2006.883151.

[1-58] C. Ranacher, C. Consani, N. Vollert, A. Tortschanoff, M. Bergmeister, T. Grille, and B. Jakoby, "Characterization of Evanescent Field Gas Sensor Structures Based on Silicon Photonics," *IEEE Photonics J.*, vol. 10, no. 5, pp. 1–14, 2018, doi: 10.1109/JPHOT.2018.2866628.

[1-59] T. Hu, B. Dong, X. Luo, T.-Y. Liow, J. Song, C. Lee, and G.-Q. Lo, "Silicon photonic platforms for mid-infrared applications," *Photon Res*, vol. 5, no. 5, pp. 417–430, Oct. 2017, doi: 10.1364/PRJ.5.000417.

[1-60] L. Tombez, E. J. Zhang, J. S. Orcutt, S. Kamlapurkar, and W. M. J. Green, "Methane absorption spectroscopy on a silicon photonic chip," *Optica*, vol. 4, no. 11, pp. 1322–1325, Nov. 2017, doi: 10.1364/OPTICA.4.001322.

[1-61] N. A. Yebo, S. P. Sree, E. Levrau, C. Detavernier, Z. Hens, J. A. Martens, and R. Baets, "Selective and reversible ammonia gas detection with nanoporous film functionalized silicon photonic micro-ring resonator," *Opt Express*, vol. 20, no. 11, pp. 11855–11862, May 2012, doi: 10.1364/OE.20.011855.

[1-62] G. Mi, C. Horvath, M. Aktary, and V. Van, "Silicon microring refractometric sensor for atmospheric CO2 gas monitoring," *Opt Express*, vol. 24, no. 2, pp. 1773–1780, Jan. 2016, doi: 10.1364/OE.24.001773.

[1-63] G. Mi, C. Horvath, and V. Van, "Silicon photonic dual-gas sensor for H2 and CO2 detection," *Opt Express*, vol. 25, no. 14, pp. 16250–16259, Jul. 2017, doi: 10.1364/OE.25.016250.

[1-64] S. Xiao, M. H. Khan, H. Shen, and M. Qi, "A highly compact third-order silicon microring add-drop filter with a very large free spectral range, a flat passband and a low delay dispersion," *Opt*

Express, vol. 15, no. 22, pp. 14765–14771, Oct. 2007, doi: 10.1364/OE.15.014765.

[1-65] M. S. Nawrocka, T. Liu, X. Wang, and R. R. Panepucci, "Tunable silicon microring resonator with wide free spectral range," *Appl. Phys. Lett.*, vol. 89, no. 7, p. 071110, Aug. 2006, doi: 10.1063/1.2337162.

[1-66] Q. Xu, B. Schmidt, S. Pradhan, and M. Lipson, "Micrometre-scale silicon electro-optic modulator," *Nature*, vol. 435, no. 7040, pp. 325–327, May 2005, doi: 10.1038/nature03569.

[1-67] Q. Xu, B. Schmidt, J. Shakya, and M. Lipson, "Cascaded silicon micro-ring modulators for WDM optical interconnection," *Opt Express*, vol. 14, no. 20, pp. 9431–9436, Oct. 2006, doi: 10.1364/OE.14.009431.

[1-68] Q. Xu, S. Manipatruni, B. Schmidt, J. Shakya, and M. Lipson, "12.5 Gbit/s carrier-injection-based silicon micro-ring silicon modulators," *Opt Express*, vol. 15, no. 2, pp. 430–436, Jan. 2007, doi: 10.1364/OE.15.000430.

[1-69] A. W. Fang, R. Jones, H. Park, O. Cohen, O. Raday, M. J. Paniccia, and J. E. Bowers, "Integrated AlGaInAs-silicon evanescent racetrack laser and photodetector," *Opt Express*, vol. 15, no. 5, pp. 2315–2322, Mar. 2007, doi: 10.1364/OE.15.002315.

[1-70] M. de Cea, A. H. Atabaki, and R. J. Ram, "Energy harvesting optical modulators with sub-attojoule per bit electrical energy consumption," *Nat. Commun.*, vol. 12, no. 1, p. 2326, Apr. 2021, doi: 10.1038/s41467-021-22460-1.

[1-71] Q. Xu, D. Fattal, and R. G. Beausoleil, "Silicon microring resonators with 1.5-μm radius," *Opt Express*, vol. 16, no. 6, pp. 4309–4315, Mar. 2008, doi: 10.1364/OE.16.004309.

[1-72] Z. Zou, L. Zhou, X. Li, and J. Chen, "60-nm-thick basic photonic components and Bragg gratings on the silicon-on-insulator platform," *Opt. Express*, vol. 23, pp. 20784–20795, Sep. 2015, doi: 10.1364/OE.23.020784.

[1-73] H. Ito, N. Ishikura, and T. Baba, "Triangular-Shaped Coupled Microrings for Robust Wavelength Multi-/Demultiplexing in Si Photonics," *J Light. Technol*, vol. 33, no. 2, pp. 304–310, Jan. 2015.

[1-74] C.-Y. Chao, W. Fung, and L. J. Guo, "Polymer microring resonators for biochemical sensing applications," *IEEE J. Sel. Top. Quantum Electron.*, vol. 12, no. 1, pp. 134–142, 2006, doi: 10.1109/JSTQE.2005.862945.

[1-75] D. Rezzonico, A. Guarino, C. Herzog, M. Jazbinsek, and P. Gunter, "High-finesse laterally coupled organic-inorganic hybrid polymer microring resonators for VLSI photonics," *IEEE Photonics Technol. Lett.*, vol. 18, no. 7, pp. 865–867, 2006, doi: 10.1109/LPT.2006.871816.

[1-76] D. Rezzonico, M. Jazbinsek, A. Guarino, O.-P. Kwon, and P. Günter, "Electro-optic Charon polymeric microring modulators," *Opt Express*, vol. 16, no. 2, pp. 613–627, Jan. 2008, doi: 10.1364/OE.16.000613.

[1-77] J. Scheuer, G. T. Paloczi, and A. Yariv, "All optically tunable wavelength-selective reflector consisting of coupled polymeric microring resonators," *Appl. Phys. Lett.*, vol. 87, no. 25, p. 251102, Dec. 2005, doi: 10.1063/1.2149158.

[1-78] P. Rabiei, W. H. Steier, C. Zhang, and L. R. Dalton, "Polymer Micro-Ring Filters and Modulators," *J Light. Technol*, vol. 20, no. 11, p. 1968, Nov. 2002.

[1-79] F. Lou, D. Dai, L. Thylen, and L. Wosinski, "Design and analysis of ultra-compact EO polymer modulators based on hybrid plasmonic microring resonators," *Opt Express*, vol. 21, no. 17, pp. 20041–20051, Aug. 2013, doi: 10.1364/OE.21.020041.

[1-80] T. Ling, S.-L. Chen, and L. J. Guo, "High-sensitivity and wide-directivity ultrasound detection using high Q polymer microring resonators," *Appl. Phys. Lett.*, vol. 98, no. 20, p. 204103, May 2011, doi: 10.1063/1.3589971.

[1-81] X. Yan, C.-S. Ma, C.-T. Zheng, and D.-M. Zhang, "Multi-channel switch array on the base of

triple series-coupled electro-optical polymer microring resonators," *Opt. Laser Technol.*, vol. 53, pp. 9–16, 2013, doi: https://doi.org/10.1016/j.optlastec.2013.04.023.

[1-82] C. Zhang, S.-L. Chen, T. Ling, and L. J. Guo, "Review of Imprinted Polymer Microrings as Ultrasound Detectors: Design, Fabrication, and Characterization," *IEEE Sens. J.*, vol. 15, no. 6, pp. 3241–3248, 2015, doi: 10.1109/JSEN.2015.2421519.

[1-83] T. Barwicz, M. A. Popovic, P. T. Rakich, M. R. Watts, H. A. Haus, E. P. Ippen, and H. I. Smith, "Microring-resonator-based add-drop filters in SiN: fabrication and analysis," *Opt Express*, vol. 12, no. 7, pp. 1437–1442, Apr. 2004, doi: 10.1364/OPEX.12.001437.

[1-84] I. Goykhman, B. Desiatov, and U. Levy, "Ultrathin silicon nitride microring resonator for biophotonic applications at 970 nm wavelength," *Appl. Phys. Lett.*, vol. 97, no. 8, p. 081108, Aug. 2010, doi: 10.1063/1.3483766.

[1-85] Q. Li, A. A. Eftekhar, M. Sodagar, Z. Xia, A. H. Atabaki, and A. Adibi, "Vertical integration of high-Q silicon nitride microresonators into silicon-on-insulator platform," *Opt Express*, vol. 21, no. 15, pp. 18236–18248, Jul. 2013, doi: 10.1364/OE.21.018236.

[1-86] Y. Hong, H. Ge, and J. Hong, "Compact biosensors based on thin film silicon nitride microring resonators," *J. Phys. Conf. Ser.*, vol. 2012, no. 1, p. 012037, Sep. 2021, doi: 10.1088/1742-6596/2012/1/012037.

[1-87] A. Kaźmierczak, L. Vivien, K. B. Gylfason, B. Sanchez, A. Griol, D. Marris-Morini, E. Cassan, F. Dortu, H. Sohlström, D. Giannone, and D. Hill, "High quality optical microring resonators in Si3N 4/SiO2," in *ECIO'08 Eindhoven - Proceedings of the 14th European Conference on Integrated Optics and Technical Exhibition, Contributed and Invited Papers*, NLD, 2008, pp. 313–316. [Online]. Available: https://publications.aston.ac.uk/id/eprint/38146/

[1-88] J. Guo, M. J. Shaw, G. A. Vawter, G. R. Hadley, P. Esherick, and C. T. Sullivan, "High-Q microring resonator for biochemical sensors," in *Integrated Optics: Devices, Materials, and Technologies IX*, Y. Sidorin and C. A. Waechter, Eds., SPIE, 2005, pp. 83–92. doi: 10.1117/12.589467.

[1-89] J. Guo, M. J. Shaw, G. Allen Vawter, P. Esherick, G. Ronald Hadley, and C. T. Sullivan, "High-Q integrated on-chip micro-ring resonator," in *The 17th Annual Meeting of the IEEELasers and Electro-Optics Society, 2004. LEOS 2004.*, 2004, pp. 745-746 Vol.2. doi: 10.1109/LEOS.2004.1363454.

[1-90] X. Xue, Y. Xuan, C. Wang, P.-H. Wang, Y. Liu, B. Niu, D. E. Leaird, M. Qi, and A. M. Weiner, "Thermal tuning of Kerr frequency combs in silicon nitride microring resonators," *Opt Express*, vol. 24, no. 1, pp. 687–698, Jan. 2016, doi: 10.1364/OE.24.000687.

[1-91] S. Zhang, T. Bi, I. Harder, O. Lohse, F. Gannott, A. Gumann, Y. Zhang, and P. Del'Haye, "Room-Temperature Sputtered Ultralow-loss Silicon Nitride for Hybrid Photonic Integration." 2023.

[1-92] H. Han, B. Xiang, and J. Zhang, "Simulation and Analysis of Single-Mode Microring Resonators in Lithium Niobate Thin Films," *Crystals*, vol. 8, no. 9, 2018, doi: 10.3390/cryst8090342.

[1-93] H. Hwang, H. Heo, K. Ko, M. R. Nurrahman, K. Moon, J. J. Ju, S.-W. Han, H. Jung, H. Lee, and M.-K. Seo, "Electro-optic control of the external coupling strength of a high-quality-factor lithium niobate micro-resonator," *Opt Lett*, vol. 47, no. 23, pp. 6149–6152, Dec. 2022, doi: 10.1364/OL.472956.

[1-94] R. Zhuang, J. He, Y. Qi, and Y. Li, "High-Q Thin-Film Lithium Niobate Microrings Fabricated with Wet Etching," *Adv. Mater.*, vol. 35, no. 3, p. 2208113, 2023, doi: https://doi.org/10.1002/adma.202208113.

[1-95] R. Gao, N. Yao, J. Guan, L. Deng, J. Lin, M. Wang, L. Qiao, W. Fang, and Y. Cheng, "Lithium niobate microring with ultra-high Q factor above 108," *Chin Opt Lett*, vol. 20, no. 1, p. 011902,

Jan. 2022.

[1-96] A. Guarino, G. Poberaj, D. Rezzonico, R. Degl'Innocenti, and P. Günter, "Electro–optically tunable microring resonators in lithium niobate," *Nat. Photonics*, vol. 1, no. 7, pp. 407–410, Jul. 2007, doi: 10.1038/nphoton.2007.93.

[1-97] I. Krasnokutska, J.-L. J. Tambasco, and A. Peruzzo, "Tunable large free spectral range microring resonators in lithium niobate on insulator," *Sci. Rep.*, vol. 9, no. 1, p. 11086, Jul. 2019, doi: 10.1038/s41598-019-47231-3.

[1-98] L. Chen and R. M. Reano, "Compact electric field sensors based on indirect bonding of lithium niobate to silicon microrings," *Opt Express*, vol. 20, no. 4, pp. 4032–4038, Feb. 2012, doi: 10.1364/OE.20.004032.

[1-99] S. Y. Siew, S. S. Saha, M. Tsang, and A. J. Danner, "Rib Microring Resonators in Lithium Niobate on Insulator," *IEEE Photonics Technol. Lett.*, vol. 28, no. 5, pp. 573–576, 2016, doi: 10.1109/LPT.2015.2508103.

[1-100] R. Luo, Y. He, H. Liang, M. Li, J. Ling, and Q. Lin, "Optical Parametric Generation in a Lithium Niobate Microring with Modal Phase Matching," *Phys Rev Appl*, vol. 11, no. 3, p. 034026, Mar. 2019, doi: 10.1103/PhysRevApplied.11.034026.

[1-101] J. Lu, M. Li, C.-L. Zou, A. A. Sayem, and H. X. Tang, "Toward 1% single-photon anharmonicity with periodically poled lithium niobate microring resonators," *Optica*, vol. 7, no. 12, pp. 1654–1659, Dec. 2020, doi: 10.1364/OPTICA.403931.

[1-102] M. Pantouvaki, S. A. Srinivasan, Y. Ban, P. D. Heyn, P. Verheyen, G. Lepage, H. Chen, J. D. Coster, N. Golshani, S. Balakrishnan, P. Absil, and J. V. Campenhout, "Active Components for 50 Gb/s NRZ-OOK Optical Interconnects in a Silicon Photonics Platform," *J Light. Technol*, vol. 35, no. 4, pp. 631–638, Feb. 2017.

[1-103] G. Li, X. Zheng, J. Yao, H. Thacker, I. Shubin, Y. Luo, K. Raj, J. E. Cunningham, and A. V. Krishnamoorthy, "25Gb/s 1V-driving CMOS ring modulator with integrated thermal tuning," *Opt Express*, vol. 19, no. 21, pp. 20435–20443, Oct. 2011, doi: 10.1364/OE.19.020435.

[1-104] Y. Zhang, H. Zhang, J. Zhang, J. Liu, L. Wang, D. Chen, N. Chi, X. Xiao, and S. Yu, "240 Gb/s optical transmission based on an ultrafast silicon microring modulator," *Photon Res*, vol. 10, no. 4, pp. 1127–1133, Apr. 2022, doi: 10.1364/PRJ.441791.

[1-105] H. Han and B. Xiang, "Simulation and analysis of electro-optic tunable microring resonators in silicon thin film on lithium niobate," *Sci. Rep.*, vol. 9, no. 1, p. 6302, Apr. 2019, doi: 10.1038/s41598-019-42818-2.

[1-106] X. Xiao, X. Li, H. Xu, Y. Hu, K. Xiong, Z. Li, T. Chu, J. Yu, and Y. Yu, "44-Gb/s Silicon Microring Modulators Based on Zigzag PN Junctions," *IEEE Photonics Technol. Lett.*, vol. 24, no. 19, pp. 1712–1714, 2012, doi: 10.1109/LPT.2012.2213244.

[1-107] J. Müller, F. Merget, S. S. Azadeh, J. Hauck, S. R. García, B. Shen, and J. Witzens, "Optical Peaking Enhancement in High-Speed Ring Modulators," *Sci. Rep.*, vol. 4, no. 1, p. 6310, Sep. 2014, doi: 10.1038/srep06310.

[1-108] Y. Hu, X. Xiao, H. Xu, X. Li, K. Xiong, Z. Li, T. Chu, Y. Yu, and J. Yu, "High-speed silicon modulator based on cascaded microring resonators," *Opt Express*, vol. 20, no. 14, pp. 15079–15085, Jul. 2012, doi: 10.1364/OE.20.015079.

[1-109] X. Xiao, H. Xu, X. Li, Y. Hu, K. Xiong, Z. Li, T. Chu, Y. Yu, and J. Yu, "25 Gbit/s silicon microring modulator based on misalignment-tolerant interleaved PN junctions," *Opt Express*, vol. 20, no. 3, pp. 2507–2515, Jan. 2012, doi: 10.1364/OE.20.002507.

[1-110] H. Yu, D. Ying, M. Pantouvaki, J. V. Campenhout, P. Absil, Y. Hao, J. Yang, and X. Jiang, "Trade-off between optical modulation amplitude and modulation bandwidth of silicon micro-ring

modulators," *Opt Express*, vol. 22, no. 12, pp. 15178–15189, Jun. 2014, doi: 10.1364/OE.22.015178.

[1-111] G. Fan, W. Sang, X. Liu, and Z. Zhen, "Silicon waveguide racetrack resonators with 1.5 μm radius using junction offsets," *Microw. Opt. Technol. Lett.*, vol. 54, no. 6, pp. 1470–1471, 2012, doi: https://doi.org/10.1002/mop.26836.

[1-112] J.-H. Song, T. D. Kongnyuy, P. D. Heyn, S. Lardenois, R. Jansen, and X. Rottenberg, "Low-Loss Waveguide Bends by Advanced Shape for Photonic Integrated Circuits," *J. Light. Technol.*, vol. 38, pp. 3273–3279, 2020.

[1-113] M. Bahadori, M. Nikdast, Q. Cheng, and K. Bergman, "Universal Design of Waveguide Bends in Silicon-on-Insulator Photonics Platform," *J. Light. Technol.*, vol. 37, no. 13, pp. 3044–3054, 2019, doi: 10.1109/JLT.2019.2909983.

[1-114] H. Ishio, J. Minowa, and K. Nosu, "Review and status of wavelength-division-multiplexing technology and its application," *J. Light. Technol.*, vol. 2, no. 4, pp. 448–463, 1984, doi: 10.1109/JLT.1984.1073653.

[1-115] M. A. SOOLE J. B. D; SCHERER, A; LEBLANC, H. P; ANDREADEKIS, N. C; BHAT, R; KOZA, "Monolithic InP-based grating spectrometer for wavelength-division multiplexed systems at 1•5 μm," *Electron. Lett.*, 1991.

[1-116] M. B. J. Diemeer, L. H. Spiekman, R. Ramsamoedj, and M. K. Smit, "Polymeric phased array wavelength multiplexer operating around 1550nm," *Electron. Lett.*, vol. 32, no. 12, pp. 1132–1133, 1996.

[1-117] K. Takada, M. Abe, T. Shibata, and K. Okamoto, "A.2.5 GHz-spaced 1080-channel tandem multi/demultiplexer covering the. S-, C-, and L-bands using an arrayed-waveguide grating with Gaussian passbands as a primary filter," *IEEE Photonics Technol. Lett.*, vol. 14, no. 5, pp. 648–650, 2002, doi: 10.1109/68.998713.

[1-118] K. Sasaki, F. Ohno, A. Motegi, and T. Baba, "Arrayed waveguide grating of 70×60 μm^2 size based on Si photonic wire waveguides," *Electron. Lett.*, vol. 41, no. 14, pp. 801-802(1), Jul. 2005.

[1-119] A. Kaneko, S. Kamei, Y. Inoue, H. Takahashi, and A. Sugita, "Athermal silica-based arrayed-waveguide grating (AWG) multiplexers with new low loss groove design," in *OFC/IOOC . Technical Digest. Optical Fiber Communication Conference, 1999, and the International Conference on Integrated Optics and Optical Fiber Communication*, 1999, pp. 204–206 vol.1. doi: 10.1109/OFC.1999.767839.

[1-120] A. Alduino, L. Liao, R. Jones, M. Morse, B. Kim, W.-Z. Lo, J. Basak, B. Koch, H.-F. Liu, H. Rong, M. Sysak, C. Krause, R. Saba, D. Lazar, L. Horwitz, R. Bar, S. Litski, A. Liu, K. Sullivan, O. Dosunmu, N. Na, T. Yin, F. Haubensack, I. -wei Hsieh, J. Heck, R. Beatty, H. Park, J. Bovington, S. Lee, H. Nguyen, H. Au, K. Nguyen, P. Merani, M. Hakami, and M. Paniccia, "Demonstration of a High Speed 4-Channel Integrated Silicon Photonics WDM Link with Hybrid Silicon Lasers," in *Integrated Photonics Research, Silicon and Nanophotonics and Photonics in Switching*, Optica Publishing Group, 2010, p. PDIWI5. doi: 10.1364/IPRSN.2010.PDIWI5.

[1-121] C.-H. Chen, C. Li, A. Shafik, M. Fiorentino, P. Chiang, S. M. Palermo, and R. G. Beausoleil, "A WDM silicon photonic transmitter based on carrier-injection microring modulators," *2014 Opt. Interconnects Conf.*, pp. 121–122, 2014.

[1-122] Y. Zhang, S. Yang, X. Zhu, Q. Li, H. Guan, P. Magill, K. Bergman, T. Baehr-Jones, and M. Hochberg, "Quantum dot SOA/silicon external cavity multi-wavelength laser," *Opt. Express*, vol. 23, Feb. 2015, doi: 10.1364/OE.23.004666.

[1-123] Y. Xu, J. Lin, R. Dube-Demers, S. Larochelle, L. A. Rusch, and W. Shi, "Integrated flexible-grid

WDM transmitter using an optical frequency comb in microring modulators.," *Opt. Lett.*, vol. 43 7, pp. 1554–1557, 2018.

[1-124] J. V. Hryniewicz, P. P. Absil, B. E. Little, R. A. Wilson, and P.-T. Ho, "Higher order filter response in coupled microring resonators," *IEEE Photonics Technol. Lett.*, vol. 12, no. 3, pp. 320–322, 2000, doi: 10.1109/68.826927.

[1-125] B. E. Little, S. T. Chu, P. P. Absil, J. V. Hryniewicz, F. G. Johnson, F. Seiferth, D. Gill, V. Van, O. King, and M. Trakalo, "Very high-order microring resonator filters for WDM applications," *IEEE Photonics Technol. Lett.*, vol. 16, no. 10, pp. 2263–2265, 2004, doi: 10.1109/LPT.2004.834525.

[1-126] H. Kaneshige, R. Gautam, Y. Ueyama, R. Katouf, T. Arakawa, and Y. Kokubun, "Low-voltage quantum well microring-enhanced Mach-Zehnder modulator," *Opt Express*, vol. 21, no. 14, pp. 16888–16900, Jul. 2013, doi: 10.1364/OE.21.016888.

[1-127] K. Alexander, J. P. George, J. Verbist, K. Neyts, B. Kuyken, D. Van Thourhout, and J. Beeckman, "Nanophotonic Pockels modulators on a silicon nitride platform," *Nat. Commun.*, vol. 9, no. 1, p. 3444, Aug. 2018, doi: 10.1038/s41467-018-05846-6.

[1-128] G. T. Reed and A. P. Knights, *Silicon photonics : an introduction*. Wiley, 2004. [Online]. Available: https://cir.nii.ac.jp/crid/1130282270165979008

[1-129] G. Cocorullo and I. Rendina, "Thermo-optical modulation at 1.5µm in silicon etalon," *Electron. Lett.*, vol. 28, no. 1, pp. 83-85(2), Jan. 1992.

[1-130] M. Dahlem, C. Holzwarth, A. Khilo, F. Kärtner, H. Smith, and E. Ippen, "Reconfigurable multi-channel second-order silicon microring-resonator filterbanks for on-chip WDM systems," *Opt. Express*, vol. 19, pp. 306–16, Jan. 2011, doi: 10.1364/OE.19.000306.

[1-131] K. Padmaraju, D. F. Logan, X. Zhu, J. J. Ackert, A. P. Knights, and K. Bergman, "Integrated thermal stabilization of a microring modulator," *Opt Express*, vol. 21, no. 12, pp. 14342–14350, Jun. 2013, doi: 10.1364/OE.21.014342.

[1-132] M.-H. Kim, L. Zimmermann, and W.-Y. Choi, "A Temperature Controller IC for Maximizing Si Micro-Ring Modulator Optical Modulation Amplitude," *J. Light. Technol.*, vol. 37, no. 4, pp. 1200–1206, 2019, doi: 10.1109/JLT.2018.2889899.

[1-133] Y. Kim, J.-H. Han, D. Ahn, and S. Kim, "Heterogeneously-Integrated Optical Phase Shifters for Next-Generation Modulators and Switches on a Silicon Photonics Platform: A Review," *Micromachines*, vol. 12, no. 6, 2021, doi: 10.3390/mi12060625.

[1-134] B. Wang, Q. Huang, K. Chen, J. Zhang, G. Kurczveil, D. Liang, S. Palermo, M. R. T. Tan, R. G. Beausoleil, and S. He, "Modulation on Silicon for Datacom: Past, Present, and Future," *Prog. Electromagn. Res.*, vol. 166, 2019.

[1-135] W. Zhang, M. Ebert, K. Li, B. Chen, X. Yan, H. Du, M. Banakar, D. T. Tran, C. G. Littlejohns, A. Scofield, G. Yu, R. Shafiiha, A. Zilkie, G. Reed, and D. J. Thomson, "Harnessing plasma absorption in silicon MOS ring modulators," *Nat. Photonics*, vol. 17, no. 3, pp. 273–279, Mar. 2023, doi: 10.1038/s41566-023-01159-3.

[1-136] S. Tanaka, T. Simoyama, T. Aoki, T. Mori, S. Sekiguchi, S.-H. Jeong, T. Usuki, Y. Tanaka, and K. Morito, "Ultralow-Power (1.59 mW/Gbps), 56-Gbps PAM4 Operation of Si Photonic Transmitter Integrating Segmented PIN Mach–Zehnder Modulator and 28-nm CMOS Driver," *J Light. Technol*, vol. 36, no. 5, pp. 1275–1280, Mar. 2018.

[1-137] C. Li, C.-H. Chen, B. Wang, S. Palermo, M. Fiorentino, and R. G. Beausoleil, "An Energy-Efficient Silicon Microring Resonator-Based Photonic Transmitter," *IEEE Des. Test*, vol. 31, no. 5, pp. 46–54, 2014, doi: 10.1109/MDAT.2014.2347932.

[1-138] A. Liu, L. Liao, D. Rubin, H. Nguyen, B. Ciftcioglu, Y. Chetrit, N. Izhaky, and M. Paniccia,

"High-speed optical modulation based on carrier depletion in a silicon waveguide," *Opt Express*, vol. 15, no. 2, pp. 660–668, Jan. 2007, doi: 10.1364/OE.15.000660.

[1-139] J. Sun, R. Kumar, M. Sakib, J. B. Driscoll, H. Jayatilleka, and H. Rong, "A 128 Gb/s PAM4 Silicon Microring Modulator With Integrated Thermo-Optic Resonance Tuning," *J. Light. Technol.*, vol. 37, no. 1, pp. 110–115, 2019, doi: 10.1109/JLT.2018.2878327.

[1-140] Y. Tong, Z. Hu, X. Wu, S. Liu, L. Chang, A. Netherton, C.-K. Chan, J. E. Bowers, and H. K. Tsang, "An Experimental Demonstration of 160-Gbit/s PAM-4 Using a Silicon Micro-Ring Modulator," *IEEE Photonics Technol. Lett.*, vol. 32, no. 2, pp. 125–128, 2020, doi: 10.1109/LPT.2019.2960238.

[1-141] M. Sakib, P. Liao, C. Ma, R. Kumar, D. Huang, G.-L. Su, X. Wu, S. Fathololoumi, and H. Rong, "A high-speed micro-ring modulator for next generation energy-efficient optical networks beyond 100 Gbaud," in *Conference on Lasers and Electro-Optics*, Optica Publishing Group, 2021, p. SF1C.3. doi: 10.1364/CLEO_SI.2021.SF1C.3.

[1-142] J.-B. You, M. Park, J.-W. Park, and G. Kim, "12.5 Gbps optical modulation of silicon racetrack resonator based on carrier-depletion in asymmetric p-n diode," *Opt Express*, vol. 16, no. 22, pp. 18340–18344, Oct. 2008, doi: 10.1364/OE.16.018340.

[1-143] P. Dong, S. Liao, D. Feng, H. Liang, D. Zheng, R. Shafiiha, C.-C. Kung, W. Qian, G. Li, X. Zheng, A. V. Krishnamoorthy, and M. Asghari, "Low Vpp, ultralow-energy, compact, high-speed silicon electro-optic modulator," *Opt Express*, vol. 17, no. 25, pp. 22484–22490, Dec. 2009, doi: 10.1364/OE.17.022484.

[1-144] Z.-Y. Li, D.-X. Xu, W. R. McKinnon, S. Janz, J. H. Schmid, P. Cheben, and J.-Z. Yu, "Silicon waveguide modulator based on carrier depletion in periodically interleaved PN junctions," *Opt Express*, vol. 17, no. 18, pp. 15947–15958, Aug. 2009, doi: 10.1364/OE.17.015947.

[1-145] H. Yu, M. Pantouvaki, J. V. Campenhout, D. Korn, K. Komorowska, P. Dumon, Y. Li, P. Verheyen, P. Absil, L. Alloatti, D. Hillerkuss, J. Leuthold, R. Baets, and W. Bogaerts, "Performance tradeoff between lateral and interdigitated doping patterns for high speed carrier-depletion based silicon modulators," *Opt Express*, vol. 20, no. 12, pp. 12926–12938, Jun. 2012, doi: 10.1364/OE.20.012926.

[1-146] M. T. Wade, J. M. Shainline, J. S. Orcutt, C. Sun, R. Kumar, B. Moss, M. Georgas, R. J. Ram, V. Stojanović, and M. A. Popović, "Energy-efficient active photonics in a zero-change, state-of-the-art CMOS process," in *Optical Fiber Communication Conference*, Optica Publishing Group, 2014, p. Tu2E.7. doi: 10.1364/OFC.2014.Tu2E.7.

[1-147] J. C. Rosenberg, W. M. J. Green, S. Assefa, D. M. Gill, T. Barwicz, M. Yang, S. M. Shank, and Y. A. Vlasov, "A 25 Gbps silicon microring modulator based on an interleaved junction," *Opt Express*, vol. 20, no. 24, pp. 26411–26423, Nov. 2012, doi: 10.1364/OE.20.026411.

[1-148] X. Li, Z. Li, X. Xiao, H. Xu, J. Yu, and Y. Yu, "40 Gb/s All-Silicon Photodetector Based on Microring Resonators," *IEEE Photonics Technol. Lett.*, vol. 27, no. 7, pp. 729–732, 2015, doi: 10.1109/LPT.2015.2390619.

[1-149] T. Y. L. Ang, C. E. Png, S. T. Lim, and J. R. Ong, "Silicon modulators with optimized vertical PN junctions for high-modulation-efficiency and low-loss in the O-band," in *Silicon Photonics XIII*, G. T. Reed and A. P. Knights, Eds., SPIE, 2018, p. 105370H. doi: 10.1117/12.2290385.

[1-150] G. Zhou, L. Zhou, Y. Guo, S. Chen, L. Lu, L. Liu, and J. Chen, "32-Gb/s OOK and 64-Gb/s PAM-4 Modulation Using a Single-Drive Silicon Mach–Zehnder Modulator with 2 V Drive Voltage," *IEEE Photonics J.*, vol. 11, no. 6, pp. 1–10, 2019, doi: 10.1109/JPHOT.2019.2954597.

[1-151] S. Manipatruni, Q. Xu, B. Schmidt, J. Shakya, and M. Lipson, "High Speed Carrier Injection 18 Gb/s Silicon Micro-ring Electro-optic Modulator," in *LEOS 2007 - IEEE Lasers and Electro-*

Optics Society Annual Meeting Conference Proceedings, 2007, pp. 537–538. doi: 10.1109/LEOS.2007.4382517.

[1-152] S. Manipatruni, K. Preston, L. Chen, and M. Lipson, "Ultra-low voltage, ultra-small mode volume silicon microring modulator," *Opt Express*, vol. 18, no. 17, pp. 18235–18242, Aug. 2010, doi: 10.1364/OE.18.018235.

[1-153] P. Dong, R. Shafiiha, S. Liao, H. Liang, N.-N. Feng, D. Feng, G. Li, X. Zheng, A. V. Krishnamoorthy, and M. Asghari, "Wavelength-tunable silicon microring modulator," *Opt Express*, vol. 18, no. 11, pp. 10941–10946, May 2010, doi: 10.1364/OE.18.010941.

[1-154] W. Shen, G. Zhou, J. Du, L. Zhou, K. Xu, and Z. He, "High-speed silicon microring modulator at the 2um waveband with analysis and observation of optical bistability," *Photon Res*, vol. 10, no. 3, pp. A35–A42, Mar. 2022, doi: 10.1364/PRJ.439583.

[1-155] M. Pantouvaki, H. Yu, M. Rakowski, P. Christie, P. Verheyen, G. Lepage, N. Van Hoovels, P. Absil, and J. Van Campenhout, "Comparison of Silicon Ring Modulators With Interdigitated and Lateral p-n Junctions," *IEEE J. Sel. Top. Quantum Electron.*, vol. 19, no. 2, pp. 7900308–7900308, 2013, doi: 10.1109/JSTQE.2012.2228169.

[1-156] S. Tanaka, T. Usuki, and Y. Tanaka, "Accurate SPICE Model of Forward-Biased Silicon PIN Mach–Zehnder Modulator for an Energy-Efficient Multilevel Transmitter," *J. Light. Technol.*, vol. 36, no. 10, pp. 1959–1969, 2018, doi: 10.1109/JLT.2018.2797184.

[1-157] M. Shin, Y. Ban, B.-M. Yu, M.-H. Kim, J. Rhim, L. Zimmermann, and W.-Y. Choi, "A Linear Equivalent Circuit Model for Depletion-Type Silicon Microring Modulators," *IEEE Trans. Electron Devices*, vol. 64, no. 3, pp. 1140–1145, 2017, doi: 10.1109/TED.2017.2648861.

[1-158] X. Xiao, X. Li, X. Feng, K. Cui, F. Liu, and Y. Huang, "Eight-Channel Optical Add-Drop Multiplexer With Cascaded Parent-Sub Microring Resonators," *IEEE Photonics J.*, vol. 7, no. 4, pp. 1–7, 2015, doi: 10.1109/JPHOT.2015.2464103.

[1-159] P. Dong, J. Lee, K. Kim, Y.-K. Chen, and C. Gui, "Ten-Channel Discrete Multi-Tone Modulation Using Silicon Microring Modulator Array," in *Optical Fiber Communication Conference*, Optica Publishing Group, 2016, p. W4J.4. doi: 10.1364/OFC.2016.W4J.4.

[1-160] J. Komma, C. Schwarz, G. Hofmann, D. Heinert, and R. Nawrodt, "Thermo-optic coefficient of silicon at 1550 nm and cryogenic temperatures," *Appl. Phys. Lett.*, vol. 101, no. 4, p. 041905, Jul. 2012, doi: 10.1063/1.4738989.

[1-161] D. B. Leviton and B. J. Frey, "Temperature-dependent absolute refractive index measurements of synthetic fused silica," in *Optomechanical Technologies for Astronomy*, E. Atad-Ettedgui, J. Antebi, and D. Lemke, Eds., SPIE, 2006, p. 62732K. doi: 10.1117/12.672853.

[1-162] H. Jayatilleka, K. Murray, M. Á. Guillén-Torres, M. Caverley, R. Hu, N. A. F. Jaeger, L. Chrostowski, and S. Shekhar, "Wavelength tuning and stabilization of microring-based filters using silicon in-resonator photoconductive heaters," *Opt Express*, vol. 23, no. 19, pp. 25084–25097, Sep. 2015, doi: 10.1364/OE.23.025084.

[1-163] J. M. Shainline, J. S. Orcutt, M. T. Wade, K. Nammari, B. Moss, M. Georgas, C. Sun, R. J. Ram, V. Stojanović, and M. A. Popović, "Depletion-mode carrier-plasma optical modulator in zero-change advanced CMOS," *Opt Lett*, vol. 38, no. 15, pp. 2657–2659, Aug. 2013, doi: 10.1364/OL.38.002657.

[1-164] Y. Li and A. W. Poon, "Active resonance wavelength stabilization for silicon microring resonators with an in-resonator defect-state-absorption-based photodetector," *Opt Express*, vol. 23, no. 1, pp. 360–372, Jan. 2015, doi: 10.1364/OE.23.000360.

[1-165] S. Manipatruni, R. K. Dokania, B. Schmidt, N. Sherwood-Droz, C. B. Poitras, A. B. Apsel, and M. Lipson, "Wide temperature range operation of micrometer-scale silicon electro-optic

modulators," *Opt Lett*, vol. 33, no. 19, pp. 2185–2187, Oct. 2008, doi: 10.1364/OL.33.002185.

[1-166] C. Li, R. Bai, A. Shafik, E. Z. Tabasy, G. Tang, C. Ma, C.-H. Chen, Z. Peng, M. Fiorentino, P. Chiang, and S. Palermo, "A ring-resonator-based silicon photonics transceiver with bias-based wavelength stabilization and adaptive-power-sensitivity receiver," in *2013 IEEE International Solid-State Circuits Conference Digest of Technical Papers*, 2013, pp. 124–125. doi: 10.1109/ISSCC.2013.6487665.

[1-167] P. Dong, W. Qian, H. Liang, R. Shafiiha, N.-N. Feng, D. Feng, X. Zheng, A. V. Krishnamoorthy, and M. Asghari, "Low power and compact reconfigurable multiplexing devices based on silicon microring resonators," *Opt Express*, vol. 18, no. 10, pp. 9852–9858, May 2010, doi: 10.1364/OE.18.009852.

[1-168] P. Dong, W. Qian, H. Liang, R. Shafiiha, D. Feng, G. Li, J. E. Cunningham, A. V. Krishnamoorthy, and M. Asghari, "Thermally tunable silicon racetrack resonators with ultralow tuning power," *Opt Express*, vol. 18, no. 19, pp. 20298–20304, Sep. 2010, doi: 10.1364/OE.18.020298.

[1-169] K. Padmaraju and K. Bergman, "Resolving the thermal challenges for silicon microring resonator devices," *Nanophotonics*, vol. 3, no. 4–5, pp. 269–281, 2014, doi: doi:10.1515/nanoph-2013-0013.

[1-170] L.-W. Luo, G. S. Wiederhecker, K. Preston, and M. Lipson, "Power insensitive silicon microring resonators," *Opt Lett*, vol. 37, no. 4, pp. 590–592, Feb. 2012, doi: 10.1364/OL.37.000590.

[1-171] K. Padmaraju, J. Chan, L. Chen, M. Lipson, and K. Bergman, "Thermal stabilization of a microring modulator using feedback control," *Opt Express*, vol. 20, no. 27, pp. 27999–28008, Dec. 2012, doi: 10.1364/OE.20.027999.

[1-172] Y. Kokubun, N. Funato, and M. Takizawa, "Athermal waveguides for temperature-independent lightwave devices," *IEEE Photonics Technol. Lett.*, vol. 5, no. 11, pp. 1297–1300, 1993, doi: 10.1109/68.250049.

[1-173] S. S. Djordjevic, K. Shang, B. Guan, S. T. S. Cheung, L. Liao, J. Basak, H.-F. Liu, and S. J. B. Yoo, "CMOS-compatible, athermal silicon ring modulators clad with titanium dioxide," *Opt Express*, vol. 21, no. 12, pp. 13958–13968, Jun. 2013, doi: 10.1364/OE.21.013958.

[1-174] M. Uenuma and T. Motooka, "Temperature-independent silicon waveguide optical filter," *Opt Lett*, vol. 34, no. 5, pp. 599–601, Mar. 2009, doi: 10.1364/OL.34.000599.

[1-175] B. Guha, B. B. C. Kyotoku, and M. Lipson, "CMOS-compatible athermal silicon microring resonators," *Opt Express*, vol. 18, no. 4, pp. 3487–3493, Feb. 2010, doi: 10.1364/OE.18.003487.

[1-176] X. Zheng, E. Chang, P. Amberg, I. Shubin, J. Lexau, F. Liu, H. Thacker, S. S. Djordjevic, S. Lin, Y. Luo, J. Yao, J.-H. Lee, K. Raj, R. Ho, J. E. Cunningham, and A. V. Krishnamoorthy, "A high-speed, tunable silicon photonic ring modulator integrated with ultra-efficient active wavelength control," *Opt Express*, vol. 22, no. 10, pp. 12628–12633, May 2014, doi: 10.1364/OE.22.012628.

[1-177] B. Desiatov, I. Goykhman, J. Shappir, and U. Levy, "Defect-Assisted Sub-Bandgap Avalanche Photodetection in Interleaved Carrier-Depletion Silicon Waveguide for Telecom Band," in *CLEO: 2014*, Optica Publishing Group, 2014, p. STh4I.4. doi: 10.1364/CLEO_SI.2014.STh4I.4.

[1-178] C. Qiu, J. Shu, Z. Li, X. Zhang, and Q. Xu, "Wavelength tracking with thermally controlled silicon resonators," *Opt Express*, vol. 19, no. 6, pp. 5143–5148, Mar. 2011, doi: 10.1364/OE.19.005143.

[1-179] J. A. Cox, A. L. Lentine, D. C. Trotter, and A. L. Starbuck, "Control of integrated micro-resonator wavelength via balanced homodyne locking," *Opt Express*, vol. 22, no. 9, pp. 11279–11289, May 2014, doi: 10.1364/OE.22.011279.

[1-180] P. Dong, R. Gatdula, K. Kim, J. H. Sinsky, A. Melikyan, Y.-K. Chen, G. de Valicourt, and J. Lee, "Simultaneous wavelength locking of microring modulator array with a single monitoring signal,"

Opt Express, vol. 25, no. 14, pp. 16040–16046, Jul. 2017, doi: 10.1364/OE.25.016040.

[1-181] K. Tanizawa, K. Suzuki, M. Toyama, M. Ohtsuka, N. Yokoyama, K. Matsumaro, M. Seki, K. Koshino, T. Sugaya, S. Suda, G. Cong, T. Kimura, K. Ikeda, S. Namiki, and H. Kawashima, "Ultra-compact 32 × 32 strictly-non-blocking Si-wire optical switch with fan-out LGA interposer," *Opt Express*, vol. 23, no. 13, pp. 17599–17606, Jun. 2015, doi: 10.1364/OE.23.017599.

[1-182] K. Ikeda, K. Suzuki, R. Konoike, S. Namiki, and H. Kawashima, "Large-scale silicon photonics switch based on 45-nm CMOS technology," *Opt. Commun.*, vol. 466, p. 125677, 2020, doi: https://doi.org/10.1016/j.optcom.2020.125677.

[1-183] P. Dasmahapatra, R. Stabile, A. Rohit, and K. A. Williams, "Optical crosspoint matrix using broadband resonant switches," *IEEE J. Sel. Top. Quantum Electron.*, vol. 20, no. 4, 2014, doi: 10.1109/JSTQE.2013.2296746.

[1-184] A. Youssefi, I. Shomroni, Y. J. Joshi, N. R. Bernier, A. Lukashchuk, P. Uhrich, L. Qiu, and T. J. Kippenberg, "A cryogenic electro-optic interconnect for superconducting devices," *Nat. Electron.*, vol. 4, no. 5, pp. 326–332, May 2021, doi: 10.1038/s41928-021-00570-4.

[1-185] M. H. Devoret and R. J. Schoelkopf, "Superconducting Circuits for Quantum Information: An Outlook," *Science*, vol. 339, no. 6124, pp. 1169–1174, 2013, doi: 10.1126/science.1231930.

[1-186] U. Vernik Igor V. (Yorktown Heights, NY, US), Mukhanov, Oleg A. (Putnam Valley, NY, US), Kadin, Alan M. (Princeton Junction, NJ, US), Phare, Christopher Thomas (New York, NY, US), Lipson, Michal (New York, NY, US), Bergman, Keren (Princeton, NJ, "System and method for cryogenic optoelectronic data link," 10097281, Oct. 2018 [Online]. Available: https://www.freepatentsonline.com/10097281.html

[1-187] U. Willer and W. Schade, "Photonic sensor devices for explosive detection," *Anal. Bioanal. Chem.*, vol. 395, no. 2, pp. 275–282, Sep. 2009, doi: 10.1007/s00216-009-2934-2.

[1-188] Y. Feng, Y. Zheng, F. Zhang, J. Yang, T. Qin, and W. Wan, "Passive fine-tuning of microcavity whispering gallery mode for nonlinear optics by thermo-optical effect," *Appl. Phys. Lett.*, vol. 114, no. 10, p. 101103, Mar. 2019, doi: 10.1063/1.5085923.

[1-189] K. D. Heylman and R. H. Goldsmith, "Photothermal mapping and free-space laser tuning of toroidal optical microcavities," *Appl. Phys. Lett.*, vol. 103, no. 21, p. 211116, Nov. 2013, doi: 10.1063/1.4833539.

[1-190] H. C. Tapalian, J.-P. Laine, and P. A. Lane, "Thermooptical switches using coated microsphere resonators," *IEEE Photonics Technol. Lett.*, vol. 14, no. 8, pp. 1118–1120, 2002, doi: 10.1109/LPT.2002.1021988.

[1-191] N. Ota, T. Miyauchi, and H. Shimizu, "221 K Local Photothermal Heating in a Si Plasmonic Waveguide Loaded with a Co Thin Film," *Sensors*, vol. 21, no. 19, 2021, doi: 10.3390/s21196634.

[1-192] N. Ota, K. Shinohara, M. Hasumi, and H. Shimizu, "Quantification of 288 K local photothermal heating and miniaturization in Si plasmonic waveguides integrated with resonators," *Jpn. J. Appl. Phys.*, vol. 62, no. 4, p. 042002, Apr. 2023, doi: 10.35848/1347-4065/acc917.

[1-193] Z. Liang, S. Liu, and Y. Shoji, "Improvement of extinction in optically-controlled silicon thermo-optic switch based on micro-ring resonator with distinct probe signal," *Jpn. J. Appl. Phys.*, vol. 62, no. 3, p. 032001, Mar. 2023, doi: 10.35848/1347-4065/acbc5d.

[1-194] V. R. Almeida, C. A. Barrios, R. R. Panepucci, and M. Lipson, "All-optical control of light on a silicon chip," *Nature*, vol. 431, no. 7012, pp. 1081–1084, Oct. 2004, doi: 10.1038/nature02921.

[1-195] F. Gan, T. Barwicz, M. A. Popovic, M. S. Dahlem, C. W. Holzwarth, P. T. Rakich, H. I. Smith, E. P. Ippen, and F. X. Kartner, "Maximizing the Thermo-Optic Tuning Range of Silicon Photonic

Structures," in *2007 Photonics in Switching*, 2007, pp. 67–68. doi: 10.1109/PS.2007.4300747.

[1-196] N. Sherwood-Droz, H. Wang, L. Chen, B. G. Lee, A. Biberman, K. Bergman, and M. Lipson, "Optical 4×4 hitless silicon router for optical Networks-on-Chip (NoC)," *Opt Express*, vol. 16, no. 20, pp. 15915–15922, Sep. 2008, doi: 10.1364/OE.16.015915.

[1-197] M. Geng, L. Jia, L. Zhang, L. Yang, P. Chen, T. Wang, and Y. Liu, "Four-channel reconfigurable optical add-drop multiplexer based on photonic wire waveguide," *Opt Express*, vol. 17, no. 7, pp. 5502–5516, Mar. 2009, doi: 10.1364/OE.17.005502.

[1-198] P. Dong, S. Liao, D. Feng, H. Liang, R. Shafiiha, N.-N. Feng, G. Li, X. Zheng, A. V. Krishnamoorthy, and M. Asghari, "Tunable high speed silicon microring modulator," in *CLEO/QELS: 2010 Laser Science to Photonic Applications*, 2010, pp. 1–2. doi: 10.1364/CLEO.2010.CThJ5.

[1-199] P. Dong, R. Shafiiha, S. Liao, H. Liang, C.-C. Kung, W. Qian, D. Feng, G. Li, X. Zheng, A. V. Krishnamoorthy, and M. Asghari, "Broadly tunable high speed silicon micro-ring modulator," in *IEEE Photonics Society Summer Topicals 2010*, 2010, pp. 197–198. doi: 10.1109/PHOSST.2010.5553682.

[1-200] M. R. Watts, W. A. Zortman, D. C. Trotter, G. N. Nielson, D. L. Luck, and R. W. Young, "Adiabatic Resonant Microrings (ARMs) with Directly Integrated Thermal Microphotonics," in *Conference on Lasers and Electro-Optics/International Quantum Electronics Conference*, Optica Publishing Group, 2009, p. CPDB10. doi: 10.1364/CLEO.2009.CPDB10.

[1-201] H. Jayatilleka, H. Shoman, L. Chrostowski, and S. Shekhar, "Photoconductive heaters enable control of large-scale silicon photonic ring resonator circuits," *Optica*, vol. 6, no. 1, pp. 84–91, Jan. 2019, doi: 10.1364/OPTICA.6.000084.

[1-202] A. M. Zin, M. S. Bongsu, S. M. Idrus, and N. Zulkifli, "An overview of radio-over-fiber network technology," in *International Conference On Photonics 2010*, 2010, pp. 1–3. doi: 10.1109/ICP.2010.5604429.

[1-203] C. Lim and A. Nirmalathas, "Radio-Over-Fiber Technology: Present and Future," *J. Light. Technol.*, vol. 39, no. 4, pp. 881–888, 2021, doi: 10.1109/JLT.2020.3024916.

[1-204] A. Kohmura, S. Futatsumori, N. Yonemoto, and K. Okada, "Optical fiber connected millimeter wave radar for FOD detection on runway," in *2013 European Radar Conference*, 2013, pp. 41–44.

[1-205] P. T. Dat, A. Kanno, N. Yamamoto, and T. Kawanishi, "WDM RoF-MMW and linearly located distributed antenna system for future high-speed railway communications," *IEEE Commun. Mag.*, vol. 53, no. 10, pp. 86–94, 2015, doi: 10.1109/MCOM.2015.7295468.

[1-206] A. Malacarne, S. Maresca, F. Scotti, B. Hussain, L. Lembo, G. Serafino, A. Bogoni, and P. Ghelfi, "A Ultrawide-Band VCSEL-Based Radar-Over-Fiber System," in *2019 International Topical Meeting on Microwave Photonics (MWP)*, 2019, pp. 1–4. doi: 10.1109/MWP.2019.8892243.

[1-207] Y. Yao, F. Zhang, Y. Zhang, X. Ye, D. Zhu, and S. Pan, "Demonstration of Ultra-high-resolution Photonics-based Kaband Inverse Synthetic Aperture Radar Imaging," in *2018 Optical Fiber Communications Conference and Exposition (OFC)*, 2018, pp. 1–3.

[1-208] M.-Y. Huang, Y.-W. Chen, P.-C. Peng, H. Wang, and G.-K. Chang, "A Full Field-of-View Self-Steering Beamformer for 5G mm-Wave Fiber-Wireless Mobile Fronthaul," *J. Light. Technol.*, vol. 38, no. 6, pp. 1221–1229, 2020, doi: 10.1109/JLT.2019.2956667.

[1-209] K. Sun, Q. Wang, D. Yu, L. Cao, X. Zhai, and J. Zhao, "The Ubiquitous Power Internet of Things Based on Dynamic and Reconfigurable ROF Technology," in *2019 IEEE 3rd Conference on Energy Internet and Energy System Integration (EI2)*, 2019, pp. 440–444. doi: 10.1109/EI247390.2019.9062207.

[1-210] Y. Tong, C.-W. Chow, G.-H. Chen, C.-W. Peng, C.-H. Yeh, and H. K. Tsang, "Integrated Silicon Photonics Remote Radio Frontend (RRF) for Single-Sideband (SSB) Millimeter wave Radio-Over-Fiber (ROF) Systems," *IEEE Photonics J.*, vol. 11, no. 2, pp. 1–8, 2019, doi: 10.1109/JPHOT.2019.2898938.

[1-211] K. Van Gasse, J. Verbist, H. Li, G. Torfs, J. Bauwelinck, and G. Roelkens, "Silicon Photonics Radio-Over-Fiber Transmitter Using GeSi EAMs for Frequency Up-Conversion," *IEEE Photonics Technol. Lett.*, vol. 31, no. 2, pp. 181–184, 2019, doi: 10.1109/LPT.2018.2889537.

[1-212] L. Bogaert, H. Li, K. Van Gasse, J. Van Kerrebrouck, J. Bauwelinck, G. Roelkens, and G. Torfs, "36 Gb/s Narrowband Photoreceiver for mmWave Analog Radio-Over-Fiber," *J. Light. Technol.*, vol. 38, no. 12, pp. 3289–3295, 2020, doi: 10.1109/JLT.2020.2968149.

[1-213] M. Ko, M.-J. Lee, H. Rücker, and W.-Y. Choi, "Silicon photonics-wireless interface ICs for micro-/millimeter wave fiber-wireless networks," *Opt Express*, vol. 21, no. 19, pp. 22962–22973, Sep. 2013, doi: 10.1364/OE.21.022962.

[1-214] G.-H. Chen, C.-W. Peng, M.-W. Cheng, P.-C. Guo, J.-F. Tsai, Y. Tong, C.-W. Chow, C.-H. Yeh, and H. K. Tsang, "Silicon-photonics based remote-radio-head using mode and wavelength division multiplexing with capacity of 4.781 Tbit/s for radio-over-fiber massive MIMO," in *45th European Conference on Optical Communication (ECOC 2019)*, 2019, pp. 1–3. doi: 10.1049/cp.2019.0746.

[1-215] M. Lyu, W. Shi, and L. A. Rusch, "Silicon photonic subsystem for broadband and RoF detection while enabling carrier reuse," *Opt Express*, vol. 28, no. 10, pp. 14897–14907, May 2020, doi: 10.1364/OE.391194.

[1-216] C. Browning, Q. Cheng, N. C. Abrams, M. Ruffini, L. Y. Dai, L. P. Barry, and K. Bergman, "A Silicon Photonic Switching Platform for Flexible Converged Centralized-Radio Access Networking," *J. Light. Technol.*, vol. 38, no. 19, pp. 5386–5392, 2020, doi: 10.1109/JLT.2020.2984379.

[1-217] B. Brian, "High Speed Imaging Of Magnetic Fields," Hackaday. Accessed: Nov. 02, 2023. [Online]. Available: https://hackaday.com/2018/02/15/high-speed-imaging-of-magnetic-fields/

[1-218] "Electromagnetic Field Visualization System EPS-02Ev3 - NOISE LABORATORY CO.,LTD.," NOISE LABORATORY CO.,LTD. - NOISE LABORATORY offers a broad range of the noise-related testers and measuring equipment, CE mark emission and immunity test equipment and far beyond. Accessed: Nov. 02, 2023. [Online]. Available: https://www.noiseken.com/products/emc/eps/6411/

Chapter 2
Si Photonics Components

2.1 Overview

Thanks to CMOS technology, Si photonics has seen significant growth in recent years. However, not every research organization possesses its own Si chip processing equipment, as it would be costly to establish and maintain. To address this, many Si photonics foundries have introduced multi project wafer (MPW) services, which aim to reduce chip fabrication costs by sharing mask and wafer processing expenses among users from various organizations and institutes. This approach effectively lowers the overall cost of fabricating Si photonics chips and contributes to the development of the Si photonics industry. In this chapter, we provide an overview of Si optical foundries and the processes involved in Si device fabrication using MPW. We also present an overview of common Si optical devices.

2.2 Fabrication

2.2.1 Si Photonics Foundry

The Si photonics industry is based on the highly developed semiconductor industry, or the integrated circuit industry. Manufacturers in this field can be categorized into three major types depending on whether they handle the design, manufacturing, and sales of chips within the same enterprise: Integrated Device Manufacturing (IDM), fabless, and foundry. IDM companies have sufficient funds to cover all processes, from chip design and manufacturing to sales. Fabless manufacturers, on the other hand, lack their own wafer manufacturing facilities and outsource chip production to specialized wafer manufacturing companies, while handling the design and sales themselves, making them more flexible. Foundries, with their mature processing technology, strictly follow received layout for chip design and manufacturing, without participating in the design and sales aspects. This has led to a growing preference among universities and research institutions for using foundries to produce and verify their designs, driven by cost considerations and copyright concerns. Common wafer diameters include 200 mm (8 inches) and 300 mm (12 inches), etc., and the number of Dies Per Wafer (DPW) can vary depending on die size. Due to the excessive cost, research institutes often share the same die with other institutions through the MPW approach, rather than fully occupying each die with their own designs. The designer submits the design drawings to the foundry, where they undergo a Design Rule Check (DRC). If errors are detected, the design is returned to the designer for modifications. Once confirmed as correct, the foundry proceeds with manufacturing, which called the tape out. The production cycle can range from a few months to half year, depending on factors such as the foundry's capabilities, wafer type, design complexity, special processing requirements, and the expertise of the parties involved in the MPW process. After the wafers are fabricated, they are sent to specialized dicing companies to partition the devices among different organizations on each die. In this study, we utilized a domestic foundry in Japan and engaged in MPW to manufacture the various devices proposed in this design.

2.2.2 Design Rule

The foundry used in this study is the National Institute of Advanced Industrial Science and Technology (AIST) in Japan, which utilizes 300 mm wafers and employs the ArF excimer laser immersion exposure process on Si waveguides to achieve a minimum linewidth of 80 nm. For a standard foundry, the supported design rules are provided to the user in advance. Table 2-1 shows the layer numbers used by the foundry for each layer mask and their respective representations. As indicated in Table 2-2, for low

concentration doping, Boron (B) and Phosphorus (P) ions were implanted at acceleration voltages of 38 keV and 100 keV with doses of 1.05×10^{13} cm^{-2} and 1.12×10^{13} cm^{-2}, while for high concentration doping, acceleration voltages of 25 keV and 50 keV were used, respectively, both with a doping concentration of 5×10^{15} cm^{-2}. After ion implantation doping, a 1050 °C, 5 s Rapid Thermal Annealing (RTA) process was performed to repair the lattice damage caused by energetic ion implantation and to activate the dopant ions. The minimum width of rectangular shaped dope is 4 μm, and the accuracy of doping positioning with the doped Si rib waveguide is smaller than 0.1 μm.

Some typical Si-based components supported by the used foundry, including channel waveguides (or strip waveguides, Si wire), Rib waveguides, modulators, heaters, etc., are illustrated in Fig. 2-1. Figures 2-1(a), (b), and (c) depict the top view, A-A' cross-section, and B-B' cross-section, respectively. A 220 nm-thick Si layer was deposited on top of a 3 μm buried oxide (BOX) layer. In the case of the Si rib waveguide, it was half-etched to a depth of 110 nm. For a typical rib modulator, or photonic crystal waveguide (PCW) modulator, both high and low doped ridge waveguides or PCW waveguides are used, and a contact hole is employed to connect the high-doped Si slab to the aluminum (Al) layer. Additionally, a 50 nm-thick titanium nitride (TiN) electrical heater was deposited 1.2 μm above the Si layer and connected to the Al layer through a contact hole used for TiN. Above the metallic Al layer, there is a 600 nm oxide film to insulate the surroundings. In the bonding pad section, the oxide film above the Al was removed, exposing the Al to the air to facilitate probe contact or wire bonding.

Table 2-1 Mask layers definition.

Layer Number	Layer
30	Si Waveguide
31	n Dope
32	p Dope
33	n+ Dope
34	p+ Dope
35	Contact (for pn)
36	Metal
38	TiN Heater
39	Contact (for TiN Heater)
40	Rib
41	Pad Window

Table 2-2 Doping parameters.

Doping Type	p$^+$-Si	p-Si	n-Si	n$^+$-Si
Dopant	Boron (B)		Phosphorus (P)	
Concentration [cm^{-2}]	5×10^{15}	1.05×10^{13}	1.12×10^{13}	5×10^{15}
Acceleration Voltage [keV]	25	38	50	100

(a) Top View

A — A'

Al

TiN

B — B'

Heater

Rib Modulator

PCW Modulator

Pad Window

Si Channel Waveguide

Si Rib Waveguide

(b) Cross Sectional View (A-A')

Pad Window

2100 nm
220 nm
110 nm
3000 nm

SiO₂
Si

(c) Cross Sectional View (B-B')

500 nm
Contact Hole
TiN
1200 nm

450 nm

p⁺-Si   p-Si   n-Si   n⁺-Si

SiO₂
Si
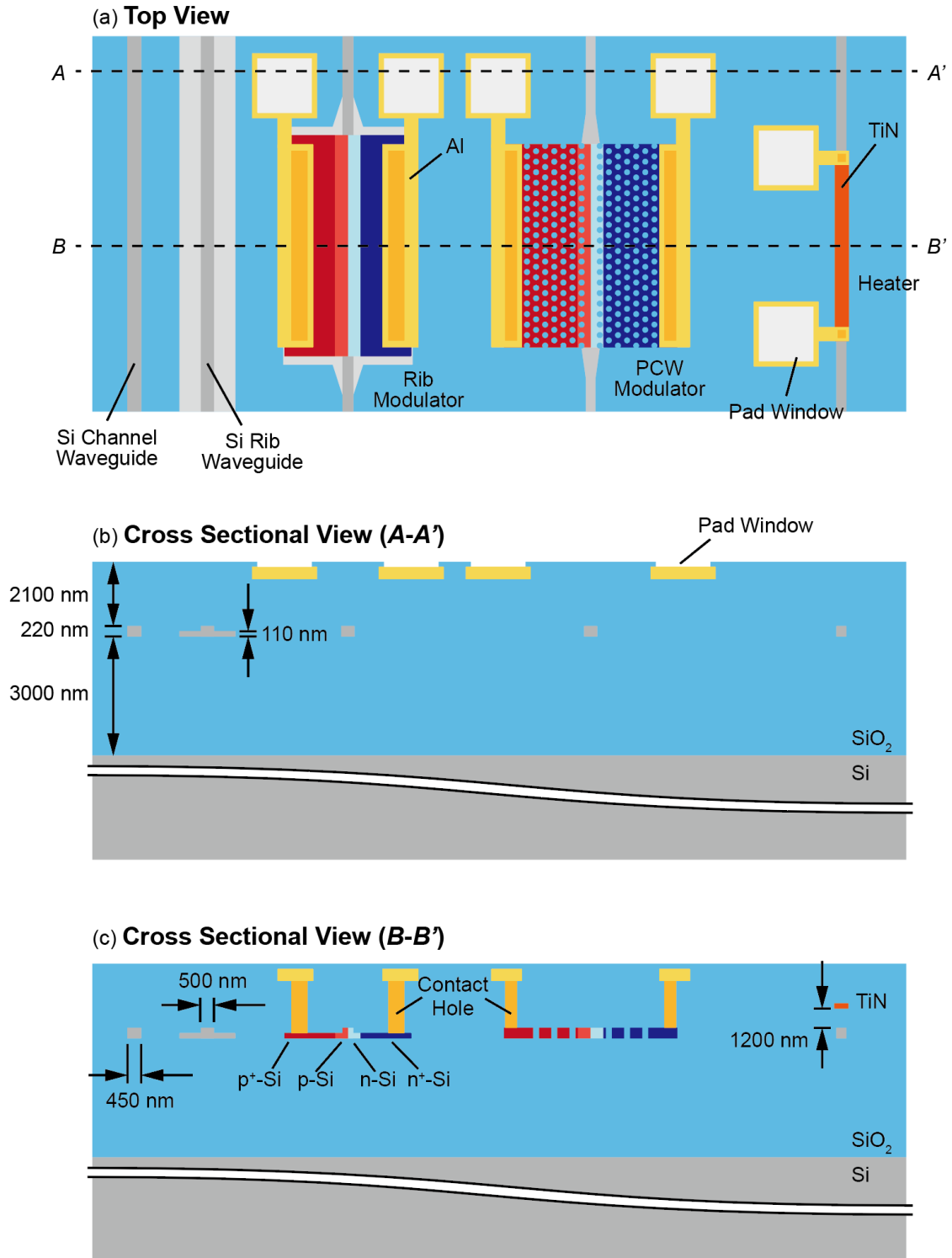
Figure 2-1 Illustration of some fundamental components and their size in fabrication. (a) Top view. (b) Cross section of A-A' plane. (c) Cross section of B-B' plane.

In this study, we followed the design flow as shown in Fig. 2-2. First, we calculated various parameters, such as waveguide width, bending radius, pattern shape, etc., necessary to realize the desired device functionality based on the basic data provided by the foundry, which includes the thickness of the Si slab, the depth of the ridge waveguide etching, and the doping concentration, etc. These parameters are often designed in sets with consistent spacing to mitigate potential deviations in device performance

caused by fabrication errors. Typically, we use Microsoft Excel to store all the design data and utilize macro functions to generate a parameter list (.h file) for use in the subsequent steps. Next, we use the Visual Studio to import the parameter tables for each device and generate a computer aided design (CAD) file based on specific rules using a layout generation script written in C++. The resulting file has a .dxf extension and can be opened by various CAD software such as AutoCAD or KLayout. However, for the foundry we are working with, the accepted layout format is .gds, so we must further convert the .dxf file into a .gds file. This conversion can be done using KLayout or specialized format conversion software like Dvogue. With the converted .gds file, we can then submit it to the foundry for design rule checking (DRC). Typically, the foundry conducts the DRC, but occasionally they may provide the DRC program and another rule file (.txt) to the user for checking design rules until they meet production requirements. This approach enhances design efficiency. Common design errors identified during DRC include issues like the minimum size of mask patterns and minimum spacing not meeting the requirements. At this stage, we need to adjust the design parameters until the DRC no longer reports errors. Once the factory's requirements are satisfied, they will accept the CAD layout and initiate the fabrication process. At this point, the user's design process is completed.

Next, the foundry will manufacture the chips according to the CAD provided by the user. After production, the factory will dice the chips within different shot areas on the whole wafer, segregating chips belonging to different users in the same shot area and distributing them to respective users. After receiving the chips, we can conduct basic performance tests or use them directly for experimental evaluation. For most small-scale devices, we employ edge coupling or grating coupling for inputting and outputting light and use electrical probes or simple wire bonding for electrical signals. For devices requiring packaging, such as large-scale optical switches or LiDAR systems, which necessitate stable and convenient electrical/optical connections, we need to dice out the parts that require packaging from the chip. This step often involves the assistance of specialized dicing companies. The whole chip that will be directly packaged, for example LiDAR chips, does not require dicing. After dicing, the chip is handed over to a specialized packaging company for optical and electrical packaging. The packaged chip is then ready for evaluation experiments.
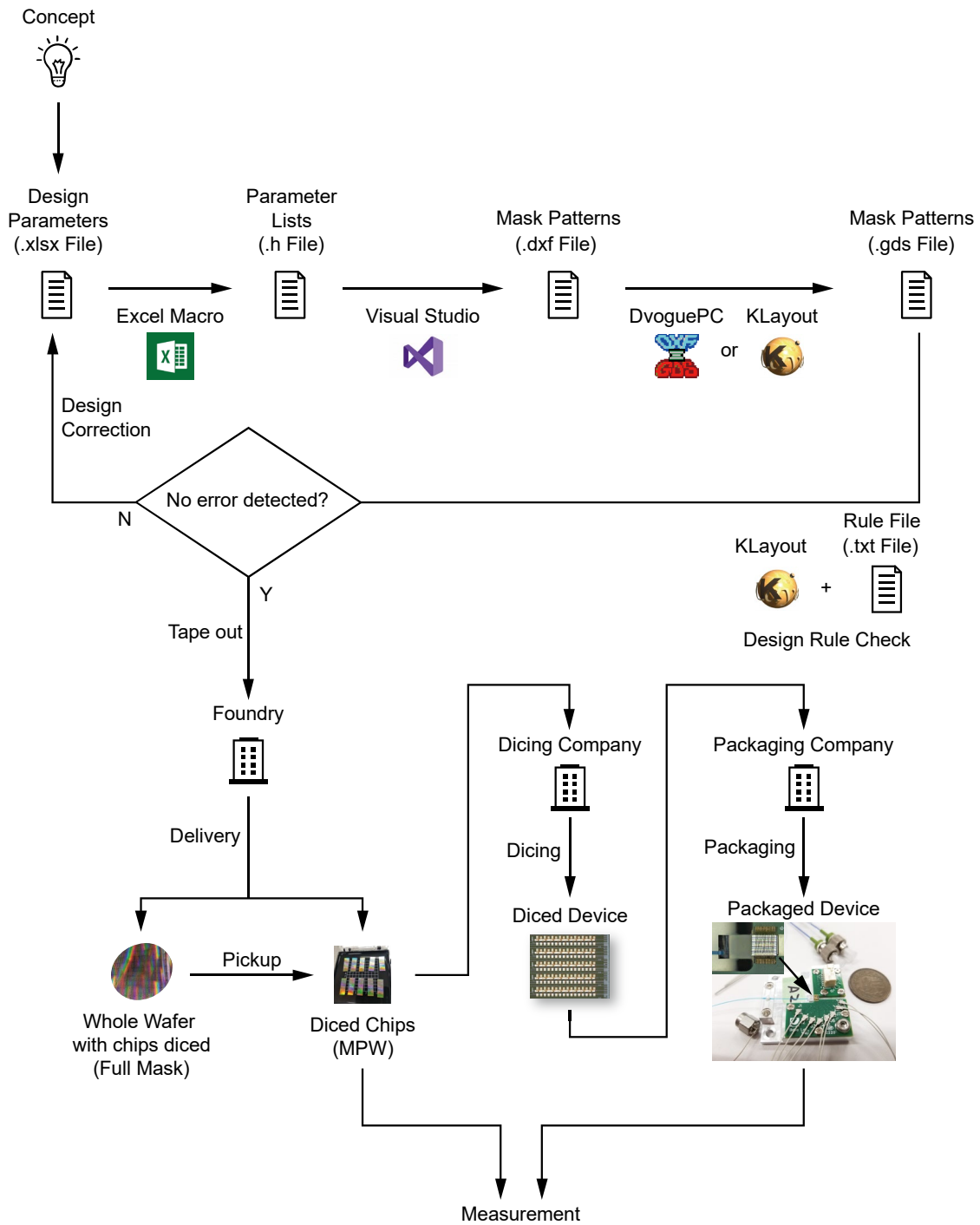
Figure 2-2 Fabrication and test flow of Si photonics chips using foundry.

2.2.3 CAD Pattern Creation

The creation of the CAD pattern is described in detail next. For simple patterns, like a fundamental single waveguide-type device, we have the flexibility to use CAD software for manual drawing to create CAD files. In the case of some larger-scale devices, such as LiDAR's optical switch arrays, where the same cell is extensively reused, duplicate components within it can be saved as a cell and manually called up when needed. The connections between cells can be easily made through manual drawing. However, for comprehensive designs that incorporate various types of devices, especially when there's

a need to easily modify a specific parameter in one of the parts, using a script to generate a CAD file proves to be a more efficient method. In this study, we utilized the pattern generation method employing scripts. First, we use Microsoft Excel to manage the parameters needed for each design. For instance, in this design, for a single MRM, we need to calculate in advance the optimal width of the waveguide corresponding to a given thickness of the Si slab, the radius of the microring, the spacing between the microring and the bus waveguide, and so on. For those parameters susceptible to large fabrication errors or where even extremely small variations can greatly affect the results, such as the spacing between the microring and the bus, we set around 3 to 5 parameter sets where only that variable varies. This approach ensures that even if the measured values of the parameters deviate from the design values, there will be devices similar to the design values among those produced using these sets of parameter groups. Figure 2-3 (a) shows the worksheet of the parameter table used. Generally, each row of the worksheet represents a device (i.e., a general term for all the components connected to the same waveguide), and each column represents the value of a particular parameter. Figure 2-3(b) displays the same parameter table (.h file) generated by Excel's Macro, based on the parameter table in Fig. 2-3(a). This file does not require manual editing. The reason for using the Excel worksheet is that it is more manageable. Next, we use Visual Studio's CAD generation script to first read the parameter table shown in Fig. 2-3(b). Specific sub-functions written in C++ (e.g., Fig. 2-4 (a)) are then employed to directly generate a .dxf file containing all the graphic vertices, lines, layers, etc., which can be opened and read by CAD software, as shown in Fig. 2-4 (b). As shown in Figs. 2-5(a) and (b), the generated layout file can be viewed in image form by using CAD software, such as AutoCAD and KLayout, to open the .dxf file. An important consideration is that for arc objects, as the script approximates them as polygons connected by a specific number of points, it is crucial to appropriately increase the number of vertices in polygons, particularly for objects with a large radius. This adjustment is necessary to ensure the actual device remains sufficiently smooth, avoiding any impact on the device's performance. Finally, using KLayout or Dvogue, .dxf files can be converted to .gds files accepted by the foundry. Notably, the latter employs a finer polygonization when handling curved objects, which is crucial for objects with small bending radii, such as holes in photonic crystal waveguides. Conversion using Dvogue needs a rule file (.rul) additionally. At this point, we have completed CAD pattern creation.

(a)   (b)
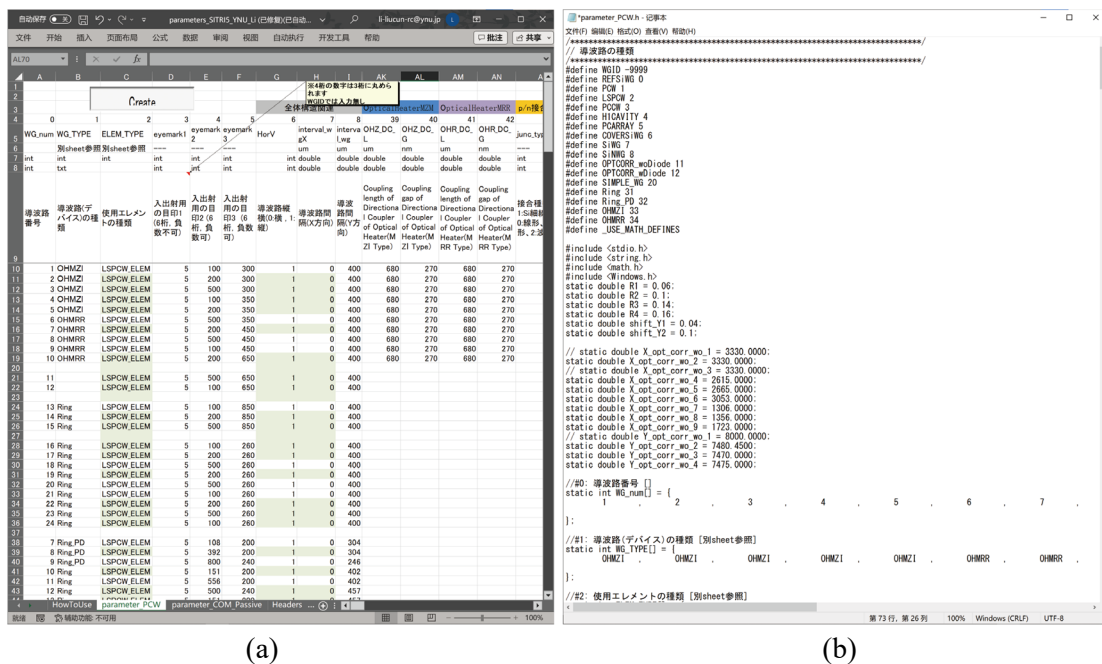
Figure 2-3 (a) Parameter lists in Excel worksheet. (b) Parameter lists generated by Excel macro using (a).
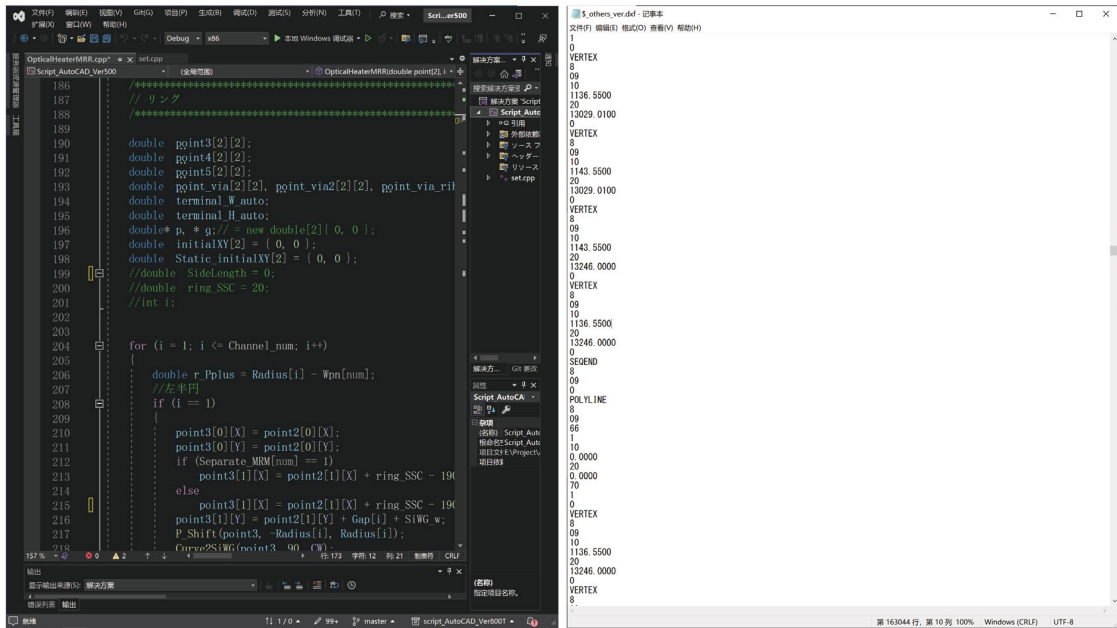
(a)   (b)

Figure 2-4 (a) CAD generation script in C++. (b) Generated CAD file (opened by Notepad).
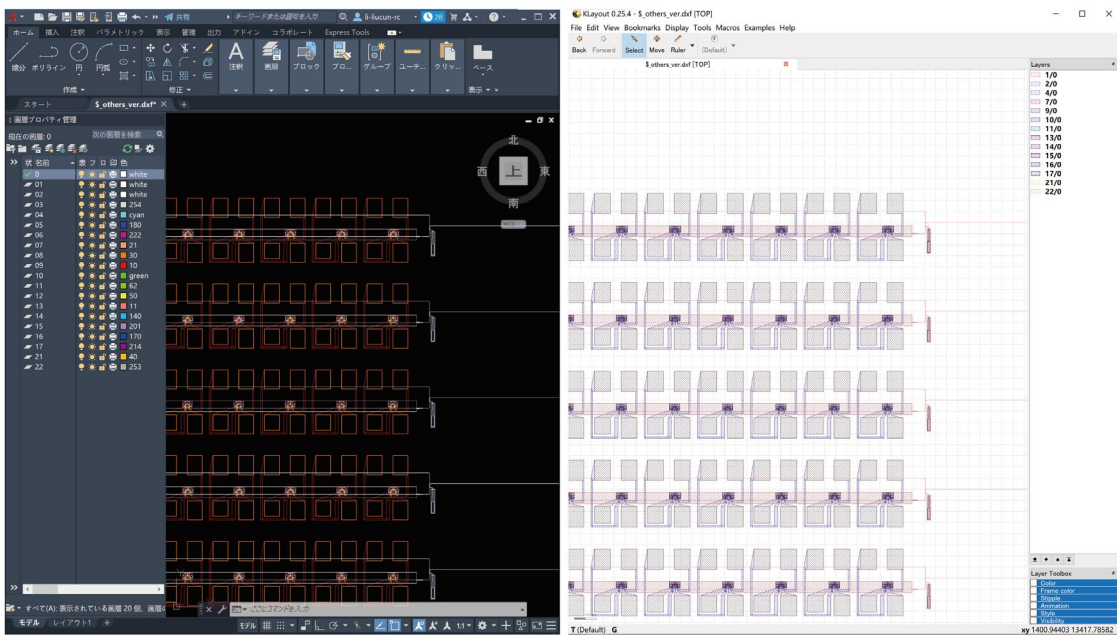
(a)   (b)

Figure 2-5 Generated CAD file opened by (a) AutoCAD. (b) KLayout.

2.2.4 Design Rule Check

After the initial generation of the CAD file, it undergoes a crucial stage of DRC to ensure compliance with the foundry's requirements. To facilitate this process, objects on the same layer within the CAD file may need to be merged using KLayout in advance. The DRC process involves employing the foundry-provided DRC program through KLayout's built-in macro function. With the CAD file open, the macro program is run, prompting the selection of the rule file provided by the foundry in a dialog box. KLayout then automatically executes the DRC, comparing various objects within or between layers—evaluating

minimum spacing, width, vertex angles, and more—against the specifications outlined in the rule file. Upon detection of non-compliance, the DRC program marks these errors using an error layer (often a layer number over 100), indicating the position of the error through geometrical shapes. Large-scale, complex designs might necessitate extensive time and memory to traverse all layers during the DRC process. Once the DRC is complete, any nonconformities are highlighted by displaying only the error layers. Iterative corrections are then targeted to rectify these errors, eventually producing a CAD layout that aligns with the foundry's design requirements.

It is important to note that certain design errors, such as waveguide breaks, dimensional errors, and layer errors, may not be detected even with the implementation of DRC. As a result, DRC does not entirely guarantee the accuracy of the design. To ensure that the design is realized as intended, a thorough human check is indispensable. Another notable point is that when employing Dvogue for file format conversion, minor breaks of 1 nm may occasionally appear in Si waveguide layers. However, the importance of these errors relies on the actual fabrication resolution and might be negligible in practical terms.

2.3 Components

2.3.1 Spot Size Converter

A spot size converter (SSC) serves as one of the on-chip I/O components, facilitating efficient coupling of light from an optical fiber into/out of an on-chip optical waveguide. The SSC enables end face coupling of light by converting light modes from optical fibers with large mode field diameters (MFD) to small MFD light modes that can be confined within the Si waveguide. This conversion is achieved through an adiabatic change in the waveguide width.

Figure 2-6 shows CAD layouts and optical microscopic photograph of the SSC employed in this study. The SSC's tip consists of a section of straight waveguide with a width of 180 nm and a length of 100 μm, connected to a taper section with a length of 100 μm, featuring a gradual transition to a width of 440 nm, and ultimately leading to the waveguide with a width of 440 nm. The Si thickness of the SSC is 220 nm. As the standard SSC from the Foundry's Process Design Kit (PDK) is employed in this study, the final width of the SSC remains unadjustable. When a desired waveguide width deviates from 440 nm, a taper section must be added at the end to gradually increase the waveguide width to the desired dimension, which is implemented in our study. The SSC specifically supports transverse electric (TE) like mode of optical coupling.

(a)

(b)
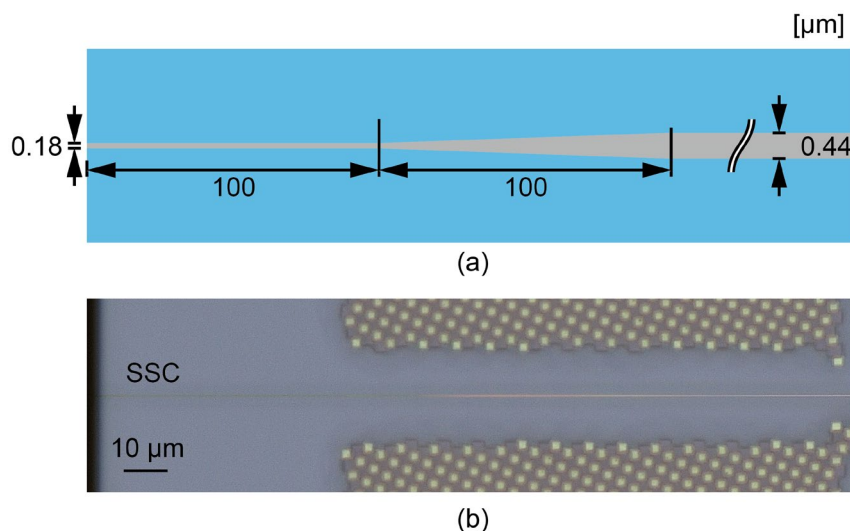
Figure 2-6 (a) Design model of SSC. (b) Fabricated SSC.

2.3.2 Si Waveguide

After coupling light from an optical fiber into an on-chip waveguide using an SSC, the light propagates along a waveguide with a certain width. In the case of the strip waveguide, illustrated in Fig. 2-7(a), the optical waveguide's thickness is 220 nm, and the width is denoted as w. Altering w enables accommodation of one or more optical modes inside the waveguide. To explore these optical modes for different w values, we conducted simulations using the Lumerical Finite-Difference Eigenmode (FDE) solver with perfectly matched layer (PML) boundary conditions. The computational conditions are detailed in Table 2-1, and the results are presented in Fig. 2-8. The simulation reveals that when w is smaller than 0.45 μm, basic optical modes, including TE and Transverse Magnetic (TM) modes, emerge. As w increases, higher-order optical modes appear sequentially. While some studies have specifically explored multimode waveguides for mode conversion and optical signal processing [2-1], in our study, we concentrate on single-mode waveguides supporting TE modes. To achieve the single mode condition, we set w to 0.45 μm. At this point, the effective refractive index n_{eff} and group refractive index n_{g} of the strip waveguide are 2.35 and 4.34, respectively. The modal profiles (Electrical field intensity) of TE-like and TM-like mode for strip waveguide with w = 0.45 μm are shown in Figs. 2-9 (a) and (b), respectively.

Similarly, for the rib waveguide depicted in Fig. 2-7(b), with total thickness of 220 nm, and half-etched. Simulation calculations were performed for its width w, and the resulting dispersion curve is shown in Fig. 2-9. The single-mode transmission condition in this case is when w is less than 0.5 μm. We determined w as 0.5 μm for rib waveguide. The TE-like profile is shown in Fig. 2-9 (c). The n_{eff} and n_{g} of the rib waveguide are 2.61 and 3.89, respectively.
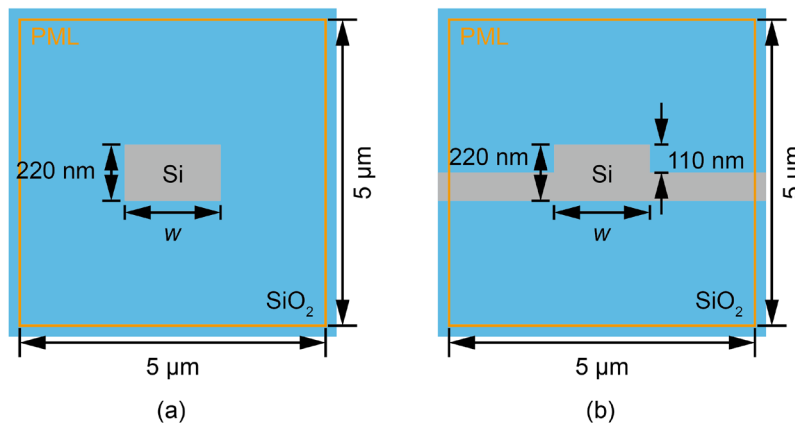
Figure 2-7 Simulation model of (a) strip waveguide and (b) rib waveguide.
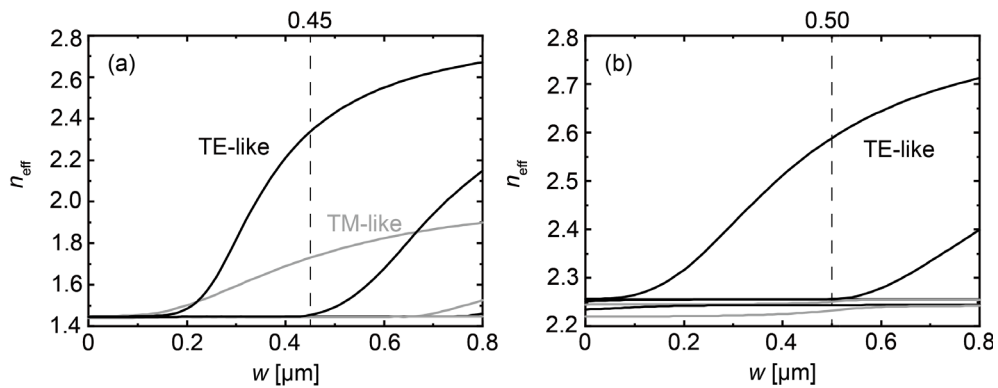
Figure 2-8 Dispersion curve of different optical mode in waveguides with varies w. (a) Strip waveguide. (b) Rib waveguide.

Table 2-1 Simulation condition of waveguide	
Wavelength	1550 nm
n_{Si}	3.48
n_{SiO2}	1.44
Mesh size	0.01 μm
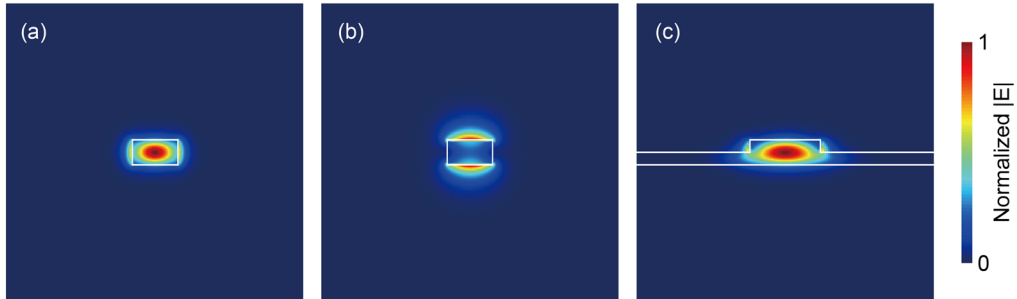
Figure 2-9 Modal profile of (a) TE-like and (b) TM-like mode with w = 0.45 μm for strip waveguide. (c) TE-like mode with w = 0.5 μm for rib waveguide.

2.3.3 Bending

Bending is a crucial aspect of waveguide-type optical devices. Bending with a large radius is detrimental to the compact integration of an optical device, while bending with a small radius results in large bending losses. Si waveguides in silica cladding allow for a relatively small bending radius due to the strong light confinement ability of Si waveguide. The model and optical photographs are presented in Figs. 2-10(a), (b). Here, we only showed the concept model for bending of strip waveguide. The bending radius is defined as the distance from the center of the bending circle to the center of the waveguide.

In this study, for the 90-degree bend in the strip waveguide, a bending radius of 5 μm was employed to ensure that the bending loss is sufficiently low and negligible throughout the device. For the rib waveguide, where there is more bending loss at the same radius, it becomes necessary to increase the bending radius to maintain minimal bending loss in the MRM. We conducted simulations to assess the propagation loss of the rib waveguide at different radii using the Lumerical FDE solver. We employed a simulation model similar to that of Fig. 2-7(b), with the only difference being the bending radius R. The simulation conditions are detailed in Table 2-1, and the results are depicted in Fig. 2-11. A bending loss of 0.03 dB/Round is obtained for R = 10 μm, which is deemed small enough for the purposes of this research. We set R = 10 μm for rib waveguide in this research.
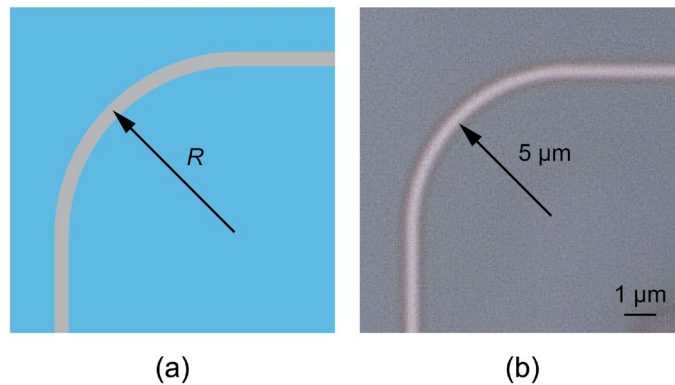
Figure 2-10 (a) Model of bending of strip waveguide. (b) Microscopic photograph of a 5 μm radius bending.
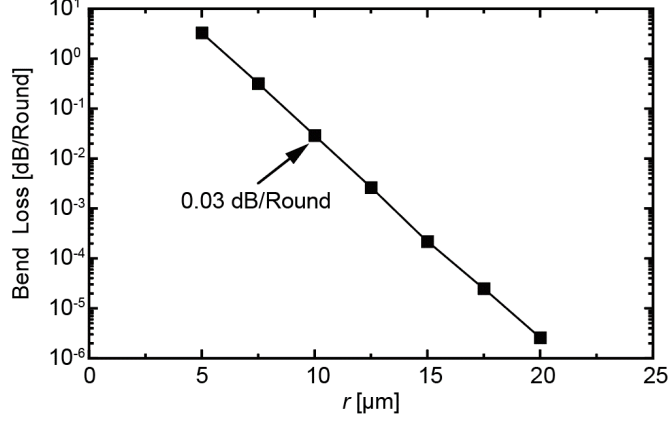
Figure 2-11 Simulation of bend loss with different bending radius r
in rib waveguide.

2.3.4 Directional Coupler

A directional coupler is a device used to couple light from one waveguide into another neighboring waveguide. It can function as a power splitter or as a monitor of the optical power within the waveguide. In this study, the directional coupler is primarily employed for optical coupling between the microring and the bus waveguide in an MRM consisting of rib waveguides. Figure 2-12 (a) illustrates the model of the directional coupler. We chose a bending radius of 10 μm because, in this study, the directional coupler is primarily employed for the coupling part of the MRM. The MRM consists of rib waveguides, which necessitate a larger bending radius. When light with power P_0 is input to the bus waveguide, the optical power P_1 output from the drop waveguide satisfies Eq. 2-1, where κ is the power coupling ratio, L is the coupling length, λ is the optical wavelength, and Δn is the difference in effective indices of the odd and even modes of the super mode formed by the two waveguides. Figure 2-12(b) displays a microscopic photograph of a directional coupler used as a power monitor in this study.

To achieve a specific coupling ratio κ, we simulated the directional coupler using the Lumerical Finite-Difference Time-Domain (FDTD) solver, with simulation conditions outlined in Table 2-2. For both the light source and power monitor, we used ports to simplify the simulation calculations. Two critical design parameters are the gap distance G between the waveguides and the length L of the coupling section. Given that the gap distance G is more susceptible to fabrication errors than the coupling length L, G is fixed in this study. Different L values are set to achieve the desired power coupling ratio κ. The computational results obtained from the simulation are presented in Fig. 2-13. In this study, as the minimum gap of two rib waveguide is 250 nm, here, G is fixed at 260 nm. To achieve a κ value of 0.1, L is set to 0.18 μm. The determination for the κ will be detailed in Chapter 3.

$$\kappa = \frac{P_1}{P_0} = \sin^2\left(\frac{\pi L \Delta n}{\lambda}\right) \tag{2-1}$$

Table 2-2 Simulation condition of directional coupler

Wavelength	1550 nm
n_{Si}	3.48
n_{SiO2}	1.44
Port size	3×3 μm^2
Mesh size	0.01 μm

47
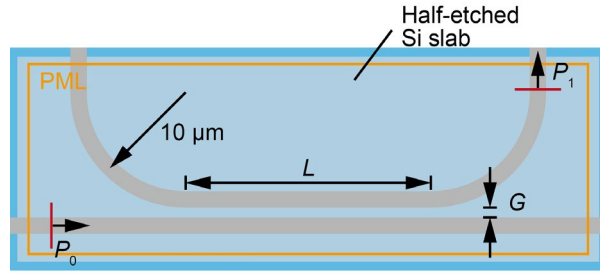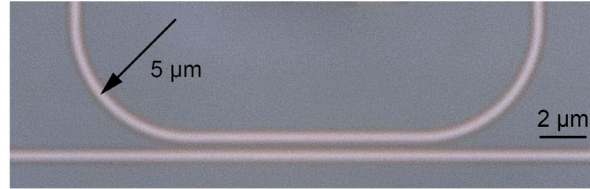
Figure 2-12 (a) Model of directional coupler with a 10 μm bend used in an MRM. (b) Microscopic photograph of a directional coupler sample as a power monitor with a 5 μm bend.
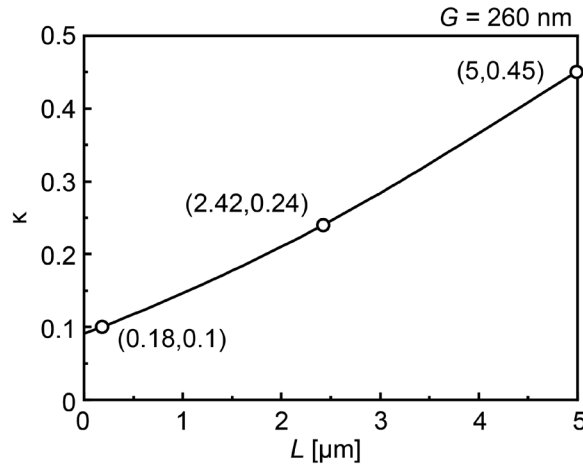
Figure 2-13 Simulation result of power coupling ratio of directional coupler with gap $g = 260$ nm and coupling length L varies.

2.3.5 P-N Junction

As illustrated in Fig. 2-14, this study employed a symmetric horizontal p-n junction to achieve modulation of the optical signal. We doped the previously mentioned rib waveguide with different types and concentrations. In this study, the p-typed doping concentration is 1.05×10^{13} cm^{-3}, n-typed doping concentration is 1.12×10^{13} cm^{-3}, while for high concentration doping, both with a doping concentration of 5×10^{15} cm^{-3}. Here, the length W_{pn} of the high-concentration doping region from the center of the waveguide is a critical factor in determining the doping loss of the microring. When W_{pn} is too small, the high-concentration doping is too close to the waveguide, leading to high carrier absorption and, consequently, high optical loss. On the other hand, if W_{pn} is too large, the optical loss in the microring may be too small to achieve the critical coupling condition at a given Q value. In this study, we set W_{pn} equal to 0.65 μm. Detailed calculations are provided in Chapter 3.

We utilized the Lumerical CHARGE solver to simulate the carrier distribution inside the waveguide under different bias conditions at $W_{pn} = 0.65$ μm. The simulation model is depicted in Fig. 2-15(a). Constant doping was employed, and the doping concentration in each doped region was set as described earlier. The CHARGE monitor was established to record carrier changes in the monitor region. The 2D

48

simulation results are presented in the left column of Fig. 2-16. As the reverse bias increases, the depletion region formed in the center of the waveguide widens.

At the same time, the junction capacitance based on electrons and holes is calculated, as shown in Fig. 2-17(a). The analytic junction capacitance is also included in the same plot, illustrating that the junction capacitance decreases with an increase in reverse bias [2-2]. Meanwhile, the Lumerical FDE solver was employed to import the carrier density distribution profile from the CHARGE simulation and load it onto the simulation model, as illustrated in Fig. 2-15(b). The optical modes and effective refractive indices in the center region of the waveguide are recorded. The optical mode variations are depicted in the middle column of Fig. 2-16. By comparing the carrier concentration within the waveguide with the optical mode, it is evident that the optical mode overlaps with the pn junction depletion region.

Additionally, we calculated the optical modes with the 10 μm bending, shown in the right column of Fig. 2-16. The sufficiently large bending radius of 10 μm does not lead to significant optical mode leakage. For the simulation of effective index and propagation loss of the optical modes under different bias states (only the loss due to doping is calculated here, excluding the loss due to bending), we used the simulation model as depicted in Fig. 2-15(b), and the results are shown in Fig. 2-17(b). With an increase in reverse bias, the carrier concentration inside the optical waveguide diminishes, causing the effective refractive index to increase by an order of magnitude of 10^{-4}, while the optical loss due to carrier absorption decreases. This follows the equations describing the variation of the Si refractive index and loss with carrier concentration, as shown in Eqs. 1-4 and 1-5 [2-3]. Therefore, by altering the voltage applied to the two electrodes of the pn junction, adjustments in the intensity and phase of light passing through the waveguide formed by the pn structure can be made to achieve the modulation purpose.
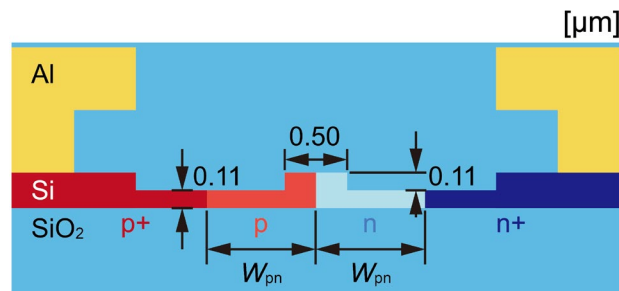
Figure 2-14 Model of p-n junction in this study.
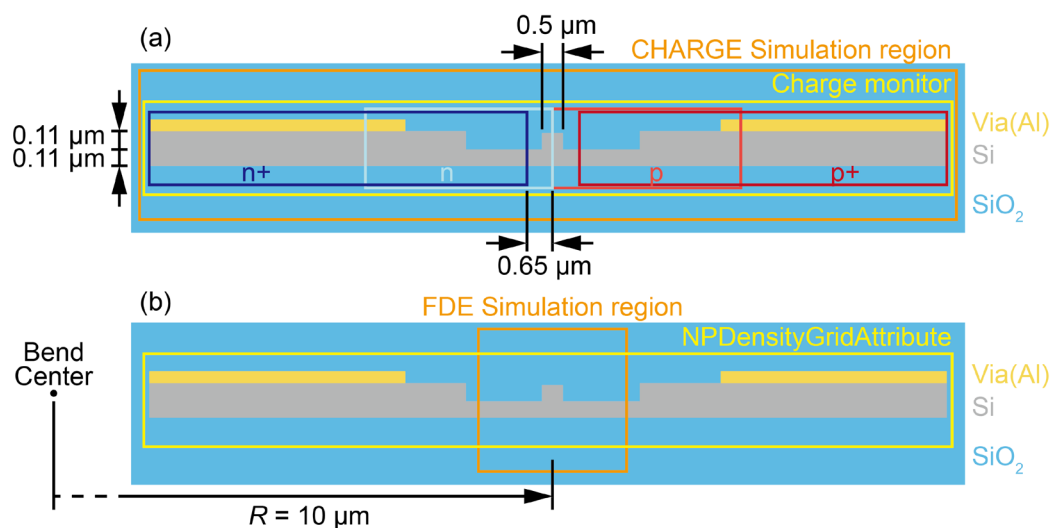
Figure 2-15 Simulation model of pn junction in Lumerical (a) CHARGE solver and (b) FDE solver.
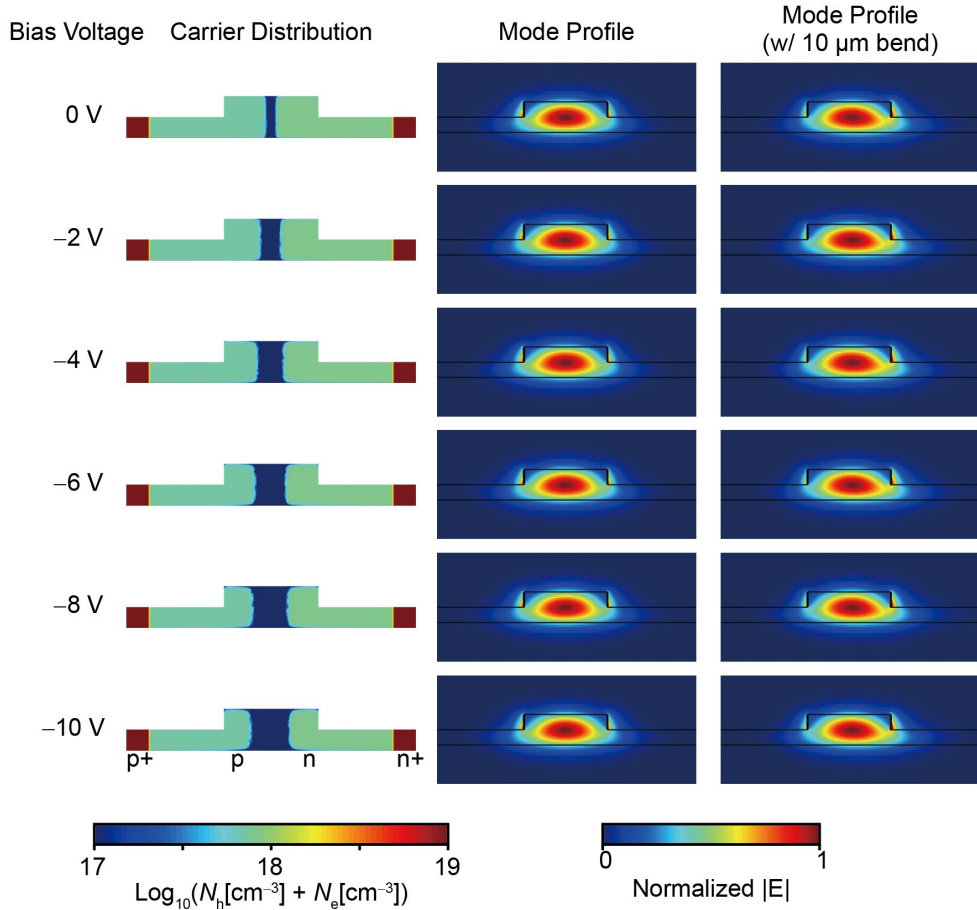
Figure 2-16 Carrier distribution and optical modal profile with/without bending of p-n junction section with varies bias voltages.
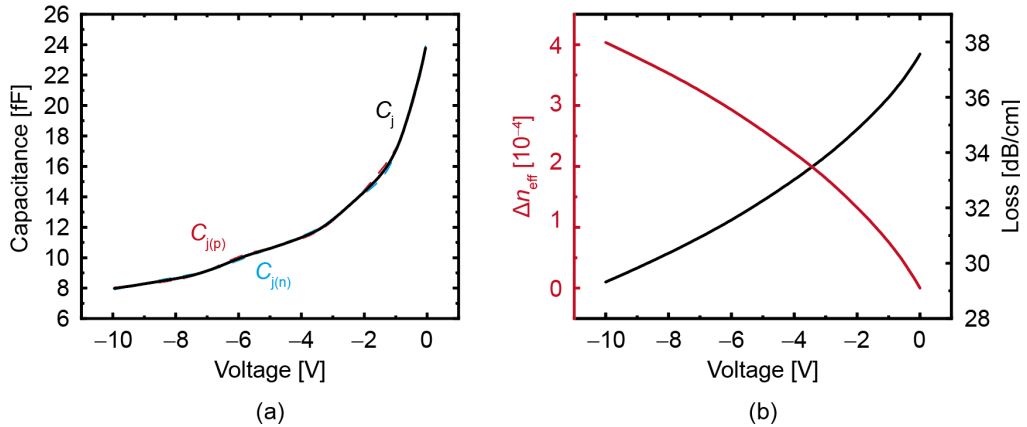
Figure 2-17 Simulation result of (a) capacitance of pn junction, (b) effective index change and doping loss of waveguide.

2.3.6 Microring Resonator

In this study, although we do not directly utilize the microring resonator (MRR) to realize functions like filtering and WDM, the MRM in this study is based on the MRR. The model of the MRR is illustrated in Fig. 2-18, and it is categorized into all-pass type MRR and add-drop type MRR based on whether it has multiple straight waveguides. Most MRRs, including the MRM, need to operate near the critical coupling condition. This condition implies that the optical power coupled into the microring must be

equal to the optical power lost inside the microring. This ensures that the microring has a maximum resonance depth near the resonance point, achieving the maximum stopband attenuation of the MRR or the maximum modulation efficiency of the MRM.

To achieve critical coupling in the MRR, for the all-pass type MRR, we only need to adjust the optical power coupling ratio between the microring and the bus waveguide, specifically, the κ of the directional coupler mentioned earlier. This adjustment is made to ensure that it is equal to the internal optical loss of the MRR. However, the internal loss of a microring consisting of a Si strip waveguide depends almost exclusively on the loss in the bending part and the loss due to sidewall roughness. These losses are often so small that accurately predicting the actual loss value from simulations is challenging. Therefore, multiple sets of MRRs with different κ values are often fabricated to ensure that there is always a device with a similar value to that of the design. To achieve critical coupling, an exceedingly small loss in the ring implies a very small κ. Hence, employing a circular microring allows for the reduction of the coupling length while simultaneously increasing the coupling spacing to minimize κ. On the other hand, the add-drop configuration is more common since MRRs are more often used in filters. In this case, if the internal loss of the microring is almost negligible, realizing critical coupling only requires ensuring that the optical power coupling ratio between the microring and the two waveguides is the same. This means ensuring that the design of the coupling sections at both coupler remains consistent. Figure 2-19 displays a microscopic photograph of an add-drop type MRR sample consisting of a Si rib waveguide which is irrelevant with this study but designed by the author.

2.3.7 Microring Modulator

The microring modulator (MRM) is created by doping the waveguide portion of the MRR. The MRM used in this study follows an all-pass configuration and consists of a doped rib waveguide, as depicted in Fig. 2-20. For the doped microring, the primary source of losses in the ring becomes doping losses.

(a)   (b)
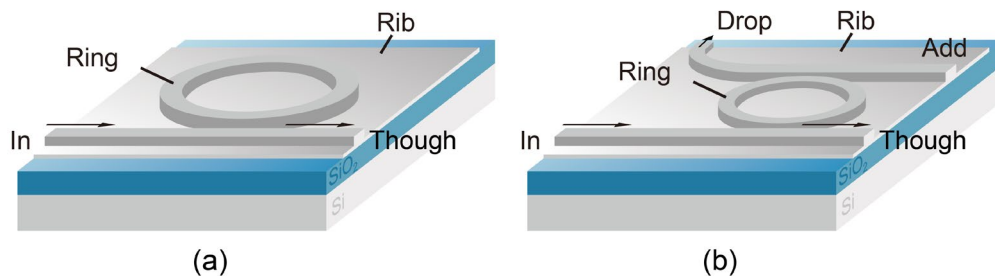
Figure 2-18 Model of microring resonator in (a) all-pass configuration and (b) add-drop configuration.
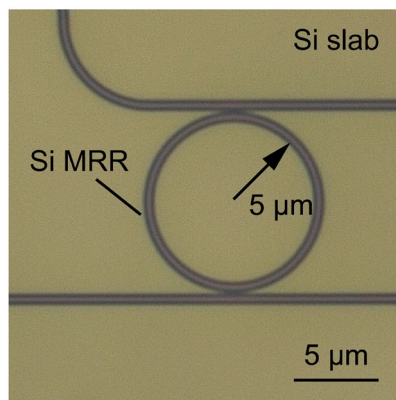
Figure 2-19 Microscopic photograph of a microring resonator consists of rib waveguide (not used in this study).

By adjusting the doping concentration or, when the doping concentration is not adjustable, by changing the distance of the high-concentration doped region from the center of the waveguide, an approximate control of the intra-ring loss can be achieved. Similarly, by adjusting the relationship between the intra-ring loss and the optical power coupling ratio of the coupling region, a critical coupling condition of the MRM can be realized. However, due to the presence of the straight waveguide, the microring cannot be fully doped, although this reduces the modulation efficiency.

Figures 2-21 (a), (b) displays an optical microscopic photograph of the MRM used in this study. The microring has a radius of 10 μm and is shaped like a racetrack with a 180 nm straight waveguide portion (per up or down side). The entire MRM was formed on a half-etched Si slab, with a small footprint of 230×300 μm², including a sizable portion of a pad window for electrical access. A TiN heater was placed on top of the microring to facilitate thermal tuning. Further detailed design considerations will be discussed in Chapter 3.

2.3.8 Electrical Heater

In this study, an electrical heater was employed for the thermal tuning of the MRM, and heating efficiency comparing with that of the optical heater. The CAD layout of the electrical heater is depicted in Fig. 2-21(c). This figure only depicts the microring Si waveguide, the TiN layer serving as the electrical heater, the Al layer as the electrical link, and the via layer between them. The sheet resistance
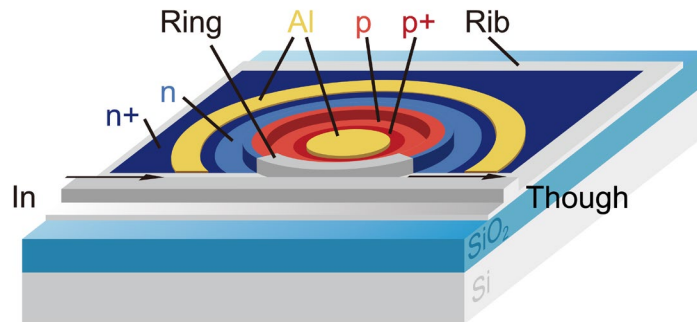
Figure 2-20 Model of MRM.
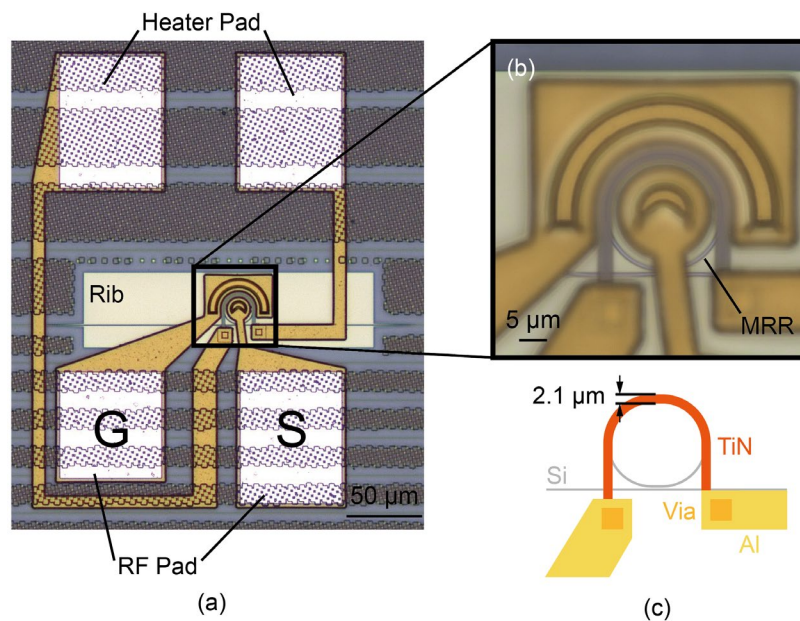
Figure 2-21 (a) Microscopic photograph of an MRM device. (b) Enlarged view of MRR. (c) Electrical heater for thermal tuning.

of the 50 nm thick TiN is 27 Ω/□, and the width of the TiN is 2.1 μm, with a total length of approximately 56 μm. Therefore, the estimated resistance of the TiN heater is 720 Ω. The distance between TiN layer and Si layer is 1.2 μm, which can be confirmed in Fig. 2-1. Detailed evaluations of its voltammetric characteristics, resistance value, and tuning efficiency will be discussed in Chapter 3.

2.3.9 Optical Heater

In addition to the electrical heater, this study introduces an innovative optical heater to enhance heating efficiency and reduce electrical wiring. The conceptual diagram of the optical heater is illustrated in Fig. 2-22. Two adjacent waveguides are connected by a Si slab, with one waveguide doped with a high concentration, while the other waveguide functions as a normal rib waveguide for signal transmission. When control light is injected into the doped waveguide, referred to as the control waveguide, the control light is absorbed, generating heat that is conducted through the slab to the neighboring signal light waveguide. Consequently, the phase of the signal light can vary with the power of the control light. Figure 2-23 presents an optical microscopic photograph of an actual fabricated optical heater loaded on one arm of the MZI. The highly doped portion is indicated by the light white-shaded area, with no visible color change in the doped region itself. A 30 μm long optical heater was utilized to achieve a sufficiently long heating length. Further details of the design can be found in Chapter 5.
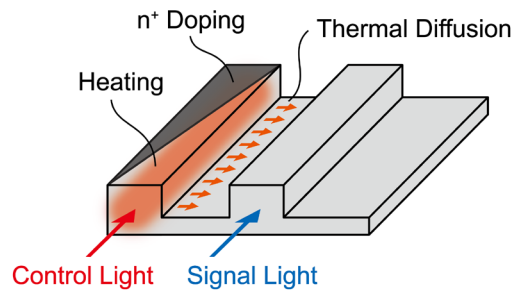
Figure 2-22 Concept of optical heater.
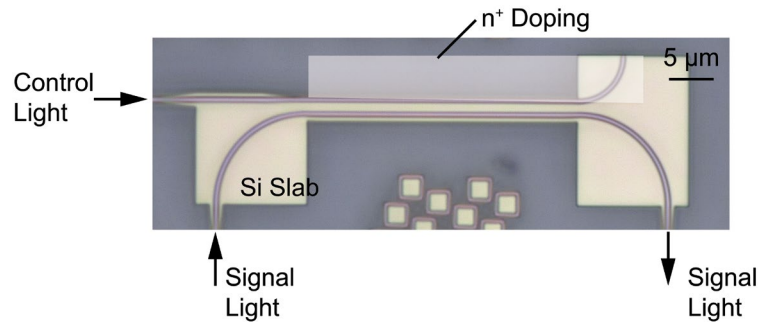
Figure 2-23 Microscopic photograph of optical heater.

Reference

[2-1] W. Zhao, R. Liu, M. Zhu, Z. Guo, J. He, H. Li, B. Pan, Z. Yu, L. Liu, Y. Shi, and D. Dai, "High-Performance Mode-Multiplexing Device with Anisotropic Lithium-Niobate-on-Insulator Waveguides," *Laser & Photonics Reviews*, vol. 17, no. 5, p. 2200774, 2023, doi: 10.1002/lpor.202200774.

[2-2] "pn junction diode," Ansys Optics. Accessed: Nov. 20, 2023. [Online]. Available: https://optics.ansys.com/hc/en-us/articles/360042273134-pn-junction-diode

[2-3] R. Soref and B. Bennett, "Electrooptical effects in silicon," *IEEE Journal of Quantum Electronics*, vol. 23, no. 1, pp. 123–129, 1987, doi: 10.1109/JQE.1987.1073206.

Chapter 3
MRM

3.1 Overview

As discussed in the previous two chapters, the microring modulator is a crucial electro-optical device in silicon photonics and forms the cornerstone of this study. This chapter provides a comprehensive overview of the microring modulator, detailing the design process, optical and electrical properties, modulation characteristics of the fabricated microring, and a brief description of the observed self-heating phenomenon.

3.2 Theory

(1) FSR, Q Factor, Finesse

The optical distance OPL (Optical Path Length) in an optical waveguide is determined by Eq. 3-1.

$$OPL = L \cdot n_{eff} \tag{3-1}$$

where L is the actual distance traveled by the light, and n_{eff} is the equivalent refractive index. For microrings, optical resonance occurs within the ring when the OPL traveled by the incident light is an integer multiple of the incident light wavelength. In other words, if the incident light wavelength satisfies Eq. 3-2, a notch appears in the spectrum. Figure 2.1 shows the resonance spectrum of a microring resonator with a radius R of 5 μm and a n_{eff} of 1 over a wide bandwidth. According to Eq. 3-2, the first resonance wavelength λ is $L \cdot n_{eff} = 2\pi R \cdot n_{eff} = \pi \times 10^{-5}$ m.

$$L \cdot n_{eff} = m \cdot \lambda, \quad m = 1,2,3,\dots \tag{3-2}$$

Taking the derivative of Eq. 3-2 with respect to λ, we obtain Eq. 3-3. When resonance occurs, we take the partial derivative because the ring circumference L is a function of both the wavelength λ and the resonance order m; we take the derivative since the n_{eff} is related only to the wavelength.

$$\frac{\partial L}{\partial \lambda} n_{eff} + \frac{dn_{eff}}{d\lambda} L = m \tag{3-3}$$

Sorting it out, we get Eq. 3-3.

$$\frac{\partial L}{\partial \lambda} = \frac{m}{n_{eff}} \left(1 - \frac{L}{m} \frac{dn_{eff}}{d\lambda} \right) \tag{3-4}$$
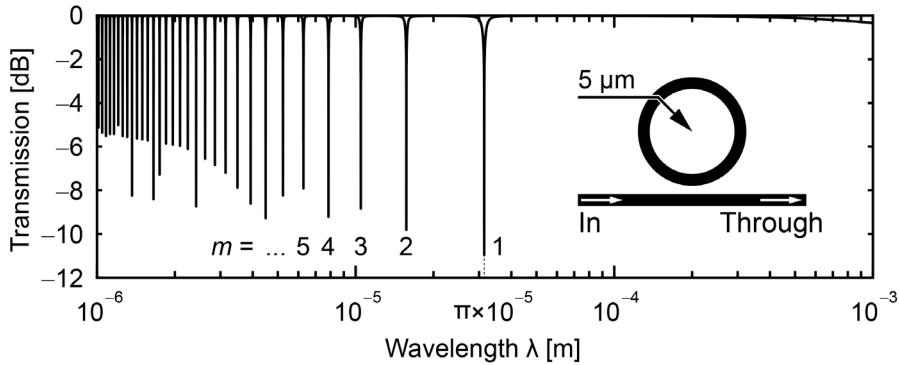
Fig. 3-1 Resonance of microring resonator. Radius of microring is 5μm, effective index n_{eff} is assumed as 1. First resonance notch appears at wavelength of $\pi \times 10^{-5}$ m.

In addition, there is a relationship between the equivalent refractive index and the group refractive index, as described in Eq. 3-5.

$$n_{\mathrm{g}} = n_{\mathrm{eff}} - \lambda \frac{\mathrm{d}n_{\mathrm{eff}}}{\mathrm{d}\lambda} \tag{3-5}$$

Then we can get

$$\frac{\partial L}{\partial \lambda} = \frac{m}{n_{\mathrm{eff}}} \left(n_{\mathrm{eff}} - \lambda \frac{\mathrm{d}n_{\mathrm{eff}}}{\mathrm{d}\lambda} \right) \frac{L}{m\lambda} = \frac{n_{\mathrm{g}}L}{\lambda n_{\mathrm{eff}}} = \frac{m \cdot n_{\mathrm{g}}}{n_{\mathrm{eff}}^2} \tag{3-6}$$

When the circumference L is fixed, the derivative of Eq. 3-2 yields Eq. 3-7.

$$L \frac{\mathrm{d}n_{\mathrm{eff}}}{\mathrm{d}\lambda} = \frac{\mathrm{d}m}{\mathrm{d}\lambda} \lambda + m \tag{3-7}$$

Since m is an integer, $\mathrm{d}m$ can be replaced by Δm. Therefore, the equation becomes:

$$L \frac{\mathrm{d}n_{\mathrm{eff}}}{\mathrm{d}\lambda} \cdot \Delta m = m\Delta\lambda + \lambda\Delta m \tag{3-8}$$

When $\Delta m = -1$, Eq. 3-8 becomes

$$\lambda = \Delta\lambda \left(n_{\mathrm{eff}} - \lambda \frac{\mathrm{d}n_{\mathrm{eff}}}{\mathrm{d}\lambda} \right) \frac{L}{\lambda} = \frac{L\Delta\lambda n_{\mathrm{g}}}{\lambda} \tag{3-9}$$

When the resonance order m is reduced by one, the change in resonance wavelength $\Delta\lambda$, also known as FSR (Free Spectral Range), is given by Eq. 3-10.

$$\Delta\lambda = \frac{\lambda^2}{Ln_{\mathrm{g}}} = \frac{\lambda n_{\mathrm{eff}}}{mn_{\mathrm{g}}} = FSR \tag{3-10}$$

As shown in Fig. 3-1, the FSR between two adjacent resonant notches gradually decreases as m increases. It can also be seen that the FSR increases as the wavelength λ increases.

Another important indicator of microrings is the Q-value, which is defined by Eq. 3-11.

$$Q = \frac{\lambda}{\Delta\lambda_{\mathrm{FWHM}}} \tag{3-11}$$

where $\Delta\lambda_{\mathrm{FWHM}}$ is the Full Width at Half Maximum of the resonance notch.

(2) Optical Circuit Analysis

Abstracting from the microring model shown in Fig. 3-2(a), we obtain the equivalent optical circuit shown in (b). Here, a is the single-pass amplitude transmission, t is the self-coupling coefficient, k is the cross-coupling coefficient, t^* and k^* are conjugates of t and k. The k related with the power coupling ratio κ as $\kappa = k^2$. The coupling part can be approximated by a two-terminal pair circuit, and the ring part can be approximated by a phase shifter and an attenuator. α is the power attenuation coefficient in the ring, and β is the phase constant. The propagation constants are given by $\gamma = \alpha + \mathrm{j}\beta$. The diagram represents the relationship in Eq. 3-12.
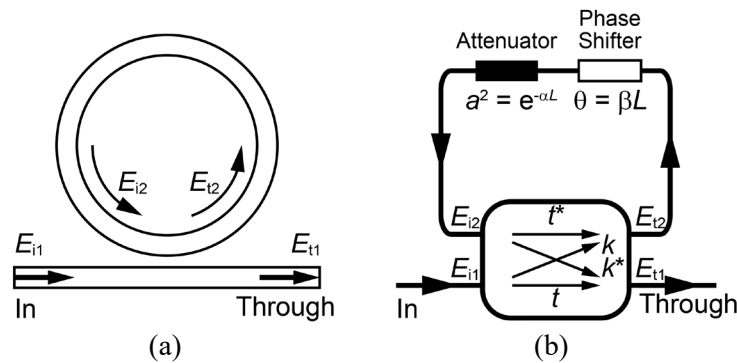
Fig. 3-2 (a)Simplified model of microring and (b)equivalent circuit. a: single-pass amplitude transmission, t: self-coupling coefficient, k: cross-coupling coefficient, α: power attenuation coefficient.

$$E_{t2} = t^* E_{i2} + k E_{i1}$$
$$E_{t1} = t E_{i1} - k^* E_{i2}$$
(3-12)

Written in matrix form, it becomes Eq. 3-13.

$$\begin{bmatrix} E_{t1} \\ E_{t2} \end{bmatrix} = \begin{bmatrix} t & k \\ -k^* & t^* \end{bmatrix} \begin{bmatrix} E_{i1} \\ E_{i2} \end{bmatrix}$$
(3-13)

The electric field within the ring is Eq. 3-14:

$$E_{i2} = a e^{j\theta} E_{t2}, \quad a^2 = e^{-\alpha L}$$
(3-14)

By Eqs. 3-13 and 3-14, the electric field relationships at the In and Through ports are given by the equations below.

$$\frac{E_{t1}}{E_{i1}} = \frac{r - a|t|^2 e^{j\theta} - a|k|^2 e^{j\theta}}{1 - a t^* e^{j\theta}}$$
(3-15)

While the coupler is lossless, $|k|^2 + |t|^2 = 1$. Then we get

$$\frac{E_{t1}}{E_{i1}} = \frac{t - a e^{j\theta}}{1 - a t^* e^{j\theta}}$$
(3-16)

Squaring Eq. 3-16 yields the ratio of the power of the output light to that of the input light, which is the transmission function T (Eq. 3-17).

$$T = \frac{P_{t1}}{P_{t2}} = \frac{|E_{t1}|}{|E_{i1}|} = \frac{|t|^2 + |a|^2 - 2|t||a|\cos(\varphi_t + \theta)}{1 + |t|^2 |a|^2 - 2|t||a|\cos(\varphi_t + \theta)}$$
(3-17)

Here, $t = |t| e^{j\varphi_t}$. φ_r is the phase change due to coupling. Considering symmetry, critical coupling occurs when $t = a$. Considering the periodicity of the equation, resonance occurs when $\varphi_t + \theta$ is an integer multiple of 2π. The phase shift of the incident light is determined in Eq. 3-18. When $\delta = 2\pi m$, Eq. 3-19 is obtained. It is the same as Eq. 3-2 in the previous section. In that case, when resonance occurs, Eq. 3-17 becomes Eq. 3-20, and the deepest resonant notch is obtained (theoretically infinite depth). $t > a$ is called undercoupling, and $t < a$ is called overcoupling.

$$\delta = \varphi_r + \theta = \frac{2\pi n_{\text{eff}} L}{\lambda}$$
(3-18)

$$\lambda = \frac{n_{\text{eff}} L}{m}$$
(3-19)

$$T = \frac{|t|^2 + |t|^2 - 2|t||t|}{1 + |t|^2 |t|^2 - 2|t||t|} = \frac{2|t|^2 - 2|t|^2}{\left(|t|^2 - 1\right)^2} = 0$$
(3-20)

By Eq. 3-16, the phase change Φ of the propagated light is given by Eq. 3-21. Near the resonant wavelength, the phase change Φ changes rapidly[3-1].

$$\Phi = \arg\left(\frac{E_{t1}}{E_{i1}}\right) = \pi + \theta + \arctan\left(\frac{t\sin\theta}{a - t\cos\theta}\right) + \arctan\left(\frac{ta\sin\theta}{1 - ta\cos\theta}\right)$$
(3-21)

Using Eqs. 3-17 and 3-21, the transmission and phase change of the three couplings, Undercoupling, Critical coupling, and Overcoupling, are shown in Fig. 3-3(a) and (b). In (b), it can be seen that an abrupt phase change of π occurred near the resonance wavelength at critical coupling. The phase and amplitude changes are summarized in a polar coordinate system as shown in Fig. 3-4. In the case of Undercoupling, the amplitude change is small, and the curve is limited to the right side of the figure. The amplitude variation also appears to be small. In the case of critical coupling, on the other hand, the amplitude is almost zero at the resonance wavelength, and the curve passes through the center of the figure. In the case of Overcoupling, the amplitude change is small, but a continuous phase change of $0 \sim 2\pi$ is obtained.
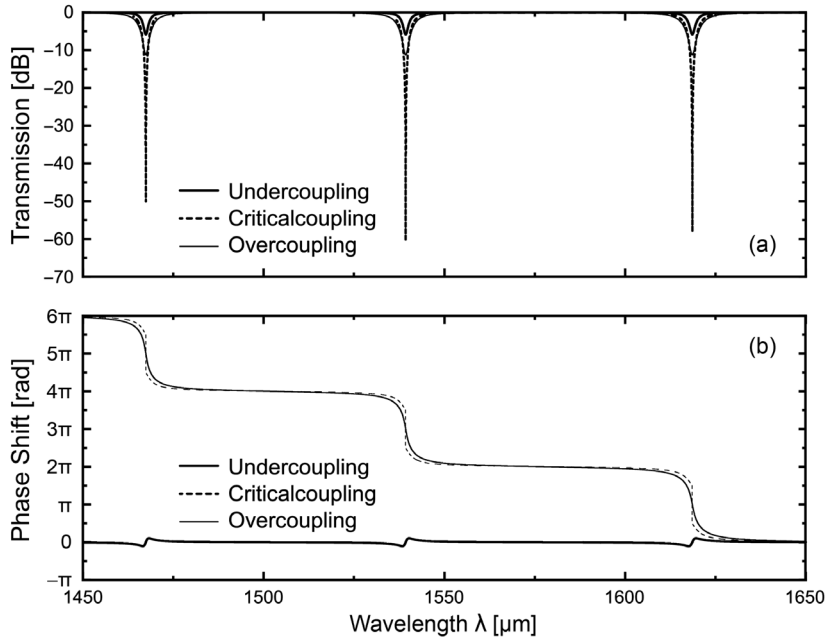
Fig. 3-3 (a) Transmission and (b) phase shift of microring resonator under different coupling situation.
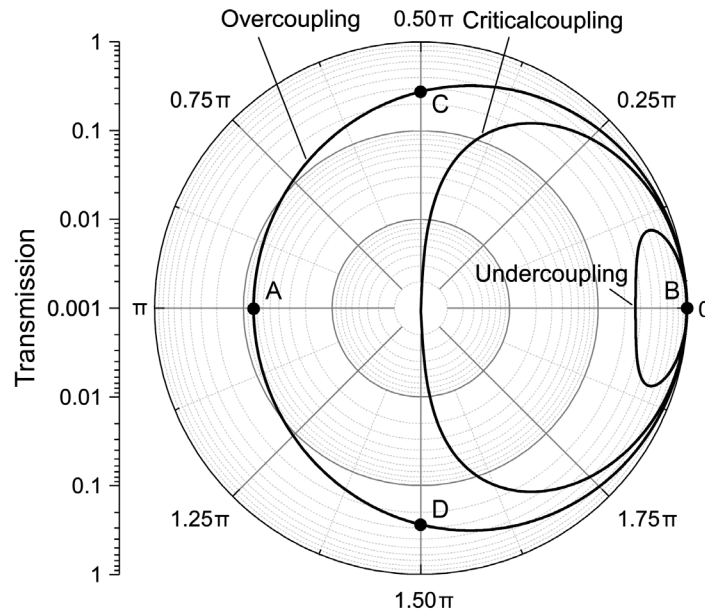
Fig. 3-4 Polar plot for transmission and phase shift of microring resonator under different coupling situation. Curve of critical coupling with an abrupt phase change past the center, which means the transmission of light at resonance wavelength is almost zero.

3.3 Design

3.3.1 FDTD Calculation

(1) Single Mode Condition

Because the slab has the same thickness as the rib waveguide (0.11 µm) in AIST, light is tend to be diverted from the core. Using FDE solver of Lumerical, we calculated the single-mode conditions for the channel waveguide and rib waveguide. The single-mode conditions for the channel waveguide and rib waveguide are already shown in Fig. 2-8(a) and (b), respectively. The single-mode conditions are $w < 0.45$ µm and $w < 0.5$ µm, respectively. Therefore, the waveguide widths were set to 0.45 µm and 0.5

µm, respectively.

(2) Bending Radius Determination

Fig. 2-11 shows the relationship between bending loss and waveguide width for a rib waveguide. The bending radius is 5 µm, but the bending loss corresponding to w satisfying the single mode condition is more than 3 dB/Round, making it unusable for microrings. At $R = 10$ µm, a low bending loss of 0.029 dB/Round is obtained.

(3) Design of MRM

To maximize the modulation efficiency, it's crucial to maintain the microring modulator in a critical coupling state after doping. For the rib waveguide, with a fabrication resolution (minimum rib waveguide spacing) of 250 nm, we set the gap at the coupling to 260 nm to minimize fabrication bias. We simulated the directional coupler shown in Fig. 2-12(a) using Lumerical's FDTD solver. The relationship between the obtained coupling coefficient κ and the coupling length L is shown in Fig. 2-13. In this study, the three data points shown in the figure were used to fabricate the microring modulator, but the design with $L = 0.18$ µm of them was finally selected for practical packaging.

On the other hand, to achieve critical coupling, we need to control the lost power by doping inside the microring to the same level as the coupled optical power. In general, this can be achieved by varying the doping concentration in the waveguide, but for foundries with fixed concentrations or those that offer only a few doping concentration levels, an alternative solution is needed. Here, we achieve different levels of absorption of the evanescent field of the optical modes in the waveguide by high concentration dopants by adjusting the distance W_{pn} between the high concentration doping region and the center of the waveguide.

Using the Lumerical CHARGE solver, we calculated the waveguide propagation loss for different W_{pn}. Note that the bending loss of the rib waveguide is almost negligible compared to the doping loss. The simulation model is shown in Fig. 2-15(a). The simulation results are shown in Fig. 3-5(a). It can be found that when W_{pn} is equal to 0, i.e., when the waveguide is completely doped with high concentration dopants, the doping loss reaches 5000 dB/cm; and when the highly doped region is removed from the waveguide, the doping loss gradually decreases until it no longer changes completely. The converged doping loss is the loss caused by the low concentration doping, which is about 10 dB/cm.

Additionally, we calculated the effective index n_{eff} and group index n_g of the optical modes in the waveguide under different W_{pn} conditions using the Lumerical FDE solver. The simulation model is shown in Fig. 2-15(b). The simulation results are shown in Fig. 3-5(b). Using these results, we can calculate the intra-ring losses and the energy coupling ratio of the coupled part of the microring that can realize the critical coupling condition for different target Q values.

We simulated the Q-κ relationship for different W_{pn} using the Lumerical INTERCONNECT solver, and the computational results obtained are shown in Fig. 3-6. Each colored line in the figure corresponds to a W_{pn}, and an in-ring loss value. When changing the coupling ratio κ between the microring and the bus waveguide, the Q value of the microring will become smaller and then larger. The microring realizes critical coupling when κ and each intra-ring loss α satisfy Eq. 3-22. Connecting each critical coupling point, we obtain all the points on the entire Q-κ plane that fulfill the critical coupling condition. In this study, we set the target Q values to 1000, 2000 and 5000, and their corresponding κ and W_{pn} values are shown in Table 3-1. However, for the actual fabrication, we expanded the W_{pn} corresponding to each Q value into four values: 300 nm, 350 nm, 450 nm, and 650 nm to prevent the effects of fabrication errors.

$$\kappa = k^2 = 1 - r^2 = 1 - a^2 = 1 - \exp(-\alpha L) \tag{3-22}$$

Table. 3-1. Parameters for designed MRM.

Q	κ	L [μm]	G [nm]	W_{pn} [nm]	Actual W_{pn} [nm]	Device No.
1000	0.45	5.00	260	304	300	1
					350	2
					450	3
					650	4
2000	0.24	2.42	260	390	300	5
					350	6
					450	7
					650	8
5000	0.1	0.18	260	500	300	9
					350	10
					450	11
					650	12
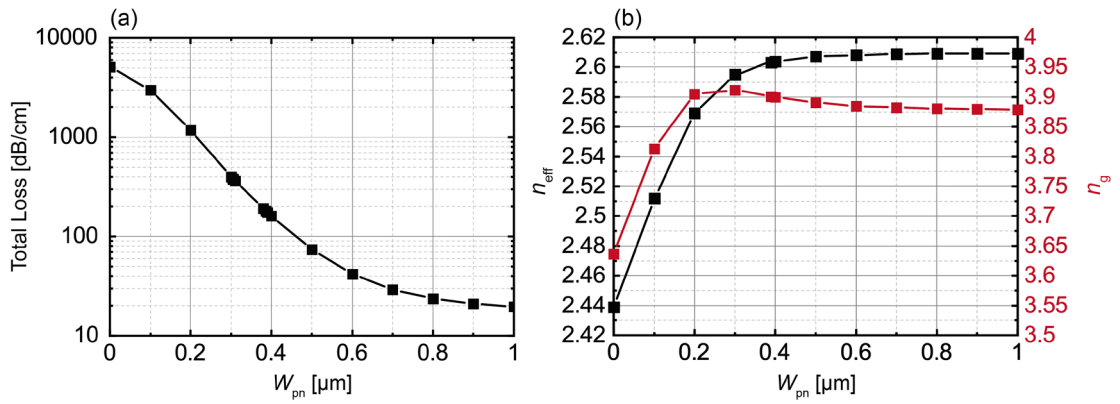
Fig. 3-5. (a)Function of total loss in microring and doping region width W_{pn}. (b)Relationship between effective index n_{eff}, group index n_g with W_{pn}.
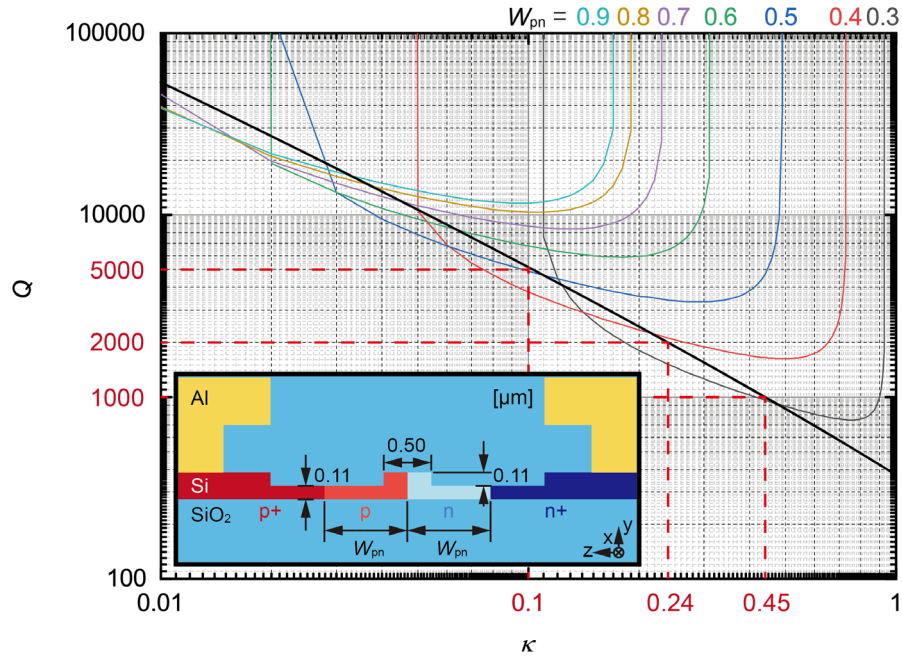
Fig. 3-6. Relation between Q and κ with critical coupling condition.

60

3.3.2 Mask Pattern

Figure 3-7 displays the CAD layout and Fig. 3-8 shows several key dimensions of a single microring modulator. Each color in these figures represent a layer, including the Ridge Layer (partially etched silicon layer), Si Layer, dopant layers (p, n, p+, n+ Layer), Contact Holes for the pn junction and TiN heater, TiN Heater, Al Wire Layer, and Probing/Bonding Pad (with the oxide on top of the metal removed). These layers are configured according to the manufacturing requirements of the foundry.

The chip measures 5 mm in width and 15 mm in height, accommodating both individual micro ring modulators for testing (12 designs) and arrays of micro ring modulators, each with 8 channels. The 8 microring modulators within each array share identical designs. To optimize space, we created arrays of 12 designs and mirrored half of them by 180 degrees. Consequently, testing the performance of the micro ring modulator array with the input port on the right side of the chip requires rotating the entire chip by 180 degrees.

Furthermore, we produced three copies of these 12 microring modulator arrays, employing 160 nm and 100 nm Si SSCs, as well as SiN SSCs for optical input and output. Experimental results indicated that the coupling efficiency of the 100 nm SSC was lower than that of the 160 nm SSC. While the SiN SSC theoretically offers high coupling efficiency and a maximum input power limit, we ultimately opted for the 160 nm Si SSC due to a mismatch between the mode field diameter of the lensed fiber used in the experiments and the SiN SSC device.

As shown in Fig. 3-8, in this design, the interface of the doped region near the straight waveguide side is set at an angle of 60° to the plumb line from the center of the ring to the straight waveguide. This angle is chosen to prevent the coupled portion from being doped with a high concentration. Additionally, the overlap width of the n and n+ regions, as well as the p and p+ regions, is set to 1 μm to avoid regions being undoped due to doping misalignment. The size of the bonding pad is configured as 72×92 μm². This sizing accommodates both probe contact and wire bonding requirements. The upper pair of bonding pads is connected to the TiN heater for inputting the heating voltage, while the lower pair is connected to the p-region and n-region of the microring for inputting the RF signals.

In Fig. 3-9, we delve into the intricacies of the microring modulator array design. While the ultimate goal is to use this array for packaging, initial optical measurements are necessary to identify the optimal array for packaging. To achieve this, we extract a small portion of power from the bus waveguide through a directional coupler, directing it to the monitor port at the right end. During actual packaging, the monitor waveguide is truncated, and input and output fibers are accessed on the same side. Additionally, we incorporate a high concentration of n doping at the add port of the directional coupler to absorb scattered light. Figure 3-9 provides further insights into these design details.

Test Pattern
(With 160 nm SSC)

MRM Array
(With 160 nm SSC)

MRM Array
(With 100 nm SSC)

MRM Array
(With SSC Using SiN)

15 mm

5 mm

	Si		Si p+ implant		Contact hole (TiN)
	Si n implant		Contact hole (pn)		Ridge
	Si p implant		Al		Pad Window
	Si n+ implant		SSC		TiN
	SiN				
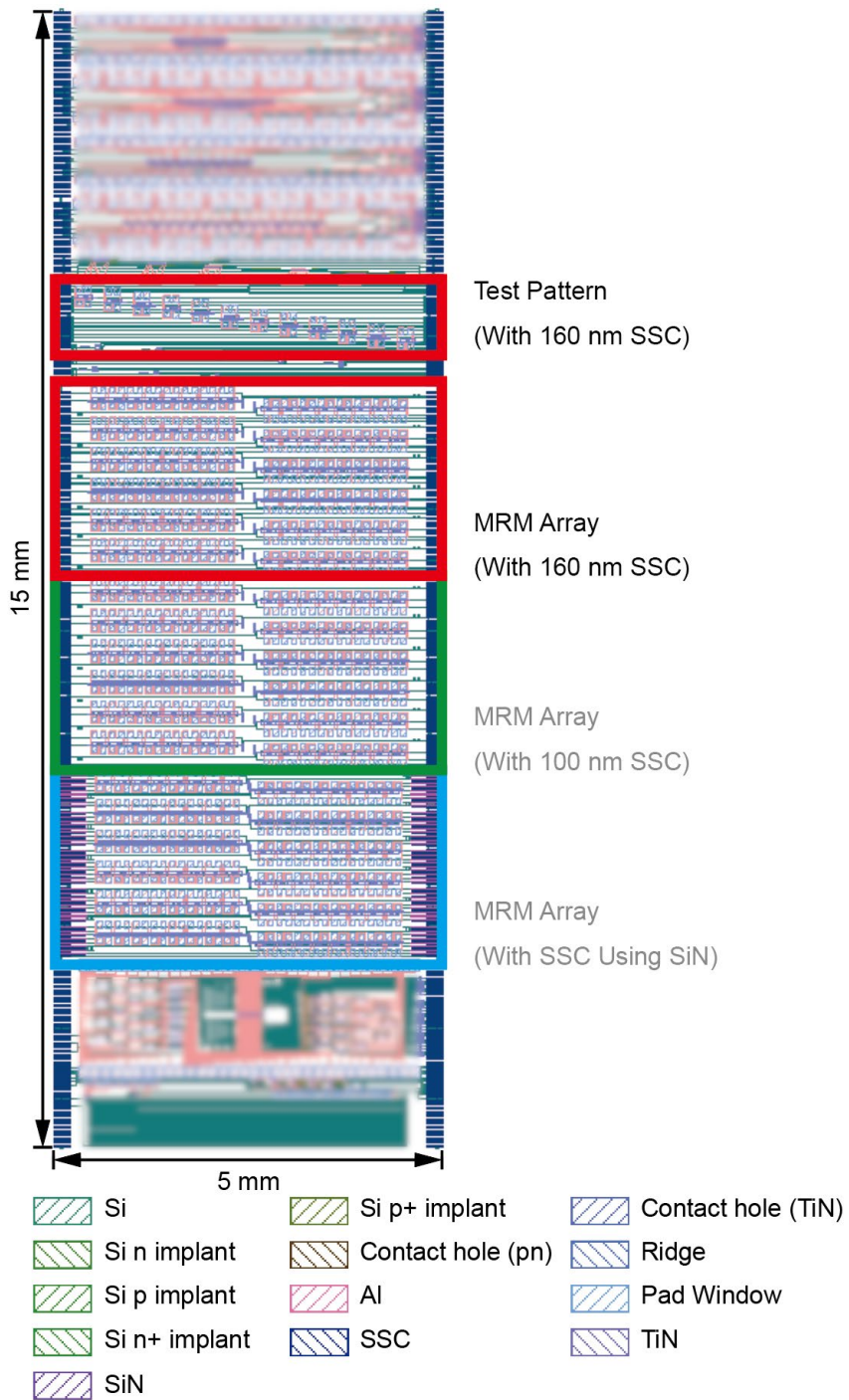
Fig. 3-7 CAD layout of the entire chip.
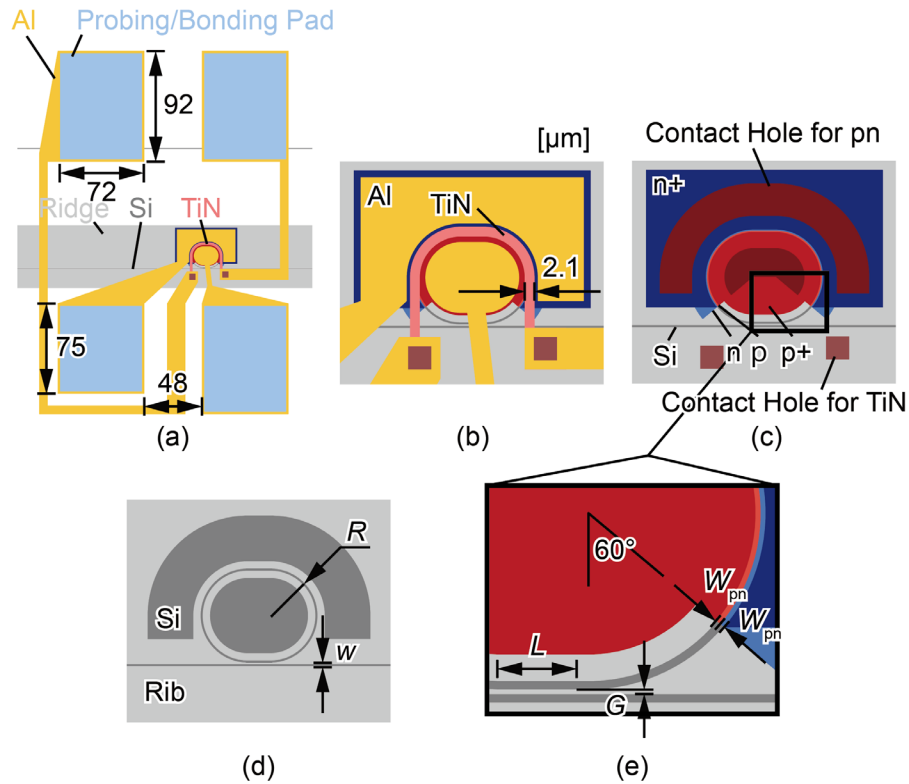
Figure 3-8 (a) CAD layout of a single microring modulator. (b) Enlarged view of the area around the microring modulator. (c) (b) without the Al and TiN layers. (d) Si layer and rib layer. (e) Enlarged view of the black frame in (c).
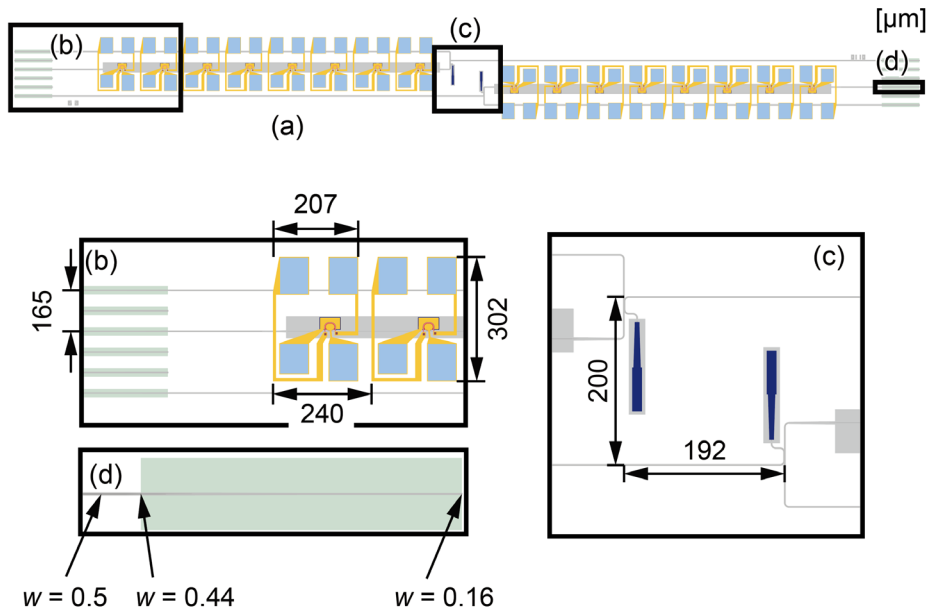
Figure 3-9 (a) CAD view of the microring modulator array. (b) Enlarged view of the left side of the array. (c) Spacing in the center of the array. (d) Enlarged view of the SSC (vertical direction is enlarged).

3.4 Fabricated Device

Figure 3-10 provides an encompassing perspective of the AIST device, accompanied by detailed microscopic views of microring modulator. In Fig. 3-10(a), the sections outlined from top to bottom

represent the 12 test patterns of MRM, MRM arrays employing standard SSCs (tip width 160 nm), MRM arrays using fine SSCs (tip width 100 nm), and MRM arrays using SiN SSCs. It also contains all-optical control device, and the microring modulator array with different SSC. In Fig. 3-10(b), the top two white regions represent the DC pads for connecting to the electrical heater, and the bottom two white regions are the RF pads for connecting to the microring modulator.

3.5 Fundamental Characteristics

3.5.1 Optical Transmission

Figure 3-11 illustrates the optical transmission intensity measurement system. Continuous-wave (CW) light emitted from a wavelength-tunable laser enters the device through a polarization-maintaining fiber equipped with a lens. The light emanating from the device is directed to the power meter via a lensed fiber and a polarization-maintaining fiber. To measure the optical transmission spectrum, the LabView program on the PC is used to record the power of the received light while sweeping the wavelength of the tunable laser.
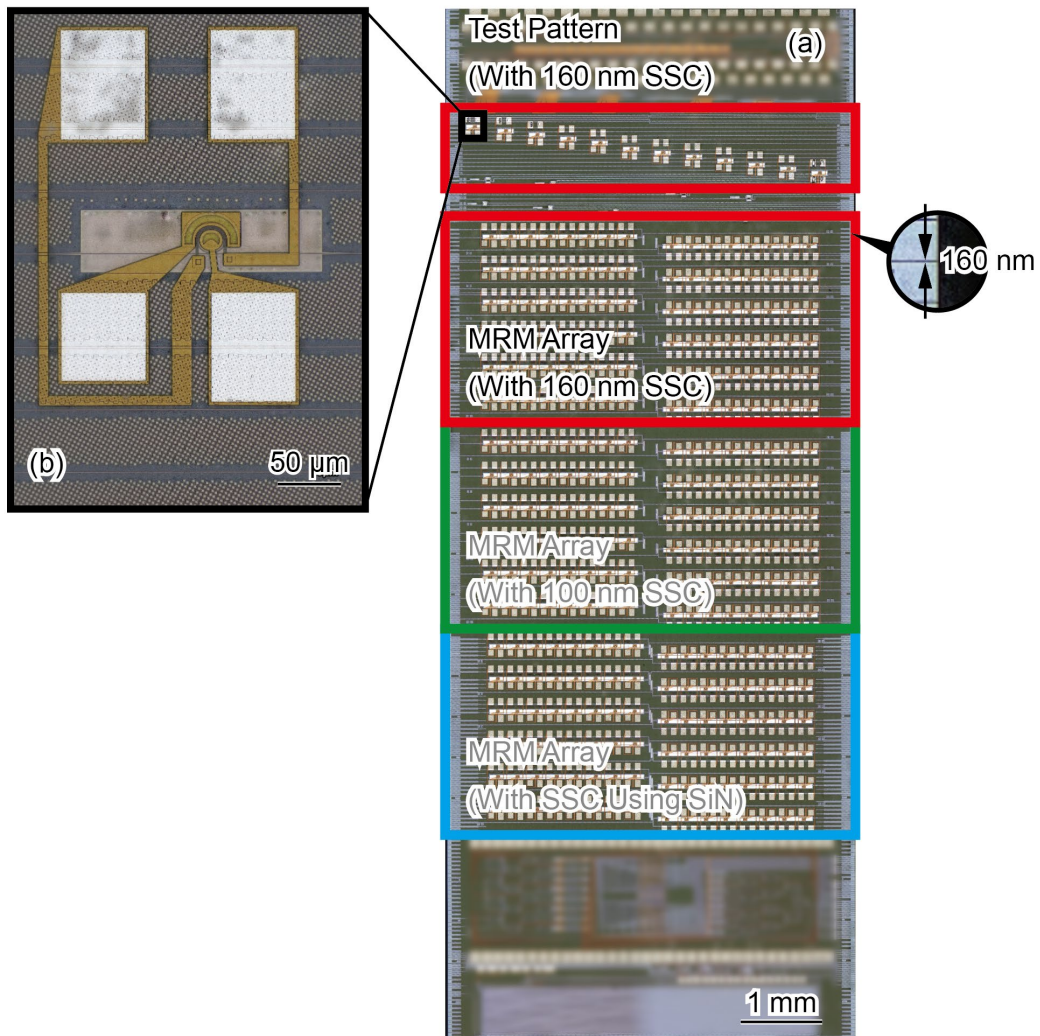
Fig. 3-10 (a) Photo of Si photonics chip fabricated by AIST. (b) Enlarged view of MRM.
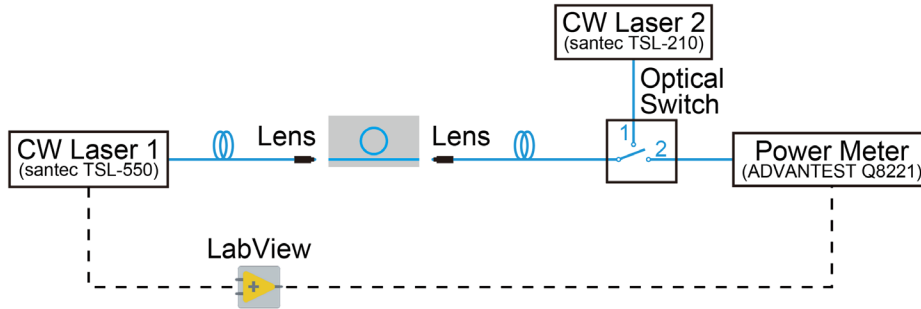
Fig. 3-11 Measurement setup for optical transmission.
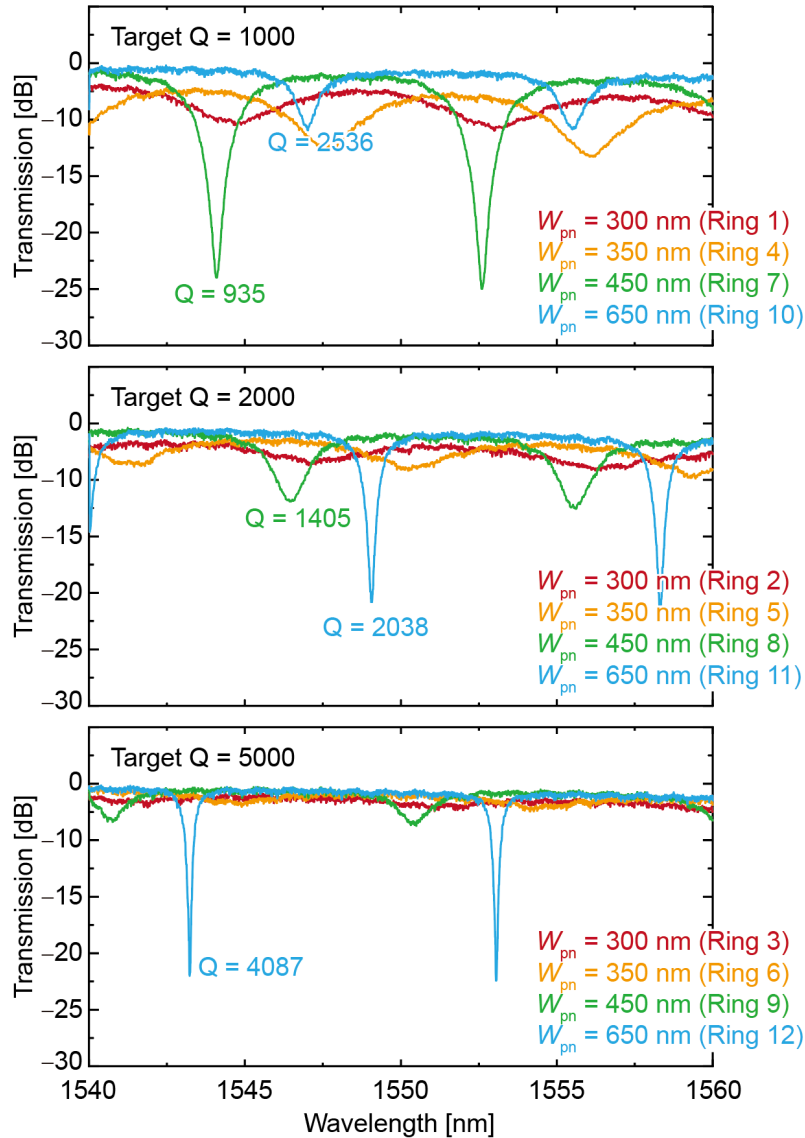
Fig. 3-12 Optical transmittance of all MRMs in test pattern.

In Fig. 3-12, the optical transmission spectra of the standalone AIST microring modulator are presented. The spectra corresponding to target Q-values of 1000, 2000, and 5000 are depicted in (a), (b), and (c) respectively. Each target Q-value encompasses four variations of W_{pn}, resulting in a total of 12 distinct microring modulators. The results reveal a consistent FSR of 10 nm, with the measured Q values closely aligning with the designed values. Notably, a resonance strength drop of approximately 20 dB is observed when the distance W_{pn} from the center of the waveguide to the highly doped region reaches its maximum.

65

3.5.2 Parameter Extraction

Subsequently, we extracted and compared the internal loss and coupling coefficient of the MRMs using established methodologies [3-1, 2]. The transmission spectra for the designed MRMs, labeled as R1 to R12, are presented in Fig. 3-13, with the measured wavelength range spanning 1500 nm to 1630 nm. Notably, the transmission spectra indicate that the deepest resonances were achieved for R7, R11, and R12, prompting a detailed extraction of the MRM parameters.

First, the MRM transmission spectrum T (normalized by the maximum power) is determined by Eq. 3-23 (Simplified from Eq. 3-17).

$$T \equiv \frac{t^2 + a^2 - 2at\cos\phi}{1 + a^2t^2 - 2at\cos\phi} \tag{3-23}$$

where t is the self-coupling coefficient, a is the single-pass amplitude transmission, and ϕ is the single-pass phase shift. If k is defined as amplitude coupling coefficient, the relation $t^2 + k^2 = 1$ is valid under the assumption that the coupling part is lossless. *Finesse* and *ER* are defined as follows.

$$Finesse \equiv \frac{FSR}{FWHM} \tag{3-24}$$

$$ER \equiv \frac{T_{max}}{T_{min}} \tag{3-25}$$

Then

$$ER = \left(\frac{(t+a)(1-at)}{(t-a)(1+at)}\right)^2 \tag{3-26}$$

$$\cos(\pi / Finesse) = \frac{2at}{1 + a^2t^2} \tag{3-27}$$

Among these, ER and Finesse are directly measurable, allowing the calculation of the product of at. However, extracting individual values for a and t is not possible. To address this, we define the intermediate variables A and B:

$$A \equiv \frac{\cos(\pi / Finesse)}{1 + \sin(\pi / Finesse)} \tag{3-28}$$

$$B \equiv 1 - \left(\frac{1 - \cos(\pi / Finesse)}{1 + \cos(\pi / Finesse)}\right)\frac{1}{ER} \tag{3-29}$$

Then

$$(a,t) = \left(\frac{A}{B}\right)^{\frac{1}{2}} \pm \left(\frac{A}{B} - A\right)^{\frac{1}{2}} \tag{3-30}$$

The values a and t correspond to the two solutions of Eq. 3-30, respectively. However, it is not yet determined which solution corresponds to a and which one to t. In [3-2], the distinction between a and t was made based on the property that the wavelength dependence of the coupling coefficient k in the coupling part of the MRM is stronger than that of a. In this study, we adopted a different method since the wavelength dependence of the coupling part hardly changes within the range of 1500 nm to 1630 nm. Given that 12 MRMs were designed with different a and k it becomes possible to distinguish a and

t by matching them with their respective design values.

Subsequently, *a* and *t* were computed using the aforementioned equations with the actual transmission spectra of the 12 MRMs. In Fig. 3-14, the red and black lines represent *a* and *t* while the green and blue lines depict the round-trip internal power loss ratio α and power coupling ratio κ. The relationships are given by $a^2 = 1 - \alpha$ and $\kappa = k^2 = 1 - t^2$. For specific targets of κ, R1, R4, R7, and R10 aimed for $\kappa = 0.45$, R2, R5, R8, and R11 targeted $\kappa = 0.24$, and R3, R6, R9, and R12 corresponded to $\kappa = 0.10$ (indicated by the blue dashed lines). Each set of targets was designed for a wavelength of 1550 nm. The values for *a* and *t* or α and κ could be easily distinguished if they aligned with the design values. However, R7, R11, and R12, which exhibit the deepest resonance, are close to the critical coupling condition, resulting in a small difference between the values of *a* and *t* making them challenging to distinguish. Additionally, the resonances of R2, R3, and R6 are very weak, leading to large fluctuate for the wavelengths of *a* and *t* calculated using the extracted FWHM values. Comparing the α and κ values of the other MRMs with the design values revealed that the coupling coefficient κ was approximately consistent with the design value, while the α value was slightly smaller than the design value. In other words, setting W_{pn} slightly smaller than the target value results in a more desirable intra-ring loss. Finally, the loaded Q was calculated using λ_{res}/FWHM, confirming an increase in Q value due to the decrease in intra-ring loss (Fig. 3-15).
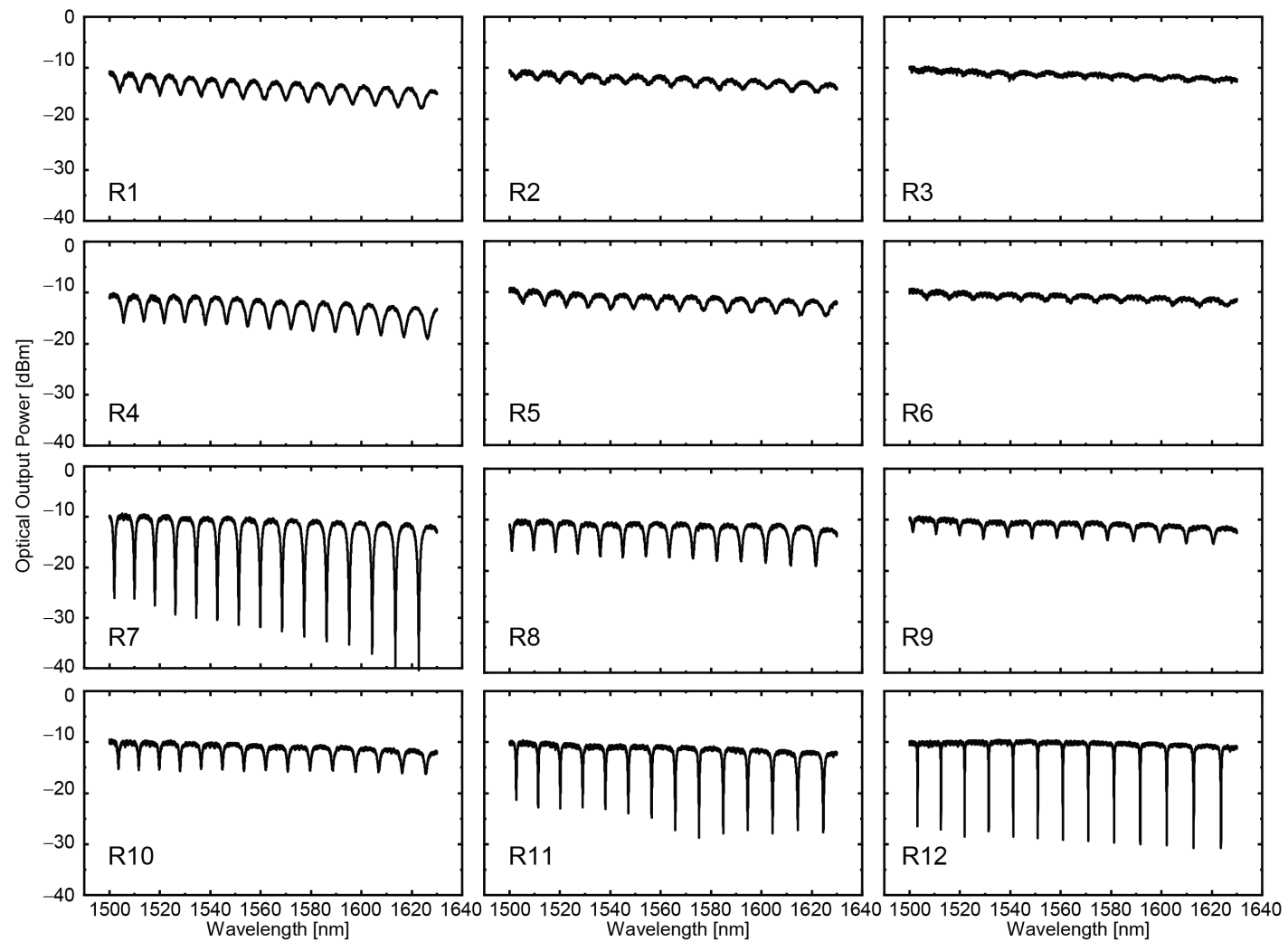
Fig. 3-13. Optical transmission spectrum of MRM R1~R12 in wide wavelength range.
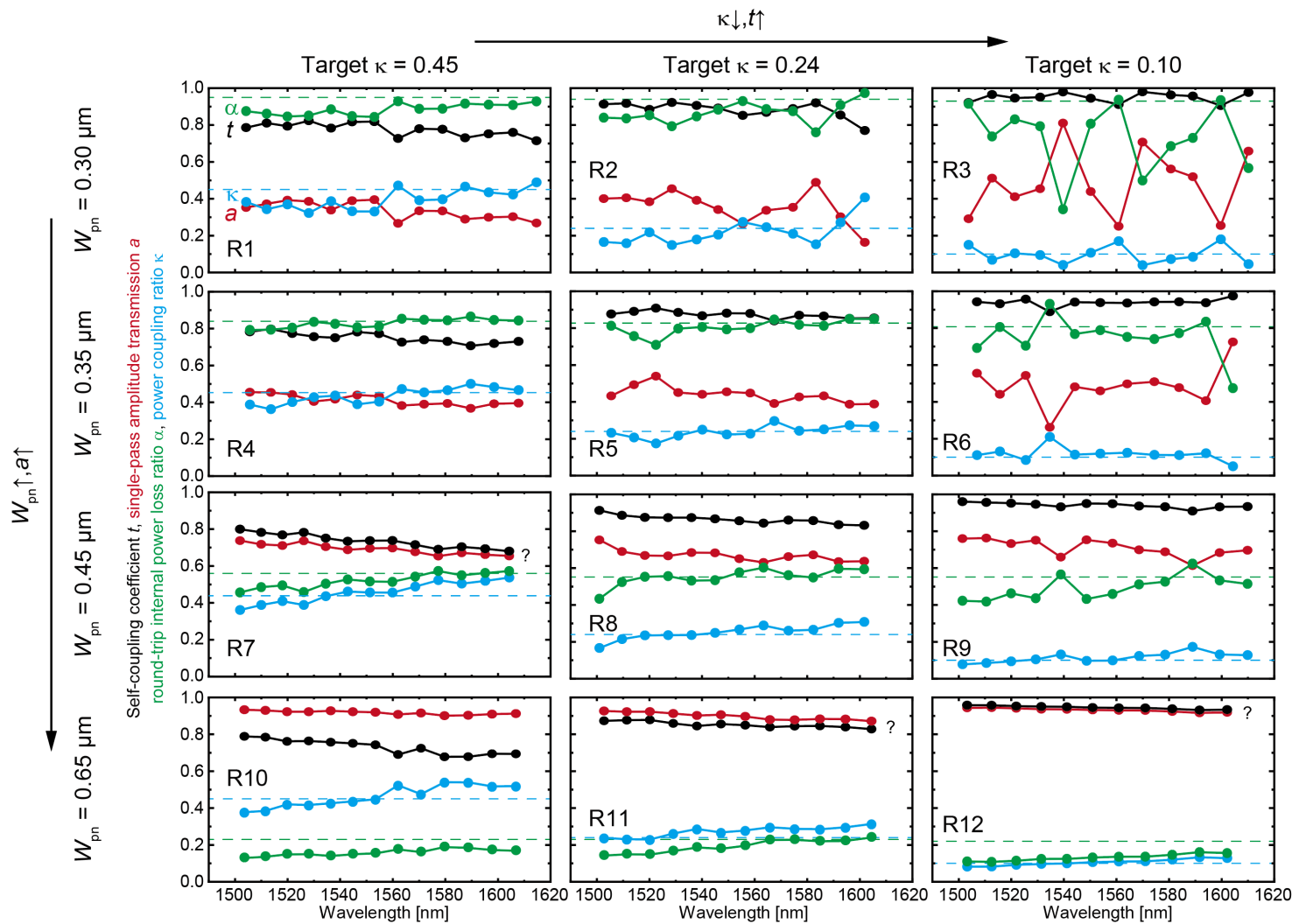
Fig. 3-14. Extracted self-coupling coefficient *t*, single-pass amplitude transmission *a*, round-trip internal power loss ratio α and power coupling ratio κ of all MRMs.
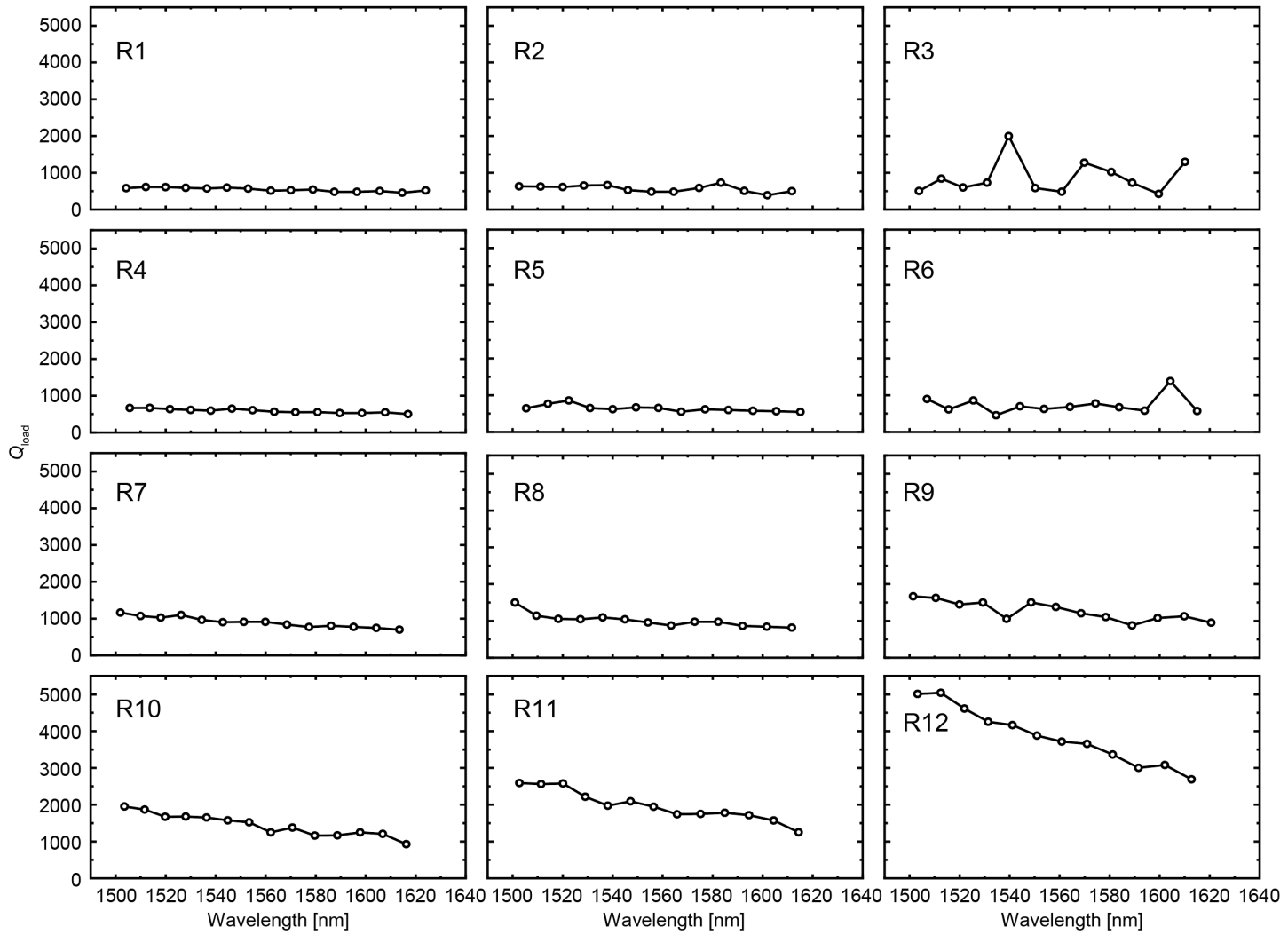
Fig. 3-15. Measured loaded Q factor of all MRMs at C band.

3.6 Thermo-Optic Switching

3.6.1 Measurement Setup

A TiN heater was integrated to shift the resonance wavelength of the microring modulator. To investigate the thermal tuning characteristics of the heater, we used the experimental setup for measuring the heating characteristics shown in Fig. 3-16. The thermal tuning characteristics of the heater are obtained by measuring the optical transmission spectrum of the device while varying the DC voltage applied to the heater.

3.6.2 Electrical Characteristics and Thermal-tuning Result

The I-V characteristics, resonance wavelength shift due to thermal tuning, and thermal tuning efficiency of the designed TiN heater are shown in Fig. 3-17, where the heater resistance stabilizes around 900 Ω when the DC voltage applied to the TiN heater is within 2~6 V. Panel (a) shows the same resonance notch shifting corresponding to different heating voltages. Displayed in panel (b) is the shift of the identical resonance notch corresponding to different heating voltages, where a wavelength shift of 11 nm was observed for a heating voltage of 8 V. Since the FSR of the ring is 10 nm, thermal tuning is obtained over one FSR range. In other words, the resonance wavelength can be shifted to any wavelength with the TiN heater. Figure 3-17(c) shows the calculated thermal tuning efficiency using (a) and (b), which is 0.17 nm/mW.

3.7 Modulation Characteristics

3.7.1 Equivalent Circuit Analyze and Parameter Extraction

First, the S11 parameter was measured to determine the electrical characteristics of the MRM. The measurement system is shown in Fig. 3-18. The vector network analyzer (VNA) used in this laboratory can be calibrated normally using a calibration kit, but when measuring elements on a chip, it is necessary to use a calibration substrate as shown in Fig. 3-19 (a). During chip measurements, it is crucial to set the Offset Length of the VNA to 0, as shown in Fig. 3-19 (b) (in normal calibration, a calibration element with an electrical path length is used, but here the electrical path is ignored because the distance from the probe tip to the device is short). With these settings, we obtained the S11 measurement results shown in Fig. 3-20. The original file contained magnitude and phase information, which was then converted into real and imaginary parts for fitting. The specific parameter settings are shown in Table 3-2, and due to the small differences between the parameters, the S11 measurement results were almost identical.

A circuit analysis was conducted using the MRM equivalent circuit shown in Fig. 3-21. In (a), a cross-sectional view of the MRM is presented, along with the corresponding electrical elements for each part. This model represents the most commonly used MRM equivalent circuit. It includes the parasitic capacitance C_p between the electrical pads, the parasitic capacitance C_{Si} between the Si slab and the Si substrate, the resistance R_{Si} of the Si slab, the junction capacitance C_j of the pn junction, and its series resistance R_s. A simplified model is shown in (b). When forward bias is applied, the pn junction conducts, transforming the equivalent circuit into (c). The resistance of the circuit can be approximated by the series resistance R_s of the pn junction. As illustrated in Fig. 3-22, R_s could be directly measured by I-V measurement with forward bias. When forward biased, the pn junction broke down at around 3 V due to the ease of current flow. The minimum resistance at that time was taken as R_s.
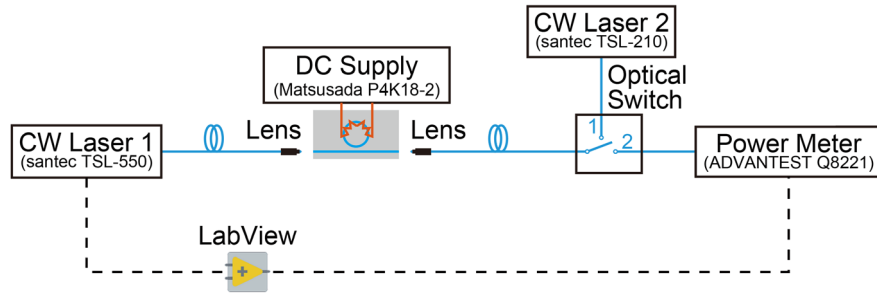
Figure 3-16 Measurement setup for thermal tuning characteristics.

(a)

(b)

(c)
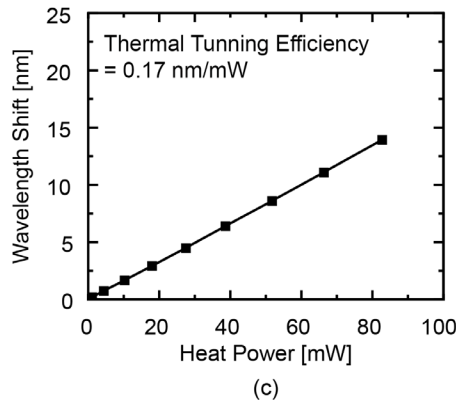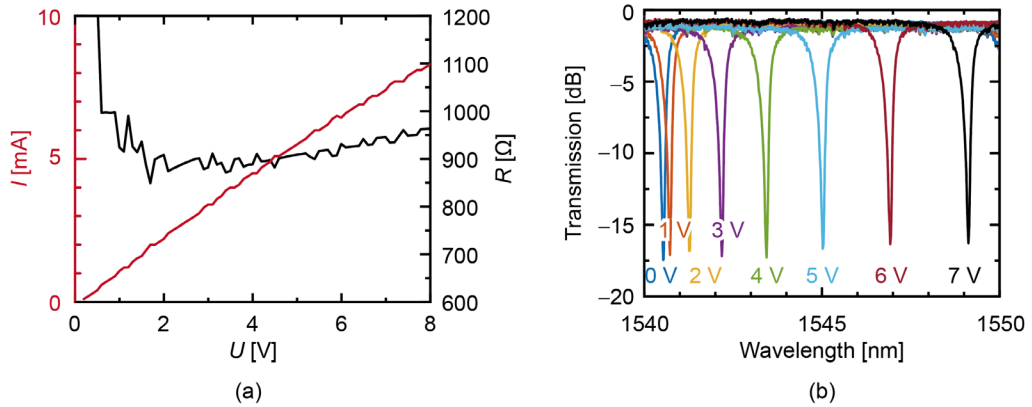
Figure 3-17 (a) I-V characteristics of the heater designed by AIST. (b) Resonance wavelength shift due to thermal tuning. (c) Thermal tuning efficiency.
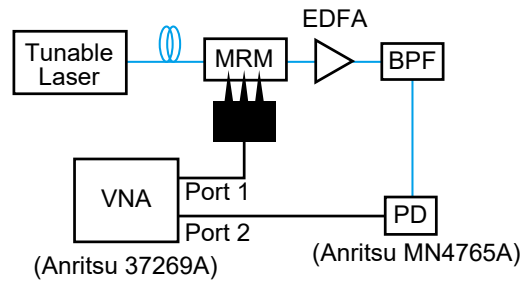
Fig. 3-18. Setup for S21 measurement.

Calibration Substrate

(a)
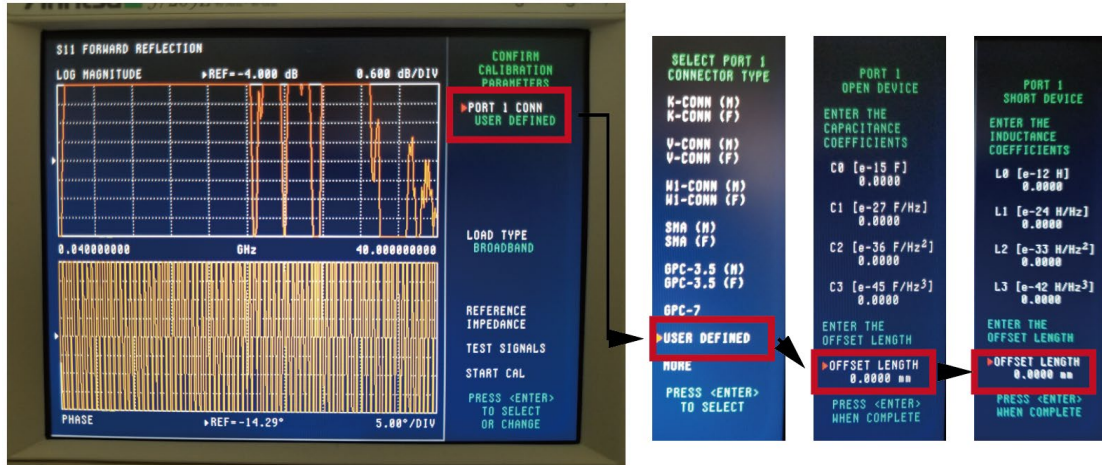
(b)

Fig. 3-19. (a) Calibration substrate with chip holder. (b) Setup of offset length in VNA when using calibration substrate.
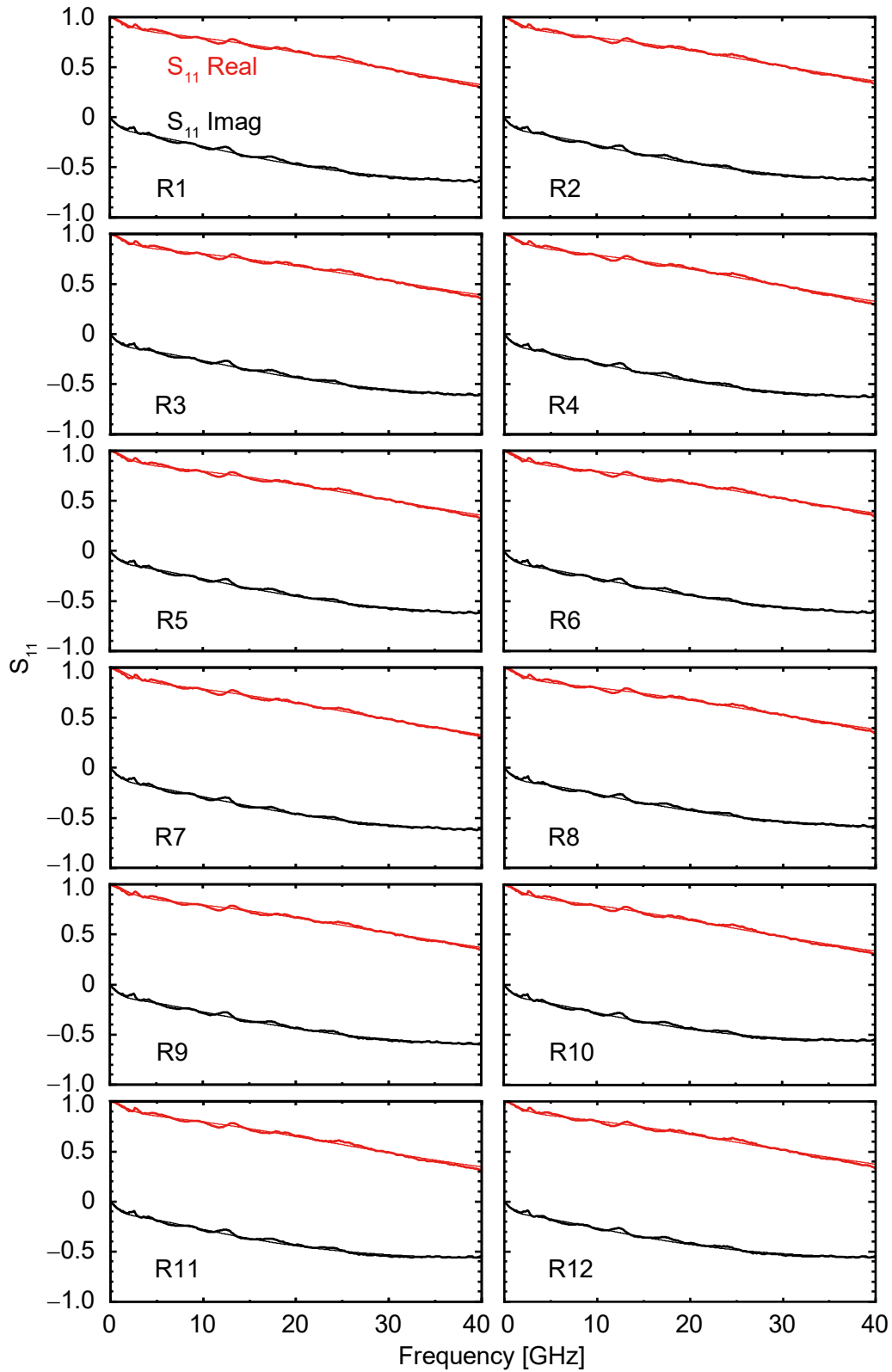
Fig. 3-20. Measured and fitted S11 of MRMs.

Parameter fitting of the circuit was then conducted with R_s as a fixed value. The fitting was carried out using the fitting function of the data processing software Origin, employing Eq. 3-31. Here, Z_{DUT} represents the impedance of the device calculated by Eq. 3-32, and Z_0 is the impedance on the VNA side (set to 50 Ω).

$$S_{11} = \frac{Z_{DUT} - Z_0}{Z_{DUT} + Z_0} \tag{3-31}$$

$$Z_{DUT} = \frac{1}{j\omega C_{pad}} \parallel \left(\frac{1}{j\omega C_j} + R_s \right) \parallel \left(\frac{1}{j\omega C_{Si}} + R_{Si} \right) \tag{3-32}$$

The fitting results are depicted in the lines of Fig. 3-20. The corresponding parameters are summarized in Table 3-2. The two most important parameters, R_s and C_j, are shown in (a) and (b) of Fig. 3-23. On the other hand, increasing L increases the area of the capacitor pair, which in turn increases C_j and decreases R_s. Figures 3-24(a) and 3-23(b) illustrate the expected trend. The overall electrical bandwidth was also calculated using Eq. 3-33 [3-3–5] and is presented in Fig. 3-24(c). Calculations using this formula indicate that the 3 dB bandwidth of all MRMs is above 40 GHz. When W_{pn} is small and L is also small, the electrical bandwidth is the widest. However, when W_{pn} is small, the optical loss is likely to be large.

$$f_{3dB(ele)} = \frac{1}{2\pi(R_s + R_{dr})C_j} \tag{3-33}$$

The last section of Table 3-2 compares each MRM in this study with each parameter of MRMs from other studies. Each parameter of the MRMs in this study falls within a reasonable range. The last two columns show the bandwidths calculated by different methods (Eqs. 3-33 and 3-34). Equation 3-33 is used when parameters other than R_s and C_j of the MRM can be ignored, which is not applicable here because C_{Si} is higher than C_j. Equation 3-34 [3-6, 7] is the voltage magnitude response considering the voltage divider at the pn junction, with all factors considered. Using Eq. 3-34, the voltage magnitude response when all parameters are substituted is shown in Fig. 3-23 (for R12). From the results, an electrical 3 dB bandwidth is extracted. The calculated bandwidth using Eq. 3-34 is presented in Fig. 3-24 (d). The electrical bandwidth is widest when both W_{pn} and L are small.

$$\left| V_j(\omega) \right| = \left| V_g \cdot \frac{Z_{DUT}}{Z_{DUT} + Z_0} \cdot \frac{1/(j\omega C_j)}{1/(j\omega C_j) + R_s} \right| \tag{3-34}$$

The overall EO bandwidth of the MRM is determined by both the RC time constant and the Q value (Eq. 3-35 [3-5]). However, in this study, the Q value is within 5000, so the EO bandwidth should be determined mainly by the RC time constant.

$$\frac{1}{f_{EO}^2} = \frac{1}{f_{opt}^2} + \frac{1}{f_{ele}^2}$$

$$= (2\pi\tau)^2 + \left[2\pi(R_s + R_{dr})C_j \right]^2 \tag{3-35}$$

$$= \left(\frac{\lambda Q}{c} \right)^2 + \left[2\pi(R_s + R_{dr})C_j \right]^2$$
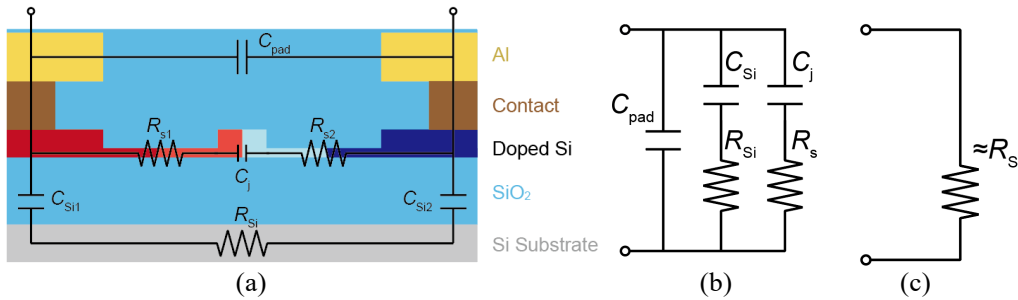
Fig. 3-21. (a) Cross section of MRM and corresponding electrical components. (b) Equivalent circuit model of MRM. (c) Equivalent circuit of MRM while large forward DC bias applied.
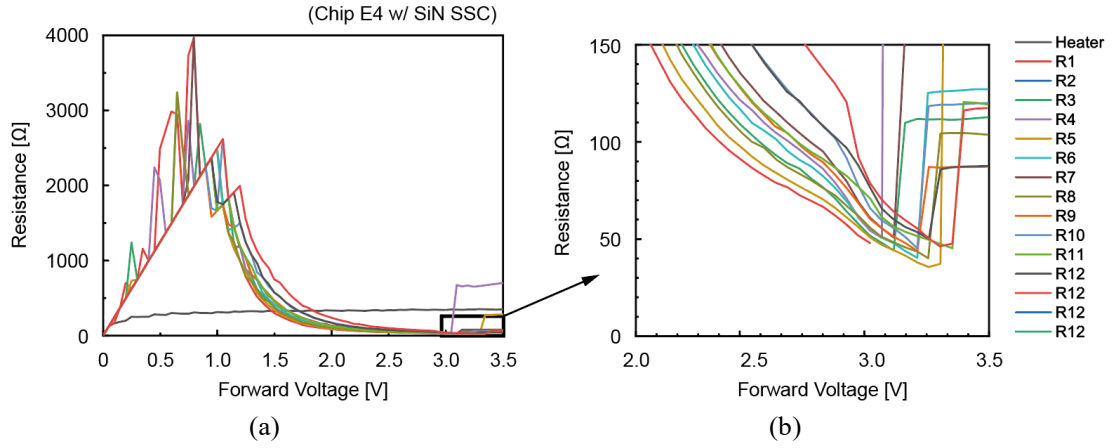
Fig. 3-22. (a) Resistance of MRM with forward bias voltage applied. (b) Enlarged view.
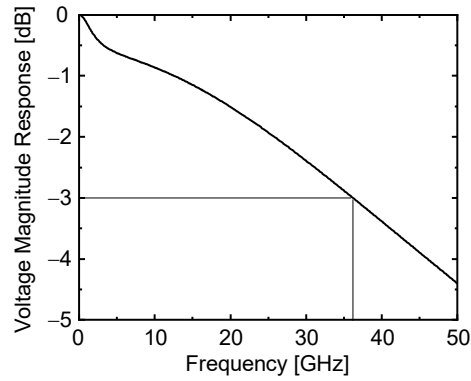
Fig. 3-23. Calculated voltage magnitude response using Eq. 3-38 for R12. f_{3dB} was calculated as 36 GHz.

Table 3-2. Extracted electrical parameters of varies MRMs in this research and references.

No.	W_{pn} [μm]	L [μm]	C_{pad} [fF]	R_{Si} [Ω]	C_{Si} [fF]	R_s [Ω]	C_j [fF]	f_{3dB} [GHz] (Eq. 3-33)	f_{3dB} [GHz] (Eq. 3-34)
R1	0.3	5	14.5	600.9	122.0	38.4	36.2	49.8	38
R2	0.3	2.42	15.4	600.5	119.0	44.0	32.4	52.3	39.5
R3	0.3	0.18	15.7	607.3	125.2	50.4	30.0	52.8	40
R4	0.35	5	11.6	596.8	123.7	35.5	38.6	48.2	38
R5	0.35	2.42	13.1	595.6	117.7	40.2	34.7	50.9	39.5
R6	0.35	0.18	16.6	586.7	115.0	50.6	30.0	52.8	39.5
R7	0.45	5	13.1	568.6	109.8	40.1	36.6	48.2	37
R8	0.45	2.42	10.6	601.7	122.2	43.8	34.7	48.9	39
R9	0.45	0.18	12.4	590.88	113.7	45.1	34.0	49.2	38.5
R10	0.65	5	8.8	615.6	117.2	45.1	40.6	41.2	34
R11	0.65	2.42	10.7	635.7	115.6	50.1	38.4	41.4	34
R12	0.65	0.18	8.4	655.9	116.4	46.2	38.0	43.6	36
[3-3] LowQ	--	--	5	1380	55	65	22.7	61.0	55
[3-3] HighQ	--	--	6.5	1160	52	177	15	46.7	42

76

[3-6]	--	--	20	1500	400	75	170	7.5	7
[3-8]	--	--	12	400	120	32	140	13.9	21
[3-9]	--	--	4.9	23000	7	365.5	8.2	46.7	79
[3-10]	--	--	13.4	19300	21.3	211	14.7	41.5	39
[3-11]	--	--	6.4	16700	21.1	205	20.5	30.4	29
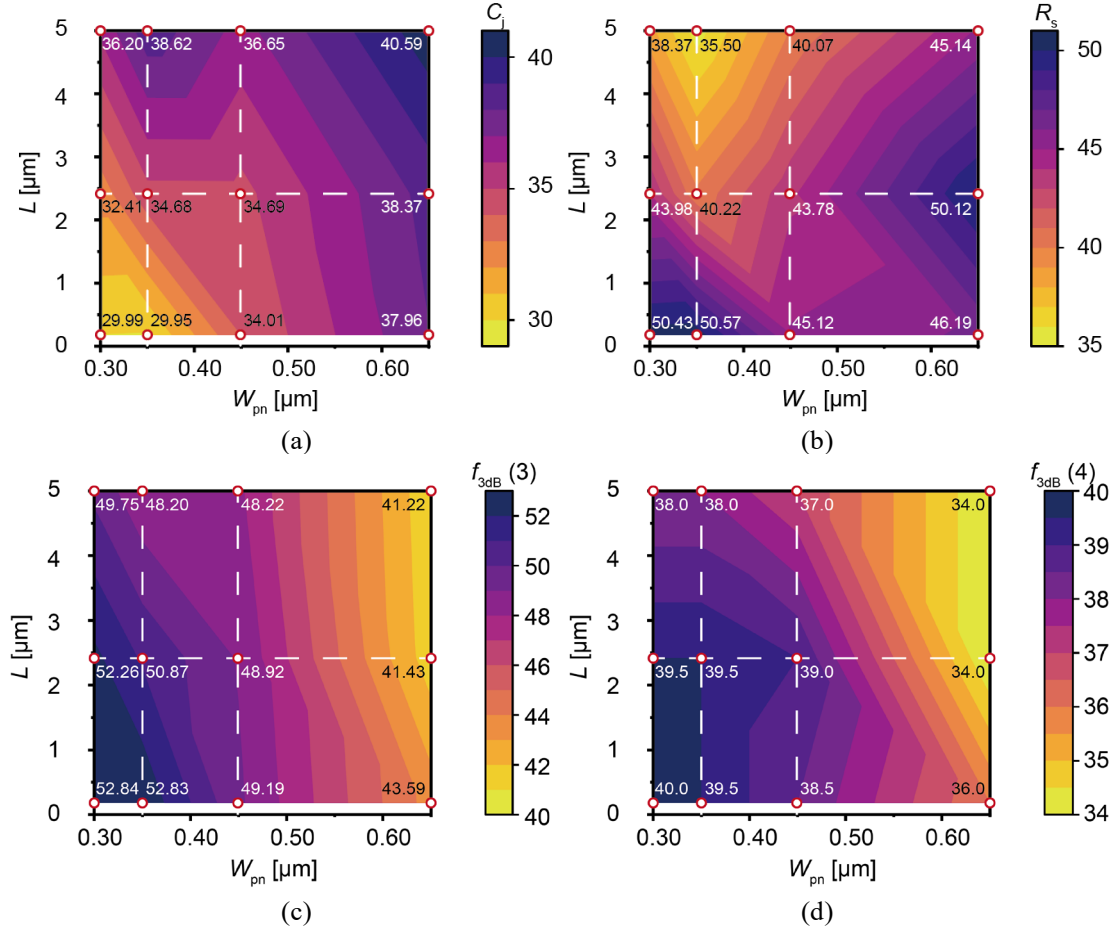
Fig. 3-24. Extracted (a) junction capacitance C_j and (b) series resistance R_s of MRMs. (c) Calculated electrical 3 dB bandwidth of MRM using Eq. 3-33. (d) Calculated electrical 3 dB bandwidth of MRM using Eq. 3-34.

3.7.2 MRM Modulation Efficiency Survey

The MRM modulation efficiency was also investigated using the measurement system shown in Fig. 3-25. Static modulation characteristics were examined for R7, R11, and R12, as depicted in Fig. 3-26. The transmission spectra of R1~R6 and R8~R10 in (a) deviate significantly from the critical coupling condition, as the resonance notch is less than 7 dB. The resonance wavelength shift due to the externally applied voltage was almost invisible. Subfigures (b)~(d) represent R7, (e)~(g) represent R11, and (h)~(i) represent R12. From (b), (e), and (h), the Q-value of R12 (4281, f_{opt} = 45.5 GHz) is larger than that of R7 (1101, f_{opt} = 175.6 GHz) and R11 (2495, f_{opt} = 77.7 GHz).

When a bias voltage is applied to each, the resonance wavelength shift is observed, as shown in different colors. The resonance wavelength information is extracted from (c), (f), and (i), respectively. The modulation efficiency is 8.01 pm/V for R7, 7.33 pm/V for R11, and 9.94 pm/V for R12. This difference is mainly related to the steepness of the resonance wavelength, i.e., the
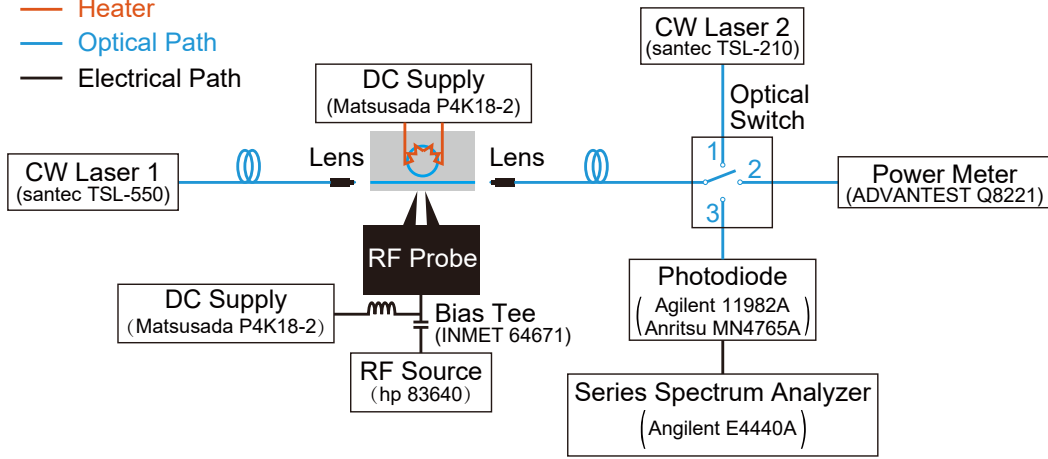
Fig. 3-25 Experimental setup for testing of modulation properties.

Q-value. For high-frequency modulation, e.g., 40 GHz millimeter wave modulation, a Q-value within 3420 is sufficient (when the optical bandwidth is equal to the electrical bandwidth); for R12, the electrical bandwidth must be extended to 85.8 GHz or higher to achieve 40 GHz millimeter wave modulation. The balance between high Q-value and wide bandwidth is important.

The $V_\pi L$ of the three MRMs can be calculated from Eqs. 3-36~38. The 78% here is the percentage of the modulation section. The $V_\pi L$ of R7, R11, and R12 are 3.01 Vcm, 3.29 Vcm, and 2.42 Vcm, respectively. Here, $n_g = 3.89$ for a rib waveguide width of 0.5 μm, a waveguide thickness of 0.22 μm, and a slab thickness of 0.11 μm.

$$\frac{\Delta\phi}{L} = \frac{\pi}{L_\pi} \tag{3-36}$$

$$\Delta\phi = \frac{2\pi\Delta\lambda}{FSR} \tag{3-37}$$

$$\begin{aligned}
V_\pi L_\pi &= \frac{V_\pi \pi L}{\Delta\phi} \\
&= \frac{V_\pi \pi \cdot 2\pi R \cdot 78\%}{2\pi\Delta\lambda} \cdot FSR \\
&= \frac{V_\pi \pi \cdot 2\pi R \cdot 78\%}{2\pi\Delta\lambda} \cdot \frac{\lambda^2}{n_g \cdot 2\pi R} \\
&= \frac{\lambda^2 78\%}{2n_g(\Delta\lambda / V_\pi)}
\end{aligned} \tag{3-38}$$

The extinction ratios and normalized insertion losses for R7, R11, and R12 at −1.5 V_{Bias} and 3 V_{pp} are presented in Fig. 3-26 (d), (g), and (j). The asymmetry of the transmission spectrum due to the thermal bistability of MRMs is evident in (b), (c), and (d) in Fig. 3-26. Therefore, asymmetric peaks also appear in the extinction ratio. The calculations of insertion loss and extinction ratio are referenced from [3-3]. Due to the low modulation efficiency, the extinction ratios of R7 and R11 are smaller than that of R12. On the other hand, the maximum extinction ratio of R12 is 7 dB, and the insertion loss is 15 dB. The difference in optical loss due to doping (related to Q-value) should be small. The effect of production fluctuations is most significant, as the W_{pn} of R7 (0.45 μm) is smaller than that of R11 and R12 (0.65 μm), resulting in larger optical loss due to doping and lower modulation efficiency. In the case of R12, the extinction ratio at 1541.112 nm (peak extinction ratio on the left) is 5.7 dB, and the insertion loss is 10.7 dB.
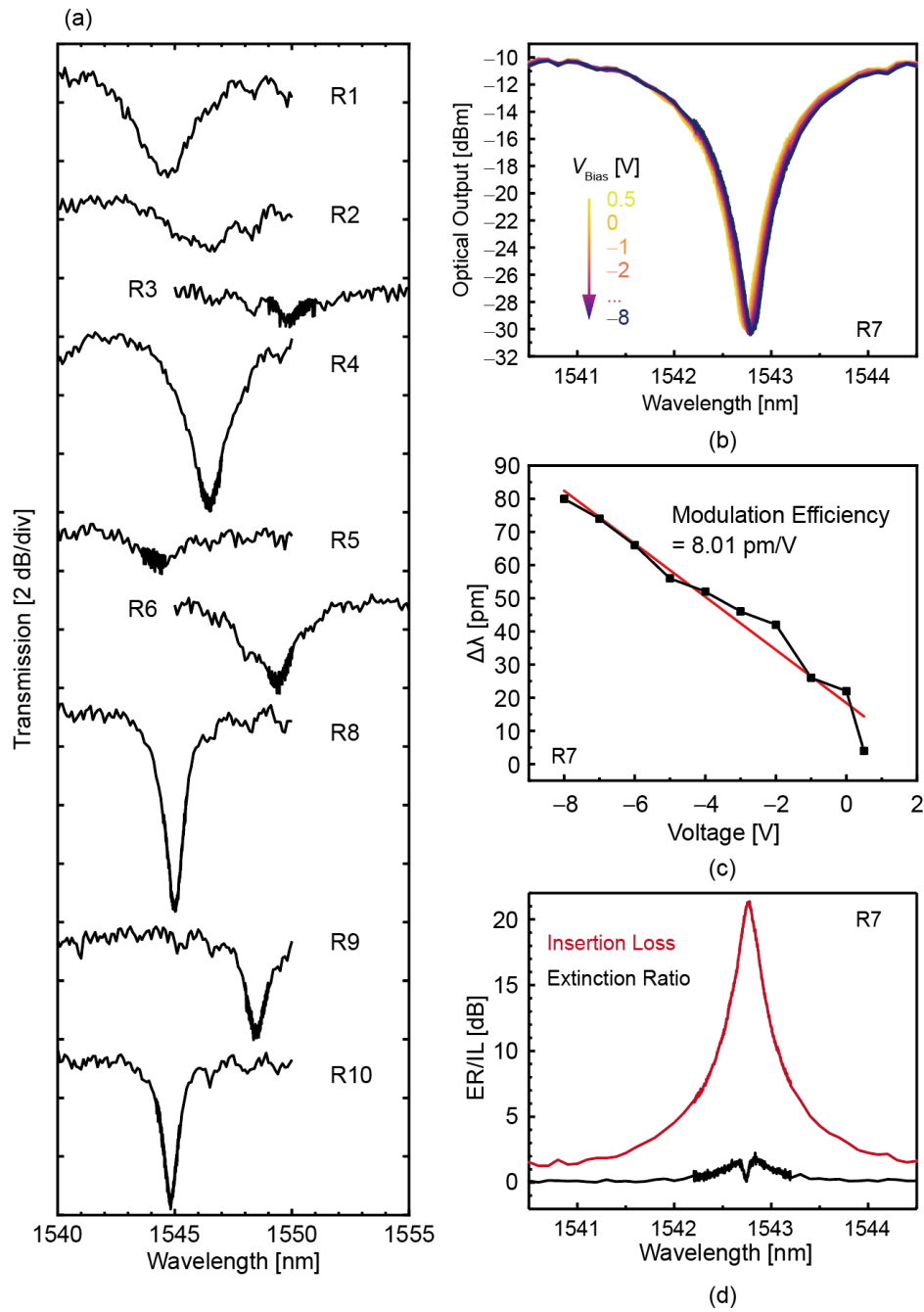
Fig. 3-26. (a) Optical transmission spectrums of R1~R6, R8~R10, which were not under critical coupling conditions. (b), (e), (h): Resonant wavelength shift with backward voltage up to −8 V applied. (c), (f), (i): resonant shift as a function of bias voltage. (d), (g), (j): extinction ration and normalized insertion loss of MRMs. (b) ~ (d) for R7, (e) ~ (g) for R11, (h) ~ (j) for R12.
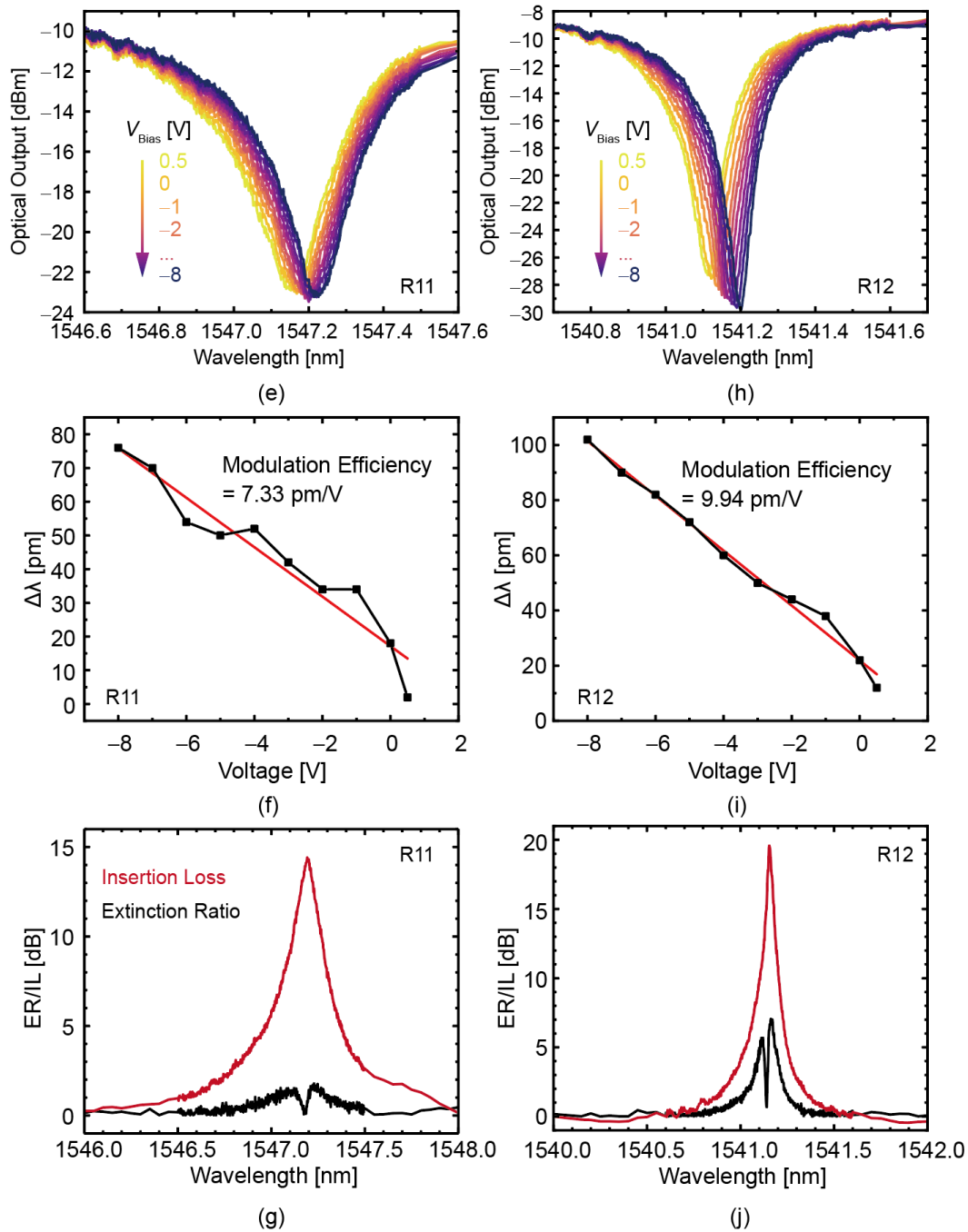
Fig. 3-26. (a) Optical transmission spectrums of R1~R6, R8~R10, which were not under critical coupling conditions. (b), (e), (h): Resonant wavelength shift with backward voltage up to −8 V applied. (c), (f), (i): resonant shift as a function of bias voltage. (d), (g), (j): extinction ration and normalized insertion loss of MRMs. (b) ~ (d) for R7, (e) ~ (g) for R11, (h) ~ (j) for R12.

3.7.3 S21 Parameter Analyze

The experimental system depicted in Fig. 3-18 was utilized to measure the S21 of MRMs R7, R11, and R12. Given that the maximum input power of the photodiode is 10 dBm, the EDFA was adjusted to ensure that the output of the EDFA is approximately 8.5 dBm. Here, 8.5 dBm represents the output power when the MRM is non-resonant.

Before using the VNA, calibration is essential. The chip calibration was performed by connecting Port 1 to the calibration board via a probe and Port 2 to the corresponding element

in the calibration kit in the Short, Open, and Load steps. To maximize agreement, Port 2 was also connected to the calibration board via another probe. In the final through step of the calibration, Port 1 and Port 2 are connected via a through line on the calibration board. Since MRM is typically measured with two probes, two probes were also used in the through line calibration. However, since the directions of the two probes are opposite, S of probe 1 is connected to G of probe 2, and S of probe 2 is connected to G of probe 1 via the Through Line, resulting in a problem that prevents correct Through Line calibration (Fig. 3-27(a)). Therefore, we changed from three to two probes in all calibration steps. In this way, the S of the 3-probe can be connected to the S of the 2-probe. An example of the measured S21 is shown in Fig. 3-27(d). This result shows that S21 is abnormally high in the high-frequency region. This is because the right G of the probe on the Port 2 side is floating. Therefore, as shown in Fig. 3-27 (c), we changed to a 5 probe to 3 probe configuration, where Port 2 is connected to S on the left side, since the 5 probe needle is in GSGSG configuration. In this case, all the needles of the 3-probe connected to Port 1 were connected to the 5-probe. The measurement results are shown in Fig. 3-27 (e). It was confirmed that the rise in the high-frequency range was eliminated.

With that configuration, the S21 parameters of R7, R11, and R12 were measured at different incident optical powers, and the results are shown in Fig. 3-28. With a fixed laser power, R7 exhibited the flattest frequency response. This is attributed to R7 having the smallest Q-value and the largest bandwidth. Moreover, R12 demonstrated the highest modulation efficiency, signifying that S21 is higher overall than the others (11 dB higher than R7 and 5 dB higher than R11). The laser wavelengths used for these measurements were 1543.4 nm, 1547.5 nm, and 1541.5 nm when $P_{LD} = 10$ dBm.

Laser wavelengths were also detuned near the wavelength of maximum modulation efficiency, and S21 was recorded. When the wavelength was detuned from the wavelength at which the maximum modulation efficiency was obtained, the S21 in the low-frequency region dropped faster than in the high-frequency region, resulting in an overall flattened frequency response—the peaking effect. This reduces the modulation intensity but provides a wider frequency bandwidth. Utilizing the peaking effect, all MRMs exhibited bandwidths above 40 GHz.

It is also observable that the S21 of all MRMs gradually increases when the laser power P_{LD} is set to 0 dBm, 5 dBm, and 10 dBm. At $P_{LD} = 10$ dBm, the S21 of R12, which has the highest Q value, suddenly drops at the long wavelength side of the maximum modulation efficiency point as it detunes to the long wavelength side. The highest asymmetry of the optical transmission spectrum of R12 was observed indirectly due to the high Q value of R12 at $P_{LD} = 10$ dBm. This phenomenon is due to the bistability of MRR at high incident optical power. Nevertheless, in some measurements at high laser power, the S21 curve near the point of maximum modulation efficiency fluctuates significantly. This is due to the large thermal instability of the MRM when measuring near the point of maximum modulation efficiency at high power.
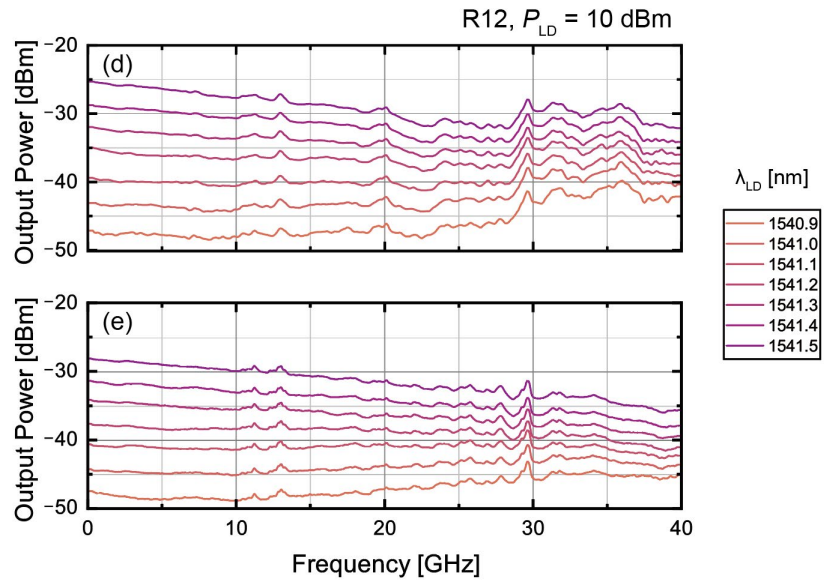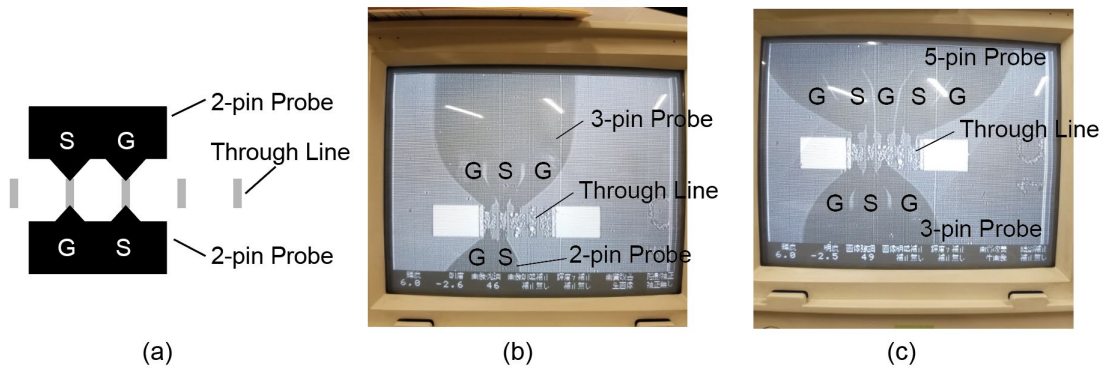
Fig. 3-27. Through line step in VNA calibration using (a) 2-pin/2-pin probe, (b) 3-pin/2-pin probe and (c) 5-pin/3-pin probe. (d) Measured S21 sample with setup (b). (e) Measured S21 sample with setup (c).
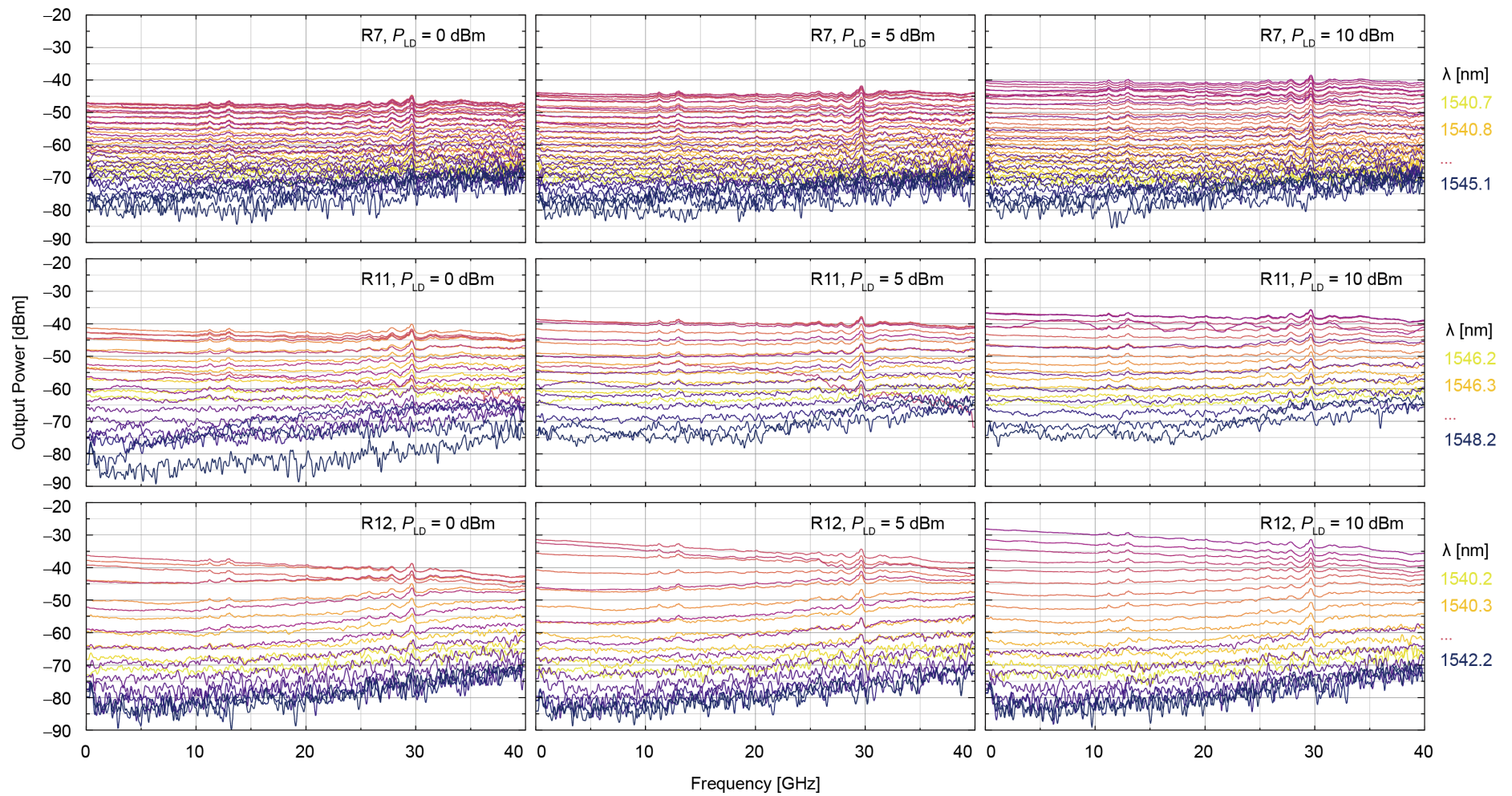
Fig. 3-28. Measured S21 of MRM R7, R11 and R12 with different P_{LD} and wavelength detuning.

3.7.4 MRM Wide Range Modulation

Based on the aforementioned S21 measurements, a broadband modulation was performed. First, from Fig. 3-28, the frequency response at 40 MHz (the lowest frequency at which a VNA can be obtained) and the 3 dB cutoff frequency are shown in Fig. 3-29. As depicted in the figure, the frequency response increases with increasing laser power and Q-value at low-frequency modulation. The 3 dB bandwidth of R7 and R11 is consistently above 40 GHz near the wavelength of maximum modulation efficiency. The bandwidth of R12 was 10 ~ 30 GHz near the point of maximum modulation efficiency.

Since the Q-values of R7, R11, and R12 are 1101, 2495, and 4281, respectively, the corresponding optical bandwidths in terms of photon lifetime are 175.6 GHz, 77.7 GHz, and 45.5 GHz, respectively. As the electrical bandwidths are 37.0 GHz, 38.4 GHz, and 38.0 GHz, respectively, the overall EO bandwidths are calculated to be 36.2 GHz, 34.4 GHz, and 29.1 GHz, respectively. These calculations are bandwidth estimates at the wavelength of maximum modulation efficiency and do not differ significantly from the actual measured results.

Finally, the modulation eye patterns at different frequencies at the point of maximum modulation efficiency were measured using the experimental system shown in Fig. 3-30, with the PRBS NRZ signals -3 V_{pp} and -3 V_{Bias} output from PPG and the BPF output power (non-resonant) set near 8.5 dBm. The output power of the BPF (at non-resonance) was set around 8.5 dBm. The measurement results are shown in Fig. 3-31 (R7), Fig. 3-32 (R11), and Fig. 3-33 (R12). The "L" and "R" correspond to the results at the maximum modulation efficiency wavelength at the short wavelength side and the maximum modulation efficiency wavelength at the long wavelength side, respectively. For the same MRM, higher laser power corresponds to a higher extinction ratio. In addition, except for R7 with 0 dBm laser power input, all MRMs showed a clear eye pattern for modulations up to 32 Gbps. As the modulation efficiency increases, the eye aperture of R12 is the largest: at 15 Gbps and P_{LD} = 5 dBm, the extinction ratios of R7, R11, and R12 are 1.52 dB, 1.62 dB, and 5.2 dB, respectively; at 32 Gbps and P_{LD} = 5 dBm, the extinction ratios of R7, R11, and R12 are 1.04 dB, 1.7 dB, and 4.4 dB, respectively. The top row of Fig. 3-29 shows that the slope of the peak left frequency response versus wavelength at high power input is smaller than that at the right, and that the difference between L and R increases as P_{LD} increases. At P_{LD} = 10 dBm, the maximum modulation efficiency point on the right side of R12 disappeared completely, so the "R" data could not be obtained.
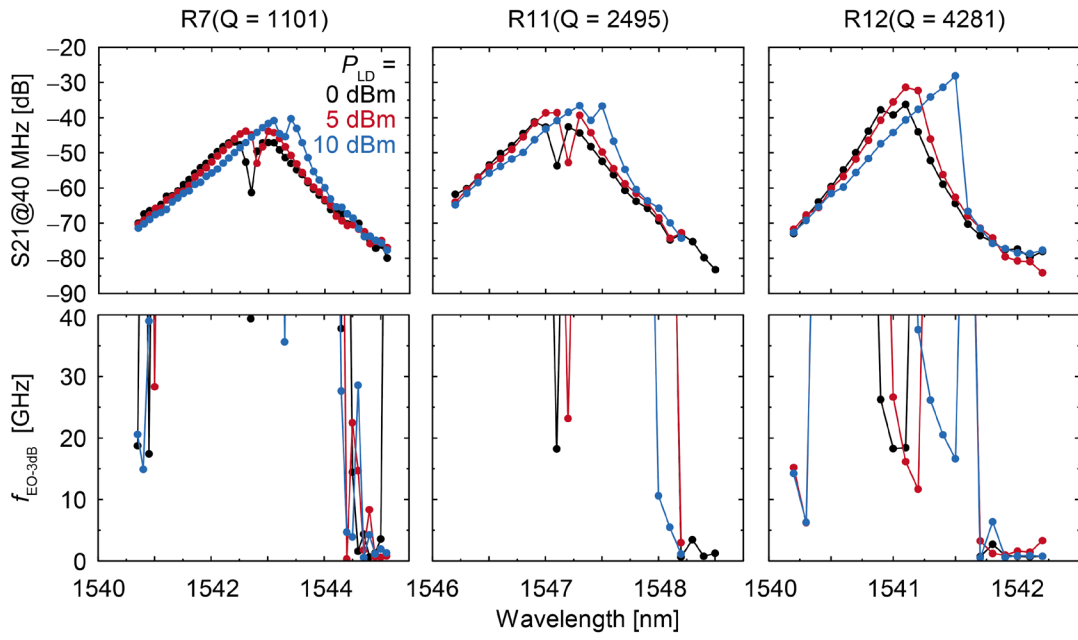
Fig. 3-29. Frequency response at 40 MHz and 3 dB bandwidth of R7, R11 and R12.
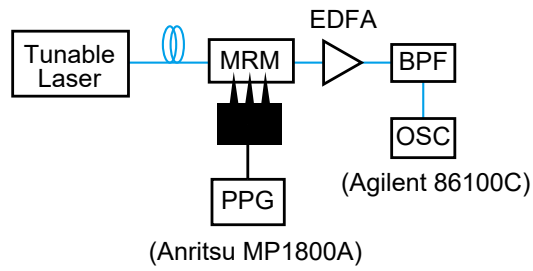
Fig. 3-30. Measurement setup for modulation.
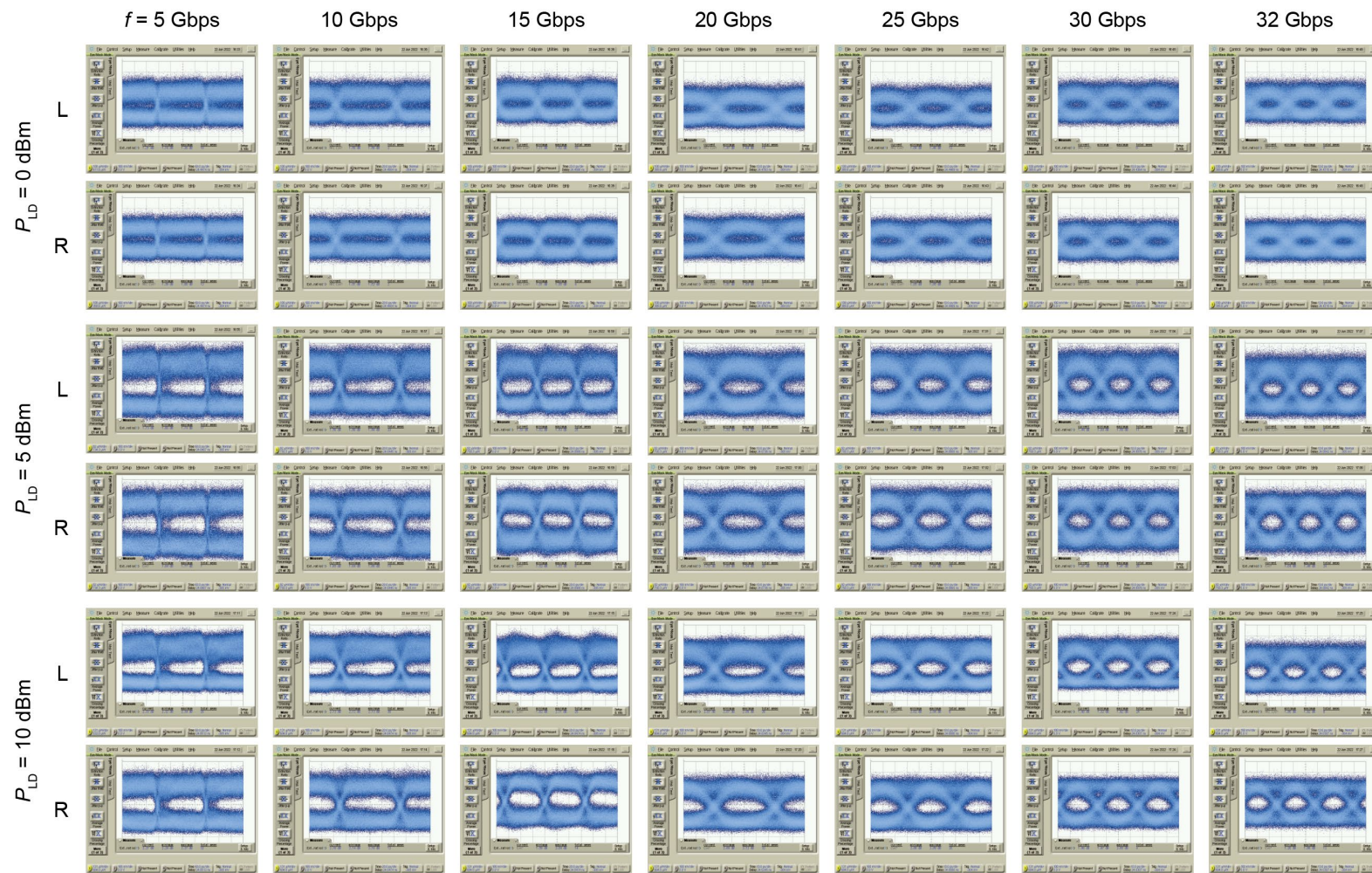
Fig. 3-31. Eye diagrams of R7 with different P_{LD} and modulate rate. L and R corresponding to max modulation points at blue and red side in wavelength tuning.
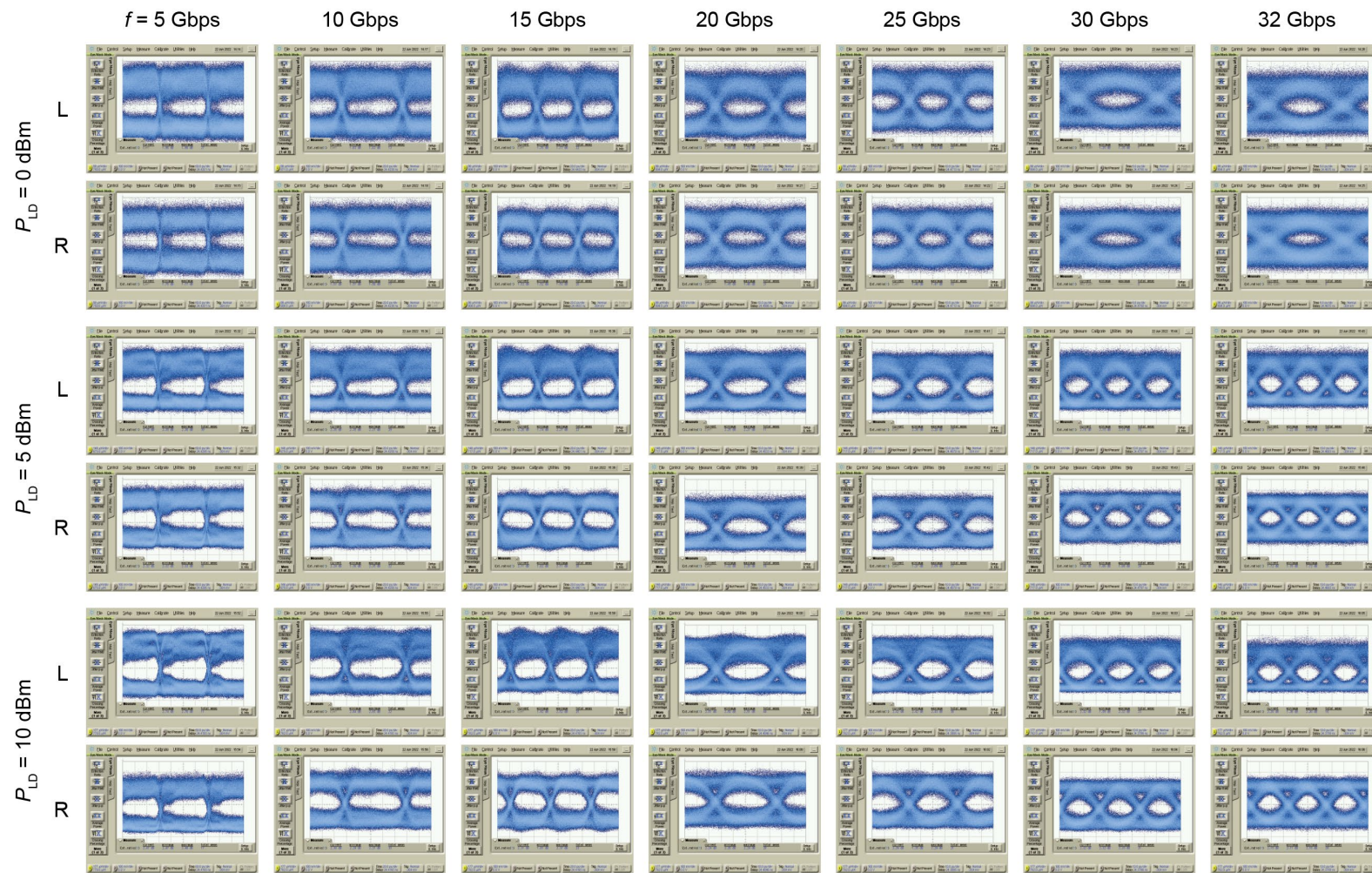
Fig. 3-32. Eye diagrams of R11 with different P_{LD} and modulate rate. L and R corresponding to max modulation points at blue and red side in wavelength tuning.
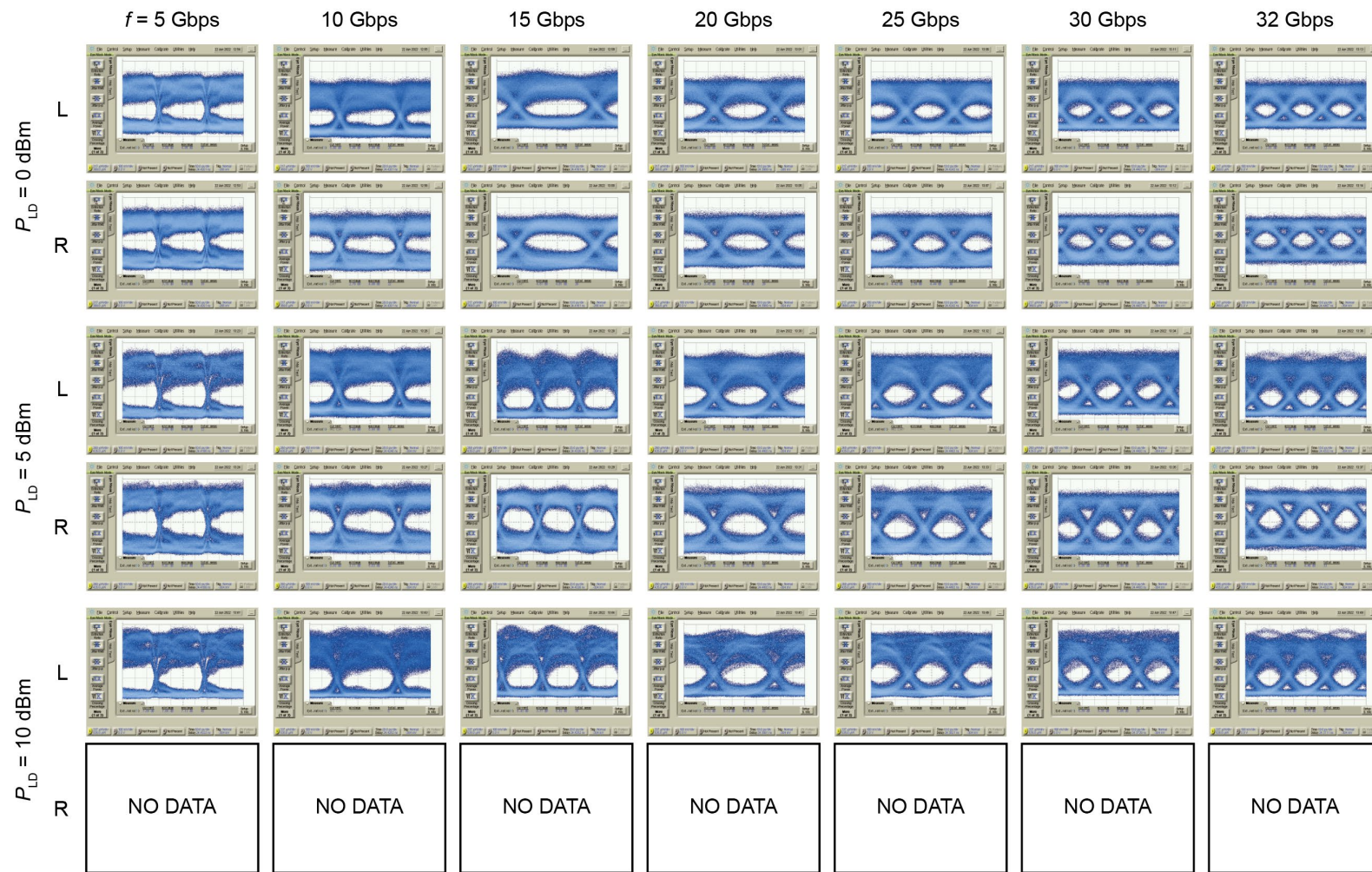
Fig. 3-33. Eye diagrams of R12 with different P_{LD} and modulate rate. L and R corresponding to max modulation points at blue and red side in wavelength tuning.

3.8 Self-Heating

3.8.1 Theory

Assuming that the optical power incident on the MRM is weak, the transmission function of the MRM can be approximated by the Lorentz function because the heat generation due to internal carrier absorption is negligible. However, in the more general case, since the optical power incident on the MRM is greater than 0 dBm, the self-heating of the MRM due to carrier absorption cannot be neglected. To the MRM transmission function expressed in Eqs. 3-39 and 3-40, we added the refractive index change term $\delta(1-T)P_{in}$ as the temperature in the ring increases, where δ is the change in the refractive index of the waveguide due to 1 mW of light absorption, T is the transmittance of the MRM, and P_{in} is the incident power of the MRM. From [3-12], δ can be calculated using Eq. 3-41, where ng is the group refractive index, $\Delta\lambda_{res}$ is the resonance wavelength shift when the incident power changes, λ_{res} is the resonance wavelength, and ΔP_{in} is the change in incident power (in mW).

$$T = \frac{a^2 - 2ar\cos\phi + r^2}{1 - 2ar\cos\phi + (ar)^2} \tag{3-39}$$

$$\phi = \frac{2\pi L}{\lambda}\left[n_{eff}(t) + \delta(1-T)P_{in}\right] \tag{3-40}$$

$$\delta = \frac{n_g \Delta\lambda_{res}}{\lambda_{res}\Delta P_{in}} \tag{3-41}$$

Using ring #12 of the AIST MRM device, δ was calculated from the resonance wavelength shift as the incident power was varied. Shown in Fig. 3-34 is the transmission spectrum of the MRM measured in the 1530 nm~1570 nm range, where the P_{LD} is −16 dBm and self-heating is negligible. The result shows that FSR = 9.79 nm around 1550 nm. From Eq. 3-42, we can calculate that the group refractive index n_g = 3.91 for the MRM waveguide.

$$FSR = \frac{\lambda_{res}^2}{n_g L} \tag{3-42}$$

where L is the ring circumference. The mode number m and equivalent refractive index n_{eff} of each resonance peak can be calculated using Eq. 3-43.

$$\lambda_{res} = \frac{n_{eff}L}{m} \tag{3-43}$$

Assuming that n_{eff} is the same at the resonance wavelengths of the neighboring wavelengths, and substituting the resonance wavelengths of the mth-order and m+1-order (shorter wavelength side) into Eq. 3-43, m at 1550 nm was calculated to be 157. The corresponding equivalent refractive index n_{eff} is 3.87. In addition, the resonance wavelength shift at high power input was measured. Figure 3-35(a) shows the measurement results using the same MRM. It can be seen that the transmission spectrum is red-shifted when the power P_{LD} of the light emitted from the laser is higher than −8 dBm. Since the propagation loss of the lensed fiber, SSC, and waveguide is about 4.1 dB, we consider that the self-heating effect of the MRM is negligible when the actual light incident on the MRM exceeds −12 dBm. The self-heating effect increases as the laser power increases, and the resonance spectrum gradually becomes asymmetric. 8 dBm P_{LD} means that if the laser wavelength exceeds the resonance wavelength even slightly, the resonance stops immediately, the self-heating almost stops, and the long wavelength side becomes linear. This state is called a bistable state, and the transmission spectrum differs depending on the direction of wavelength sweep. Figure 3-35(b) shows the change in the resonance wavelength when the laser power is increased. Except in the bistable region, there is a linear relationship between the resonance wavelength shift and the input power change.

Substituting this result into Eq. 3-41, the rate of change of the refractive index of the MRM waveguide with absorbed power δ is calculated to be 5.57×10^{-4} /mW. Substituting these results into Eqs. 3-39 and 3-40, MATLAB simulations were performed. Figure 3-36 shows the simulation results under the same experimental conditions. Compared to Fig. 3-35(a), the results are in excellent agreement in the non-bistable region (the misalignment of the resonance wavelength is a calculation error). Hence, the model was proved to be valid.

3.8.2 Possibility of Modulating ER Enhancement Using Asymmetry

As shown in Fig. 3-35(a), the spectrum becomes asymmetric at high power input. Using this characteristic, it is considered that a higher extinction ratio can be obtained at the same modulation power than at shorter wavelengths when the laser wavelength is set at the longer wavelength side and modulated. Experiments were conducted using the measurement system shown in Fig. 3-37, in which a 2 V_{pp}, -2 V_{Bias}, 10 Gbps PRBS signal from PPG is modulated using the same MRM as in Chapter 2. The output modulated light was fixed by EDFA to 0 dBm (non-resonant), passed through a bandpass filter centered at 1550 nm, and the time waveform of the output light was observed with an optical oscilloscope.

Figure 3-38 again shows the transmission spectra when the laser power P_{LD} is 0 dBm and 8 dBm. The time waveform of the output modulated light differs depending on the laser wavelength setting. Figure 3-39 shows the time waveforms of the modulated light at 0 dBm and 8 dBm, respectively. With zero bias, the pn junction may be forward biased for an input voltage of 2 V_{pp}, resulting in a nonlinear refractive index-voltage relationship that distorts the time waveform. In the reverse bias case, on the other hand, an open eye pattern was seen on both sides of the resonance wavelength. The low input power case has stable eyes on both sides, but the high input power case has a very unstable modulation on the right side, and the extinction ratio is not much different from that of the left side or the low input power case.

Next, the change in modulation ER with increasing input optical power was examined. The input electrical signal was the same as above, and the time waveform is shown in Fig. 3-40(a). The same measurement system as in Fig. 3-37 was used to record the ER of the modulated light eye pattern while changing the laser power, and the results are shown in Fig. 3-40(b). Here, Left and Right correspond to the wavelengths when the eye patterns on the left and right sides of the resonance wavelength are at their widest. As the laser power is increased, the difference between the ERs on the left and the right side remains almost the same; above 6 dBm, the modulation is unstable, and the ERs cannot be evaluated correctly. The eye pattern corresponding to each data point is shown in Fig. 3-41. From these results, the causes of the following three problems remain unclear: (1) why the ERs on the left and right sides do not change, (2) why one level of the left eye pattern is more unclear than the right, and (3) why the ER increases with increasing input power even though the output light is fixed by EDFA. We believe that (1) and (2) are related to the rate of self-heating, while (3) is related to the nonlinearity of the EDFA. In addition, it is inconvenient to elucidate the above causes because high power input light is used to maintain and modulate the asymmetric spectrum at the same time.
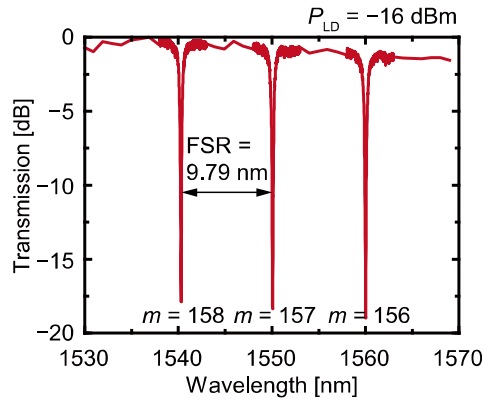
Figure 3-34 MRM transmission spectrum at low power.
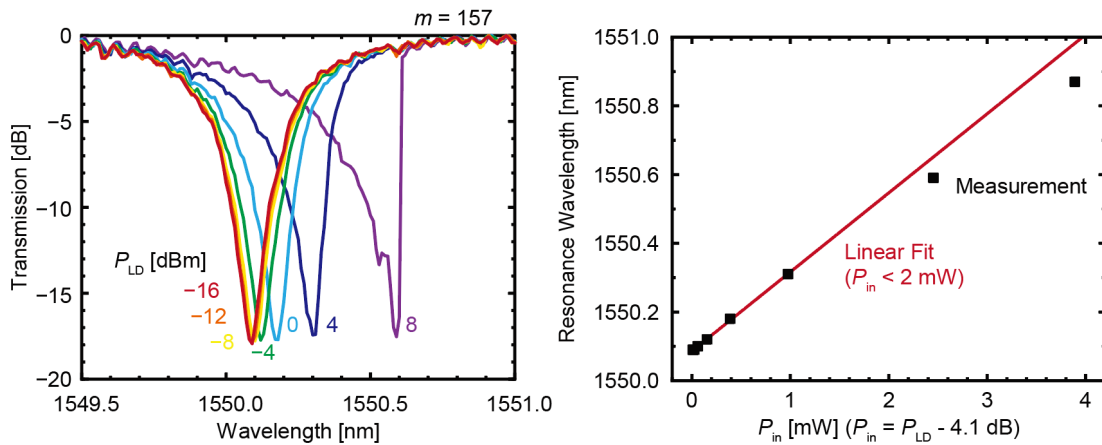
Figure 3-35 (a) Change in transmission spectrum with increasing incident power. (b) Change in resonance wavelength with increasing incident power.
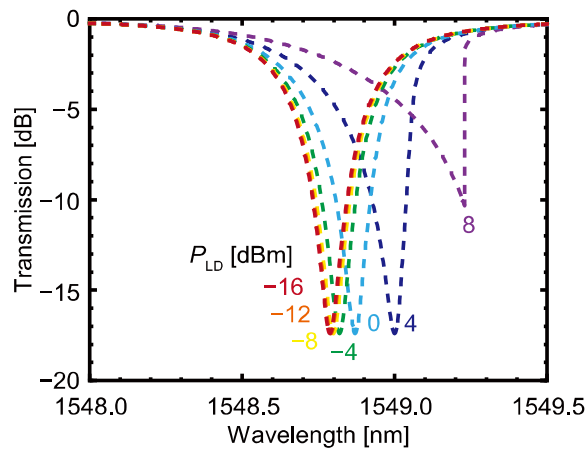
Fig.3-36 Simulation results of transmission spectrum change with increasing incident power.
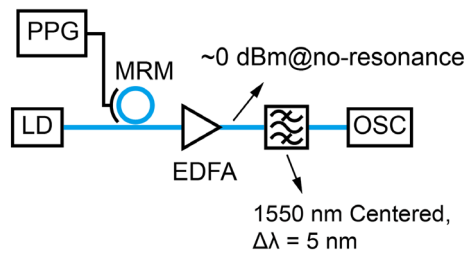
Figure 3-37 Modulation measurement setup.
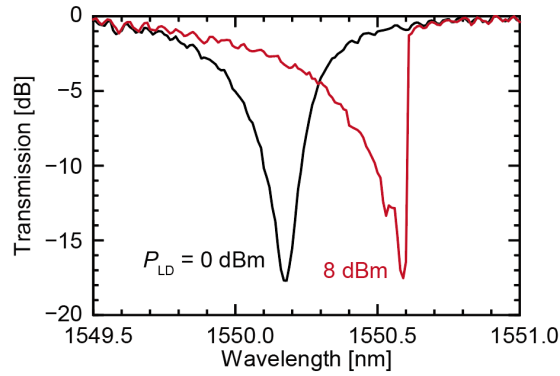
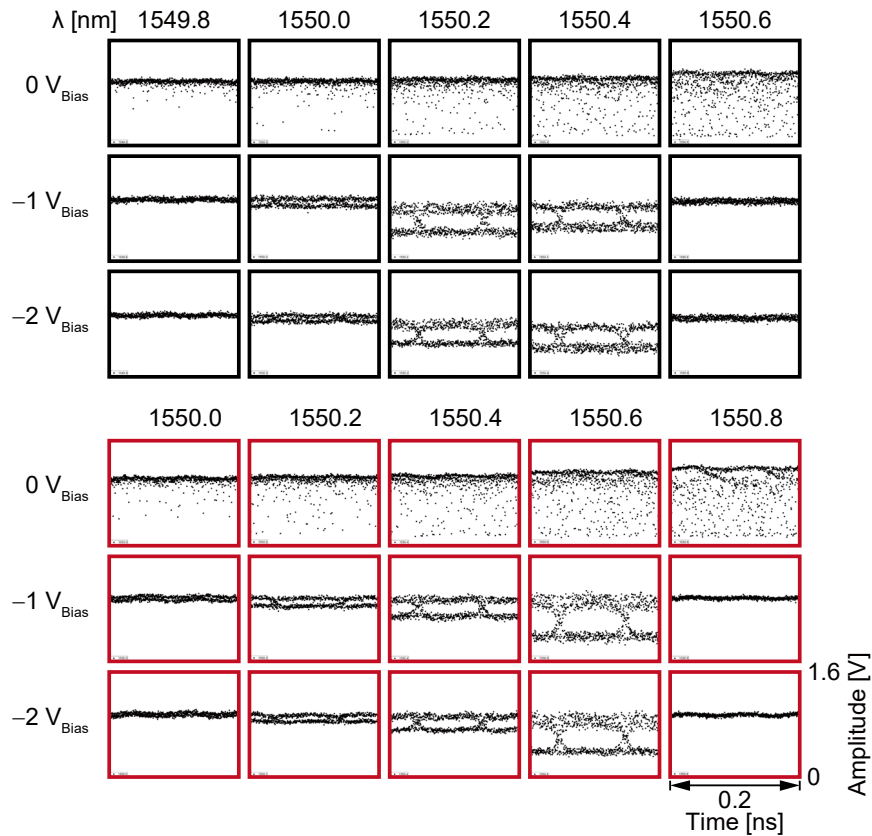Figure 3-38 Transmission spectra at laser power of 0 dBm and 8 dBm.

Figure 3-39 Modulated light waveforms at different wavelengths when modulating incident light at 0 dBm and 8 dBm.

Therefore, we next modified the experimental system as shown in Fig. 3-42, incorporating two wavelengths of light. The respective optical wavelengths are referred to as λ_{Pump} and λ_{Probe}. The pump light is high-power light designed to create and maintain asymmetric spectra, while the probe light is low-power light intended for modulation. Here, λ_{Pump} and λ_{Probe} are positioned around 1560 nm and 1550 nm, respectively. As illustrated in Fig. 3-34, the pump and probe beams were arranged with FSR spacing. The center wavelengths of BPD1 and BPD2 in Fig. 3-42 were set to 1550 nm and $\Delta\lambda$ to 4.5 nm. Each is utilized for filtering the pump light and EDFA noise; the EDFA is adjusted to an optical output power of 0 dBm when non-resonant.

By configuring the pump light to high power and positioning it near the resonance wavelength of the MRM ($m = 156$), the ring can be maintained in a self-heating state. As all resonance wavelengths are also shifted, stable modulation with high ER can be achieved by placing the probe light near the shifted resonance wavelength ($m = 157$). Figure 3-43 illustrates
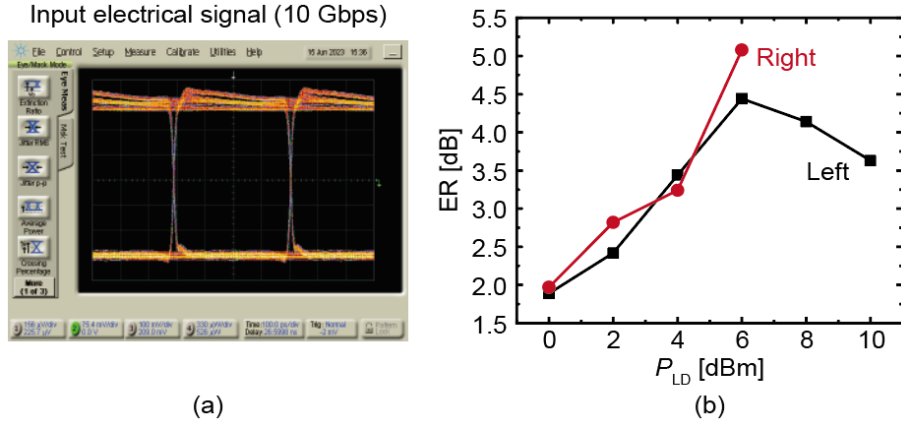
Figure 3-40 (a) Time waveform of the input electrical signal. (b) Modulation extinction ratio of the output light measured when the input optical power is varied, where Left and Right are the results at the wavelengths when the eye patterns on the left and right sides of the resonance wavelength are the widest, respectively.

the ER obtained when the pump and probe wavelengths are concurrently swept. The modulation signal consists of a 10 Gbps PRBS signal from PPG with V_{pp} = 3 V and V_{Bias} = −2 V. The oscilloscope eye pattern ER was recorded using the LabVIEW program while the pump and probe light wavelengths were automatically swept. When the pump light is at 11 dBm, the light incident on the ring is equivalent to the 8 dBm case depicted in Fig. 3-35(a), given the 3 dB loss of 2by1. Therefore, an abrupt change in the pump light wavelength near 1560.4 nm is observed in Fig. 3-43. As the pump light deviates from the resonant wavelength, the ER intensity gradually increases while the probe light sweeps, and two peaks of maximum values are obtained at the resonant wavelength. These two peaks are nearly symmetrical with respect to the resonance wavelength, irrespective of the self-heating of the ring due to the pump light. This indicates that stable modulation can be achieved even when the ring is heated by self-heating. However, the maximum ERs on both sides of the resonance wavelength are still approximately the same. Since the PRBS signal used here includes a low-frequency component, a simple 2 GHz sine wave was then utilized in SG. In this case, since an eye pattern cannot be captured with an oscilloscope, the time waveforms of the light were time-averaged eight times, V_{top} and V_{base} were recorded, respectively, and the ER was calculated using Eq. 3-44.

$$ER = 10\log_{10}\frac{V_{top} - V_{dark}}{V_{base} - V_{dark}} \tag{3-44}$$

The V_{dark} here represents the level without light and is set to 0. Figure 3-44 illustrates the measurement results in (a)~(d) when the pump power is set to 3 dBm, 7 dBm, and 11 dBm, and the probe power is set to 0 dBm. The results indicate a red-shift of the resonance wavelength with an increase in pump power; at 7 dBm, the ER of the upper oblique band is slightly larger than that of the lower band by about 0.2~0.4 dB, but no significant change has been observed yet. (d) presents the results when the probe light is stronger, and a pronounced asymmetry is visible in the vertical direction.

93
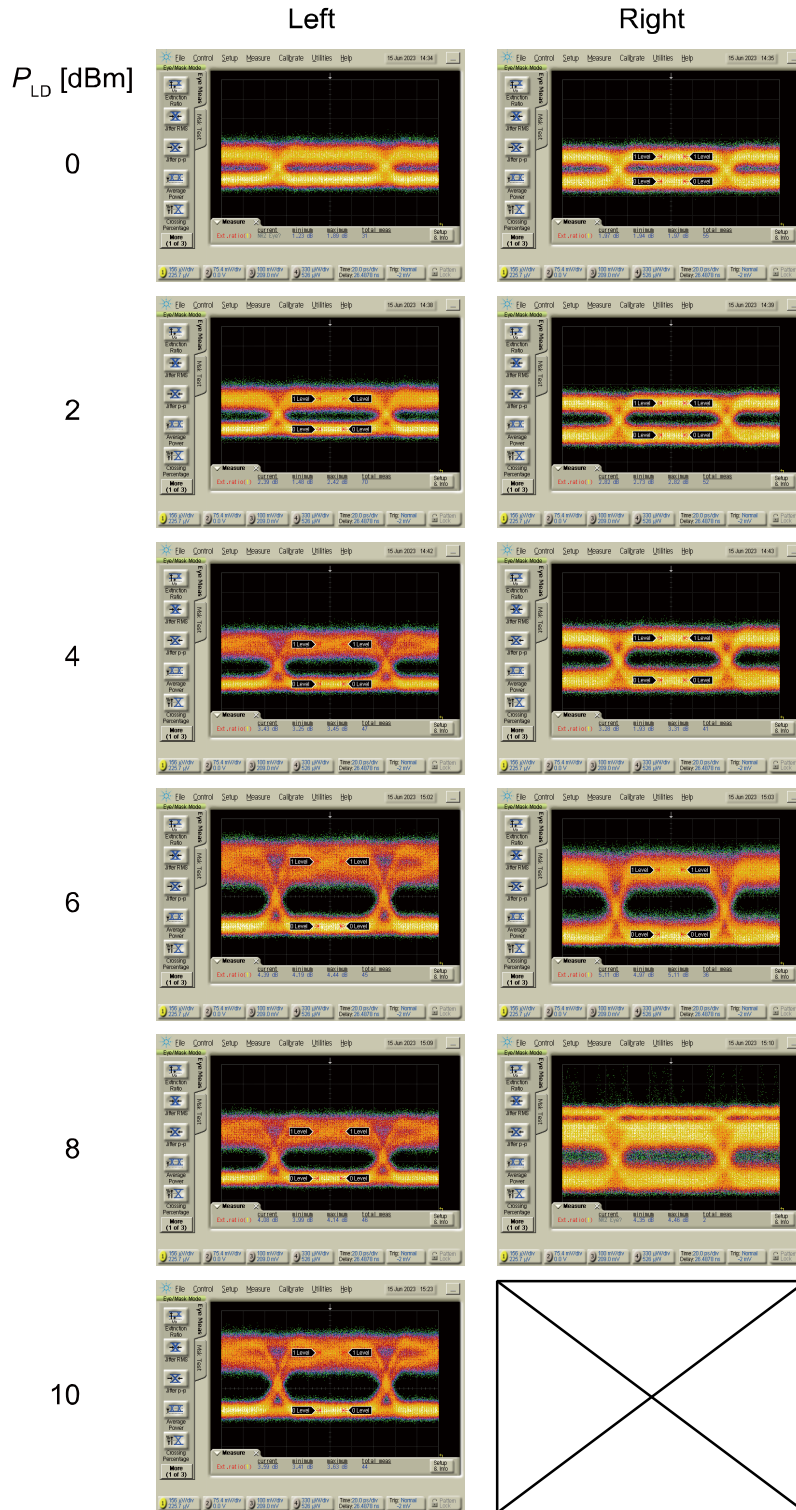
Figure 3-41 Eye pattern corresponding to each data point in Fig. 3-39(b).
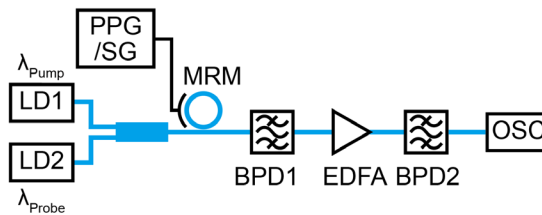
Fig.3-42 Experimental system modulated by pump and probe light.
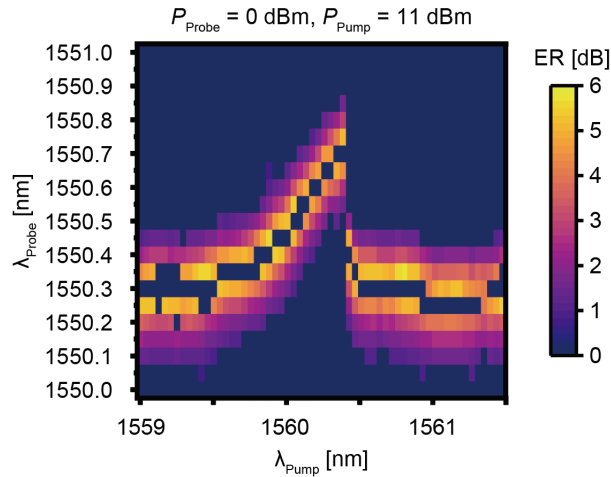
Figure 3-43 ER measurement results when modulated with a 10 Gbps PRBS signal.
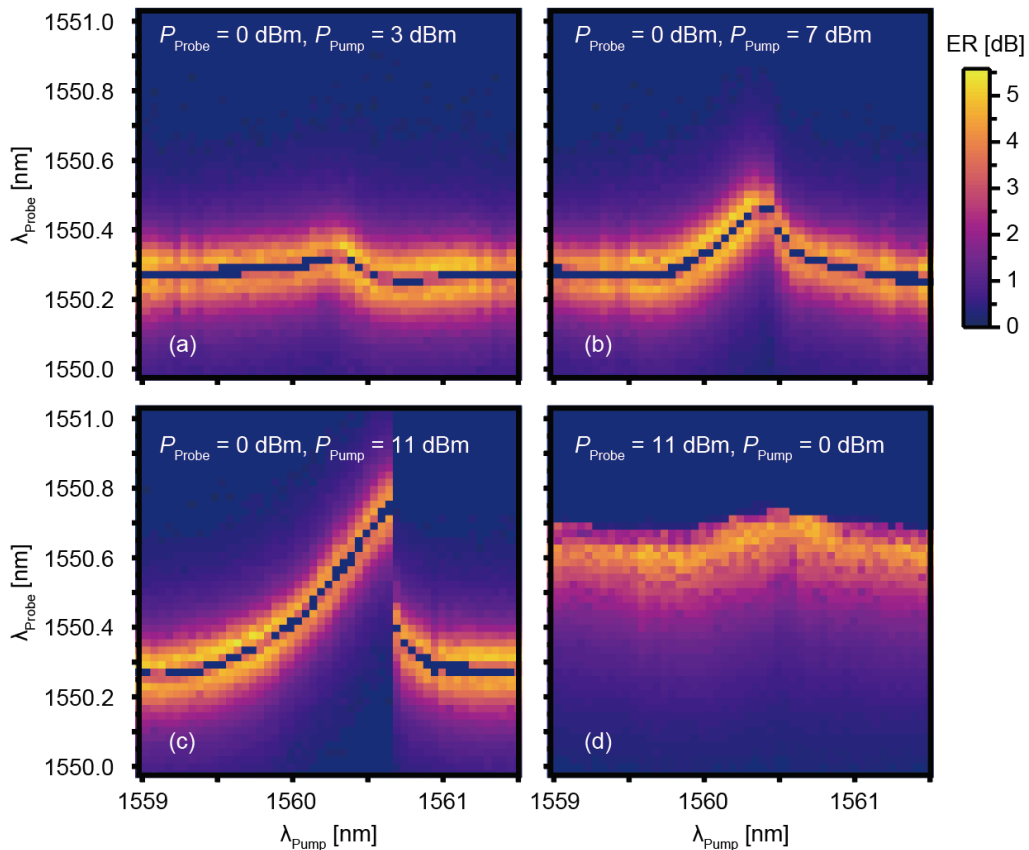
Figure 3-44 Results of modulation with an electrical signal at 2 GHz, 10 dBm RF power, -2 V_{Bias}. (a)~(d): Results measured using probe and pump light with different powers.

3.9 Summary

In this chapter, we first gave a comprehensive guide to the theoretical foundations of microring modulators, covering essential parameters and their interrelationships. Then, we provided a comprehensive exploration of the design considerations for the microring modulator, covering theoretical calculations, simulations, and practical design implementations. Here, we designed a microring modulator capable of achieving critical coupling and devised various parameter sets, including doping position, coupling gap, and coupling length, for fabrication. After fabrication of the microring modulator by foundry, we firstly conducted fundamental optical

measurements, revealing an FSR of approximately 10 nm and a Q value of around 4000. Subsequently, we extracted optical parameters such as intra-ring loss and coupling coefficient from the microring modulator's transmission spectrum, and these values closely matched the design specifications. We also examined the voltammetric characteristics and thermal tuning performance of the TiN electrical heater integrated above the microring. The electrical heater demonstrated effective thermal tuning with a comparable FSR.

Further investigations delved into the static/dynamic modulation performance of three microring modulators positioned closest to critical coupling condition. We explored the microring modulator's equivalent circuit parameters, electrical frequency response concerning the RC time constant, optical frequency response concerning the Q value, and opto-electronic frequency response (S21 parameter) considering both. Remarkably, high-speed modulation up to 32 Gbps was achieved. Finally, we discuss the self-heating phenomenon observed in the microring during high-power optical input and its impact on modulation. These discussions pave the way for potential applications, such as electromagnetic wave imaging using arrays of MRM, which will described from next chapter.

Reference

[3-1] J. E. Heebner, V. Wong, A. Schweinsberg, R. W. Boyd, and D. J. Jackson, "Optical transmission characteristics of fiber ring resonators," *IEEE Journal of Quantum Electronics*, vol. 40, no. 6, pp. 726–730, Jun. 2004, doi: 10.1109/JQE.2004.828232.

[3-2] W. R. McKinnon, D.-X. Xu, C. Storey, E. Post, A. Densmore, A. Delâge, P. Waldron, J. H. Schmid, and S. Janz, "Extracting coupling and loss coefficients from a ring resonator," *Opt. Express*, vol. 17, no. 21, pp. 18971–18982, Oct. 2009, doi: 10.1364/OE.17.018971.

[3-3] M. Pantouvaki, S. A. Srinivasan, Y. Ban, P. D. Heyn, P. Verheyen, G. Lepage, H. Chen, J. D. Coster, N. Golshani, S. Balakrishnan, P. Absil, and J. V. Campenhout, "Active Components for 50 Gb/s NRZ-OOK Optical Interconnects in a Silicon Photonics Platform," *J. Lightwave Technol.*, vol. 35, no. 4, pp. 631–638, Feb. 2017.

[3-4] S. Karimelahi and A. Sheikholeslami, "Ring modulator small-signal response analysis based on pole-zero representation," *Opt. Express*, vol. 24, no. 7, pp. 7585–7599, Apr. 2016, doi: 10.1364/OE.24.007585.

[3-5] Y. Zhang, H. Zhang, J. Zhang, J. Liu, L. Wang, D. Chen, N. Chi, X. Xiao, and S. Yu, "240 Gb/s optical transmission based on an ultrafast silicon microring modulator," *Photon. Res.*, vol. 10, no. 4, pp. 1127–1133, Apr. 2022, doi: 10.1364/PRJ.441791.

[3-6] H. Yu, D. Ying, M. Pantouvaki, J. V. Campenhout, P. Absil, Y. Hao, J. Yang, and X. Jiang, "Trade-off between optical modulation amplitude and modulation bandwidth of silicon micro-ring modulators," *Opt. Express*, vol. 22, no. 12, pp. 15178–15189, Jun. 2014, doi: 10.1364/OE.22.015178.

[3-7] X. Xiao, H. Xu, X. Li, Y. Hu, K. Xiong, Z. Li, T. Chu, Y. Yu, and J. Yu, "25 Gbit/s silicon microring modulator based on misalignment-tolerant interleaved PN junctions," *Opt. Express*, vol. 20, no. 3, pp. 2507–2515, Jan. 2012, doi: 10.1364/OE.20.002507.

[3-8] Y. Hu, X. Xiao, H. Xu, X. Li, K. Xiong, Z. Li, T. Chu, Y. Yu, and J. Yu, "High-speed silicon modulator based on cascaded microring resonators," *Opt. Express*, vol. 20, no. 14, pp. 15079–15085, Jul. 2012, doi: 10.1364/OE.20.015079.

[3-9] M. Shin, Y. Ban, B.-M. Yu, M.-H. Kim, J. Rhim, L. Zimmermann, and W.-Y. Choi, "A Linear Equivalent Circuit Model for Depletion-Type Silicon Microring Modulators," *IEEE Transactions on Electron Devices*, vol. 64, no. 3, pp. 1140–1145, 2017, doi: 10.1109/TED.2017.2648861.

[3-10] J. Rhim, Y. Ban, B.-M. Yu, J.-M. Lee, and W.-Y. Choi, "Verilog-A behavioral model for resonance-modulated silicon micro-ring modulator," *Opt. Express*, vol. 23, no. 7, pp. 8762–8772, Apr. 2015, doi: 10.1364/OE.23.008762.

[3-11] G. Li, X. Zheng, J. Yao, H. Thacker, I. Shubin, Y. Luo, K. Raj, J. E. Cunningham, and A. V. Krishnamoorthy, "25Gb/s 1V-driving CMOS ring modulator with integrated thermal tuning," *Opt. Express*, vol. 19, no. 21, pp. 20435–20443, Oct. 2011, doi: 10.1364/OE.19.020435.

[3-12] M. J. Shin, Y. Ban, B.-M. Yu, J. Rhim, L. Zimmermann, and W.-Y. Choi, "Parametric Characterization of Self-Heating in Depletion-Type Si Micro-Ring Modulators," *IEEE Journal of Selected Topics in Quantum Electronics*, vol. 22, no. 6, pp. 116–122, 2016, doi: 10.1109/JSTQE.2016.2560149.

Chapter 4
Electromagnetic Wave Imaging

4.1 Overview

As mentioned in Chapter 1, the MRM we designed can be used for electromagnetic (EM) wave visualization. In this chapter, we first introduce the microring modulator array and the packaged module. Then, we utilize the RoF module for EM wave imaging. We employ non-resonant slot antenna arrays as probes for detecting Sub 6 GHz band EM waves, connecting them to the individual MRMs of the RoF module via high-frequency compatible wires. By altering the relative distance and position between the transmitting antenna and the receiving antenna probe, we can measure the intensity of the EM wave at different locations. By calibrating the signal power detected by different antenna probes at the same location, we can stitch multiple small-scale imaging results into a larger-scale imaging result. We compare the electromagnetic wave imaging results for both co-polarization and cross-polarization directions, and evaluate the achievable dynamic range and cross-polarization discrimination[4-1]. Finally, we provide an outlook on electromagnetic wave imaging systems for millimeter waves.

4.2 MRM Array Device

In Fig. 4-1(a), we design and fabricated an MRM array by simultaneously integrating eight MRMs near the same bus waveguide. The spacing between two neighboring MRMs is 200 μm. We employed an MRM array with an SSC tip width of 160 nm, selecting an MRM array corresponding to R12 in the previous chapter, i.e., the second red box in Fig. 3-8(a), positioned in the upper right corner to achieve maximum modulation depth and modulation efficiency. Electrically, we connected the chip, fixed on the aluminum board, to a custom PCB board (FR4) as depicted in Fig. 4-1(b). For wire bonding, the length of the wires conducting DC power on top is not limited, while the wires on the bottom, conducting RF signals, need to be as short as possible to minimize transmission losses. However, this PCB in this research is suitable only for signal transmission at several GHz. For the connection from the PCB to the signal source, we used an RF connector (X.FL) and RF wire (X.FL-LP-040) from Hirose Electric, and RF adapter (SMA-XFLI adapter HRMP-X.FLJ), as shown in Fig. (c). For optical input and output, we utilized two core-shrunk polarization-maintaining fibers connected by a fiber block and bonded with ultraviolet curable resin. An FC/APC connector was used at the end of the fiber. We call the entire module as a RoF module. Additionally, we compared the size of the entire module to a 10-yen coin. The module's size is primarily limited by its electrical connection, and the footprint of the microring modulator array is also constrained by the electrical pad. Figure (d) presents the overall transmission spectrum of the MRM array. The resonance wavelengths of the eight MRMs overlap within a 2 nm range due to the identical design. However, individual resonance wavelengths can vary due to fabrication errors. This variability is not critical in this study since we only need to tune the resonance wavelength of one of the MRMs to the vicinity of the laser source wavelength at a time, and this tuning range is larger than the resonance wavelength difference due to fabrication error. The optical transmission spectrum when one of the MRMs in the MRM array is thermally tuned to the vicinity of the wavelength of the light source is illustrated in Fig.4-2 (d). The transmission measurement setup is shown in Fig. 4-2.
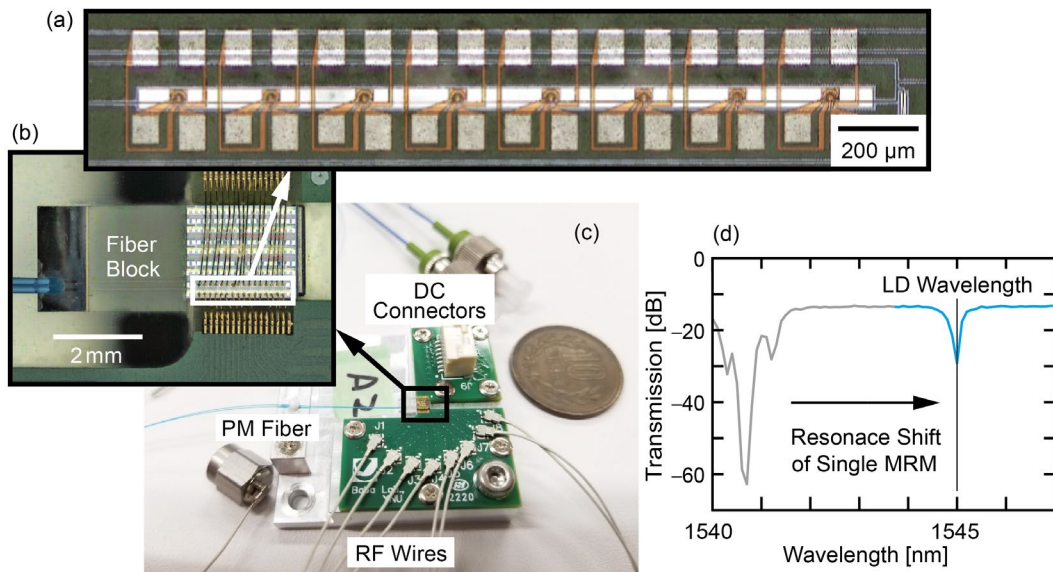
Figure 4-1 Photograph of (a) MRM array, (b) electrical bonded device with optical connection via fiber and (c) packaged module. (d) Optical spectrum of MRM array with one MRM thermally tuned.
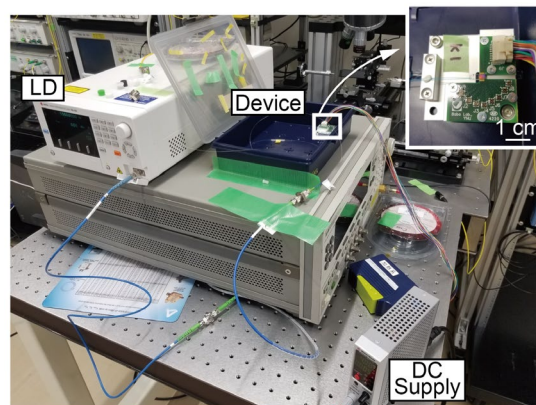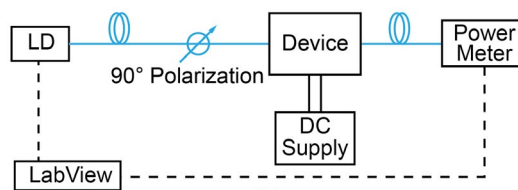
Figure 4-2 (a) Photo and (b) model of measurement setup for optical transmission.

4.3 Imaging of RF Waves

4.3.1 Measurement Setup and Calibration

Figures 4-3 and 4-4 depict the measurement setup of the electromagnetic wave imaging system implemented using the aforementioned RoF module. As shown at the far right of Fig. 4-3, a well-characterized RoF module was employed for the experiment. Its DC connector is connected to eight external DC voltage sources through a DC cable, as shown at the top of Fig. 4-4. Communication between each DC source was achieved using a GP-M Cable. The communication input of the leftmost DC source was connected to a computer and converted to the communication protocol via a USB to COM port converter and a COM to GP-M converter.
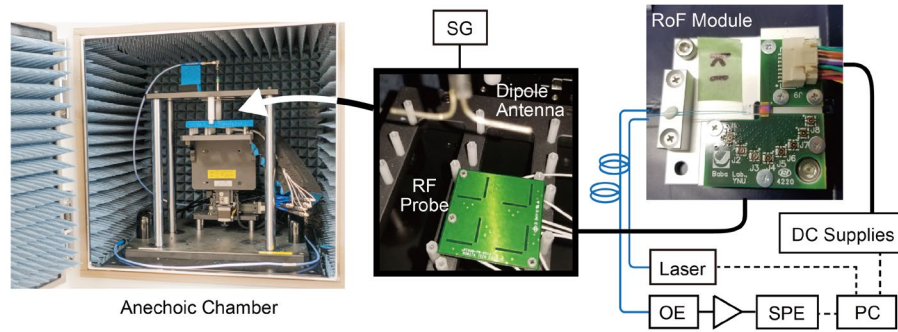
Figure 4-3 Experimental set up for EM wave visualization.
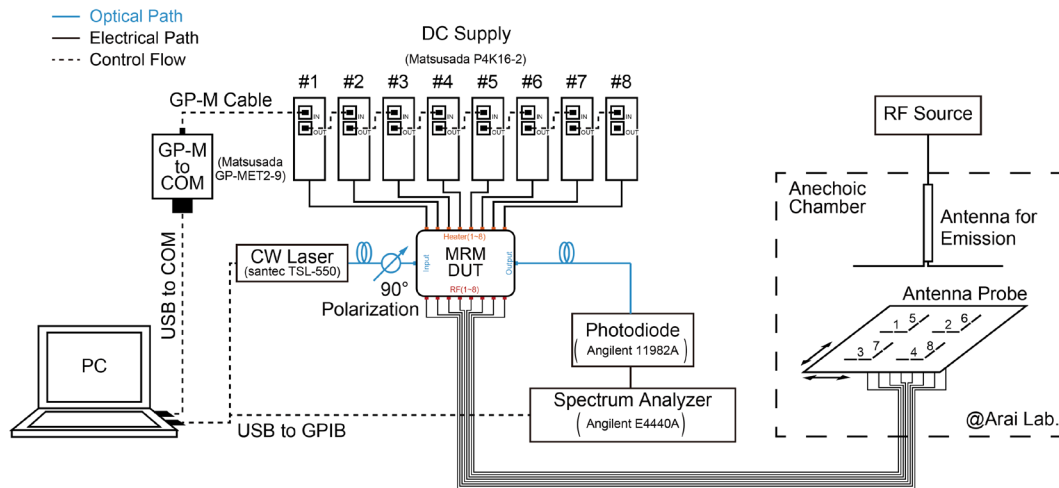
Figure 4-4 Detailed measurement setup.

LabVIEW was used on the computer to control the output of the DC supply.

For RF signals, an RF cable was used to input the signals from the RF Probe directly into the module without using additional Bias Tee, etc., to load the bias voltage. The RF Probe, shown in the middle diagram of Fig. 4-3, was provided by Arai Lab. in our university and consisted of four sets of non-resonant slot antennas. Each set contained two antennas perpendicular to each other to detect electromagnetic waves with polarization directions perpendicular to each other. The RF probe was placed on a three-axis table, and its position could be adjusted arbitrarily. Five centimeters above this RF Probe, another dipole antenna was set vertically downward for transmitting electromagnetic waves. It was connected to a signal generator as a signal source, and the relative position of this dipole antenna to the RF probe could be changed. To minimize the effect of reflected waves from the environment, the entire device was placed inside a small anechoic chamber, and the electrical cable was wrapped as much as possible with a plastic sponge block, as shown in the leftmost part of Fig. 4-3.

For optical connection, a wavelength adjustable continuous wave (CW) laser served as the light source. A 90° polarization rotate fiber was then connected to satisfy best transmission. The output light was detected by a photodiode with a pre-amplifier, converting it to an RF signal. The output RF signal was directly connected to an electrical spectral analyzer, which could be replaced by an RF power meter since the RF signal used in this study is a simple sine wave signal.

Figures 4-5 illustrate some detailed photos of the measurement setup. Figure (a) is a photograph of the entire experimental environment, located in the Arai lab. (b), on the other hand, is a photograph of the RoF module and its electrical connections. (c)(d)(e) show the three types of dipole antenna placement: x-direction, y-direction, and z-direction. Since z-direction

Figure 4-5 Detailed photos of measurement setup. (a) Entail setup. (b) RoF module and its electrical connection with RF probe. (c) x-direction, (d) y-direction and (e) z-direction placement of dipole antenna. Changing the relative position between the dipole antenna and RF probe by moving (f) RF probe and (g) dipole antenna.

placement does not provide a measurement of the forward EM wave field of the dipole antenna, this approach is not considered here. For actual measurements, we used the x direction, the y direction, and the 45° angle direction (oblique) in between. (f) and (g) show two ways to change the relative position between the dipole antenna and the RF probe: moving the RF probe and moving the dipole antenna. The difference between the two is that moving the RF probe in this way distorts or displaces the wires underneath the RF probe, and measurements are particularly sensitive to the state of these wires. This method may yield undesirable visualization results. Therefore, in this study, we used the moving method as shown in Fig. 4-5 (g).

The experiment's logic is as follows: first, we fix the relative positions and orientations of the dipole antenna and the RF probe. Second, we turn on all machine power supplies, including the SG and the LD, and fix the LD optical wavelengths to the long wavelength side of the resonance wavelengths at 2-4 nm. We need to tune the resonance wavelength of each MRM to the neighborhood of the LD optical wavelength in turn. Next, we turn on the eight DC power sources and make the output voltage of each source scan according to the timing diagram shown in Fig. 4-6. The output voltage of each voltage source is around 3 V and varies with the MRM. Specific voltage values are discussed subsequently. While each voltage was held high, we simultaneously recorded the peak output of the electrical spectral analyzer at that point. Therefore, a total of eight RF output powers were recorded during the period when eight voltage sources were high. They correspond to the power detected by each RF probe at the current antenna position.

Next, we adjust the relative position between antennas and repeat the above operation. The relative position adjustment between antennas is shown in Fig. 4-7. Figure (a) illustrates the moving range of the RF probe. The distance between two neighboring antenna pairs in the RF probe is 18.75 mm. We initially attempted a rather rough measurement, setting the moving distance of the RF probe to 18.75 mm as well, allowing it to move in a way that different antenna pairs would have a chance to make measurements at the same location. The advantage of this is that it is simple to measure the electromagnetic field strength at the same place. However, the disadvantage is that only $3 \times 3 = 9$ data points can be measured, which is too coarse for electromagnetic wave imaging. We ultimately used a travel distance of 1.875 mm, as shown in Figs. 4-7 (b) and 4-8 (a). In Fig. 4-7 (b), the dots of different colors correspond to the individual antenna pairs in Fig. 4-7 (a). Similarly, different antenna pairs can detect the electromagnetic waves at the same location, as shown at the intersection of the individual colors in Fig. 4-7 (b). For the intersection of red and yellow, we use the red data points as a baseline and calculate the average of this column of data and simultaneously calculate the average of the yellow data points at the same location. We then add the difference of these two averages to all the yellow data points so that the averages of the data points at the intersection are consistent. Similarly, for the red and green sections, we normalize the mean of the green and red data points using the mean difference correction method. For the blue section, we averaged the means of the intersections of the corrected yellow and green sections with the blue section, respectively. We differenced them with the mean of the sum of the left-most column and the top row of the blue section and added them to the entire blue data points. This gives us a $21 \times 21 = 441$ matrix of data points. This process is also shown in Figs. 4-8(b)(c).

However, the location of the dipole antenna above needs to be determined. In this case, we positioned the dipole antenna directly above the 3 positions A, B, C in Fig. 4-7(a). This approach allows us to further extend our measured matrix of 441 data points. As depicted in Fig. 4-9, we averaged all the data points in the overlapped part and replaced the original data, resulting in a visualized image formed by the misaligned overlapping of 3 square regions with a side length of 37.5 mm. It has an area of 3515 mm². While it is possible to achieve imaging of the complete large square region with a side length of $37.5 \times 2 = 75$ mm by placing the dipole antenna at the

other two diagonal points, for this study, the region shown in Fig. 4-9 contains enough information, so we ended up imaging only such a region.

Finally, it is essential to rotate the orientation of the dipole antenna to enable imaging of EM waves with different polarization directions. In this study, three orientations—parallel, perpendicular, and at a 45-degree angle to the two polarization directions of the slot antenna in the RF probe—were utilized for measurement. As depicted in Fig. 4-10, each column of illustrations employs a different relative position of the dipole antenna and the RF probe (top left, middle, and bottom right), while each row of illustrations adopts a different orientation of the dipole antenna. The adjustment of these three relative positions and antenna orientations is performed manually.
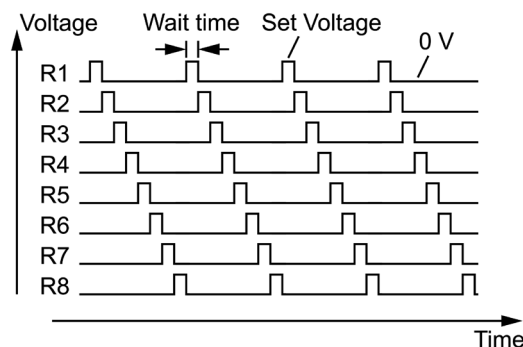
Figure 4-6 Output timing diagram for each voltage source.
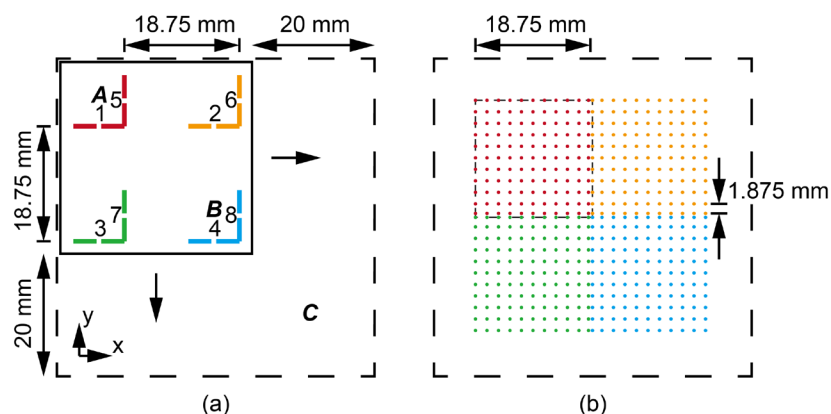
Figure 4-7 (a) Antenna probes and their movable range (dashed lines). The distance between the four antenna probe pairs (two polarization directions) is 18.75 mm, and the antenna probes can be moved an additional 20 mm in the horizontal plane. (b) Measurement points for each antenna when the antenna probes are moved at 1.875 mm intervals.
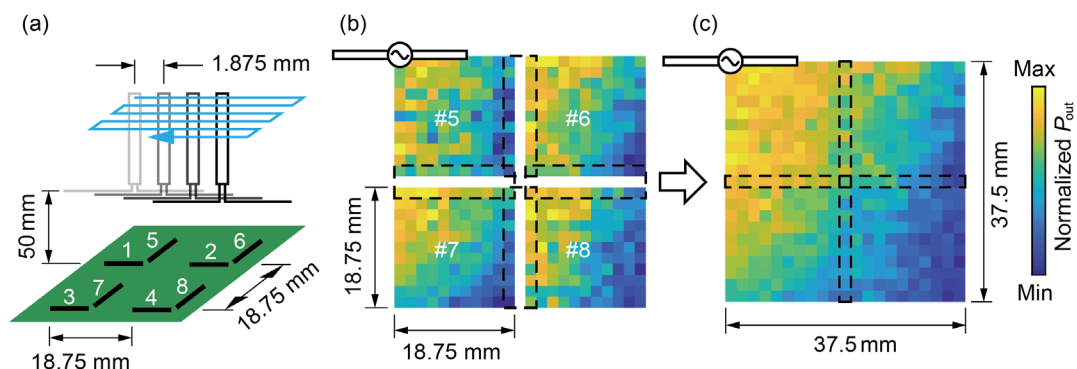
Figure 4-8. (a) Relative moving of dipole antenna and RF probe. (b) A sample of obtained colormap of RF power by different antennas in the same polarization direction. (c) Calibrated colormap with larger area by combining four results of (b).

103
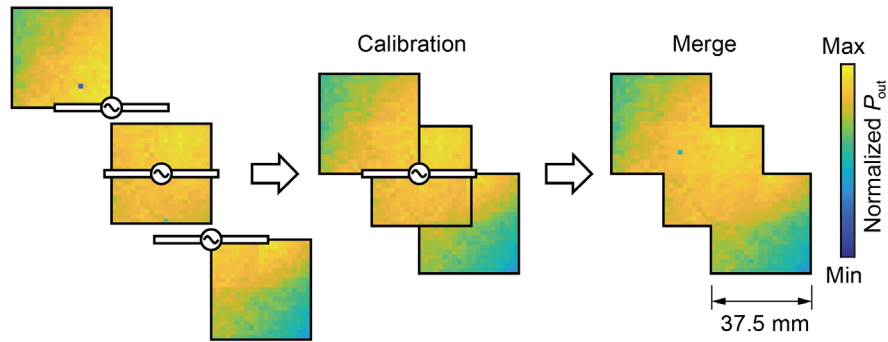
Figure 4-9. Calibration of three colormaps with dipole antenna placed at different locations.

We developed the LabVIEW program used to control the system. The front panel of this program is shown in Fig. 4-11. The main functions performed by this program are:

1. Initialization. Adjust the magnitude of the voltage applied to each MRM so that the microring is just thermally tuned to the point of maximum modulation efficiency. This requires scanning each MRM over a range of voltages and simultaneously recording the RF output power. When the program detects a peak in the RF output power as the input voltage changes and the RF power continues to remain reduced as the voltage continues to be increased, that RF peak is recorded, and the voltage at which the peak was achieved is saved. The initialization of the program is completed when this operation is performed on all the voltage sources of the MRM.

2. RF intensity scan. Using the voltage values described above, all voltage sources are scanned sequentially in the time sequence shown in Fig. 4-6. Record the RF power value while scanning and save it to the specified folder.

3. Antenna position adjustment. When the scanning of the 8 voltage sources is completed, the relative position between the dipole antenna and the RF probe needs to be changed, as shown in Fig. 4-7. This can be accomplished by a dedicated software of movable stage. The movable stage does not provide a GPIB interface, only a USB interface, but the command line used is not available. Nevertheless, full automation was achieved by embedding a program in LabVIEW that simulates mouse movements and clicks. The LabVIEW program will automatically click on the move button in the dedicated software of the movable stage after the voltage scan is finished and the data is saved, causing the stage to move in steps of 1.875 mm spacing. The move trajectory is shown in Fig. 4-8(a).

The resulting dataset will be manually calibrated, merged, and colored. Unfortunately, the program was lost due to a hard drive corruption on the lab computer. By utilizing this program, we visualized power attribution of electromagnetic wave as described in next section.
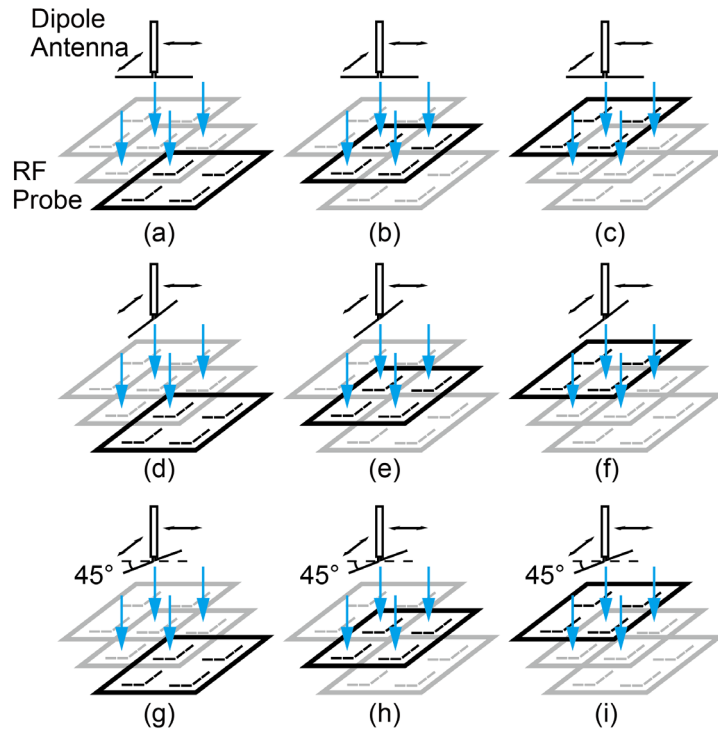
Figure 4-10 Placement of dipole antenna and RF probe. Rows: direction of dipole antenna varies. Columns: position of dipole antenna varies.
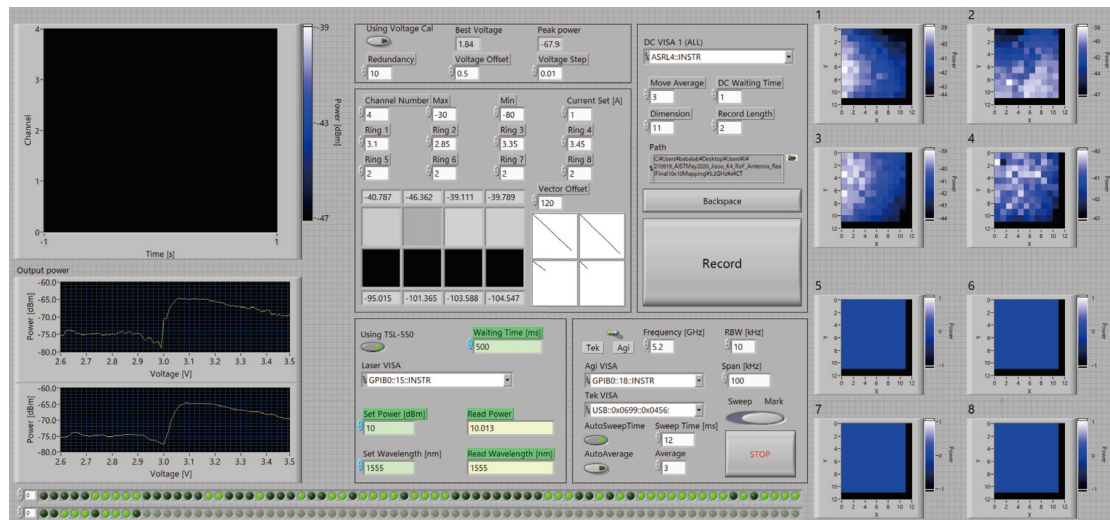
Figure 4-11 Front panel of LabVIEW program for automatic electromagnetic wave visualization.

4.3.2 Imaging Result

The experimental system illustrated in Fig. 4-4 was employed for the measurements. The laser power is 10 dBm, the laser wavelength is fixed at 1555 nm, and the optical insertion loss of the MRM module is 8 dB. A 3.5 GHz RF sine wave signal is output from the RF source (signal generator, SG), and the power is set to 15 dBm. The total loss of the antennas (dipole antenna and RF probe) is approximately 40 dB (directly faced and co-polarization case). Figures 4-12 to 4-14 depict the RF power detected by the MRM array under each condition. The top row displays the measurement results of MRM and slot antenna sets 1~4, and the bottom row showcases the measurement results of 5~8, respectively. The first row of each shows the distribution diagram when the antennas are equivalently placed at the upper left of the measurement range (first row in Fig. 4-10), the center (second row in

Fig. 4-10), and the lower right (third row in Fig. 4-10). Figures 4-12, 4-13, and 4-14 exhibit the results of measurements with the radiating antenna positioned horizontally (first row in Fig. 4-10), vertically (second row in Fig. 4-10), and diagonally (third row in Fig. 4-10), respectively. All results are normalized to the maximum detected power P_{max} in MRM-slot antenna sets 1~4 and 5~8. The display range is set from $P_{max} - 20$ to P_{max}.

The results of measurements with the slot antennas perpendicular to the radiating antenna reveal that when the radiating antenna (slot antenna) is positioned at the upper left (lower right), the values measured at each slot antenna distinctly decrease from the upper left (lower right) to the lower right (upper left). When the antenna is placed at the center, an almost uniform distribution is observed. On the other hand, the RF power detected by the slot antenna, which is parallel to the radiating antenna, appears to be significantly smaller than the vertical case (the difference in detected power is more than 10 dB). Therefore, the cross-polarization discrimination (XPD) of the antenna probe can be estimated to be about 10 dB. The diagonal results show that the slot antennas 1~4 are about 6 dB lower than 5~8, but the slot antennas in each direction measure a similar electromagnetic wave distribution.
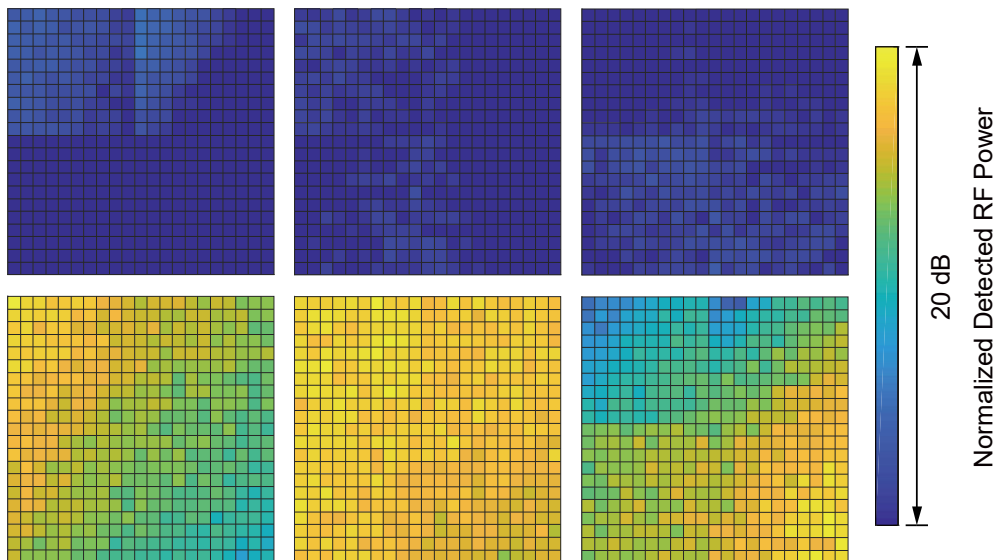
Figure 4-12. Mapping results of the power detected by the antenna probes for the 3.5 GHz input RF signal. The top row illustrates the power detected by MRM-slot antenna sets 1~4, while the bottom row showcases the power detected by sets 5~8. The left, middle, and right columns correspond to when the antennas for **horizontal** direction are placed in the upper left, middle, and lower right of the measurement range, respectively.
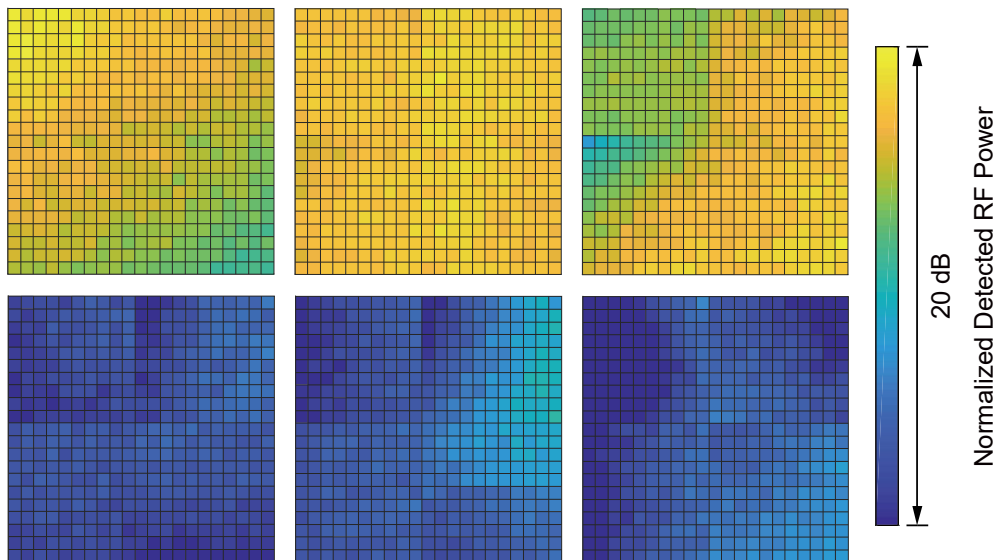
Figure 4-13. Mapping results of the power detected by the antenna probes for the 3.5 GHz input RF signal. The top row illustrates the power detected by MRM-slot antenna sets 1~4, while the bottom row showcases the power detected by sets 5~8. The left, middle, and right columns correspond to when the antennas for **vertical** direction are placed in the upper left, middle, and lower right of the measurement range, respectively.
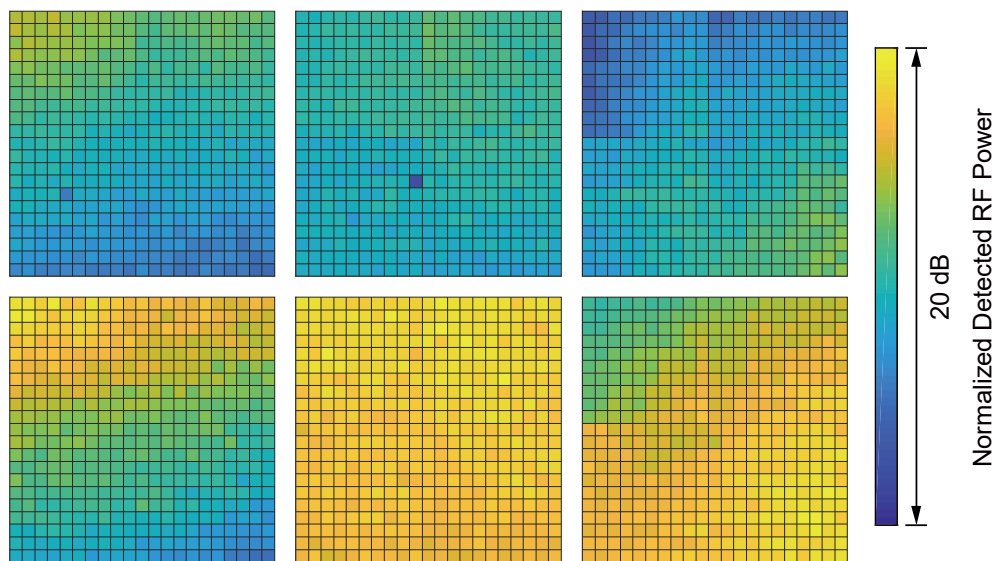
Figure 4-14. Mapping results of the power detected by the antenna probes for the 3.5 GHz input RF signal. The top row illustrates the power detected by MRM-slot antenna sets 1~4, while the bottom row showcases the power detected by sets 5~8. The left, middle, and right columns correspond to when the antennas for **oblique** direction are placed in the upper left, middle, and lower right of the measurement range, respectively.
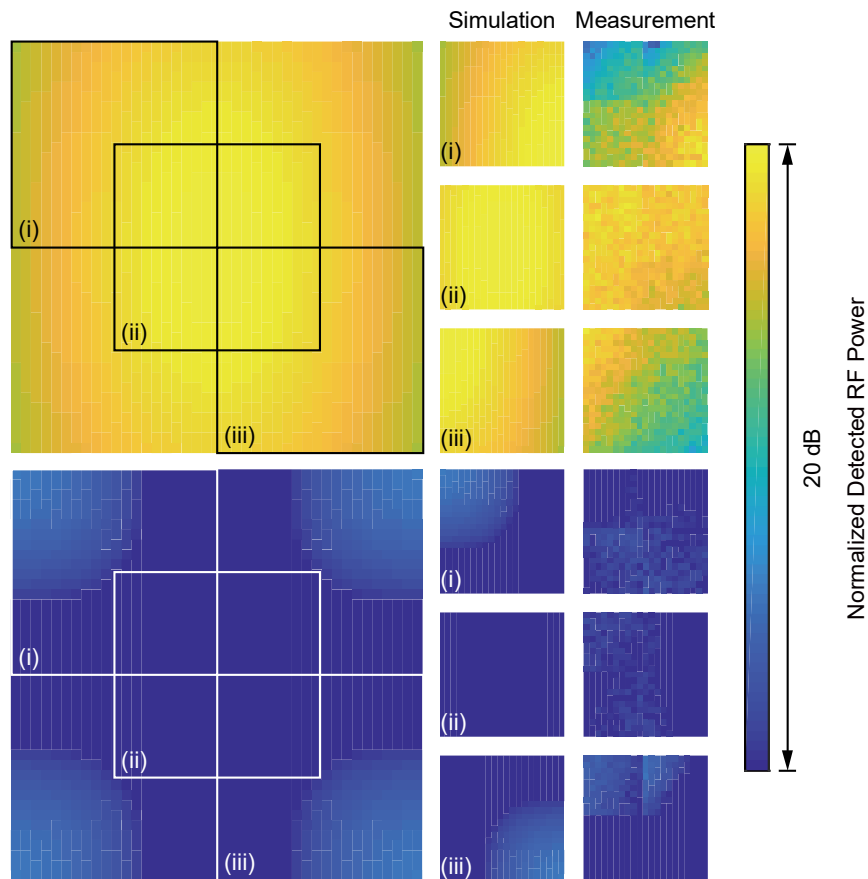
Figure 4-15. Comparison of simulated and measured power detected by the antenna probe for a **horizontally** oriented radiating antenna (top and bottom rows represent the co-polarization and cross-polarization). The distributions in the upper left, center, and lower right (i, ii, and iii) correspond to the actual measurements with the radiating antenna in the lower right, center, and upper left, respectively.

The measurement results were compared with simulation results provided by Mr. Mitsui and Mr. Sugaya of Arai Laboratory. Figures 4-15 to 4-17 correspond to the cases when the radiating antenna is oriented horizontally, vertically, and diagonally, respectively. The simulation area is four times larger than the actual measurement area, and the distributions (i, ii, iii) in the upper left, center, and lower right of the simulation results correspond to the actual measurements with the dipole antenna in the lower right, center, and upper left of the measurement area, respectively. The vertical distance between the radiating antenna and the measurement plane is 5 cm, as in the actual measurement.

Since the radiating antenna is a dipole antenna, the near-field distribution in a plane has an elliptical shape, with the long axis direction perpendicular to the dipole antenna. This phenomenon was also observed in the measurement results. However, the actual measurement results showed a larger power variation (maximum value − minimum value) than the simulation results within the same measurement range. This is considered to be due to reflections inside the anechoic chamber and effects from cables. On the other hand, the simulation results for cross-polarization show a distribution in which the power in the square is larger than the center, but the power is about 20 dB lower than the power in the same polarization direction, making it difficult to correspond to the actual measurement results.

Figure 4-18 presents the result of stitching Figs. 4-15~4-17 together, making it easier to observe the overall distribution. It is evident that for the same dipole antenna direction, the

measured EM wave distribution map shows similar results to the simulation calculation, with both indicating a more concentrated part of higher EM wave intensity. The achieved XPD is at least greater than 10 dB. For antennas with the same set of RF probes, the detected difference in the intensity of electromagnetic waves in different polarization directions can reach more than 20 dB, implying that the dynamic range achievable by the RF probes is greater than 20 dB.

Simultaneously, some less desirable characteristics are observed. In co-polarization, the experimental results exhibit more concentration than the simulation results, and the difference between the maximum and minimum values in the same region is larger than the simulation results. These discrepancies are attributed to reflections from the operating table, metal pillars, absorbing sponges, etc., and interference from the cable in the experimental environment. For orthogonal polarization results in Figs. 4-18 (a)(b), the influence from the environment is more pronounced due to the weaker intensity of the detected electromagnetic wave. Additionally, from the orthogonal polarization results (c), it is evident that the splicing between the small square areas is not smooth enough. This is primarily due to individual differences in the MRM and RF probe antennas. The already low detection power amplifies these differences, including optical loss variations in different MRMs, modulation efficiency, RF probe sensitivity, RF cable losses, etc. Using a more accurate calibration algorithm can help mitigate these differences. Figure 4-19 illustrates the one-dimensional results and compares them with the simulation results for each of the dashed line positions in Figure 4-18. It can be observed that the experimental results agree with the simulation results closely.

Figure 4-20 illustrates the system optical and electrical losses. Regarding the optical loss, the insertion loss (η_{opt}) of approximately 8 dB is primarily concentrated in the coupling part including the fiber block and the SSC. As for the electrical loss, it is mainly focused on the free-space propagation loss between the antennas and the equivalent loss caused by the modulation of the MRM. Here, the propagation loss of the antenna ($\eta_{antenna}$) is influenced by the antenna distance, relative position, and polarization direction. In this study, the antenna propagation loss ($\eta_{antenna}$) is measured as 40-60 dB when fixing the antenna distance at 5 cm and varying polarization directions and their relative positions (within the detection range of this study). Figure 4-20 (b) employs blue and red regions to indicate the propagation loss in the case of co-polarization and cross-polarization, where the overlap represents the maximum loss for co-polarization being less than the minimum loss for cross-polarization. It should be noted that these results are taken at different relative positions of the antenna. For the same relative position, the propagation loss of co-polarization always remains lower than that of cross-polarization.

As for the electrical propagation loss induced by the modulation of the MRM (η_{MRM}), it is related with the modulation efficiency of the MRM, optical loss, responsibility of PD, etc. The modulated optical power that reaches the PD can be written as $P_{opt} = \eta_{mod}\eta_{ope}\eta_{opt}P_{Laser}$, where η_{mod} is the modulation efficiency given as $\eta_{mod} = A\sqrt{R_{MRM}P_{in}}$ for the modulation slope efficiency A at the operating point in the units of V^{-1} and MRM's series resistance R_{MRM}, η_{ope} is the decrease in transmission at the operating point, η_{opt} is the optical transmission efficiency from the laser to the PD through the device excluding η_{ope}, and P_{Laser} is the laser output. The RF output from the PD is expressed as $P_{out} = \eta_{RF}(GR_{OE}P_{opt})^2 / Z_{RF}$, where η_{RF} is the RF transmission efficiency, G is the pre-amplification gain, R_{PD} is the PD responsivity in the unit of V/W, and Z_{RF} is the impedance of the RF line. Thus, P_{PD} is finally expressed in terms of total RF transmission efficiency η_{MRM} as

$$\eta_{MRM} = \frac{P_{out}}{P_{in}} = \frac{R_{MRM}\eta_{RF}(\eta_{ope}\eta_{opt}GR_{OE}AP_{Laser})^2}{Z_{RF}} \tag{4-1}$$

For the used MRM and set wavelength, we measured $R_{MRM} = 50\ \Omega$ from a converged slope of the current-voltage characteristics for a forward bias, and $A = 5\ \text{dB}/3\ \text{V}_{pp} = 0.32\ \text{V}^{-1}$ under

the zero-bias condition. We also assume $Z_{RF} = 50\ \Omega$, $\eta_{RF} \approx -1$ dB $= 0.8$, $\eta_{ope} \approx -3$ dB $= 0.5$, η_{opt} ≈ -8 dB $= 0.16$, $GR_{PD} = 300$ V/W, and $P_{Laser} = 10$ dBm $= 0.01$ W for the above experimental condition and used equipment. Then, we obtain $\eta_{MRM} = P_{out}/P_{in} = 0.005 = -23$ dB. To enhance η_{MRM}, we can try enhancing each parameter in the numerator in Eq. 4-1. A larger R_{MRM} is acceptable within the range that it does not severely degrade the operating bandwidth. Increasing the distance between the rib waveguide and highly doped regions, the spectral dip at the resonance will be sharper, and the slope efficiency A will also be increased. High η_{ope} will not be effective because η_{ope} and A are trade-offs. Whereas η_{RF} and η_{opt} should be reduced and P_{Laser} should be increased, a too high optical power will saturate the PD and suppress P_{out}, which is excluded from Eq. 4-1.
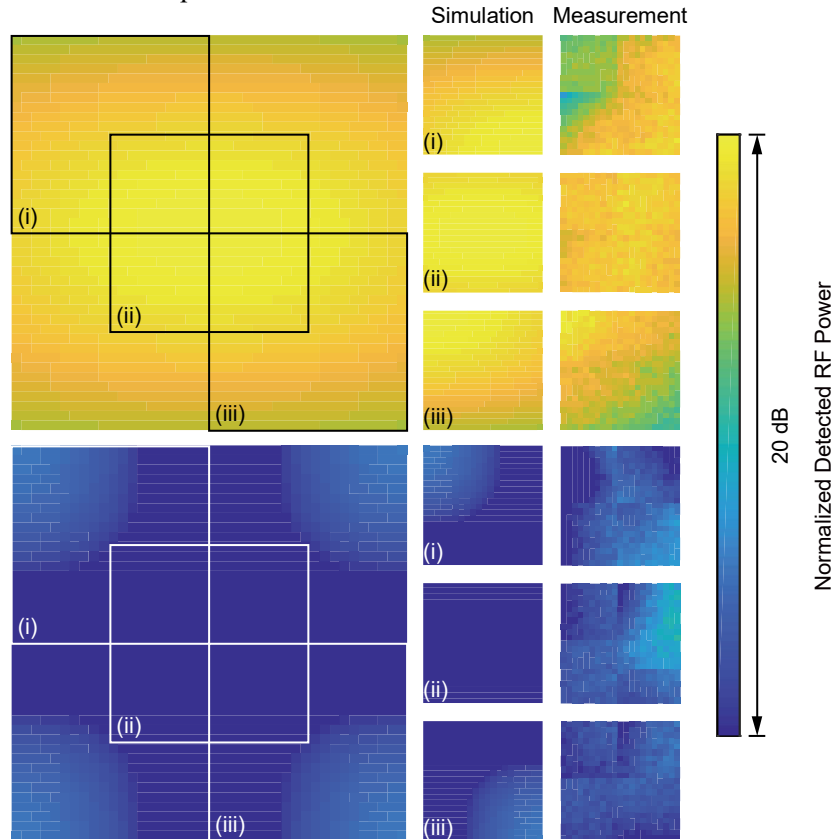
Figure 4-16. Comparison of simulated and measured power detected by the antenna probe for a **vertically** oriented radiating antenna (top and bottom rows represent the co-polarization and cross-polarization). The distributions in the upper left, center, and lower right (i, ii, and iii) correspond to the actual measurements with the radiating antenna in the lower right, center, and upper left, respectively.
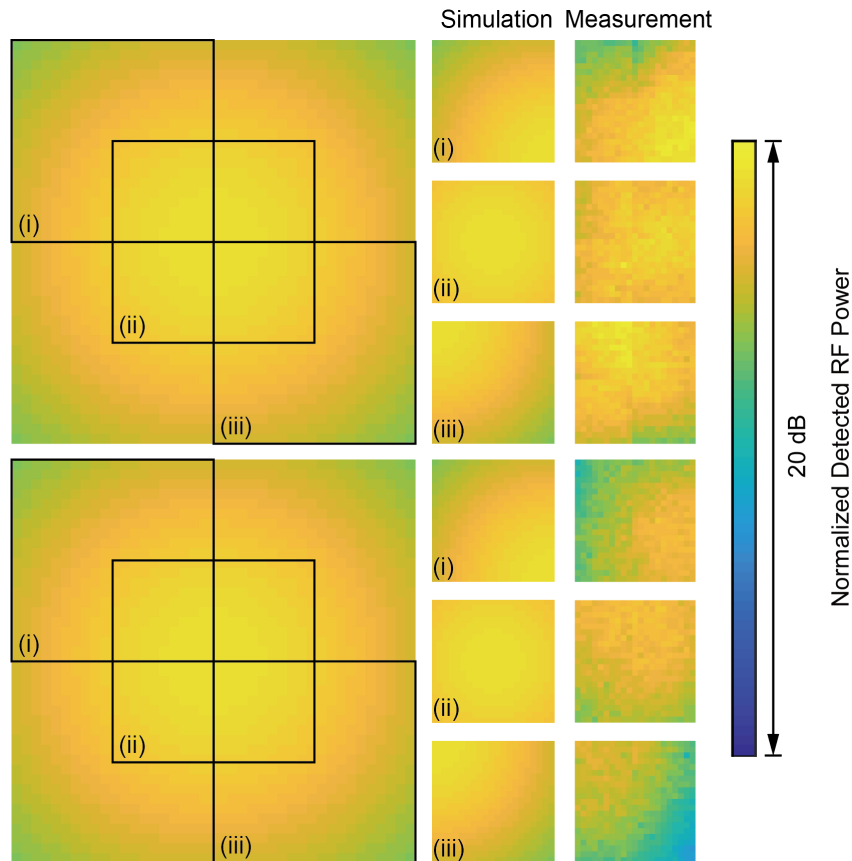
Figure 4-17. Comparison of simulated and measured power detected by the antenna probe for an **obliquely** oriented radiating antenna (top and bottom rows represent the co-polarization and cross-polarization). The distributions in the upper left, center, and lower right (i, ii, and iii) correspond to the actual measurements with the radiating antenna in the lower right, center, and upper left, respectively.

Furthermore, in the measured results, it is observed that the maximum point of RF power is often off the center of the measurement area. This is attributed to the manual alignment operation, as the dipole antenna above is not completely aligned to the center of the measurement area. The actual radiation characteristics of the dipole antenna may also be asymmetric due to fabrication errors. Additionally, the simulation calculations in this study were performed on the electromagnetic wave distribution in an ideal environment without considering interference such as reflection in the actual environment, leading to differences from the actual results. Nevertheless, this study serves as a proof-of-concept (POF) for the visualization of electromagnetic waves in RoF-based systems using MRM arrays, and the experimental results obtained are sufficient to verify the feasibility of the concept.

4.4   Toward Imaging of Millimeter Waves

As mentioned in the preceding sections, this study successfully achieves the visualization of the signal strength of electromagnetic waves at 3.5 GHz, validating the system's usability in the Sub 6 GHz band of the 5G standard. However, the concept remains applicable for millimeter waves (frequencies >30 GHz) that will be increasingly utilized in the future for 5G standards. Given that higher frequencies imply shorter wavelengths, our proposed EM wave imaging system can become more compact in the high-frequency domain.
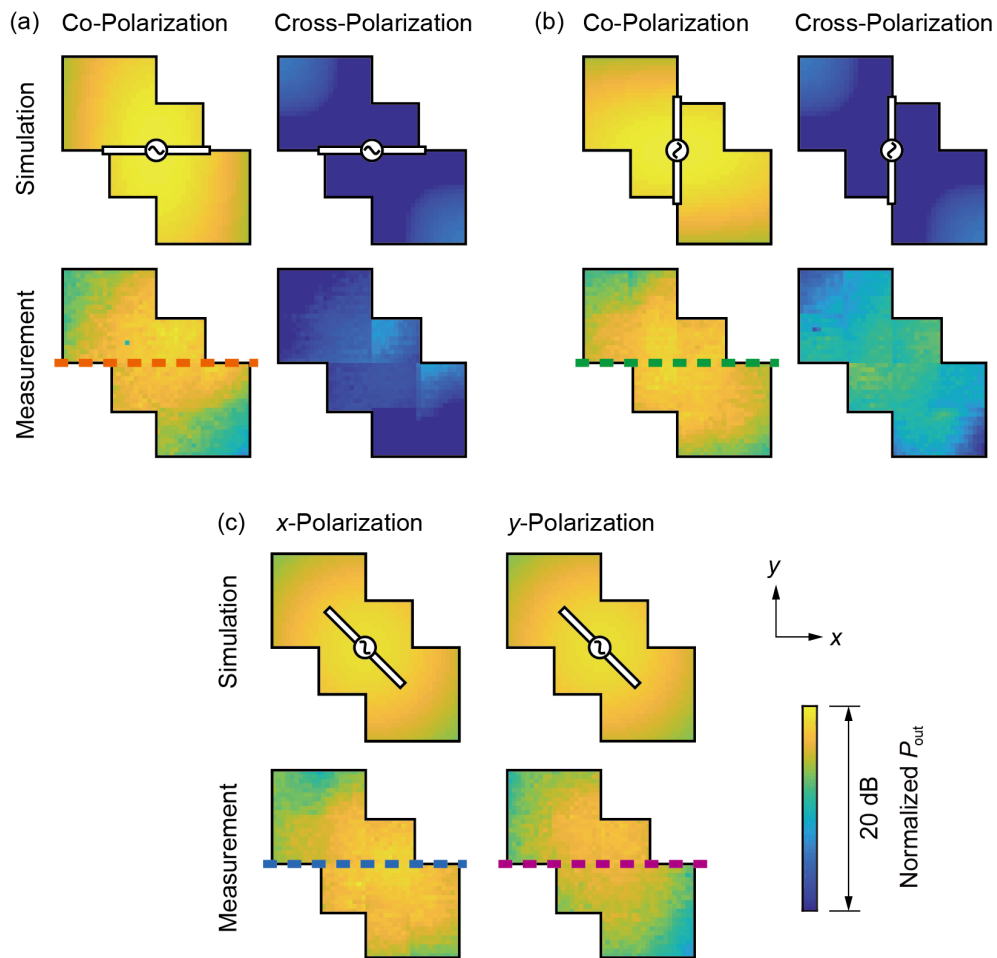
Figure 4-18 Merged visualization image results of Figs. 4-15 to 4-17. Panels (a), (b), and (c) correspond to the results when the dipole antenna is placed horizontally, vertically, and obliquely, respectively, as indicated by the antenna markers in the figures.
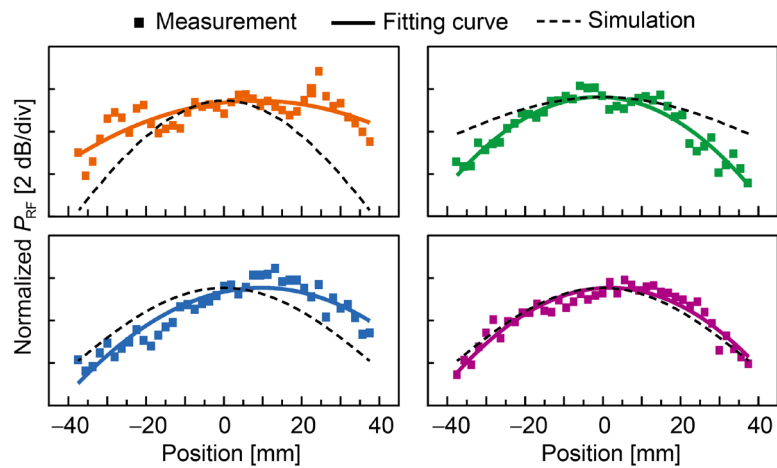
Figure 4-19. One-dimensional electromagnetic wave intensity distribution corresponds to the dashed portion of the results in Fig. 4-18.
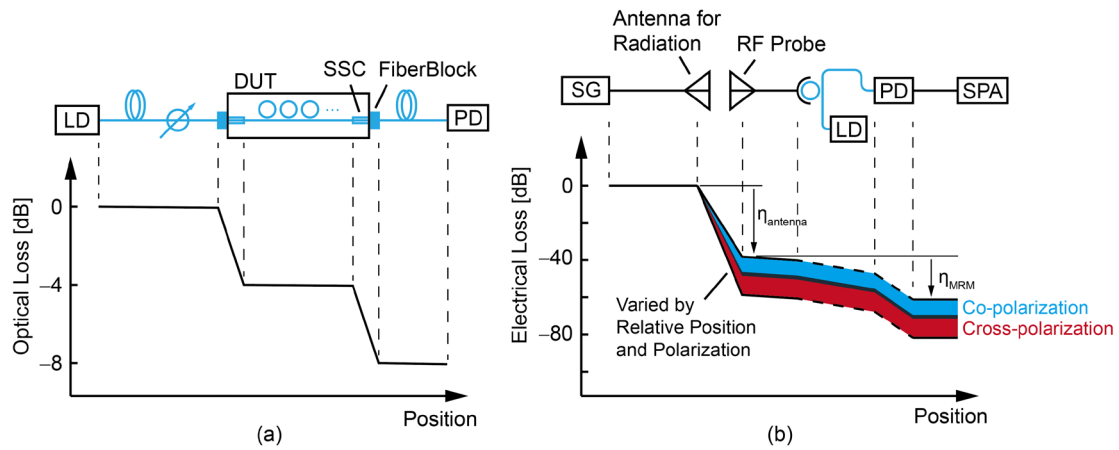
Figure 4-20 (a) Optical loss and (b) electrical loss at different positions in proposed system.

In this study, the antenna for detecting EM waves and the MRM for modulation are currently independent. However, for EM wave detection at higher frequencies, smaller antennas and shorter electrical signal transmission cables are needed. A millimeter wave antenna can be employed to detect millimeter wave signals, and a PCB suitable for millimeter wave signals can be used to packaging with the MRM. The MRM in this study can be directly used for millimeter wave modulation. Placing the antenna close to the MRM array chip allows RF signal transmission through very short high-frequency wire bonding.

Another attractive option is to integrate the high-frequency antenna directly on the chip. For instance, a 60 GHz RF antenna can be integrated directly on-chip near the MRM, acting as a signal source for direct modulation of the MRM via a Pockels effect [4-2]. However, such antennas necessitate the formation of back electrodes on the backside of the silicon chip and the use of feedthrough holes to generate an electromagnetic wave-induced electric field. Alternatively, communication between on-chip integrated antennas without the use of back electrodes has been realized [4-3]. Hence, for this study, integrating the millimeter wave antenna near the MRM array and modulating the input light using either zero bias or negative bias implemented through a clamping circuit [4-4], is a feasible approach, as shown in Fig. 4-21.

Nevertheless, thermo-optical tuning for the individual microrings is still necessary. For the heating method using electrical heater, additional electrical connections for each microring are needed. Even if these connections are DC and do not require high-frequency wires, electrical pads with a large footprint for the electrical heaters, as well as a voltage source equal to the number of MRMs and twice the number of electrical connecting wires as the MRMs, are necessary. This increases the complexity of the whole system and reduces operational freedom.

Therefore, in the next chapter, we present the concept of an optical heater without electrical connections. This concept allows the system to have all connections to the outside world with only three optical fibers (or even only one fiber if circulator is used). We will introduce the optical heater concept in Chapter 5, the implementation of the RoF system using optical heater in Chapter 6.

4.5 Summary

In this chapter, we introduced an innovative EM wave imaging RoF system comprising an RF probe array and a Si photonics MRM array. The system is designed to function within the Sub 6 GHz bands specified in 5G standards. A proof-of-concept experiment conducted in the microwave regime successfully captured the profiles of EM waves emitted by a dipole antenna.

We begin by presenting the design and packaging of the MRM array employed in this system.

Each MRM in this array can be thermally tuned to the resonance wavelength by integrating an electrical heater. This thermal tuning ensures the basic operational requirements of each microring when used as an RF signal selector. Subsequently, we outline the experimental setup for realizing EM imaging, which includes the RF probe, dipole antenna, operating table, and EM anechoic chamber. Dedicated LabVIEW scripts were developed to fully automate EM wave imaging. Simple data calibration was applied to implement the visualization data stitching. In the final step, we visualize the distribution of EM wave power for a 3.5 GHz sinusoidal EM wave signal at a distance of 5 cm over a range of 3515 mm². The measurement results, in good agreement with simulation results, demonstrate an XPD of more than 10 dB and a dynamic range of more than 20 dB. These performances can be further enhanced by reducing environmental interference of electromagnetic wave signals. Lastly, we discuss the feasibility of the system in the millimeter wave domain.
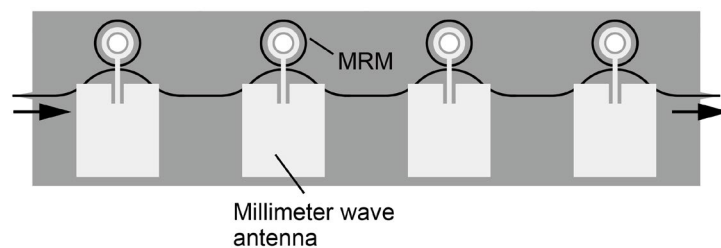
Figure 4-21. An MRM array with an on-chip integrated millimeter wave antenna can be utilized for EM wave imaging in the millimeter wave region.

Reference

[4-1]   L. Li, H. Arai, and T. Baba, "Imaging of electromagnetic waves using a radio over fiber system including an Si photonics microring modulator array," *Opt. Express*, vol. 30, no. 18, pp. 31530–31538, Aug. 2022, doi: 10.1364/OE.457459.

[4-2]   H. Kamada and T. Arakawa, "Proposal of Highly Efficient Quantum Well Microring Resonator-Loaded Optical Phase Modulator Integrated with Antenna-Coupled Electrodes for Radio-over-Fiber," *Photonics*, vol. 8, no. 2, 2021, doi: 10.3390/photonics8020037.

[4-3]   A. S. Dhillon, B. Radi, and O. Liboiron-Ladouceur, "An Analysis of RF On-Chip Antennas in Si-Based Integrated Microwave Photonics," *IEEE Photonics Journal*, vol. 13, no. 2, pp. 1–18, 2021, doi: 10.1109/JPHOT.2021.3062883.

[4-4]   A. Melikyan, K. Kim, B. Stern, and N. Kaneda, "Self-biasing of carrier depletion based silicon microring modulators," *Opt. Express*, vol. 28, no. 15, pp. 22540–22548, Jul. 2020, doi: 10.1364/OE.395182.

Chapter 5
All-Optic Control via Optical Heater

5.1 Overview

In recent years, thermo-optic and carrier plasma effects have been extensively employed in Si photonics for optical control [5-1]. These effects find applications in modulation operations of modulators, ON/OFF control of optical switches, and wavelength tuning, etc. However, there are scenarios where electrical wiring is challenging or unsafe, such as environments with explosives or reactants in hazardous material optical sensors, environments susceptible to electromagnetic noise in precision machinery, and extremely low-temperature environments where electrical elements are inoperable. In such cases, there is a need for control solely with light, without using electricity at all. Additionally, situations with complex issues involving large-scale optical elements may benefit from all-optical control to avoid intricate electrical control.

This study aims to realize Si photonic all-optical control method without the need for electricity. Our research investigates "optical heaters" that are heated by light. Two types of devices, Mach-Zehnder Interferometer (MZI) and Microring Resonator (MRR), were utilized in this study to demonstrate an optical control method that is more efficient than electrical control.

In this chapter, we initially elucidate the concepts and theoretical calculations involved in utilizing optical heaters to achieve all-optical control. Subsequently, we delve into the design and parameter optimization of the optical heaters and their application to MZI and MRR optical switches. Practical measurements were conducted on fabricated optical switches equipped with optical heaters, encompassing their fundamental optical transmission performance, optical control performance, and temporal response. Finally, we conduct a comparative analysis of these measurements with the conventional electrical control method.

5.2 Concept and Theory

Figure 5-1 illustrates the basic concept of the all optical control device. Two ribbed waveguides with a silicon (Si) core and silicon dioxide (SiO_2) cladding are arranged in parallel. The waveguides responsible for guiding control light and signal light are termed the control waveguide and the signal waveguide, respectively. The control waveguide is doped with a high concentration of n-type dopants, absorbing the incoming control light. The heat from the absorption diffuses along the Si slab to the adjacent signal waveguide, where the phase of the signal light is tuned. The relationship between the absorption of light due to doping and the phase change due to heat is shown in Equations 5-1 through 5-3, respectively. Equation 5-1 illustrates the relationship between the absorption of light generated by doping and the absorption length z, where P_{abs} represents the absorbed optical power, P_{ctrl} is the power of the control light guided to the absorbing part, and α is the absorption coefficient due to doping. In contrast, the temperature $T(r)$ of the signaling waveguide and its surroundings is determined by the absorbed optical power P_{abs} and the thermal diffusion of the waveguide. Therefore, the
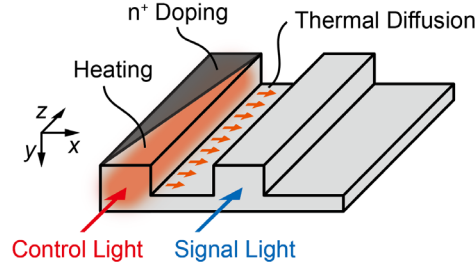
Figure 5-1 Concept of optical heater. Waveguide for signal is heated by thermal diffusion from adjacent waveguide, which is used for controlling.

change in the optical phase of the signaling light due to the thermo-optic effect $\Delta\phi$ is correlated with the change in the effective refractive index $\Delta n_{eq}(z)$ in the optical waveguide. Equation 5-2 presents the calculation formula, where k0 is the wavenumber in vacuum. And $\Delta n_{eq}(z)$ is related to the temperature $T(\boldsymbol{r})$, which can be calculated by simulation. The change in the refractive index of the material, which leads to the change in effective refractive index, is directly related to the temperature. At 1550 nm, there is $n_{Si}(\boldsymbol{r}) = 3.50 + T(\boldsymbol{r}) \times 1.8 \times 10^{-4}$ for Si core and $n_{SiO2}(\boldsymbol{r}) = 1.44 + T(\boldsymbol{r}) \times 1.2 \times 10^{-5}$ for SiO$_2$. In other words, the absorption of light is mainly related to the absorption coefficient α due to doping, and the change in optical phase is primarily associated with the change in the equivalent refractive index of the waveguide. High-efficiency all-optical control using an optical heater can be achieved by appropriately designing the shape of the doped portion, the width of the waveguide, the spacing, and other relevant parameters.

$$P_{abs}(z) = P_{ctrl}\left[1 - e^{-\alpha(z)z}\right] \tag{5-1}$$

$$\Delta\phi = \int_0^L k_0 \Delta n_{eq}(z)\,dz \tag{5-2}$$

5.3 Design

5.3.1 Fundamental Configuration

The basic structure of the optical heater is depicted in Fig. 5-1. It should be noted that this structure represents an optimized second-generation optical heater structure. The first generation of optical heaters is illustrated in Fig. 5-2 (AIST 5). Let's begin with a brief overview of the first generation of optical heaters.

In the first generation of optical heaters, two complete slab waveguides were utilized, and one of the waveguides was entirely high-concentration doped. This design offers simplicity but introduces several issues. One primary problem is the overconcentration of the heated portion due to excessive light absorption, resulting in a low phase change of the signal light and low thermal tuning efficiency. Additionally, the excess slab disperses heat in unnecessary directions, further reducing overall thermal tuning performance. Detailed optimization will be presented later.

For the second-generation optical heater shown in Fig. 5-1, we utilized an AIST SOI chip with a silicon layer thickness of 220 nm, and the Rib waveguide was half-etched. Instead of using the dimensions of the Rib waveguide used for MRMs in Chapter 3 (0.5 μm) for the waveguide width, we employed a more stringent single-mode waveguide width (0.45 μm) to
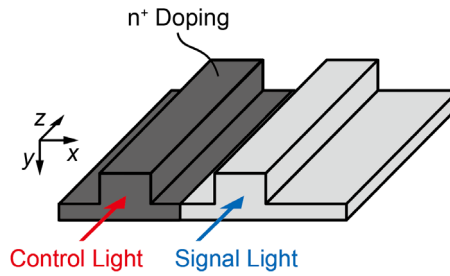
Figure 5-2 Original configuration of optical heater.

suppress higher-order mode propagation. For doping, we employed a high concentration of n+ -type doping to absorb the control light, with a doping concentration of 5×10^{15} cm^{-2} (2.273×10^{20} cm^{-3}). We designed the doping shape as a sharp triangle so that the input control light is gradually absorbed. While such a sharp shape is not feasible in actual fabrication, we adapted the doping shape to a right-angled trapezoid, ensuring its hypotenuse overlaps the control waveguide. Given the ion implantation accuracy of the used foundry is 100 nm, such a design can be realized to a large extent.

5.3.2 Optical Transmission and Absorption Simulations

Next, we conducted optical simulation calculations for the structure depicted in Fig. 5-3(a). The optical heater part of this structure is identical to that of Fig. 5-1. The total length of the doped region L is set to 30 μm. The gray background represents the half-etched slab. The actual design includes a transition structure when the control light enters the asymmetric rib waveguide. Initially, we determined the spacing g between the signal and control light waveguides. Figure 5-3(b) illustrates the equivalent refractive index change of the signal waveguide influenced by the control waveguide. The inserted figure displays the cross-section of the optical heater, which also serves as the computational model used for the Lumerical FDE calculations. In this study, g was set to the stable region (0.5 μm, 1.0 μm, and 1.5 μm). Furthermore, the width of the slab on the signal side was set to 0.5 μm, as shown in the inset—narrow enough not to affect the normal transmission of the signal light.

To calculate the absorption of control light by high concentration doping, we initially used the Lumerical CHARGE solver to perform carrier concentration calculations for the structure shown in Fig. 5-3(a). Subsequently, the obtained carrier concentration information of the doped part was imported into the Lumerical FDTD solver and simulated for the same model. When the input light wavelength is 1550 nm and $g = 0.5$ μm, the power distributions for signal light transmission, control light transmission, and control light absorption are shown in Fig. 5-4 (a), (b), and (c), respectively. The white line outlines the rib waveguide, and the half-etched slab is not represented in this figure.

It is evident that optical coupling between waveguides is minimal even with a waveguide spacing of only 0.5 μm. For the control light input into the control waveguide, the optical power is almost completely absorbed after the 30 μm highly doped portion. Utilizing the Pabs Analyze Group in the Lumerical FDTD solver, we calculated the absorbed optical power distribution, as shown in Fig. 5-4 (c). The absorbed optical power distribution closely aligns with the doping distribution, and the maximum absorbed power is at the center of the waveguide. This indicates that the maximum power of the optical modes in the control waveguide is located at the center of the modes.
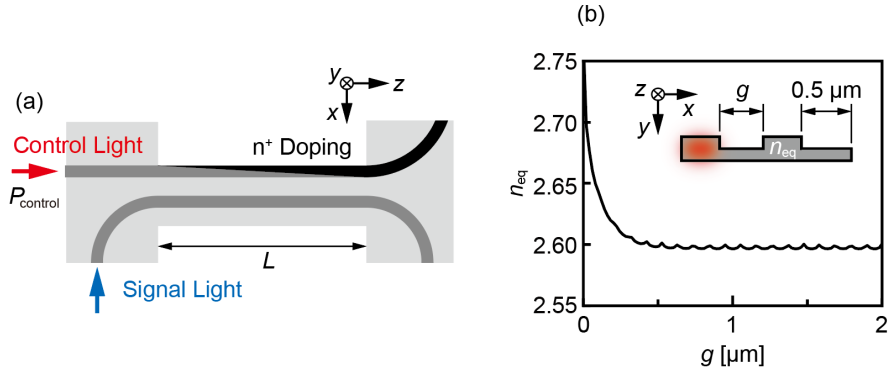
Figure 5-3 (a) Simulation model with proposed optical heater. (b) Equavilent index of signal waveguide with varies gap g.
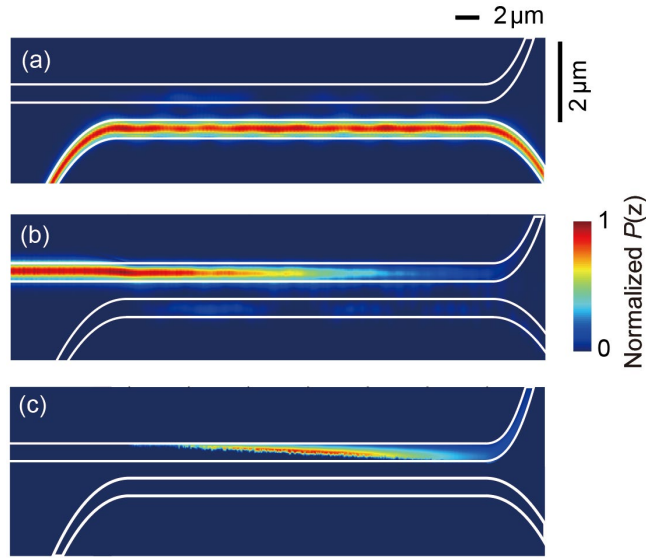
Figure 5-4 (a) Transmission of signal light. (b) Transmission of control light. (c) Absorption of control light. $g = 0.5$ μm for all simulations.
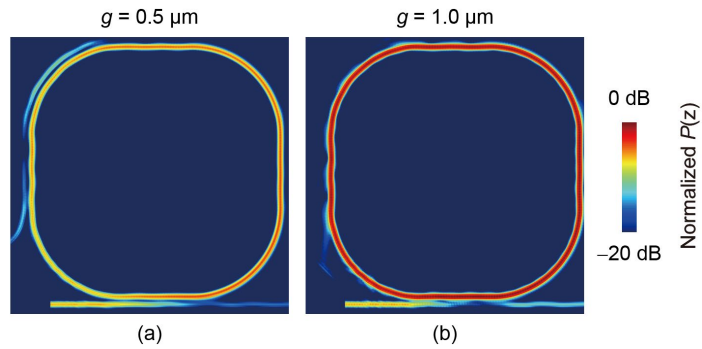

Figure 5-5 Transmission of signal light at resonance wavelength in MRR with optical heater. (a) $g = 0.5$ μm. (b) $g = 1.0$ μm.

Moreover, we conducted calculations for the signal light propagation of the optical heater integrated on the subsequently mentioned MRR-type optical switch. The structure of the MRR is illustrated in Fig. 5-10, and the propagation of the input control light is presented in Fig. 5-5 for the MRR in the resonant state. When $g = 0.5$ μm, there is a noticeable amount of optical coupling between the control light waveguide and the signal light waveguide at the waveguide bend. Conversely, when $g = 1.0$ μm, the optical coupling between the waveguides is almost negligible.

5.3.3 Thermal Distribution Simulation

Subsequently, we conducted a thermal simulation of the temperature distribution around the optical heater. Using the Lumerical HEAT solver, the previously mentioned light absorption profile was imported as a heat source into the model shown in Fig. 5-3, and the temperature distributions in the center plane of the waveguide and in the cross-section of the waveguide were recorded. The calculation results are shown in Fig. 5-6, with the heating power set to 40 mW. It can be observed that the highest temperature part of the thermal distribution is concentrated in the rear section of the optical heater, attributed to the highest intensity of light absorption in this region (Fig. 5-4). Simultaneously, thanks to the triangular doping shape, the high-temperature region is mainly concentrated in the waveguide section and is fully broadened in the light propagation direction.

For the electrical heater (TiN heater) used for comparison, the overall temperature is low, even though the heat distribution is uniform throughout the heating region. In the cross-section plot on the right, we find that the temperature of the control waveguide in the optical heater is 699 K at $g = 0.5$ μm, and the signal waveguide is also heated up to 643 K. This is due to the high thermal conductivity of silicon. However, for the electrical heater, the silicon waveguide layer is only 512 K, even though the TiN part is heated to 666 K because it is filled with poorly thermally conductive silicon dioxide between the TiN layer and the waveguide. The distance between the two layers is 2.1 μm. Certainly, the temperature is dependent on the cross-section selection, and the total phase change of the signaling light in the silicon waveguide needs to be computed by integrating the refractive index change caused by the temperature change over the entire light propagation path to be accurately calculated. This is also described in the next section.
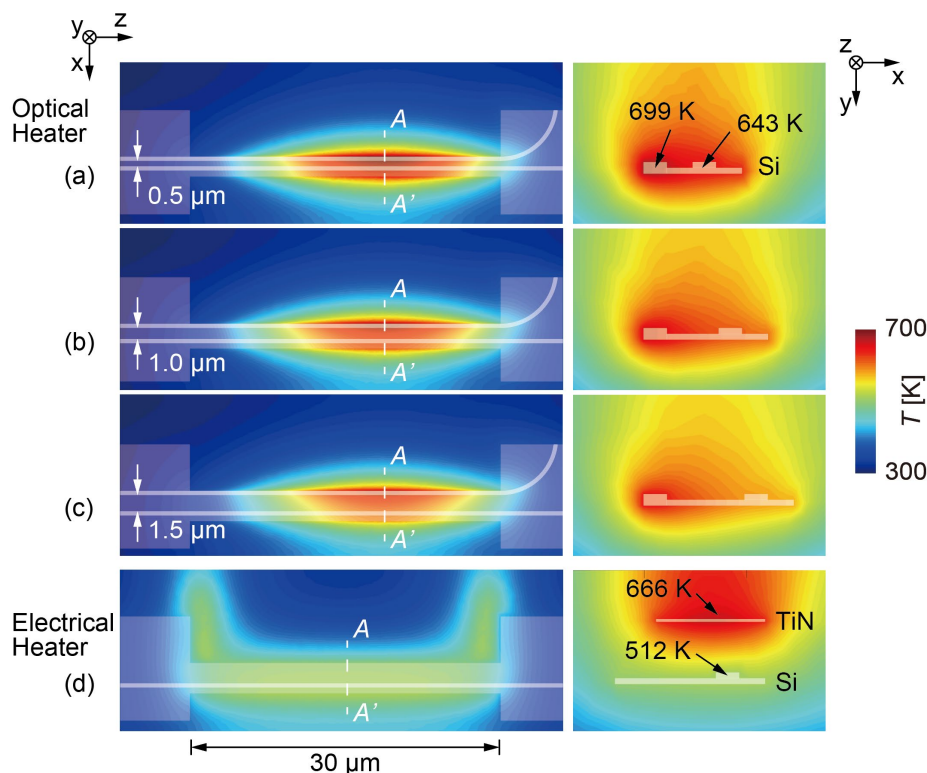
Figure 5-6 Simulation results of thermal distribution of optical heater with heating power assumed to be 40 mW. (a) $g = 0.5$ μm, (b) $g = 1.0$ μm, (c) $g = 1.5$ μm. (d) Electrical heater for comparison.

5.3.4 Effective Index and Phase Shift Calculation

Subsequently, the aforementioned temperature distribution was imported into the Lumerical FDE solver. The FDE calculation region was moved along the light propagation direction, and the effective refractive indices of the optical modes at different positions were recorded, as shown in Figs. 5-7(a)~(d). It can be observed that the shape of the effective refractive index distribution on the waveguide is similar to the thermal distribution, exhibiting a bell-shaped curve. The curve also linearly stretches in the direction of the longitudinal axis as the input power increases. The change in effective refractive index is largest when the waveguide spacing (g) is smallest. The abrupt changes at the beginning and end of the curve are due to the disappearance and appearance of the slab on the rib waveguide side. In contrast, the electrical heater in (d) shows a broad and flat trend, but the maximum value is lower than that of both optical heaters.

We subtracted the effective refractive index change at each input power from the effective refractive index change at 0 mW and integrated it using Eq. 5-2 to obtain the total phase change of the signal light, as shown in Fig. 5-7(e). It can be seen that the change in optical phase always grows linearly with the change in input power, regardless of whether the heater is optical or electrical. For the indicator Pπ commonly used in optical switches, representing the power required to realize the phase change of π, can be directly read from this figure. For the optical heaters, P_π is equal to 19 mW, 21 mW, and 22.5 mW for g = 0.5, 1.0, and 1.5 μm, respectively, while for the electrical heaters, P_π is equal to 22.5 mW. In other words, for the three waveguide pitches used in this study, the heating efficiency of each optical heater is greater than or equal to that of the usual electrical heaters.
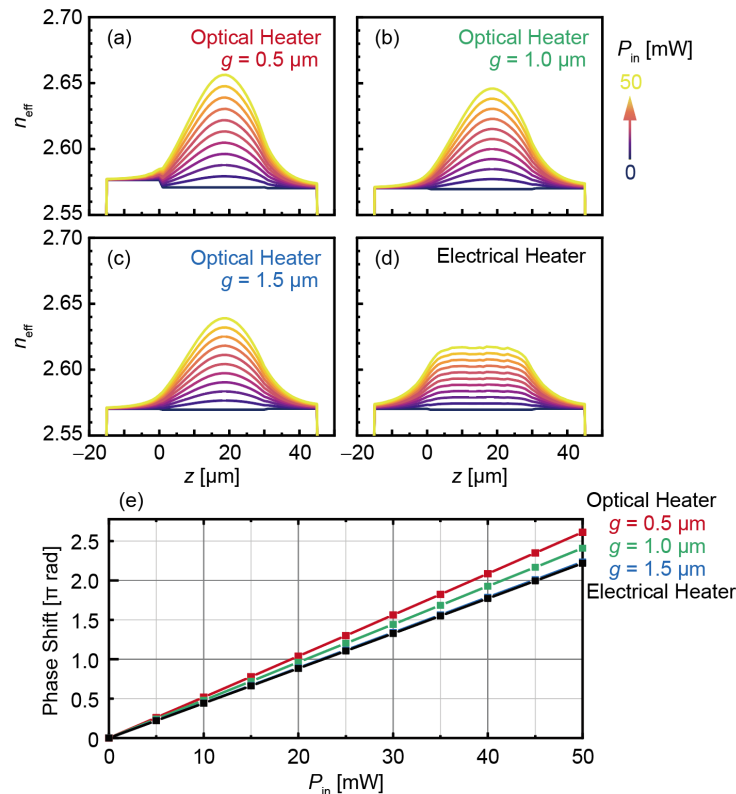
Figure 5-7 Simulated effective index of optical mode along signal waveguide. (a) g = 0.5 μm, (b) g = 1.0 μm, (c) g = 1.5 μm for optical heater. (d) Electrical heater. (e) Total phase shift of signal light caused by varies control power P_{in}.

5.3.5 Optimization

In addition, the optical heater used in this study was optimized from a first-generation design. Although the second-generation design has been described, it is necessary to revisit the optimization process of the first-generation design. The optimization process is shown in Fig. 5-8. In the left column, various structures of optical heaters with the n+ doped regions demonstrated in gray are displayed. The right column shows the corresponding thermal distributions of the various structures, with the temperatures normalized by the maximum and minimum values in each plot.

Shown in (i) is a first-generation optical heater design. As mentioned earlier, the incoming control light can be substantially absorbed by sudden dopants, leading to an overly concentrated thermal distribution. Doping only half of the waveguide, as shown in Fig. 5-8(ii), did not bring much improvement because the doped portion would always absorb the center portion of the optical mode with the highest power. Therefore, we considered making the doped portion wedge-shaped to gradually absorb the optical power, as shown in Fig. 5-8(iii). This approach makes the thermal distribution more uniform, but it can also be observed that the slab on both sides of the waveguide conducts a lot of heat. This excess heat may be unwanted in practical applications and could even affect other components in close proximity. Therefore, we aimed to remove as much as possible the slabs on both sides of the waveguide.

For the control waveguide on the left side, since its function is to absorb the input light rather than transmit signals, the slab on its left side can be completely removed. For the signal waveguide on the right side, we need to ensure that the signal light it transmits stays in a single mode, so the slab on its right side should be removed to the extent that it does not affect its effective refractive index of light. Figure 5-9(a) shows the change of the effective refractive index of the signal light in the signal waveguide when the width of the right-side slab is adjusted. It can be seen that the effective refractive index tends to stabilize when the slab width is greater than 0.5 μm. Therefore, we set $\Delta w = 0.5$ μm, which is why the width of the rightmost slab in Fig. 5-3(c) is 0.5 μm.

Returning to Fig. 5-8(iv), by reducing the width of the slab on both sides, we obtain a thermal distribution concentrated in the waveguide section. Similarly, with the change of the doping shape, we obtain a thermal distribution that is more concentrated in the waveguide and expands wider in the light propagation direction, as shown in Figs. 5-8(v) and (vi).

Figure 5-9(b) illustrates the effective refractive index variation along the signaling waveguide obtained by the aforementioned method, where each curve corresponds to (i) to (vi) in Fig. 5-8. The total phase change of the signal light for each design can be visualized by the curve area (integral). It can be found that by removing the slab from both sides of the waveguide, the refractive index change becomes approximately twice as much as before removal. Additionally, by designing the doping shape as a wedge shape, a more uniform thermal distribution can be obtained, although the maximum value is reduced.

However, in actual fabrication, sharp angles and too narrow doping shapes are not allowed. In the foundry used in this study, the minimum width of n+-type doping is 4 μm. Therefore, we made further adjustments to the shape, as shown in Fig. 5-8(vii) to meet the design requirements of the foundry in the actual design. Even though there is no slab on the left side of the waveguide, it is still possible to cover the doping layer over it, which is allowed in the AIST design.
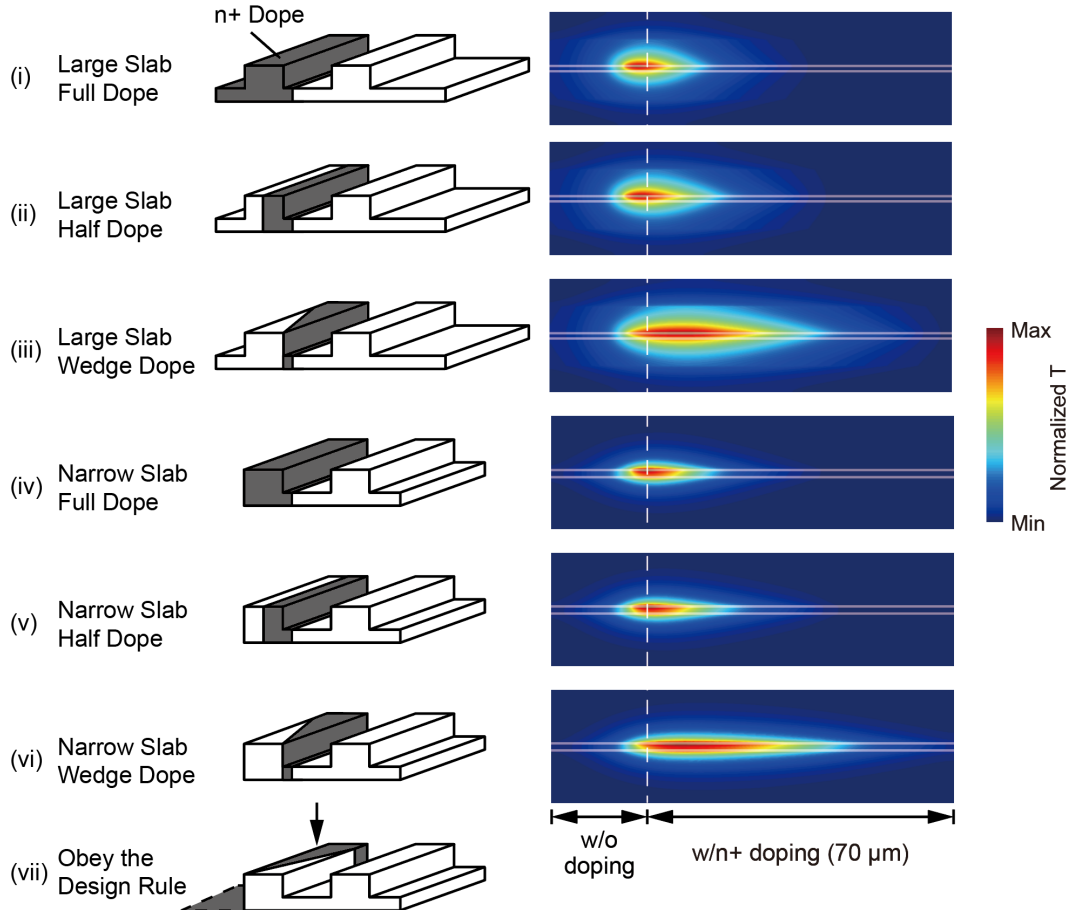
Figure 5-8 Optimization of optical heater by adjusting the shape of the Si slab and doping region.
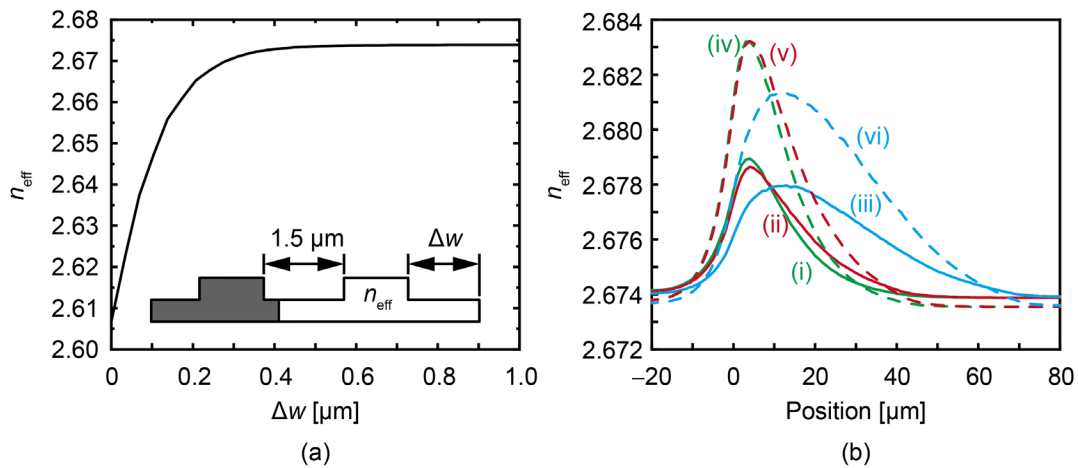

Figure 5-9 (a) Relationship between effective index n_{eff} of optical mode in signal waveguide and slab width Δw. (b) Distribution of n_{eff} along signal waveguide using variers designs in Fig. 5-8.

5.3.6 CAD Layout

Based on the above design, the actual CAD layout of the optical heater is discussed next. In this study, the optical heater is integrated into two typical optical switches in the field of optical communication: the MZI-type optical switch and the MRR-type optical switch. The CAD layout of the MZI-type optical switch is shown in Fig. 5-10, where the SSC for optical input and output is omitted. The black and dark gray parts represent Si waveguide layers, and the
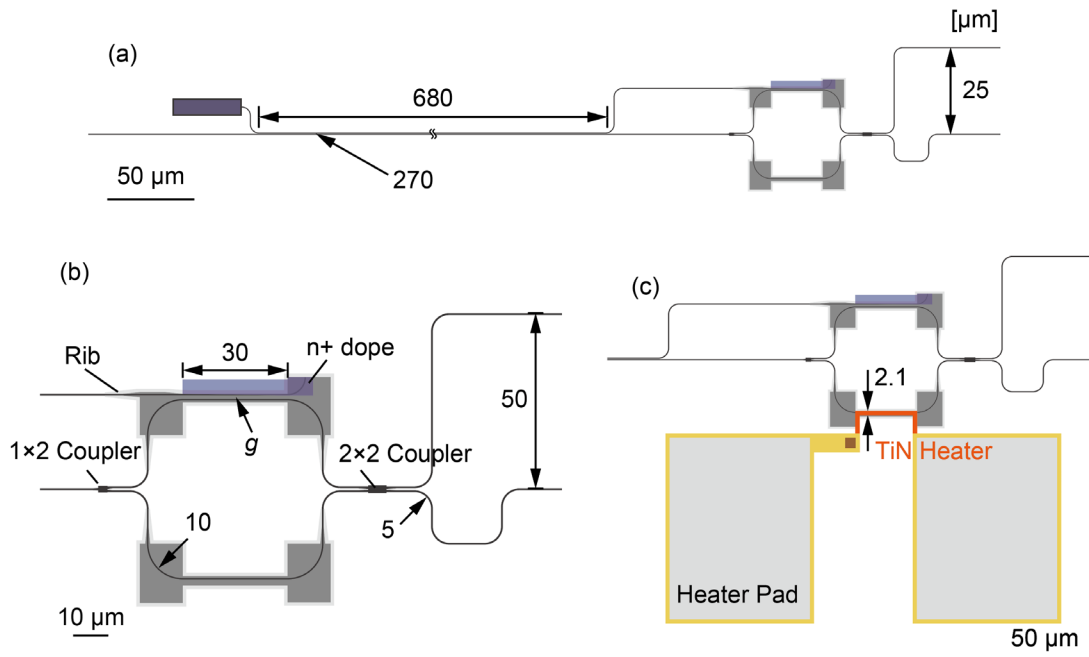
Figure 5-10 Design CAD layout of MZI optical switch with optical heater. (a) Overview. (b) Enlarged view of MZI. (c) MZI with TiN heater.
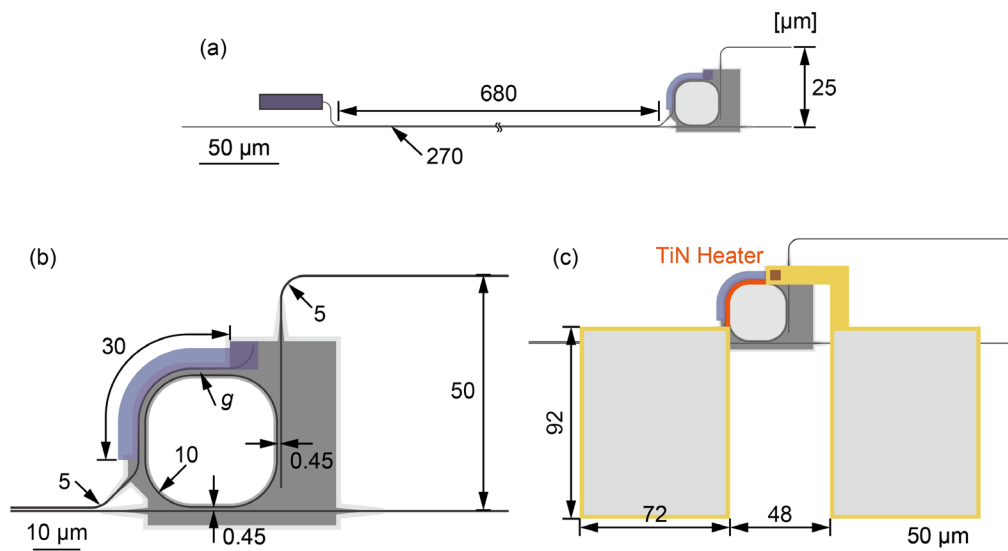
Figure 5-11 Design CAD layout of MRR optical switch with optical heater. (a) Overview. (b) Enlarged view of MRR. (c) MRR with TiN heater.

light gray and dark gray parts are Rib layers. In Fig. 5-10(a), light is input from the left end and output from the right end. Before the light enters the MZI, a 680 μm long directional coupler is designed to separate the control light from the signal light. The coupling gap width of the directional coupler is 270 μm. The control light is output from the drop port (upper right) of the directional coupler, and the signal light is output from the through port (lower right). The expanded diagram of the MZI section is shown in Fig. 5-10(b). The signal light entering the MZI is divided into two beams equally by the 1by2 coupler, passes through the two arms of the MZI, and enters a 2by2 coupler again. The two beams of light outputted by the 2by2 coupler interfere with a phase difference to produce destructive interference or constructive interference, realizing the ON/OFF of the output light. The control light is guided to the MZI and the optical heater. When the control light enters the doped portion labeled blue, the optical

power is absorbed and converted into thermal energy to heat the upper arm of the MZI. The spacing between the control and signal waveguides is *g*, as mentioned earlier. The lower arm of the MZI is made to have the same Rib waveguide to maintain symmetry, with the difference being only the absence of an optical heater. Figure 5-10(c) shows the MZI optical switch using an electrical heater for comparison. TiN electrical heaters are integrated into the lower arm of the MZI with the same dimensions, interlayer distances, etc., as the normally used electrical heaters. The distance between Si layer and TiN layer is 2.1 μm.

Figure 5-11 illustrates the CAD layout of the MRR-type optical switch. Similarly, a directional coupler is set up in front of the MRR to separate the control and signaling light. Figure 5-11(b) shows the layout of the MRR, made of rib waveguide. The coupling gap between the signal light and the MRR is 0.45 μm, while the bending radius of the MRR is 10 μm. The blue part is a highly doped section with a total length of 30 μm. To achieve this length, the straight-line length of each side of the MRR was set to 7.14 μm. The waveguide spacing of the optical heater part is g. When the input control light is absorbed, the generated heat will heat up a part of the MRR, shifting its resonant wavelength. This resonance shift can be manifested by scanning the wavelength of the input signal light and recording the output signal light intensity. When the wavelength of the signal light is fixed near the resonant wavelength of the MRR, adjusting the power of the control light changes the intensity of the output signal light, enabling ON/OFF adjustment of the output light. Similarly, the device with integrated TiN heater is shown in Fig. 5-11(c) for comparison.

5.4 Fabricated Device

The devices fabricated by AIST are shown in Fig. 5-12. Here, we used the 300 mm wafer process with multi-process wafer (MPW) service. Figures 5-12(a)(c) shows optical microscope photographs of the MZI-type optical switch and the MRR-type optical switch, respectively. The directional coupler at the front end and the MZI and MRR at the back end are clearly visible. In the respective enlarged images, the high doping concentration is indicated by the black area. While (b) and (d) show the devices with TiN electrical heaters used for comparison. In the part with lower pattern density, the foundry added dummy patterns for balancing the fabrication performance.
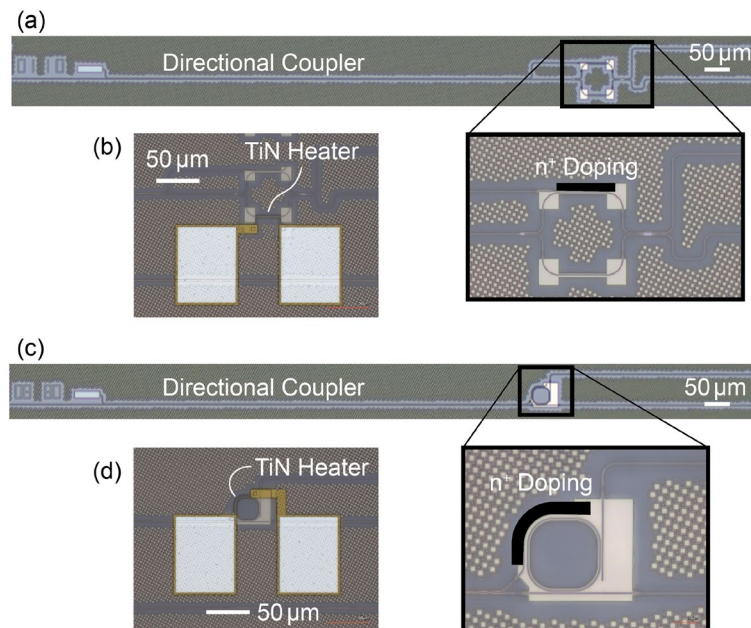
Figure 5-12 Fabricated devices with optical heater. (a) MZI optical switch. (b) MZI with TiN heater. (c) MRR optical switch. (d) MRR with TiN heater.

5.5 All-Optic Control

5.5.1 Measurement Setup

We next implemented an optically controlled experiment using a light heater. Figure 5-13(a) illustrates the experimental setup used. To input the control and signal light, we used two continuous-wave (CW) lasers. For the control light output from Laser 1, it was amplified to a sufficiently high power by an erbium-doped fiber amplifier (EDFA) and passed through a 1:99 coupler. The tap port is connected to an optical power meter (PM) to monitor the output power of the EDFA, while the through port is fed to a 50:50 optical coupler and merged with the signal light from Laser 2. The signal light power was controlled at 0 dBm, which is not a very high power. It first passes through a polarization controller (PC) to control the direction of polarization. When the signal light is combined with the control light, it is fed from the lensed fiber to the device under test (DUT), which is the MZI-type or MRR-type optical switch mentioned earlier. The signal light and control light are separated by the on-chip directional coupler and directed to the MZI/MRR and optical heater, respectively, after they are input to the device from the SSC. The signal light from the MZI/MRR passes through the output SSC again and is collected by the lensed fiber at the output port and fed into an optical bandpass filter (BPF) via a polarization-maintaining (PM) fiber to filter out the excess control light. The BPF has a bandwidth of 1 nm, and the center wavelength follows the signal light. Finally, the signal light power is detected and recorded by an optical power meter at the end. The design supports transverse-electric-polarized light propagation. While the unilateral lensed fiber loss is 1.2 dB, the SSC loss is 2.5 dB. By varying the output power of the EDFA, we can monitor in real time the change of the output signal optical power due to the optical heating in the optical heater. This was also accomplished using LabVIEW scripts.

To determine the wavelengths of the input signal light and the control light, we performed transmission spectrum measurements of the on-chip directional coupler's test pattern, the results of which are shown in Fig. 5-13(b). The inset therein shows the input and output ports of the directional coupler, for which the transmission spectrum is labeled blue for the through port and red for the drop port. The maximum and minimum values of the two alternate. To output the signal light to the through port and the control light to the drop port, we set their wavelengths to the maximum output of the transmission spectra of the respective ports. As shown in the figure, we selected the signal light wavelength λ_{sig} and the control light wavelength λ_{ctrl} near 1550 nm. The coupling loss of the directional coupler (the maximum value of the transmission spectrum) is about 0.9 dB. In the previous-generation design, the length of the directional coupler is shorter, which results in the transmission spectrum, as shown in Fig. 5-13(b), being
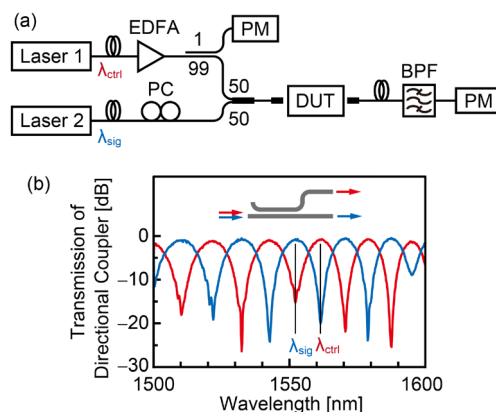

Figure 5-13 (a) Measurement setup for optical control. (b) Optical transmission of on-chip directional coupler for wavelength separation.

stretched laterally, and the wavelengths of the control and signaling light could not exist in the C band at the same time. Therefore, in this design, we sacrifice the compactness of the directional coupler in exchange for greater freedom of choice for the wavelengths of the signal and control light.

5.5.2 High Efficiency Thermal-tuning

Figure 5-14 show the experimental results using the MZI optical switch. Where (a)~(d) show the relationship between the signal light output power and control power for the optical switch using the optical heater and the optical switch with the electrical heater for $g = 0.5$ μm, 1.0 μm, and 1.5 μm, respectively. For the optical heaters, the control power P_{ctrl} here refers to the control optical power actually delivered to the optical heaters; while for the electrical heaters, the control power refers to the electrical power input to the TiN. As the input power increases, the output power of the signal light varies as a sinusoidal function regardless of which heater is used. And the initial phase of the change curve, i.e., the consistency of the output power at the two output ports of the 2by2 coupler when P_{ctrl} is equal to 0, is affected by the fabrication error.

An important parameter of the MZI optical switches is the power P_π required to realize the π phase change. For each g of the optical heater mode, P_π is 17 mW, 19 mW, and 24 mW, respectively, while for the electrical heating mode, P_π is 22.5 mW. Figure 5-14(e) illustrates the relationship between P_π and g. The power of P_π is calculated as follows, where the red circles represent the measured data. We find that when g becomes smaller, P_π is also smaller. This indicates that the heating efficiency of the optical heater increases as the spacing between the signal waveguide and the control waveguide decreases. However, closer waveguide configurations result in greater inter-waveguide optical coupling, which leads to control light mixing into the signal waveguide, and signal light mixing into the control waveguide and being absorbed. Thus there is a trade-off relationship between the increase in the heating efficiency of the optical heater and the suppression of the inter-waveguide optical coupling. The red straight line represents the simulation results, which differ from the measured results within a reasonable range. The black straight line represents the measured results of the electrical heater. Since there is no waveguide spacing g for the electrical heater, we represent it as a straight line parallel to the horizontal axis in the figure, and its value is 22.5 mW. The simulation result of P_π for the electrical heater is also 22.5 mW as seen in 5-6(e), which also proves the correctness of the simulation solver. When the waveguide spacing g of the optical heater is less than 1.5 μm, the heating efficiency of the optical heater is higher than that of the electrical heater.

In addition, as seen in Figs. 5-14(a)~(c), the output optical power no longer varies according to a sinusoidal function when the control power is greater than about 45 mW. When the same experiment was repeated again, it was found that the same experimental results could not be reproduced. This is due to the fact that the high power leads to two-photon absorption at the SSC, which in turn damages the SSC, and we can improve this phenomenon by improving the design, e.g., by using SiN SSCs and waveguides [5-2] for high-power optical input.

Figure 5-15 illustrate the measurement results of the MRR-type optical switch. (a)(b)(c) correspond to the results using an optical heater for $g = 0.5$ μm, 1.0 μm, and 1.5 μm, respectively. (d) is the result using an electrical heater. These images illustrate the changes in the optical transmission spectrum of the signal output from the through port of the MRR in the 15 nm range near 1550 nm when the control power is varied. In addition to the sharp resonance peaking from the MRR, there is a slow change in these transmission spectra. This variation is characterized from the on-chip directional coupler. For the cases of $g = 1.0$ μm and 1.5 μm, the resonance shift of the MRR can be clearly observed with the gradual increase of the control optical power P_{ctrl}. For the case of $g = 0.5$ μm, on the other hand, the MRR is in the undercoupling state, and the resonance peak becomes insignificant due to the larger inter-waveguide optical coupling as

shown in Fig. 5-5. For the optical switch using an electrical heater, a significant resonance shift is also observed. We extracted the resonance wavelength offsets and control power in Fig. 5-15 (b)(c)(d) and summarized them in Fig. 5-15(e). The thermal tuning efficiency can be derived from the slope of each curve. It can be found that when the control power is less than 13 mW, the tuning efficiency of the optical heating method with $g = 1.0$ μm is consistent with that of the electrical heater, while the tuning efficiency becomes lower as g increases. When the control optical power is greater than 13 mW, the efficiency of the optical heating with $g = 1.0$ μm becomes lower, which is probably due to the fact that the excessive power affects the performance of the directional coupler and the MRR. In any case, for the MRR-type optical switch, the thermal tuning power achieved with the optical heater is comparable to that of the electrical heater.
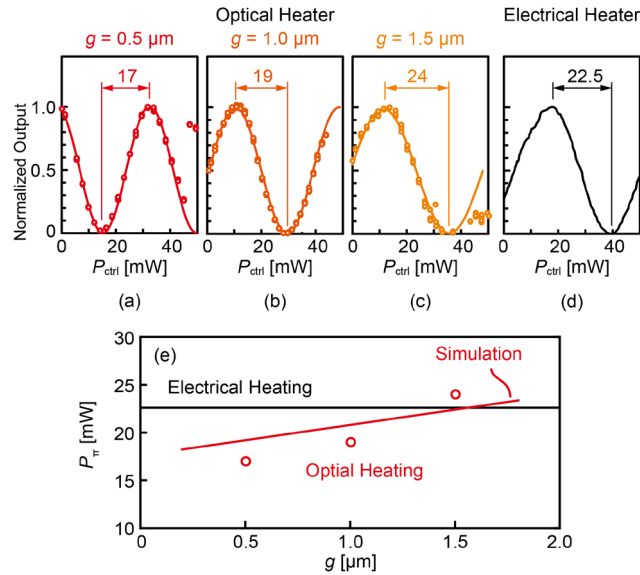
Figure 5-14 Transmission of signal light with control power P_{ctrl} changed for optical heater with (a) $g = 0.5$ μm, (b) $g = 1.0$ μm, (c) $g = 1.5$ μm and (d) electrical heater. (e) Comparison of P_π of each heating method.
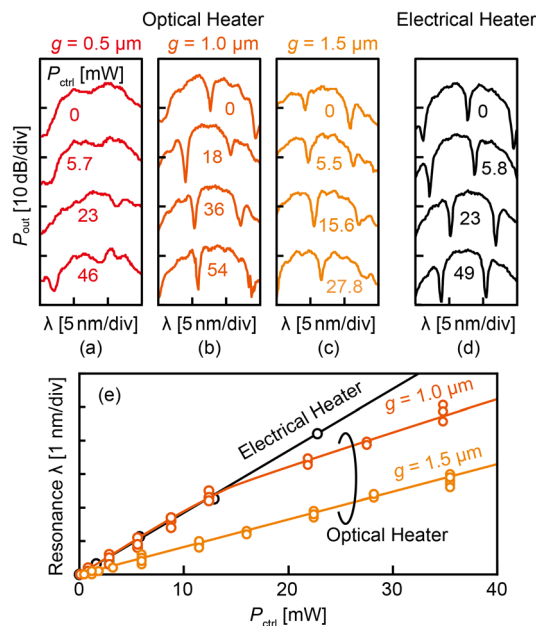
Figure 5-15 Resonance shift of MRR controlled by varies power P_{ctrl} for optical heater with (a) $g = 0.5$ μm, (b) $g = 1.0$ μm, (c) $g = 1.5$ μm and (d) electrical heater. (e) Comparison of tuning efficiency for each heating method.

128
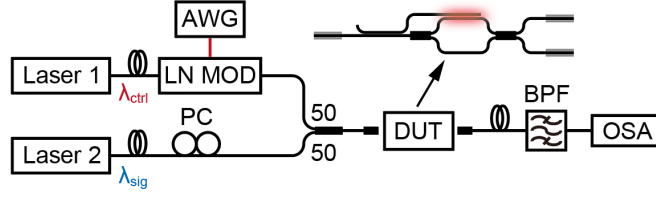
Figure 5-16 Experimental setup for switching measurement.
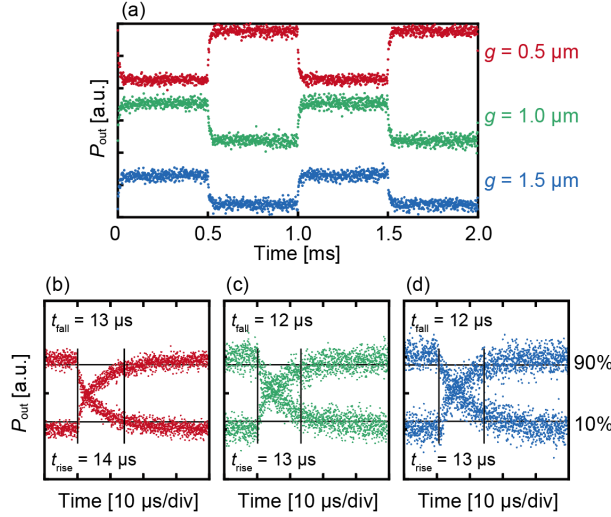
Figure 5-17 (a) Waveform of outputted signal. Frequency was set at 1 kHz. (b)~(c) Fall edge and rise edge of output signal in (a).

5.5.3　Temporal Response

Next, the basic switching operation and time response of the switching device using an optical heater were confirmed. The experimental system used is shown in Fig. 5-16. Here, an MZI-type device was used. The system is arranged so that the signal light is periodically controlled by modulating the intensity of the control light. A square wave signal with a frequency of 1 kHz and V_{pp} of 6 V was applied to a Lithium Niobate (LN) modulator (Alnair Labs LNMOD-400) from an arbitrary waveform generator (AWG, Agilent 33220A).

The signal and control optical powers were fixed at 17 dBm and 13 dBm, respectively, and the output waveforms were measured. Figure 5-17(a) shows the output waveform observed by OMA when a 1 kHz square wave was input. Both waveforms show clear square waveforms. The edges of the waveforms are shown in (b)~(d). 10 and 90% of the amplitudes are indicated by thin lines, based on the average of the ON and OFF levels, respectively. From the intersection of the waveforms, we can measure the time taken to Fall down and Rise up. g = 0.5 μm, 1.0 μm, and 1.5 μm, the Fall time and Rise time are 13 μs, 12 μs, 12 μs and 14 μs, 13 μs, 13 μs. In contrast, for optical switches using normal electrical heaters, the time constants for ON/OFF operation vary from 1 μs to tens of μs [5-3, 4]. It can be seen that the time response using an optical heater is similar to that of a normal electrical heater.

5.6　Discussion

As noted earlier, we have successfully implemented an optical heating method, which proves to be more efficient than conventional electrical heating methods, and integrated it into optical switches. Significantly, our proposed optical heating technique holds promise for various applications beyond optical switches due to its straightforward and efficient heating mechanism. For instance, envisioning a 2×2 MMI (Multimode Interferometer) utilizing an optical heater,

we can selectively apply doping to the weak part of the optical field (to prevent signal light absorption, avoiding interference with the MMI's proper function). By introducing control light from a third input port, we achieve efficient phase modulation through the doped portion, generating heat across the entire core area of the MMI.

However, there is ample room for improvement in our optical heater design. Enhancing heating efficiency can be achieved through further optimization, such as adjusting the width of the control waveguide. Unlike the signaling optical waveguide, the control waveguide need not conform to its width, as its purpose is to absorb control light rather than efficiently transmit signal light. Varying control waveguide widths impact heating efficiency and optical coupling to the signal waveguide, making optimization crucial. Additionally, despite the use of optimized triangular shapes for the doped region, there remains a considerably larger area of light absorption, indicating non-uniform absorption. Exploring alternative shapes, like curved regions overlapping the waveguide, may further flatten light absorption and heat distribution, with careful consideration of fabrication accuracy and errors.

Addressing the switching speed, mentioned in Chapter 1, our study indicates switching speeds in the order of several microseconds, achievable through direct heating of the silicon waveguide or silicon slab. However, the switching speed in this study is constrained by the heat capacity around the optical heater, suggesting potential enhancements through the introduction of an air trench or removal of the clad or substrate [5-5, 6].

Furthermore, the scalability of the optical heater poses a challenge. In the MZI-type optical switch in this study, the input optical power must be increased due to a significant reduction in optical power caused by the absorption of control light in the doped region. This reduction is insufficient to generate adequate heat for the subsequent cascaded optical heater. Excessive input optical power, on the other hand, results in damage to the SSC due to two-photon absorption, limiting the number of cascaded optical heaters. However, for specific applications, MRR-type optical switches can be employed, allowing a reduction in power requirements for each optical switch through appropriate design modifications, as detailed in Chapter 6. Additionally, leveraging the wavelength dimension of the control light, passive MRRs with varying radii can be used to select and derive the required control light for each row in the optical heater array, and control light power for each column in the array. This approach enables the realization of a large-scale optical control matrix suitable for devices such as large-scale optical switches. In conclusion, our proposed optical heater exhibits promising prospects for further research and development.

5.7 Summary

In this chapter, we propose a novel all-optical control method that leverages the exothermic phenomenon resulting from the light absorption by high concentration doping in silicon waveguides. This method enables the control of the temperature of adjacent waveguides, consequently inducing a phase change in the signal light. We initiated the process by theoretically modeling the optical heater and determining its design parameters through simulation calculations. Subsequently, we integrated these optical heaters into MZI-type and MRR-type optical switches, and the all-optical control devices were fabricated using AIST MPW service. Through comprehensive measurements, we observed that for MZI-type optical switches, the minimum power P_π required by the optical heating method is 17 mW, compared to the usual electrical heating method, which requires 22.5 mW. On the other hand, for MRR-type optical switches, the minimum P_π for the optical heating method is 22.5 mW. The heating efficiency achieved with the optical heating method for MZI-type optical switches is comparable to that of the electrical heating method. Consequently, we conclude that the thermo-

optical heating efficiency of the optical heater surpasses that of the conventional electrical heater. Regarding the time response of the optical heater, our measurements revealed that its time constant aligns closely with that of the standard electrical heating method. This implies that the optical heater can deliver higher heating efficiency, occupy a smaller footprint, and offer a more compact control mechanism than the electrical heater, all without compromising heating speed.

Reference

[5-1] R. L. Espinola, M. C. Tsai, J. T. Yardley, and R. M. Osgood, "Fast and low-power thermooptic switch on thin silicon-on-insulator," *IEEE Photonics Technology Letters*, vol. 15, no. 10, pp. 1366–1368, 2003, doi: 10.1109/LPT.2003.818246.

[5-2] Y. Maegami, M. Okano, G. Cong, M. Ohno, and K. Yamada, "Completely CMOS compatible SiN-waveguide-based fiber coupling structure for Si wire waveguides," *Opt. Express*, vol. 24, no. 15, pp. 16856–16865, Jul. 2016, doi: 10.1364/OE.24.016856.

[5-3] H. Jayatilleka, H. Shoman, L. Chrostowski, and S. Shekhar, "Photoconductive heaters enable control of large-scale silicon photonic ring resonator circuits," *Optica*, vol. 6, no. 1, pp. 84–91, Jan. 2019, doi: 10.1364/OPTICA.6.000084.

[5-4] K. Tanizawa, K. Suzuki, M. Toyama, M. Ohtsuka, N. Yokoyama, K. Matsumaro, M. Seki, K. Koshino, T. Sugaya, S. Suda, G. Cong, T. Kimura, K. Ikeda, S. Namiki, and H. Kawashima, "Ultra-compact 32 × 32 strictly-non-blocking Si-wire optical switch with fan-out LGA interposer," *Opt. Express*, vol. 23, no. 13, pp. 17599–17606, Jun. 2015, doi: 10.1364/OE.23.017599.

[5-5] P. Dong, W. Qian, H. Liang, R. Shafiiha, D. Feng, G. Li, J. E. Cunningham, A. V. Krishnamoorthy, and M. Asghari, "Thermally tunable silicon racetrack resonators with ultralow tuning power," *Opt. Express*, vol. 18, no. 19, pp. 20298–20304, Sep. 2010, doi: 10.1364/OE.18.020298.

[5-6] X. Zheng, E. Chang, P. Amberg, I. Shubin, J. Lexau, F. Liu, H. Thacker, S. S. Djordjevic, S. Lin, Y. Luo, J. Yao, J.-H. Lee, K. Raj, R. Ho, J. E. Cunningham, and A. V. Krishnamoorthy, "A high-speed, tunable silicon photonic ring modulator integrated with ultra-efficient active wavelength control," *Opt. Express*, vol. 22, no. 10, pp. 12628–12633, May 2014, doi: 10.1364/OE.22.012628.

Chapter 6
Optically-Controlled MRM Array

6.1 Overview

In Chapter 4, we introduce a Si photonics microring modulator (MRM) based electromagnetic wave visualization system designed for 5G signals within the Radio-over-Fiber (RoF) framework. In this system, off-chip antennas linked to the MRMs utilize TiN electrical heaters integrated above each MRM to facilitate modulation. As the number of MRM channels increases, the associated complexity grows with the rising count of RF cables connecting to off-chip antennas and the wires leading to the external DC power supply for the electrical heaters. This complexity poses challenges to system operation and impedes efforts towards further system miniaturization. To address this, we propose an on-chip integration approach for the RF antenna and suggest replacing the electrical heater with the optical heater described in Chapter 5. This strategic shift eliminates a considerable number of electrical connections, enhancing system simplicity. This chapter details the implementation of this novel approach.

Initially, we introduce the concept of an MRM array utilizing an optical heating method. We determine the design parameters for the modulation section of the MRM and the doping segment of the optical heater through numerical calculations. Subsequently, based on simulation results, we design a 4-channel MRM array capable of optical control. Further, we explore the fundamental optical transmission characteristics, modulation features, and optical control attributes of the fabricated optically controllable MRM array. The investigation also delves into the feasibility of optically controlled MRM modulation function. It is crucial to highlight that this study serves as a proof-of-concept experiment (POC), validating the feasibility of using light for controlling the modulation selection of multiple MRMs. This paves the way for the realization of an all-optical controlled MRM imaging system.

6.2 Design

6.2.1 Concept

The proposed device is depicted in Fig. 6-1(a). The fundamental concept involves selecting each MRM through control optical power and modulating the incident light near the laser wavelength. The directional coupler used in the optical control device in Chapter 5 separates the pre-multiplexed control light from the signal light. The control light (red arrow) is injected into the upper waveguide and partially absorbed by the highly doped n+ region. Four MRMs were utilized in this study. Since each MRM is identical (except for the optical control part), when the control light is off, the optical output spectrum of the bus waveguide appears as shown at the top of Fig. 6-1(b) (the resonance wavelengths of each ring are nearly aligned). On the other hand, when the control light power is increased, each MRM is sequentially heated, and each transmission spectrum changes, as illustrated in the left column of Fig. 6-1(b). Let ΔP represent the control power to shift the resonance wavelength of any MRM from the initial state to $\Delta\lambda$ (to bring it near the laser wavelength). Thus, the total control power to shift the fourth MRM to $\Delta\lambda$ is $10\Delta P$. With proper design, all four MRMs can be sequentially shifted to the laser wavelength within the input light power limit, enabling selection of each MRM for modulation.
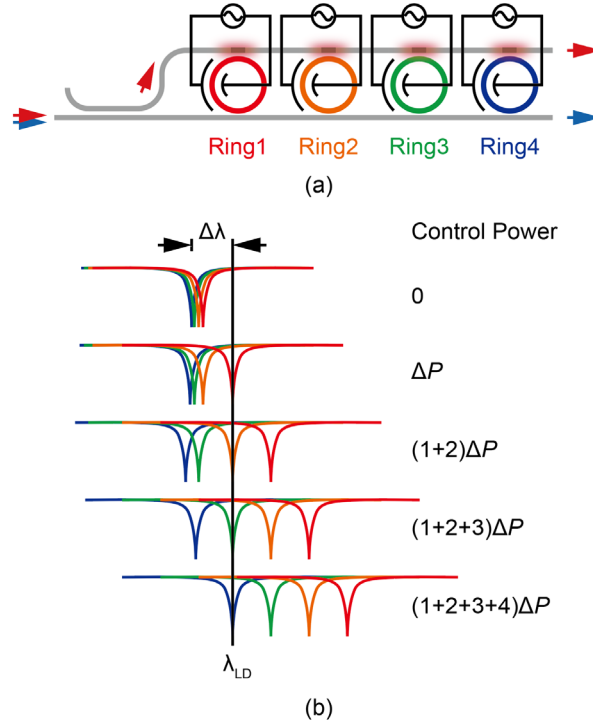
Figure 6-1 (a) Concept of optically controllable MRM array. (b) Schematic resonance shifts of MRMs against the laser wavelength when employing appropriate control powers and absorption ratios.

6.2.2 Design of Modulator Portion

The modulation part of the aforementioned MRM was designed with the center wavelength of the light set to 1550 nm. The conceptual diagram of the modulation section is presented in Fig. 6-2(a). The entire MRM comprised a ribbed waveguide of 220 nm with 110 nm partially etched. The waveguide width w is 500 nm. In contrast to the MRMs shown in Chapter 3, the area available for n-type doping was considerably limited here due to the addition of the optical control part. Adhering to the foundry design rule, the angle of gyration of the modulation region (Full-Doped) was set to 60°. The radius of the MRM, R_{MRM}, was fixed at 10 µm as in Chapter 3. The MRM is in the form of a racetrack, with the coupling length to the bus waveguide denoted as L_c, and the coupling gap as G_c. Figure 6-2(b) provides a cross-sectional view of the waveguide. The distance W_{pn} from the high-doping region to the center of the waveguide is 0.65 µm, representing the maximum W_{pn} proven for previously designed MRMs. Shown below in (b) is the optical mode profile for the full-doping state calculated using Lumerical CHARGE and the FDE solver. The calculation conditions are detailed in Table 6-1, considering a bending radius of 10 µm. The calculated propagation loss $Loss_1$ is 47.42 dB/cm, n_{eff1} is 2.609, and n_{g1} is 3.887. The cross-section and optical mode profile of the half-doped waveguide are displayed in (c). The propagation loss $Loss_2$ is 30.48 dB/cm, n_{eff2} is 2.610, and n_{g2} is 3.881. For both optical modes, a small amount of light leakage was visible due to the bending at 10 µm, but the loss due to doping was at the same level, so the difference was not significant.

From the above results, the total $Loss_{Total}$ of one MRM cycle due to doping is:

$$Loss_{Total} = \left(\frac{2\pi}{3} Loss_1 + \frac{4\pi}{3} Loss_2 \right) R_{MRM} = 0.227 \text{ dB} \qquad (6\text{-}1)$$

In this calculation, we neglected the losses in the linear part due to its short length. Here, a, r, and k are defined as the ring's single-pass amplitude transmission, self-coupling coefficient, and cross-coupling coefficient, respectively. α represents the power attenuation coefficient, and κ is defined as the power coupling ratio (Fig. 6-3) [6-1]. When there is no coupling loss, $r^2 + k^2 = 1$

is satisfied. When the critical coupling condition ($1-a^2=k^2$) is met, the power coupling ratio with the bus waveguide κ is:

$$\kappa = k^2 = 1 - a^2 = 1 - \exp(-\alpha L) = 1 - \left(\exp(-Loss_{\text{Total}})\right) = 0.203 \qquad (6\text{-}2)$$

Since the doping loss is slightly smaller than the design value for the device actually fabricated by AIST, the coupling ratio κ must also be set to a smaller value. In this case, κ is set to 0.053, 0.103, and 0.203. The corresponding Q factors are calculated using Eq. 6-3.

$$Q = \frac{\pi n_{\text{g}} L \sqrt{ra}}{\lambda(1-ra)} \qquad (6\text{-}3)$$

Here, $a = \exp(-Loss_{\text{Total}}/2) = 0.892$, where $r = \sqrt{1-\kappa} = 0.973, 0.947, 0.893$. Thus, the Q factors are 3499, 2934, and 2173, respectively. The optical bandwidth is wider than the Sub-6 GHz band.

We also calculated the coupling parameters that could realize the three κ values, using Lumerical's FDTD solver to compute the relationship between the power coupling ratio κ and the coupling. The simulation model is illustrated in Fig. 6-4. The power coupling ratio is calculated using the S-parameters extracted from each port: $\kappa = |S_{\text{Tap}}|^2/|S_{\text{In}}|^2$. The calculation conditions are detailed in Table 6-2, and the results are depicted in Fig. 6-5. A 2 µm L_{c} is required to achieve a κ of 0.203. In this case, the coupling gap G_{c} is 259 nm, 328 nm, and 395 nm, respectively.

Table 6-1 Simulation condition of MRM

Wavelength	1550 nm
n_{Si}	3.48
n_{SiO2}	1.44
n+ concentration	2.27273×10^{20} cm^{-3}
n concentration	7.31818×10^{17} cm^{-3}
p+ concentration	2.27273×10^{20} cm^{-3}
p concentration	8.13636×10^{17} cm^{-3}
Max mesh size	0.01 µm

Table 6-2 Simulation condition of directional coupler

Wavelength	1550 nm
n_{Si}	3.48
n_{SiO2}	1.44
Accuracy	2
Boundary Condition	PML
Port size	2.5×2 µm^2
Max mesh size	0.01 µm
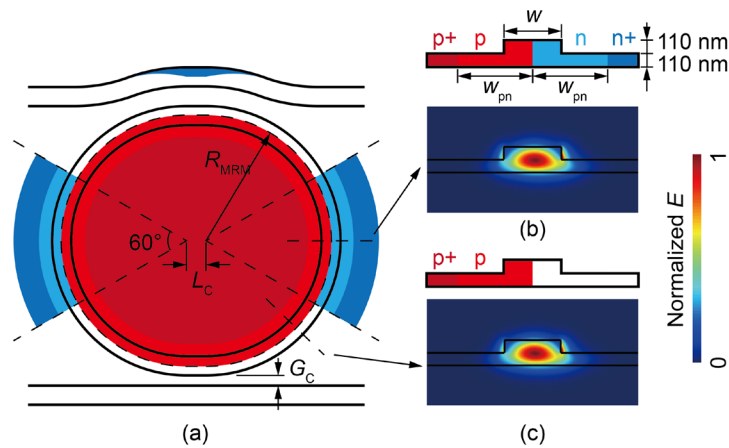
Figure 6-2 (a) Configuration of proposed MRM. (b) The cross section of fully doped waveguide and the modal profile of propagated light calculated by Lumerical FDE solver. (c) The half-doped waveguide and its modal profile. $w = 0.5$ µm, $W_{\text{pn}} = 0.65$ µm. Modal profiles was calculated with a 10-µm bending, which is also the radius of designed MRM.
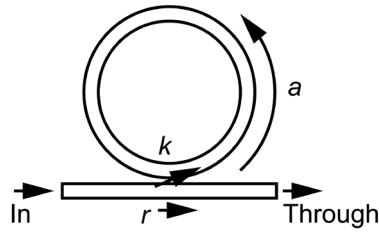
Figure 6-3 Definition of All-Pass MRR parameters. *r*: self-coupling coefficient, *k* (not κ): cross-coupling coefficient, *a*: single-pass amplitude transmission.
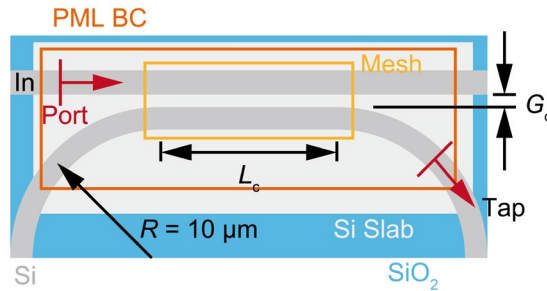
Figure 6-4 Lumerical FDTD simulation model for power coupling ratio κ calculation of directional coupler. κ is calculated as $\kappa = |S_{Tap}|^2/|S_{In}|^2$, which S_{Tap} and S_{in} are extracted S parameter from Tap and In Ports.
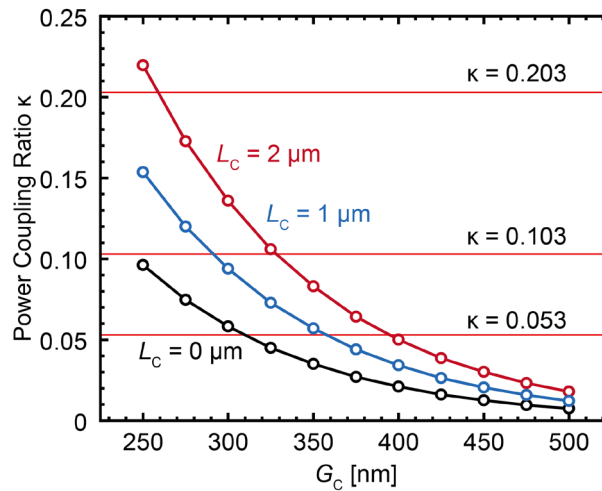
Figure 6-5 Power coupling ratio κ of bus-ring couple region with different couple length L_c and couple gap G_c, calculated using Lumerical FDTD solver. Target κ is 0.203 for achieving $Q = 2173$, but we also set smaller κ to prevent the impact of manufacturing variation. We set L_c at 2 μm in our design.

6.2.3 Design of Optical Control Portion

The optical control portion was also designed, as illustrated in Fig. 6-6, showing the basic concept. To shift the resonance spectra of the four MRMs sequentially and equally spaced by optical absorption, each control waveguide must be doped to a different degree. The doping region where the control light first enters should have the weakest absorption coefficient. The control light power is denoted as P_{in}, and the remaining control light power after passing through the four MRMs is referred to as P_1 to P_4, respectively. The optical power transmission coefficient of each doping region is denoted by a_1 to a_4, respectively (when $a = 1$, there is no loss, note that a here is different from that in Section 6.2.2.). Thus, we obtain the relationships shown in Eqs. 6-4 and 6-5.
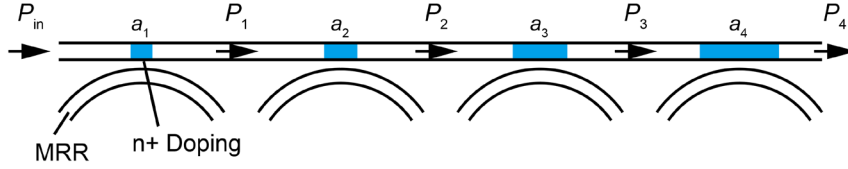
Figure 6-6 Concept of 4-channel optically controlled MRM array. Each MRM is placed adjacent to a n+ doped region with different power transmission ratio a, which achieved by changing the length or width of doped region.

$$\begin{cases} P_1 = a_1 P_{in} \\ P_2 = a_2 P_1 \\ P_3 = a_3 P_2 \\ P_4 = a_4 P_3 \end{cases} \qquad (6\text{-}4)$$

$$\begin{cases} P_{in} - P_1 = 4\Delta P \\ P_1 - P_2 = 3\Delta P \\ P_2 - P_3 = 2\Delta P \\ P_3 - P_4 = \Delta P \end{cases} \qquad (6\text{-}5)$$

The ΔP here represents the power used to shift each MRM $\Delta\lambda$ from its initial state, as shown in Fig. 6-1. Equations 6-4 and 6-5 lead to Eq. 6-6, describing the relationship between ΔP, P_{in}, and each propagation ratio.

$$\frac{\Delta P}{P_{in}} = \frac{1}{4}(1 - a_1) = \frac{1}{7}(1 - a_1 a_2) = \frac{1}{9}(1 - a_1 a_2 a_3) = \frac{1}{10}(1 - a_1 a_2 a_3 a_4) \qquad (6\text{-}6)$$

Then,

$$a_2 = \frac{7}{4} - \frac{3}{4a_1}, a_1 a_2 = \frac{7}{4}a_1 - \frac{3}{4} \qquad (6\text{-}7)$$

$$a_3 = \frac{9}{7} - \frac{8}{49a_1 - 21}, a_1 a_2 a_3 = \frac{9}{4}a_1 - \frac{5}{4} \qquad (6\text{-}8)$$

$$a_4 = \frac{10}{9} - \frac{4}{81a_1 - 45}, a_1 a_2 a_3 a_4 = \frac{5}{2}a_1 - \frac{3}{2} \qquad (6\text{-}9)$$

Since each power propagation ratio is always within the range of (0,1), the above equations yield the relationships shown in Eqs 6-10 to 6-13.

$$a_1 \in (0,1) \Rightarrow a_1 \in (0,1) \qquad (6\text{-}10)$$

$$a_2 \in (0,1) \Rightarrow a_1 \in (\frac{3}{7},1) \qquad (6\text{-}11)$$

$$a_3 \in (0,1) \Rightarrow a_1 \in (\frac{5}{9},1) \qquad (6\text{-}12)$$

$$a_4 \in (0,1) \Rightarrow a_1 \in (\frac{3}{5},1) \qquad (6\text{-}13)$$

From Eqs. 6-10 to 6-13, it can be seen that a_1 must be kept within the range of (3/5, 1). In this case, the maximum value of ΔP is 1/10 of P_{in} (Eq. 6-14). Since the maximum input power to the Si SSC is 40 mW [6-2], the maximum value of ΔP is 4 mW. To thermally tune the resonance wavelength of the MRM by as much as the half-width FWHM (FWHM = 0.44 nm when the Q factor is 3499), a thermal tuning efficiency of 0.11 nm/mW is required. Since the thermal tuning efficiency of the optical control reported in [6-2] was 0.25 nm/mW, the target can be achieved if a thermal tuning efficiency of about half of that is realized.

$$a_1 = 1 - \frac{4\Delta P}{P_{in}} \in (\frac{3}{5}, 1) \Rightarrow \frac{\Delta P}{P_{in}} \in (0, \frac{1}{10}) \tag{6-14}$$

Next, we designed the control section to achieve a specific optical power propagation ratio. Figure 6-7(a) illustrates the fundamental structure of the control section, featuring a control waveguide with four arcs, each with a 20-degree angle of gyration, and a straight waveguide with a length of L_c at the center. Doping regions are situated at the center of the straight waveguide and on the left and right arcs. Unlike a rectangular shape, as shown in Fig. 6-6, the doping shape gradually spreads in the direction of light propagation, promoting a more uniform heat distribution. The width of the control waveguide w is consistent with that used for the MRM. The control waveguide and MRM are connected by ribs (not shown here), with a spacing of G_{OH} between the waveguides. In Fig. 6-7(b), a magnified view of the doping region is presented. The width of the overlap between the doping region and the waveguide is denoted as D, with its maximum value (the straight part) represented as d. Along the light propagation direction, if the position coordinate L, where doping begins, is 0, the relationship $D(L)$ between the doping overlap D and L is established, as shown in Fig. 6-7(c). The relationship $\alpha(D)$ between the doping loss α and the doping overlap width D of the controlled waveguide is depicted in Fig. 6-7(d). We anticipate the greatest rate of change in propagation loss due to doping when the waveguide is half-doped; for $D > w$ or $D < 0$, the doping loss changes minimally. From (c) and (d), we determine the doping loss $\alpha(L)$ at each position in each optical propagation direction. Integrating $\alpha(L)$ with respect to L provides the total doping loss of the waveguide. Since the relationship between the doping loss α and the optical power propagation ratio a is $a = \exp(-\alpha/2)$, the optical power propagation ratio a of the control waveguide for each MRM can be calculated using Eq. 6-15.

$$a = \exp\left[-\frac{1}{2}\int_0^{l_3} \alpha(L)dL\right] \tag{6-15}$$

Figure 6-8(a) depicts the relationship between doping loss and doping overlap width D calculated by Lumerical's CHARGE and FDE solvers. The calculation conditions are detailed in Table 6-3. The trend illustrated in Fig. 6-7(d) is confirmed: for $D < 0$, the actual foundry design rule has a minimum width limit for the doping area, so doping is placed outside the waveguide range, and thus the loss is not zero. The optical power propagation ratio a was varied by adjusting the maximum doping width d of the control waveguide of each MRM according to Eq. 6-15. The calculation results are shown in Fig. 6-8(b). Here a_1 was calculated from Eq. 6-15, while a_2 to a_4 were calculated from Eqs. 6-7, 6-8, and 6-9, respectively. From Eq.6-13, a_1 must be greater than 3/5, and d must be greater than 0. Therefore, we set the values of d to 0.05 μm and 0.075 μm. When d_1 is 0.05 μm, a_1 is 0.663. Equations 6-7 and 6-8 are depicted in Fig. 6-8. From Eqs. 6-7, 6-8, and 6-9, a_2 is 0.619, a_3 is 0.589, and a_4 is 0.651. The corresponding d for each can be taken from the curve of a_1. The final a and d are shown in Table 6-4.

Table 6-3 Simulation condition of optical heater

Wavelength	1550 nm
n_{Si}	3.48
n_{SiO2}	1.44
n+ concentration	2.27273×10^{20} cm^{-3}
Max mesh size	0.01 μm

Table 6-4 Two types of parameters for control waveguide for each MRM (Unit of d: μm)

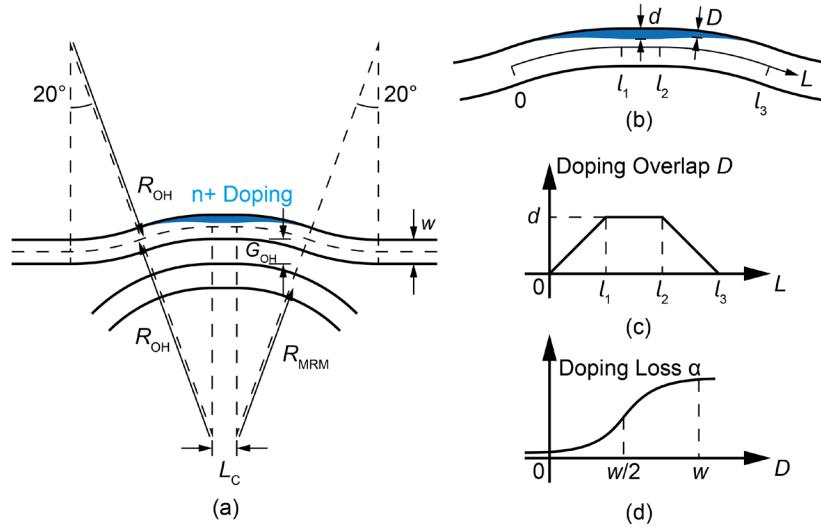| Type	(a_1, d_1) [d: μm]	(a_2, d_2)	(a_3, d_3)	(a_4, d_4)
1	(0.663, 0.05)	(0.619, 0.075)	(0.589, 0.09)	(0.651, 0.057)
2	(0.618, 0.075)	(0.537. 0.12)	(0.426, 0.18)	(0.325, 0.24)

Figure 6-7 (a) Designed optically controlled region with a partially n+ doped waveguide. The two waveguides are connected by a half-etched silicon slab, which is not shown here. The control section consists of 4 arc waveguides with a 20-degree central angle and straight waveguides. The width of the control waveguide w is the same as the MRM's. (b) Enlarged view of the doping region. The overlap between the doping region and the waveguide is represented as D, while the maximal overlap at the straight part is denoted as d. (c) Relationship between doping overlap D and the position L along the waveguide shown in (b). (d) Estimated doping loss (α) with increasing D. When $D < 0$, the propagated light is still affected by the doped region in the actual situation due to the design rule restriction that the doped region cannot be shaped with sharp vertices, as shown in (a).
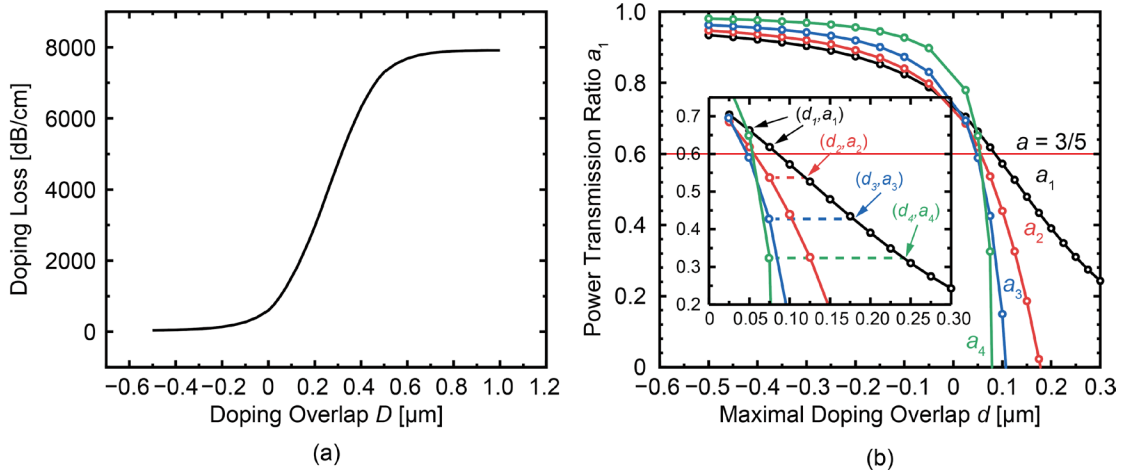
Figure 6-8 (a) Simulated loss of a doped waveguide with different doping overlap D using Lumerical CHERGE and FDE solver. (b) Calculated power transmission ratio a_1 with different maximal doping overlap d. In this context, a_2, a_3, a_4 were computed from a1 using Eq. 6-7~6-9 and plotted in the same graph. As $a_1 > 3/5$ and d should be positive, we set $d_1 = 0.05$ μm and 0.075 μm. Subsequently, the values of a_2~a_4 and their corresponding d were determined. The inset provides an enlarged view, showcasing a and d with $d_1 = 0.075$ μm in this graph.

6.2.4 CAD Design

Next, an optically controlled MRM array and its TEG pattern were designed. Figure 6-9 presents an overall view of the CAD layout, featuring a width of 5 mm and a height of 1.13 mm. There are 18 types of optically controlled MRM arrays and 2 types of optically controlled MRMs alone, with the parameters detailed in Table 6-5. The 18 types of arrays encompass three variations of the coupling gap G_c in the coupling part, three types of waveguide spacing G_{OH} in the optical control part (0.5 μm, 1.0 μm, 1.5 μm), and two types of maximum doping width d. The TEG pattern comprises two types of G_c and two types of d_4.

In Fig. 6-10, an enlarged CAD diagram of the SSC is depicted with a tip width of 160 nm. The incident light enters the MRM through a 680 μm long directional coupler, featuring a coupling gap of 270 nm, similar to the design in [6-2]. The MRM spacing is 200 μm. Figure 6-10(b) provides a closer view of the modulation section, adhering to the design rule that the minimum width of the n, n+ doping layer is 4 μm. The minimum distance between the control waveguide and the Rib layer is 100 nm to avoid just-edging, which was ignored in AIST5. The three-dimensional view is presented in Fig. 6-10(c).

6.3 Fabricated Device

The designed device was fabricated using the MPW project at AIST. Figure 6-11 depicts a full image of the chip along with a magnified view of each part. As illustrated in Fig. 6-11(b), this design comprises an MRM array with four channels. Following the previously mentioned design, a total of 20 MRM arrays were fabricated, with half of them rotated 180 degrees and placed at the right end to conserve space. Within the same array, four MRMs share identical designs, differing only in the doping widths at the optical heater. Additionally, two types of single rings were prepared (located at the top of row 3 and row 4 in Fig. 6-11(b)). An optical heater was integrated on top of each MRM.
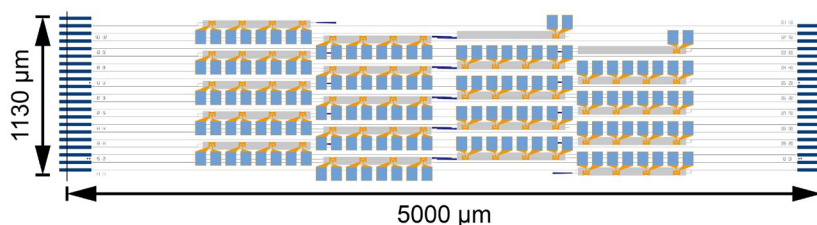
Figure 6-9 Layout of designed optically controlled MRM array.
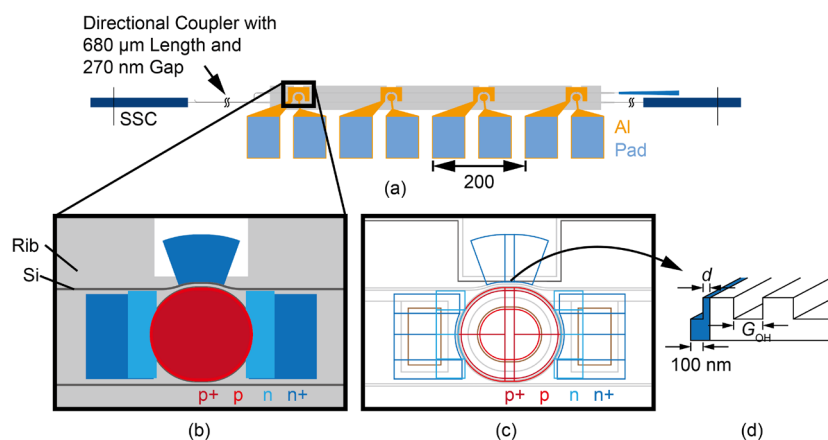
Figure 6-10 (a) Detailed layout of each MRM array. (b) Enlarged view of modulation region without Al and contact layer. (c) Outline of (b). (d) Cross sectional view of the edge at doping region. There is a bump in the control waveguide to avoid the just-edge circumstance.

140
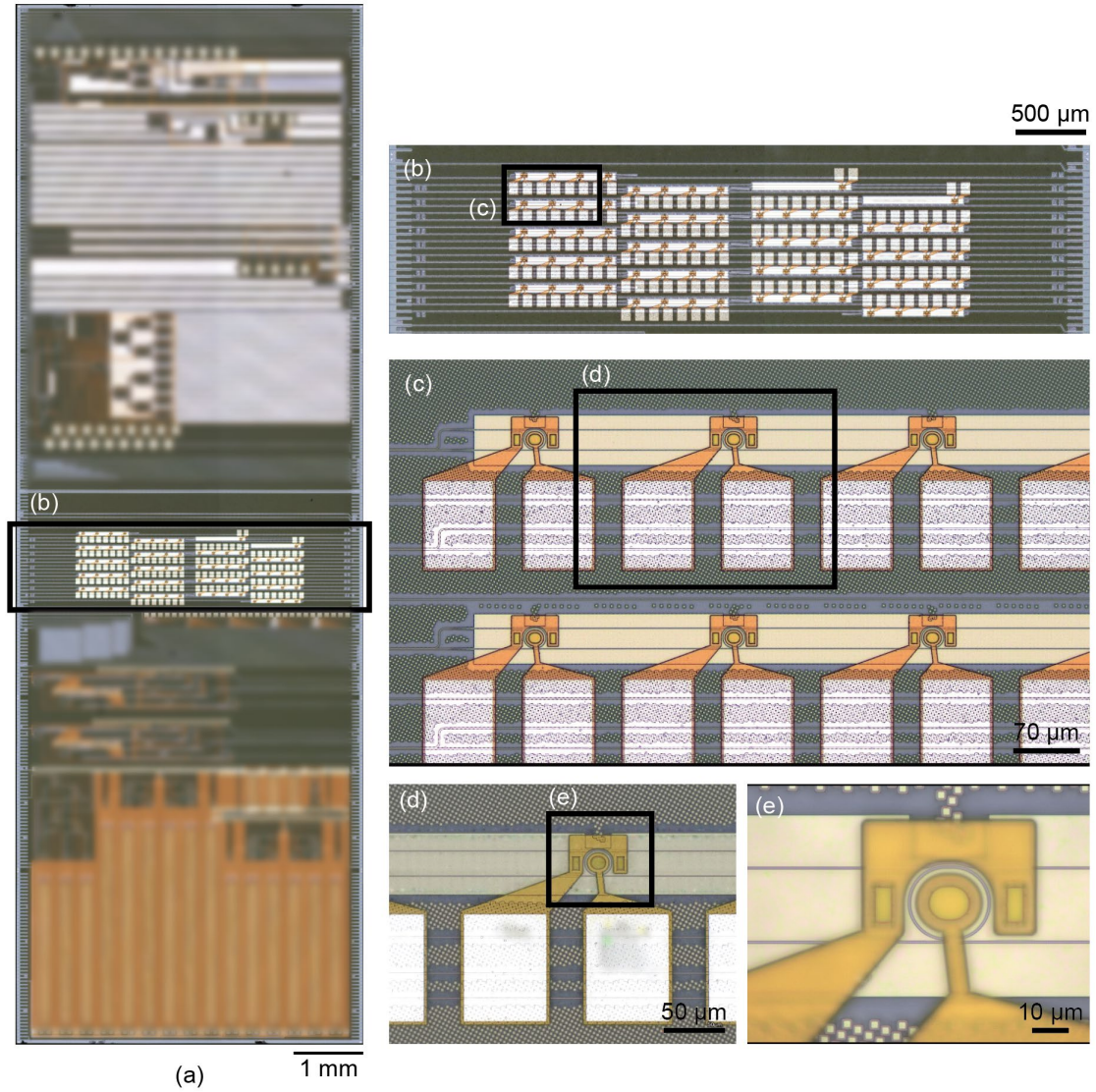
Figure 6-11 Photograph of the entire chip and enlarged view of each part.

6.4 Fundamental Characteristics

6.4.1 Optical Transmission

Figure 6-12 display the transmission spectra of the respective devices (chip AIST8 A1). The spectra were linearly scaled for subsequent fitting. The reference waveguide was measured as well; however, this result was not normalized by the reference waveguide, as we consider that the MRM parameters have a lesser influence on the fitting result. Both transmission spectra exhibit the form of the product of the sine function, representing the transmission characteristic of the directional coupler, and the four MRM transmission functions (Lorentz functions). Therefore, they can be fitted to the function as shown in Eq. 6-16.

$$T = \left[A\sin(B\lambda + C) + D\right] \cdot \prod_{m=1}^{N} \frac{a_m^2 - 2a_m r_m \cos(2\pi n_m L / \lambda) + r_m^2}{1 - 2a_m r_m \cos(2\pi n_m L / \lambda) + \left(a_m r_m\right)^2} \qquad (6-16)$$

where A, B, C, and D are parameters associated with the directional coupler, a_m and r_m represent the one-round amplitude propagation coefficient and self-coupling coefficient of each MRM, and n_m is the equivalent refractive index of each MRM. Although the design of each MRM is identical, slight variations in nm occur due to production errors. Similarly, a_m and r_m also

deviate slightly during production; however, as these deviations do not significantly impact the results, we assume that the a_m and r_m of MRMs in the same array are consistent. Under these conditions, the data were fitted using OriginPro. The fitting procedure is described next:

1. Fit only the sine function term in Eq. 6-16, excluding the resonance peaks in the data.
2. Fix the obtained A, B, C, and D, leaving only the resonance peak in the center of the data, and fit with Eq. 6-16.
3. Set $a_m = r_m = 0.99$ and manually fit the equivalent refractive indices of each MRM to the peaks.
4. Finally, fix each equivalent refractive index and fit a_m and r_m.

The fitting results are also displayed in Fig. 6-12. Due to wavelength dispersion, the refractive indices vary at each wavelength. In this case, the data points around 1550 nm served as the center for the fitting. The extracted parameters for each MRM are presented in Table 6-6. a and r are indistinguishable in the fitting, but they can be compared with the target value to differentiate between a and r. The results indicate that the measured r and target r values align quite well. The Q factor is also approximately 2000-4000. Figure 6-13 illustrates the measured r values converted to κ and compares them with the target κ. All three devices were within ± 0.02 of the target value. Additionally, the doping loss in the modulator section was as intended, given the proximity of several MRMs to critical coupling conditions.

Table 6-5 Design parameters for optically controlled MRM arrays.

Device No.	G_C	Target κ	Target r	L_C	G_{OH}	d_1	d_2	d_3	d_4
Unit	nm	1	1	μm	μm	μm	μm	μm	μm
1	259	0.203	0.89	2	0.5	0.05	0.075	0.09	0.057
2	328	0.103	0.95	2	0.5	0.05	0.075	0.09	0.057
3	395	0.053	0.97	2	0.5	0.05	0.075	0.09	0.057
4	259	0.203	0.89	2	0.5	0.075	0.12	0.18	0.24
5	328	0.103	0.95	2	0.5	0.075	0.12	0.18	0.24
6	395	0.053	0.97	2	0.5	0.075	0.12	0.18	0.24
7	259	0.203	0.89	2	1	0.05	0.075	0.09	0.057
8	328	0.103	0.95	2	1	0.05	0.075	0.09	0.057
9	395	0.053	0.97	2	1	0.05	0.075	0.09	0.057
10	259	0.203	0.89	2	1	0.075	0.12	0.18	0.24
11	328	0.103	0.95	2	1	0.075	0.12	0.18	0.24
12	395	0.053	0.97	2	1	0.075	0.12	0.18	0.24
13	259	0.203	0.89	2	1.5	0.05	0.075	0.09	0.057
14	328	0.103	0.95	2	1.5	0.05	0.075	0.09	0.057
15	395	0.053	0.97	2	1.5	0.05	0.075	0.09	0.057
16	259	0.203	0.89	2	1.5	0.075	0.12	0.18	0.24
17	328	0.103	0.95	2	1.5	0.075	0.12	0.18	0.24

18	395	0.053	0.97	2	1.5	0.075	0.12	0.18	0.24
19	328	0.103	0.95	2	1	0.057	--	--	--
20	395	0.053	0.97	2	1	0.24	--	--	--

Table 6-6 Extracted parameters by fitting.

Device	r	a	Q	Device	r	a	Q
1	0.88	0.91	2480	11	0.93	0.91	3238
2	0.94	0.91	3388	12	0.97	0.89	3805
3	0.97	0.89	3729	13	0.90	0.89	2440
4	0.89	0.89	2384	14	0.94	0.90	3246
5	0.94	0.90	3143	15	0.97	0.90	4098
6	0.97	0.90	3903	16	0.90	0.90	2489
7	0.90	0.90	2453	17	0.94	0.80	1867
8	0.94	0.90	3289	18	0.97	0.90	3872
9	0.97	0.91	4290	19	0.94	0.90	3303
10	0.90	0.90	2575	20	0.97	0.90	3988
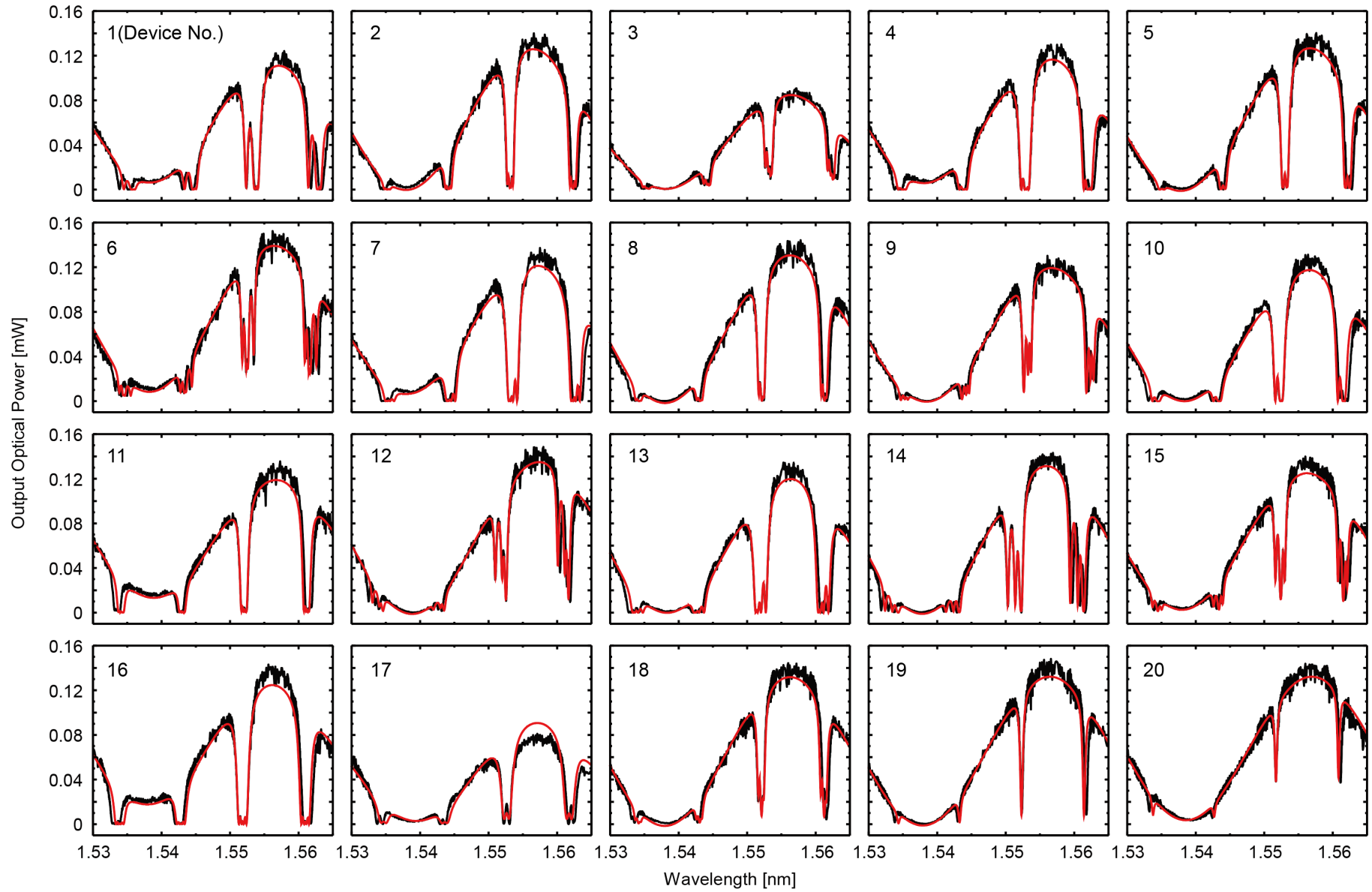
Figure 6-12 Transmission spectra and fitting curves (linear scale) for each MRM array.
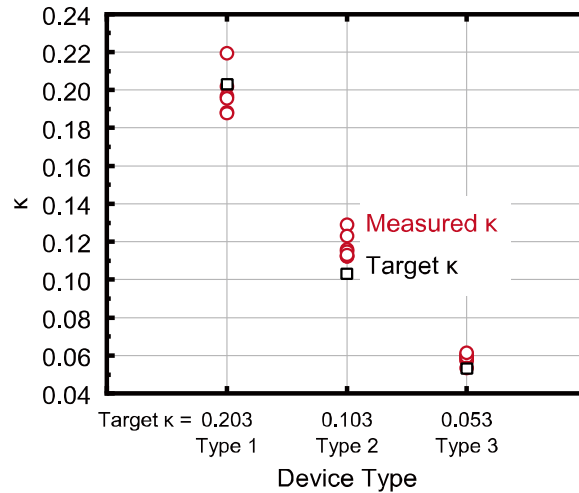
Figure 6-13 Comparison of measured κ with design values.
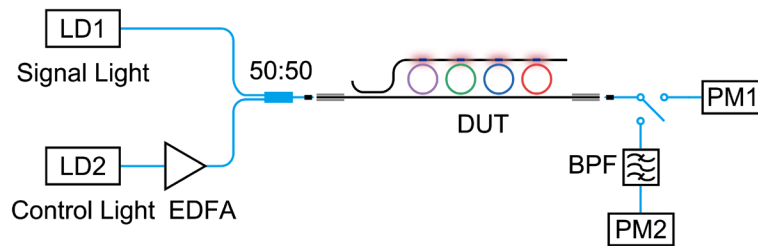
Figure 6-14 Experimental system for optical control.

6.4.2 Optical Control

A.Measurement Setup

To verify the function of the optical heater, optical control experiments were initially conducted using three different chips (A1, J2, and P2). Figure 6-14 illustrates the experimental setup for optical control. Low-power signal light and high-power control light, amplified by EDFA, were pre-multiplexed through a 2by1 coupler and input to the device via a lensed fiber. An on-chip directional coupler directed the control light to the control portion. An optical heater near each MRM gradually absorbed the control light and heated a portion of the MRM. A signal light with a specific wavelength was coupled inside the MRMs and modulated in intensity. The modulated light was output from the bus waveguide and input to the power meter through an optical switch and bandpass filter.

However, the coupling loss of the 2by1 coupler used is 3.77 dB (from the output port of the EDFA to the output port of the 2by1). The coupling loss between the lensed fiber and the SSC for each side is [9.2 dB(transmission loss from the output of 2by1 coupler to the PM) – 0.37 dB(optical switch loss)]/2 = 4.42 dB, and the directional coupler coupling loss is assumed to be 0 dB. Thus, the total loss from the amplifier to the control portion of the first MRM is 8.19 dB. The center wavelength of the bandpass filter is set to the signal wavelength (around 1550 nm), and the line width is fixed at 15 nm. The wavelength at which the directional coupler can be tapped is around 1538 nm, so the control light wavelength was set to 1538 nm. The transmission spectrum of the signal light was measured using the Santec IL Swept Test System while changing the power of the incident control light. The control light power change and transmission spectrum measurement were fully automated using LabVIEW.

B.Thermo-optic Switching

The measured results are presented in Figs. 6-15 to 17, each corresponding to chips A1, J2, and P2. The horizontal axis represents the power of the light reaching the control region (heating power), while the vertical axis denotes the wavelength of the signal light. The color indicates the transmitted intensity of the signal light, with the results normalized by their respective maximum values. Several conclusions can be drawn from the results:

145

(1) The resonance wavelength of any MRM red-shifts as the control light power increases, demonstrating successful optical control.

(2) The depth of the resonance peaks varies, ranging from large to small, and each set of three devices exhibits a consistent variation cycle. This variation is attributed to the value of the G_c, which impacts the power coupling ratio between the bus waveguide and the MRR. Among the three G_c design values in this design, a lower G_c leads to a closer critical coupling.

(3) Saturation of the resonance shift is observed with the enhancement of the control light. The saturation power of the SSC is approximately 17 dBm (50 mW), and the breakdown power is around 90 mW.

(4) The initial state of each MRM differs due to fabrication errors. While the resonance wavelengths of each MRM should ideally overlap, especially in devices with odd numbers, the resonance wavelength change trajectories often intersect as the control power increases. This trend persists even after eliminating the periodicity of the measurement procedure. We suspect that the placement of odd-numbered and even-numbered devices on the chip contributes to this phenomenon, with odd-numbered devices located on the outside of the chip and even-numbered devices on the inside. Given that the same trend was observed for different shot areas, we believe the fabrication error originates from pattern density rather than the non-uniformity of shot areas. Additionally, the trajectory at the top of the resulting figure typically corresponds to R1, intersecting with other trajectories due to the blueshifted trajectory of R1. Since the pattern density at R1 is lowest for odd-numbered devices, fabrication errors are likely the cause.

(5) Odd-numbered devices are less prone to saturation, likely due to their distance from the SSC.

(6) When differences in the initial state are accounted for, a roughly evenly spaced resonance tuning is observable in the linear region (low power region), as per the design. This observation suggests that the doping is approximately formed as intended.

(7) With increasing control power, the resonance depth of each MRM weakens (extinction ratio decreases), as illustrated in Figs. 6-18 and 6-19. Primarily, we attribute this trend to the MRMs moving away from the critical coupling condition. Further discussion will now focus on identifying the parameters that have changed.

Figure 6-18(a) illustrates the optical control results for device 19 on chip P2. Device 19 serves as a test pattern for the MRM alone. With increasing control power, the resonance depth of the MRM decreased from 8 dB to 4 dB. Parameter fitting was employed to extract the one-round amplitude propagation coefficient a of the MRM and the self-coupling coefficient r of the coupling section. The fitting equation used is shown in Eq.6-16, where A, B, C, and D are parameters related to the directional coupler, a_m and r_m are the one-round amplitude propagation coefficient and self-coupling coefficient of each MRM, and n_m is the equivalent refractive index of each MRM. In the case of a single MRM, N is set to 1. Figure 6-18(b) depicts the extracted a and r.

Since a and r are completely interchangeable in Eq. 6-16, this information alone is insufficient to distinguish them. However, a and r can be distinguished by comparing the measured and designed values. It is observed that a gradually decreases with increasing control power, while r remains almost unchanged. This implies that the internal losses in the ring increase, while the coupling coefficients in the coupled sections remain constant. One possible cause of the increased internal loss is the coupling (leakage) of the signal light in the control section, which rises with increasing temperature. Since the control section can also be likened to a directional coupler with a very small coupling coefficient, the light that leaks there is considered internal loss in the MRM.

Next, we discuss the feasibility of selecting each MRM through optical control. In Fig. 6-19(a), the results of optical control for device 3 on chip J2 are presented, representing the most promising device, accounting for the initial state's effect. The resonance spectrum of each MRM is color-coded, and all four MRMs can be chosen by setting the laser wavelength to λ_{LD} in the figure. The optimal modulation operating point lies on both sides of the resonance wavelength of each MRM, allowing modulation by tuning the resonance wavelength of each MRM to both sides of the laser wavelength. However, control

power can be conserved by setting the laser wavelength to the left of the resonance wavelength in the initial state of the first MRM (R1) and to the long wavelength side of the resonance wavelength in the selected state of the last MRM (R4). Here, all four MRMs can be selected with a control power of 53.2 mW. Figure 6-19(b) displays a and r extracted from Eq. 6-16 when each MRM is thermally tuned. Similar to previous results, the coupling between the MRMs and the bus waveguide remained almost unchanged, while the internal loss of each MRM underwent significant changes. We attribute this to the alteration in coupling at the control portion.
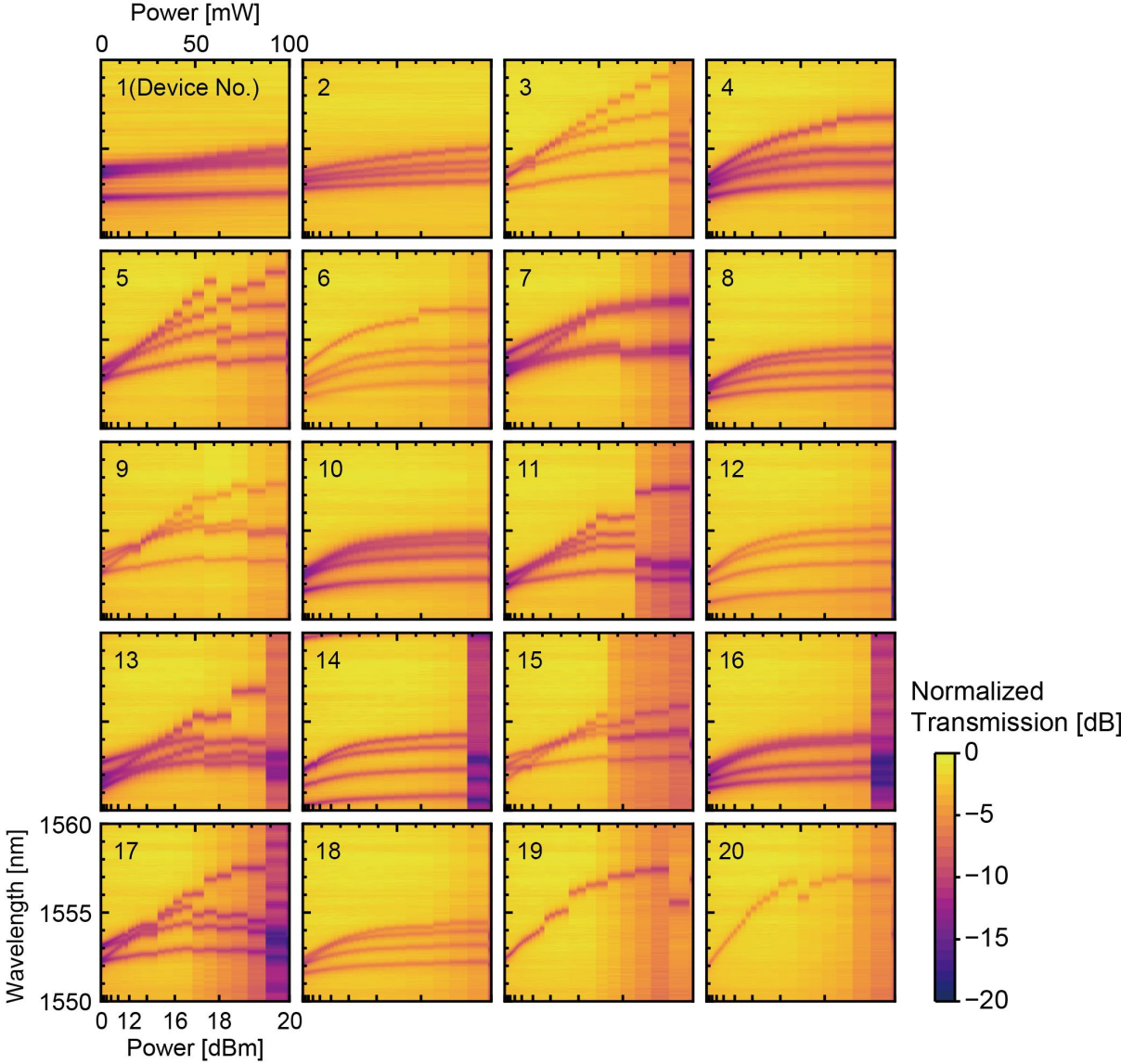
Figure 6-15 Optical control results for chip A1.
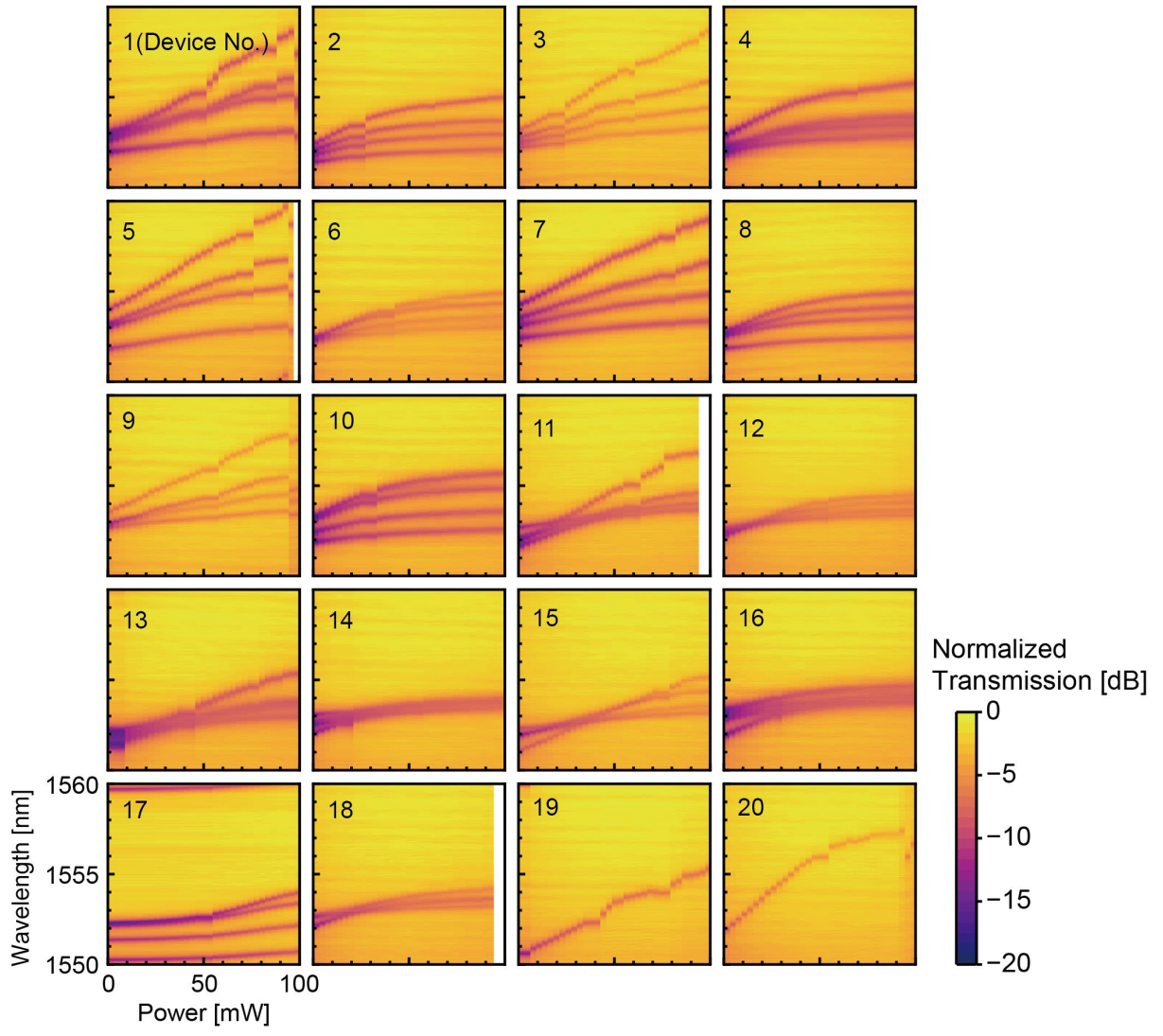
Figure 6-16 Optical control results for chip J2.
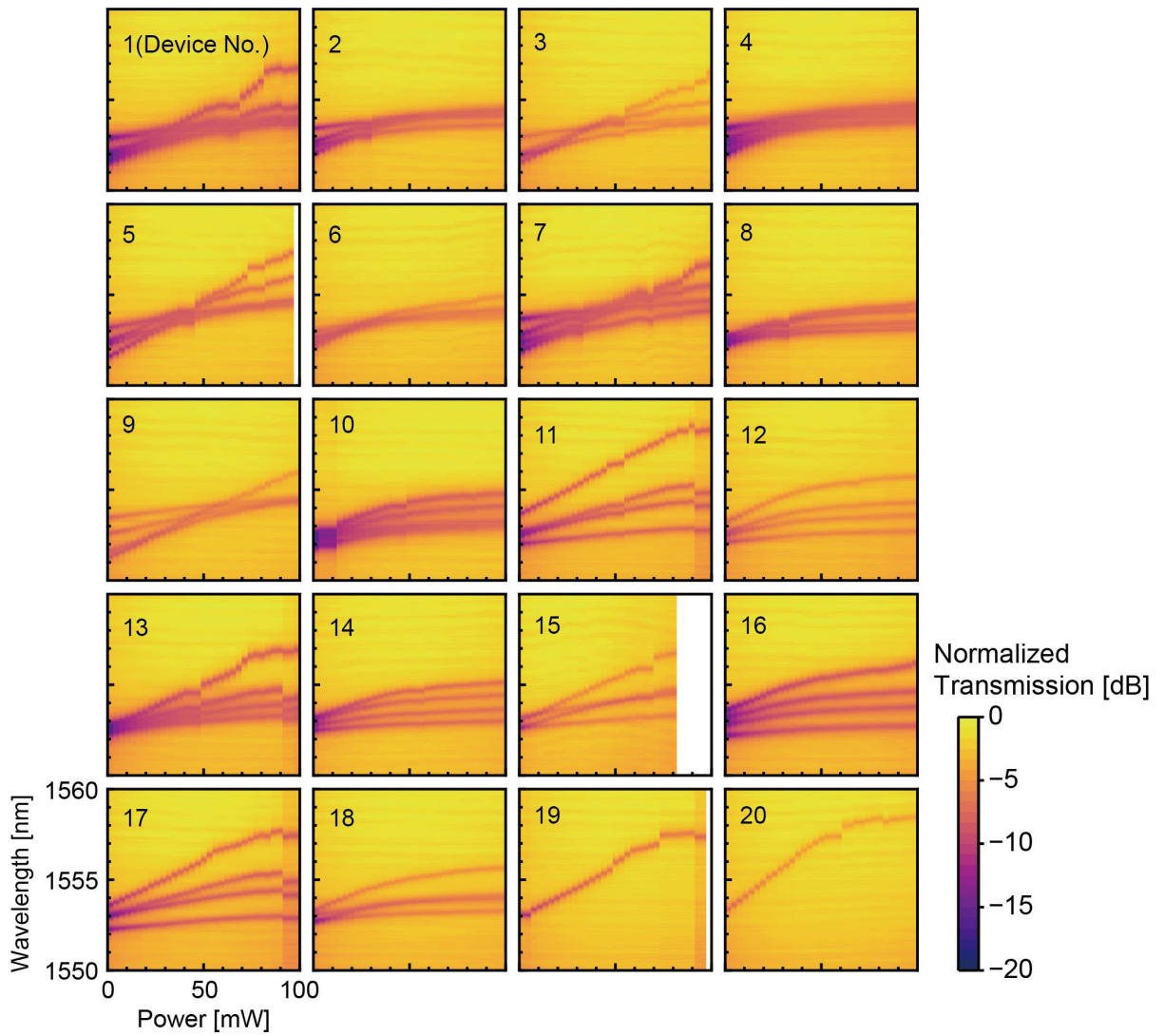
Figure 6-17 Optical control results for chip P2.
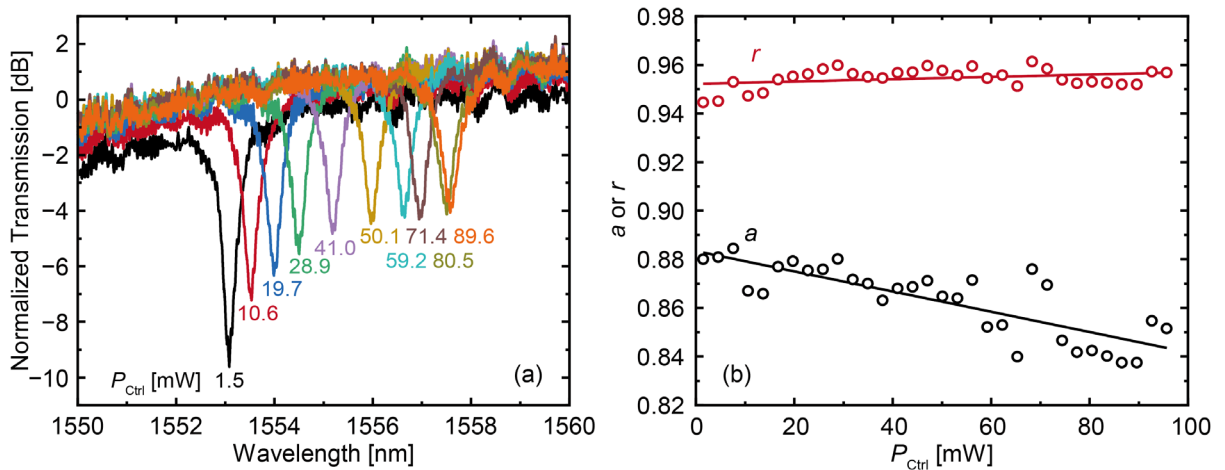
Figure 6-18 (a) Part of the optical control results for device 19 of chip P2, transmission spectrum plotted in 2D. (b) One-round propagation coefficient a and self-coupling coefficient r extracted from (a).
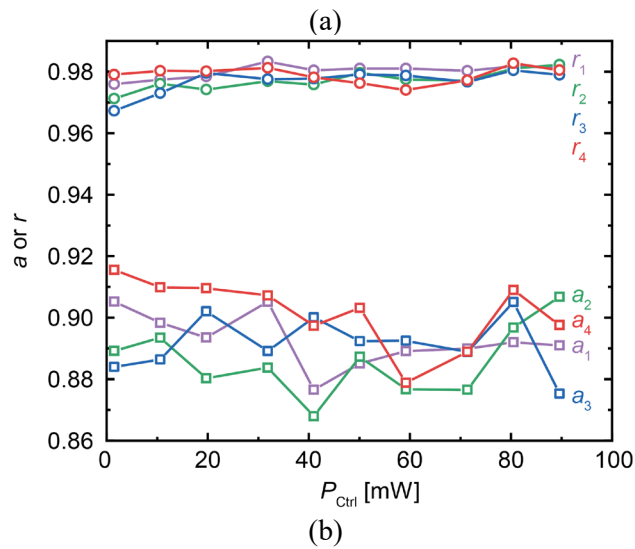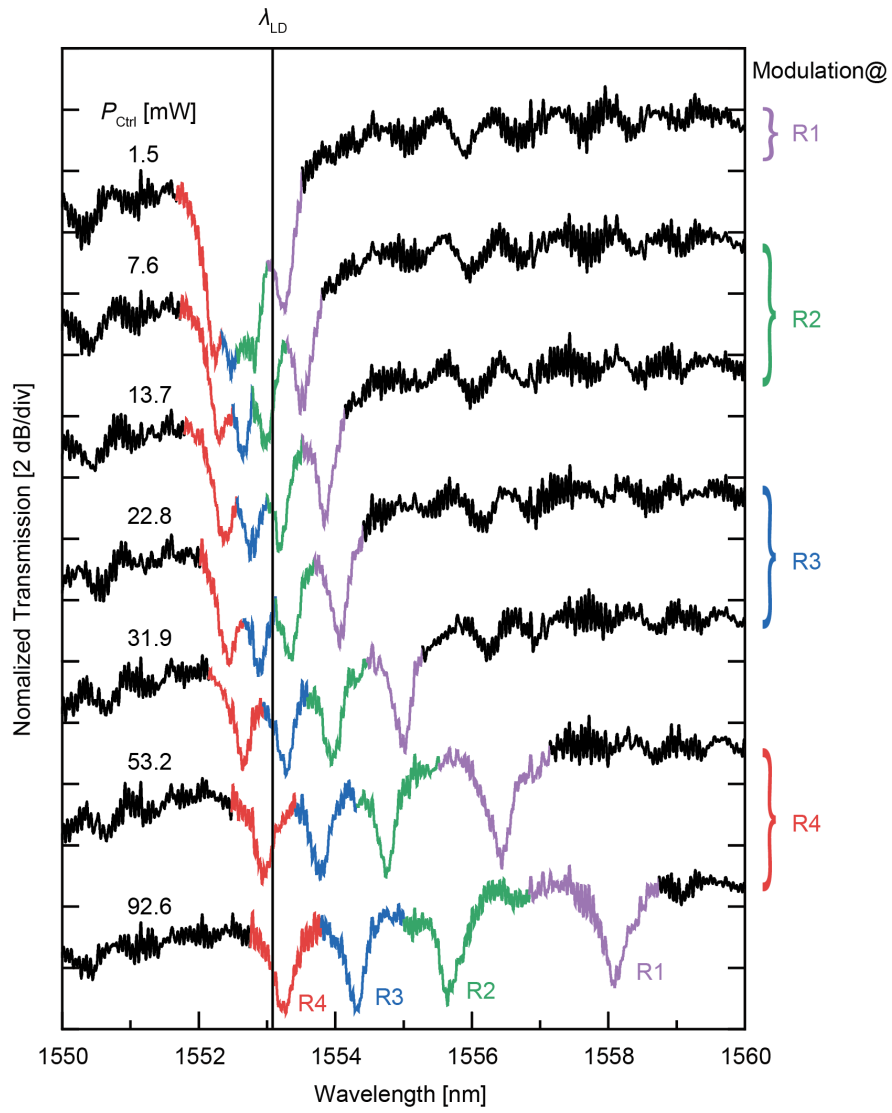
Figure 6-19 (a) Part of the optical control results for device 3 of chip J2, with transmission spectra plotted in 2D. (b) *a* and *r* for each MRM extracted from (a).

6.4.3 Modulation

The modulation characteristics of the mentioned devices were investigated. Initially, the static modulation characteristics of device 19 (MRM alone) on chip P2 were measured using the experimental setup illustrated in Fig. 6-20. In this setup, the control light was turned off, probes were sequentially applied to the four MRMs, and a DC bias voltage of 0 to −6 V was applied. The measured results are presented in Fig. 6-21(a). The transmission spectrum of the MRM red-shifts as the bias voltage increases. The modulation efficiency extracted from the resonance shift is 8.6 pm/V, with $V_\pi L = 2.37$ Vcm, which is comparable to the MRM of AIST 5 (Chapter 3) (9.94 pm/V, 2.45 Vcm [6-3]).

Next, dynamic modulation characteristics were measured when a 1 GHz RF signal was applied to the MRM (same device as above) from a signal generator (SG, hp 83640). The bias voltage was fixed at −2 V. The experimental system is depicted in Fig. 6-22. The control light was turned off, and the modulated light was injected into a photodiode (PD, Agilent 11982A) while sweeping the incident light wavelength. The output electrical signal was observed with an electrical spectrum analyzer. Figure 6-23(a) illustrates the relationship between the modulated output signal power and laser wavelength in the spectrum analyzer when the RF power was set to 0 and 10 dBm, and the laser power to 0, 5, and 10 dBm, confirming successful modulation of the MRM. The relationship between the power at each peak and the input power is summarized in Fig. 6-23(b). The nonlinearity of the MRM results in the modulation output signal power not being proportional to the RF input power.

Furthermore, all four MRMs were modulated (not simultaneously) using device 3 on chip J2. Figure 6-24 illustrates the dependence of output RF power and wavelength when a 1 GHz, 0 dBm RF signal is applied to each MRM, the bias voltage is set to −2 V, and the laser power is 0 dBm. The black line represents the transmission spectrum under the initial condition (control light OFF). All MRMs operated normally. The MRMs can be selected by thermal tuning if the laser wavelength is set to the left peak of R1, and the right peak of R4 is tuned to the laser wavelength by the control light. The initial crosstalk between R1 and R2 is 14.2 dB, and the crosstalk between R1 and R3 and R4 is more than 25 dB. The RF output spectrum of each peak is shown in Fig. 6-25.
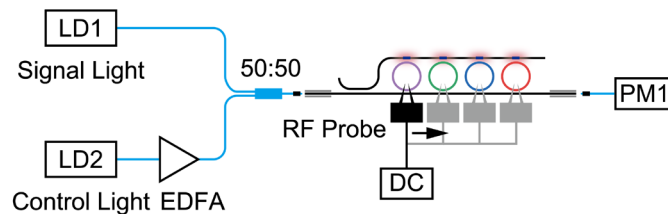
Figure 6-20 Experimental system for measuring static modulation characteristics.
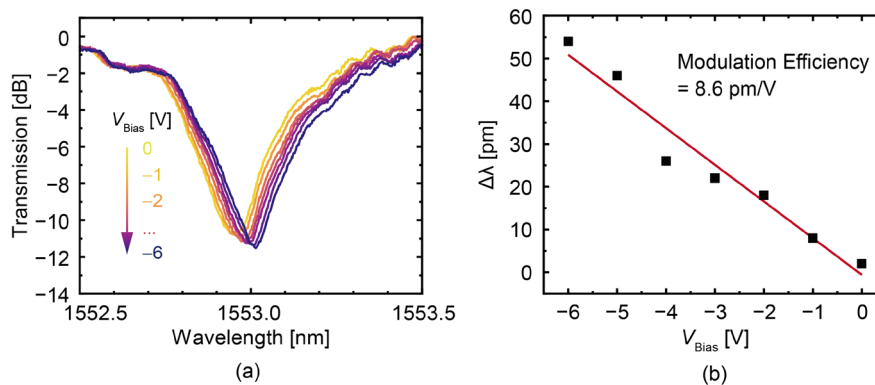
Figure 6-21 Static modulation characteristics of Chip P2, Device 19. (a) Resonance shifts with bias voltage. (b) Extracted modulation efficiency.
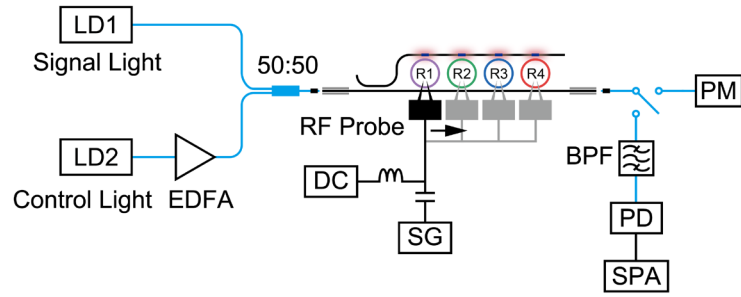
Figure 6-22 Experimental system for measuring dynamic modulation characteristics.

(a)

(b)
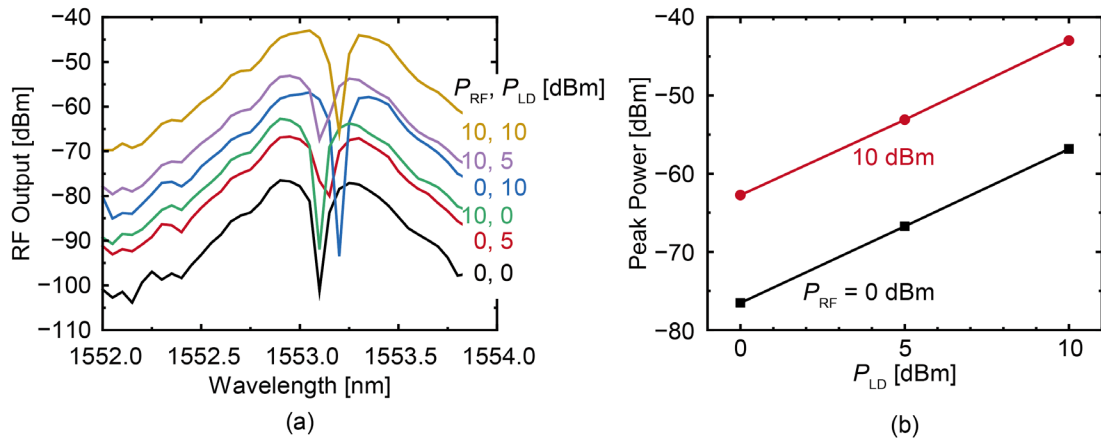
Figure 6-23 (a) Relationship between modulated signal and wavelength. (b) Relationship between RF output peak power and input RF power and LD power.
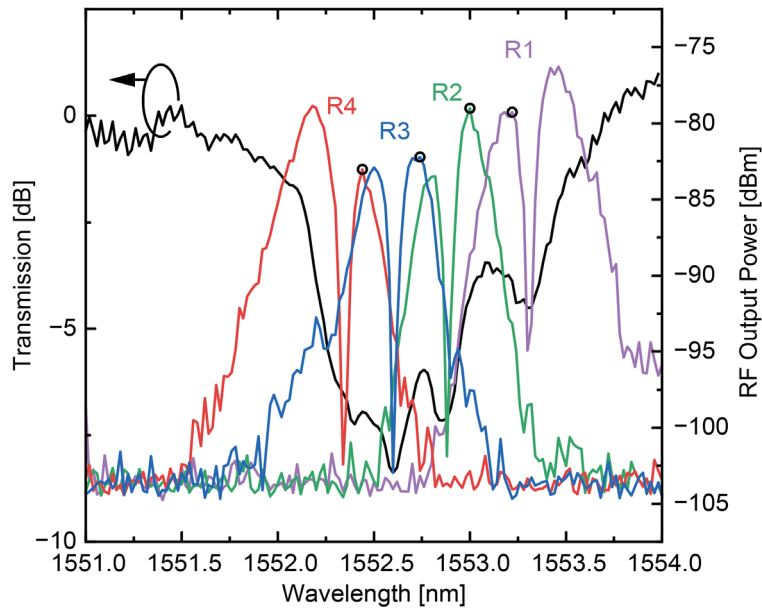

Figure 6-24 Results of modulation for all MRMs of chip J2 and device 3 when the control light is off. The black lines are transmission spectra.
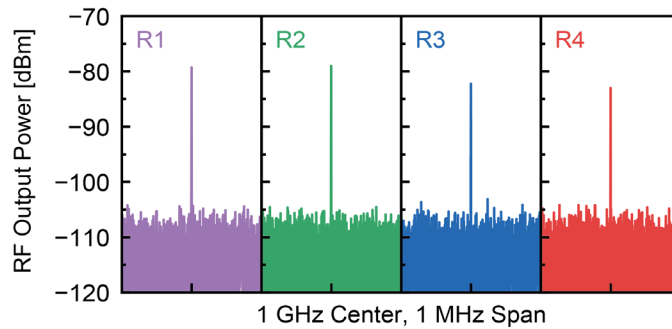
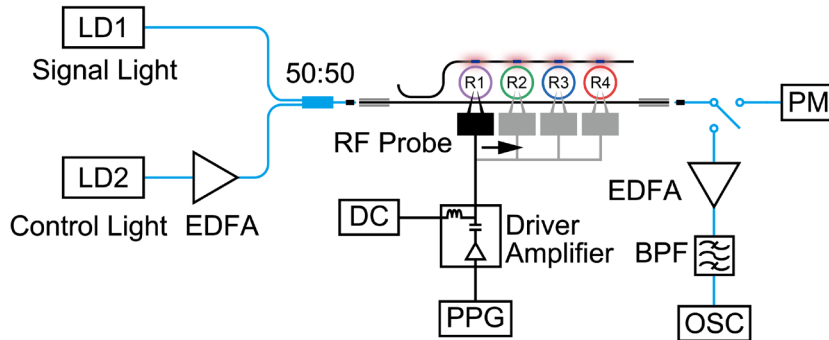Figure 6-25 RF output spectrum at each peak (black circles) in Fig. 6-24.

Figure 6-26 Measurement setup for multi-channel switching.

6.5 Multi-Channel Switching

6.5.1 Measurement Setup

Finally, we explored modulation options for MRMs using optical control. For this experiment, we utilized device1 of chip A2, characterized by a greater resonance depth and a closer initial resonance wavelength for each MRM. The experimental setup is depicted in Fig. 6-26. A Pulse Pattern Generator (PPG, Anritsu MP1800A) was employed to generate a 20 Gbps PRBS (NRZ, 2^7-1) signal. An electrical amplifier (Keysight, PS-X10-100) amplified the input signal and loaded a bias voltage of -5 Vpp, which was then passed through RF probe input to each MRM in sequence. The amplified control light was mixed with the signal light and fed into the DUT. The signal light from the DUT was amplified by the EDFA (Alnair Labs HPA-200CL-30-PM-FA-FA) and filtered by the BPF (Alnair Labs CVF-220CL) to eliminate excess control light and noise from the EDFA. Finally, the filtered signal was fed into an optical oscilloscope (OSC, Agilent E4440A) to observe the signal eye pattern.

6.5.2 All-Optic Switching

The light transmission characteristics of this device are illustrated in Fig. 6-27. At this point, the control light is switched off. The gradual change marked by the red dashed line is attributed to the transmission characteristics of the on-chip directional coupler, while the sharp change arises from the resonance characteristics of the four MRMs. When we activate the control light and progressively increase its power, the transmission spectrum changes within the wavelength range labeled in gray, as depicted in Fig. 6-28. It is evident that the resonance wavelengths of the four MRMs almost completely overlap when the control light power is 0. As the control light power increases, the four MRMs are heated to varying degrees by their respective optical heaters, causing the resonance wavelengths to gradually separate. Meanwhile, the efficiency of thermal tuning (the slope of the trajectory of resonance wavelength change in the figure) remains almost constant. Furthermore, except for R1, the wavelength shifts generated by the remaining MRMs due to thermal tuning nearly adhere to an equally spaced arrangement (with tuning efficiency of 0.07 nm/mW, 0.03 nm/mW, 0.02 nm/mW, 0.01 nm/mW for R1~R4).

153

Setting the signal light wavelength at the position indicated by the white line in the figure allows the resonance wavelength of each MRM to be sequentially shifted near the signal light wavelength. Modulation selection can be achieved by varying the control optical power within the permissible input optical power range. The transmission spectra of each state when the control optical power is set to P_{Heat1} ~ P_{Heat4} are presented in Figs. 6-29 as (a)~(d), corresponding to the states where R1~R4 are selected, respectively.

Modulation experiments were conducted on the MRM in the four selected states using the experimental setup outlined in Fig. 6-26. At this time, the control light wavelength was 1540.70 nm, and the signal light wavelength was 1560.62 nm. The signal light input power was adjusted to 11 dBm for observation. Each of the four MRMs was selected in turn, and 20 Gbps PRBS modulation signals were applied to each when selected. The eye patterns of the output optical signals were measured simultaneously, and the results are depicted in Fig. 6-30. The scales of all images are kept consistent. It is evident that a clear eye pattern is observed only when the MRM loaded with the modulation signal is optically selected by the optical heater. The MRMs that are not selected do not exhibit crosstalk from the modulation signal. In summary, the optical heater control has enabled the modulation selection of a four-channel MRM array, i.e., the optical control of the MRM array.
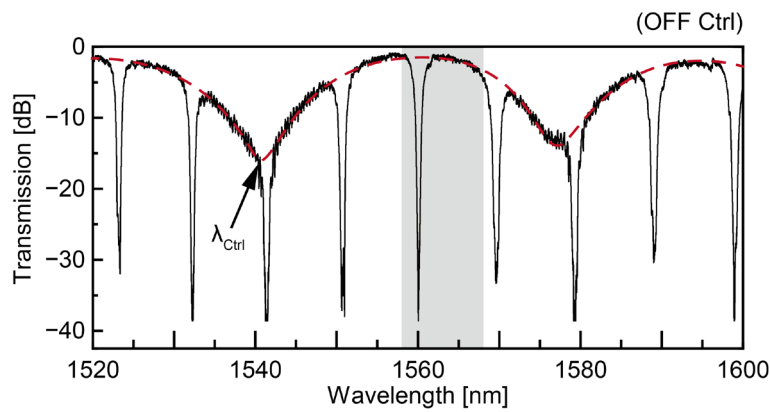
Figure 6-27 Optical transmission of device1, chip A2.
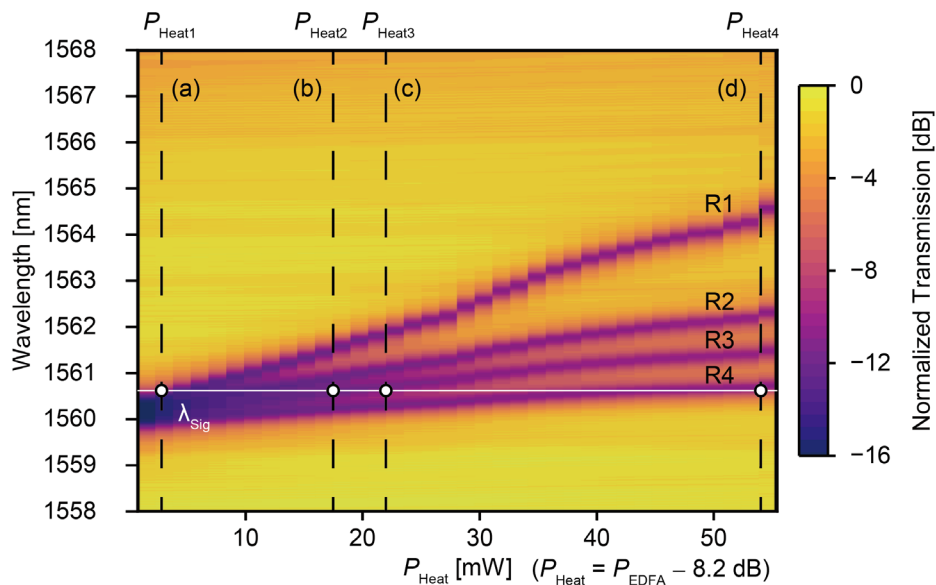
Figure 6-28 Resonance tuning of MRMs via optical heater.
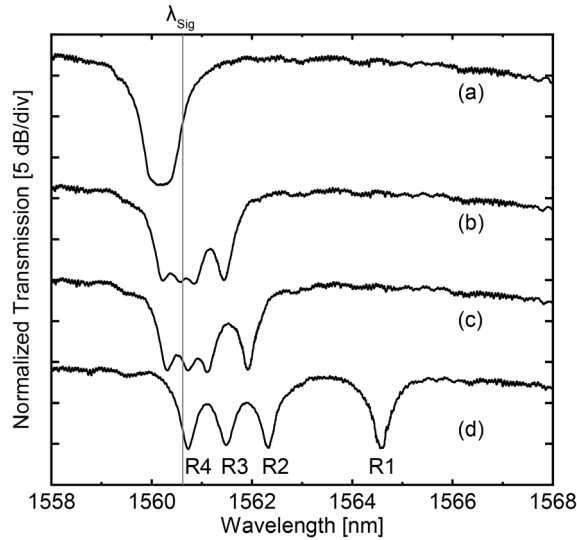
Figure 6-29 Transmission of MRM array with heating power of $P_{Heat1} \sim P_{Heat4}$ in Fig. 6-28.
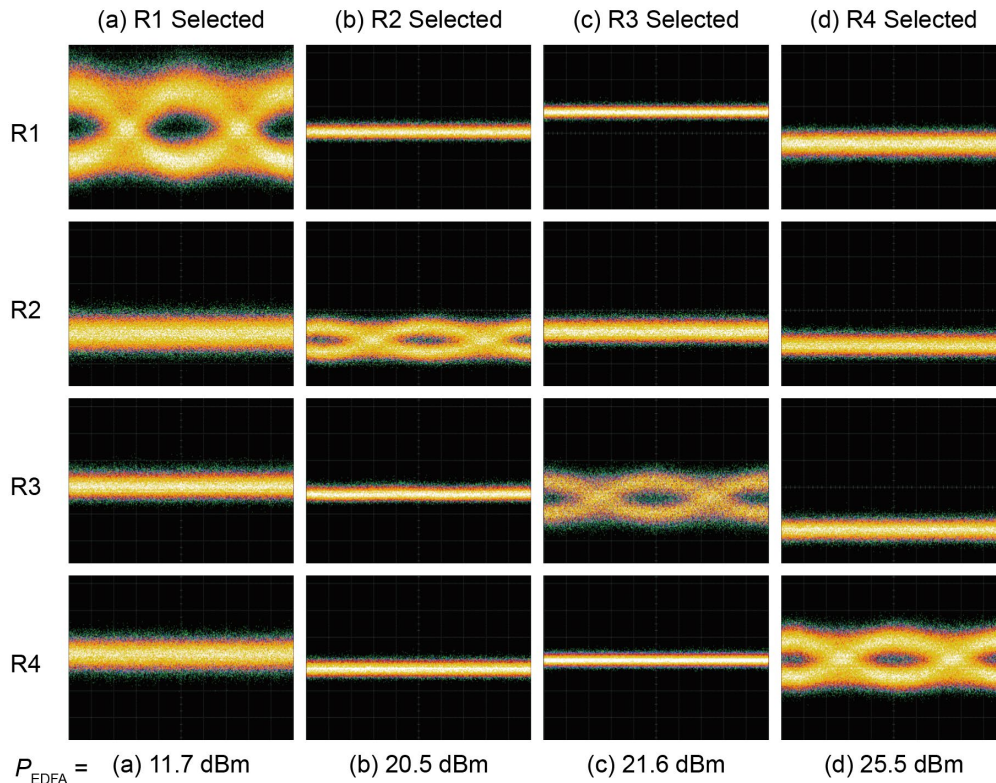
Figure 6-30 Modulation eye patterns of MRM arrays when varying the heating power.

6.5.3 Discussion

As depicted in Fig. 6-30, only the selected microring is involved in modulation. However, the magnitude of the modulation amplitude varies. This discrepancy arises from the insufficient separation of the resonance wavelengths of individual MRMs and the insufficient steepness of the MRMs' resonance (low Q), resulting in a small change in the signal light modulated by the MRMs. Therefore, the selection of the operating point (wavelength of signal light) and the power required to sequentially select all MRMs are strongly linked to the Q factor. A larger Q allows for a larger modulation amplitude, even with smaller resonance wavelength separation. However, a larger Q factor also results in a lower optical bandwidth.

Moreover, since a cascade approach is employed to control each MRM in this study, the number of
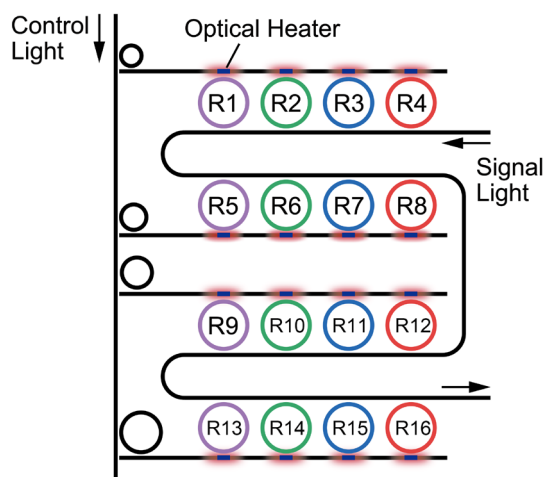
Figure 6-31 Scalability of proposed optical controllable MRM array.

MRMs that can be controlled is limited by the maximum input power. In this design, selecting the first MRM had to simultaneously shift the resonance wavelengths of all the remaining three MRMs farther away through thermal tuning. There is no efficient way to conserve power for this operation. Therefore, for an optical heater in cascade connection, this approach supports a maximum number of MRMs of about four. However, as mentioned in the previous chapter's conclusion, utilizing the dimension of controlling the optical wavelength allows for the realization of MRM arrays with more channels. To achieve this, as illustrated in Fig. 6-31, we can vertically duplicate the MRM arrays in this design for multiple replica. The control light for each array is then filtered from the control light bus waveguide by MRRs of different radii. In this manner, by controlling the wavelength and power of the control light, large-scale optical heater array-controlled MRM arrays can be realized. Such arrays can find applications in the all-optical controlled MRM imaging system based on the on-chip integrated 5G antenna discussed in Chapter 4 or other large-scale optical switches.

6.6 Summary

In summary, this chapter introduces optically controllable MRM arrays, synthesizing the concepts of MRM array RoF systems and optical heaters. We designed MRM arrays supporting four channels and integrated optical heaters into each MRM while preserving the original modulation function. The light absorption efficiency of each optical heater was designed to satisfy specific relationships. Through simulation calculations, various MRM arrays with different design parameters—such as the coupling gap of the MRM coupling part and the doping width of the optical heater part—were designed to observe the effects of these parameters on the results.

For the actual fabricated devices, parameter fitting determined that the coupling coefficients and in-ring losses of each MRM were nearly the same as the design values. The fundamental performance of each MRM as a modulator was confirmed through sine wave modulation experiments. Additionally, by introducing control light to the optical heater of each MRM, we observed the resonance wavelength shift of each MRM, confirming the normal operation of the optical heater. Although the resonance wavelengths of most MRM arrays were not consistent due to fabrication errors, limiting the number of optically selectable devices, we successfully implemented modulation selection using one MRM array device with minimal fabrication error.

When loading a 20 Gbps PRBS signal to each MRM, only the MRMs tuned by the optical heater to the vicinity of the signal light wavelength were selected and delivered the modulation signal. The unselected MRMs exhibited no significant crosstalk. This indicates the feasibility of our proposed optically controlled MRM array. Such arrays have sufficient scalability to expand into two-dimensional control matrices and can be applied to large-scale optical switches or millimeter wave imaging systems, especially if the control optical wavelength is leveraged to increase the control dimension.

Reference

[6-1] W. Bogaerts, P. De Heyn, T. Van Vaerenbergh, K. De Vos, S. Kumar Selvaraja, T. Claes, P. Dumon, P. Bienstman, D. Van Thourhout, and R. Baets, "Silicon microring resonators," *Laser & Photonics Reviews*, vol. 6, no. 1, pp. 47–73, 2012, doi: https://doi.org/10.1002/lpor.201100017.

[6-2] L. Li, T. Tamanuki, and T. Baba, "All-optic control using a photo-thermal heater in Si photonics," *Opt. Express*, vol. 30, no. 23, pp. 41874–41883, Nov. 2022, doi: 10.1364/OE.469977.

[6-3] L. Li, H. Arai, and T. Baba, "Imaging of electromagnetic waves using a radio over fiber system including an Si photonics microring modulator array," *Opt. Express*, vol. 30, no. 18, pp. 31530–31538, Aug. 2022, doi: 10.1364/OE.457459.

Chapter 7
Conclusion

This study aims to develop a silicon photonics solution for visualizing electromagnetic waves in the 5G bandwidth. In contrast to the conventional non-remote, high-loss electromagnetic wave imaging approach, this study achieves remote signal transmission with the assistance of a silicon photonics-based RoF system. This system modulates high-frequency signals onto an optical carrier and utilizes a wide bandwidth, low-loss optical fiber. A microring modulator (MRM) serves as the fundamental device for electro-optical conversion in this system. The MRM can achieve high-speed modulation up to the 40 GHz level while having a very small footprint of only a 10 μm radius. We have integrated these MRMs in series on-chip into an 8-channel MRM array for selecting and modulating the RF signals from each RF probe. Simultaneously, we use an RF probe consisting of an antenna array containing eight non-resonant slot antennas for the Sub 6 GHz band to detect the EM wave signals from the EM wave source. By automating the modulation selection of each MRM, we achieve high-density visualization of the EM wave radiation for a 3.5 GHz sine wave signal, obtaining a detection dynamic range of more than 20 dB and a cross polarization discrimination of more than 10 dB. The relevant performance is expected to improve further after optimizing the experimental environment. On the other hand, to simplify the control method of the MRM array and reduce electrical connectivity, we propose a novel optical control method. It utilizes the exothermic principle of absorption of control light by high-concentration doping and can implement the tuning of the phase of signal light in adjacent waveguides. In this study, we optimized the structure of the previous generation of optical heaters and applied it to two different optical switches. Based on the experimental results, we confirm the higher heating efficiency of the optical heater than the electrical one, while ensuring that the heating time response of the heater is not affected. Finally, we combined these two concepts to integrate the optical heater into an arrayed MRM and implemented an optically controllable MRM using an appropriate design to provide a more compact solution for electromagnetic wave visualization systems. We will now summarize each part in detail.

7.1 High-quality Modulation Achieved by MRM

Microring modulators play a pivotal role as electro-optical devices in silicon photonics and serve as the cornerstone of this study. In this investigation, we meticulously designed and manufactured MRMs with a radius of 10 μm and a Q-factor of approximately 4000. The resonant wavelengths of these MRMs can be finely tuned through the use of an integrated TiN electrical heater. To maximize modulation, we maintain the MRM as close to the critical coupling state as possible. This involves ensuring a specific relationship between the coupling efficiency of the microring and bus waveguide and the in-ring losses due to doping within the microring. The actual fabricated device aligns closely with the design specifications. The heating efficiency of the integrated TiN electrical heater is measured at 0.17 nm/mW, guaranteeing tunability of the resonant wavelength to any desired value. The utilized MRM achieves a resonance depth of 17 dB, and the in-ring losses and coupling coefficients to the bus waveguide, determined through parametric fitting, closely align, indicating proximity to the critical coupling state. This results in a modulation extinction ratio exceeding 5 dB. The MRM in this study utilizes the carrier depletion effect under reverse bias to achieve a modulation efficiency of 9.94 pm/V with a $V_\pi L$ as low as 2.42 Vcm. Additionally, the optoelectronic bandwidth of the MRM reaches about 30 GHz at maximum modulation efficiency point and can extend beyond 40 GHz with the assistance of the peaking effect (limited by the equipment bandwidth). Modulating PRBS signals at speeds up to 32 Gbps with the MRM yields clear eye patterns and ER surpassing 5 dB. Importantly, this high-performance modulation remains unaffected by the self-heating of the MRM induced by the high-power optical input.

7.2 Electromagnetic Wave Imaging

We arranged the designed high-performance MRMs and electrically connected them to an RF probe consisting of non-resonant slot antennas supplied by Arai Labs, forming an electromagnetic wave imaging system. A 3.5 GHz sine wave signal from the source was transmitted by a dipole antenna and received by the RF probe. Each antenna in the RF probe was connected to each MRM in the MRM array. With the assistance of a LabVIEW automation program, we modulated the electrical signals received by each MRM and output them sequentially. This process allowed us to obtain the spatial intensity distribution of the electromagnetic waves emitted by the dipole antenna. The obtained results closely match the simulation results, enabling the imaging of EM wave signals with different polarization directions. In this study, the number of imaging points is 441, covering a total area of 3515 mm². The dynamic range of imaging exceeds 20 dB, and the cross polarization discrimination is more than 10 dB. These metrics can potentially be enhanced further with the optimization of the measurement environment. Consequently, the successful visualization of the signal strength of electromagnetic waves in the Sub 6 GHz band within the 5G spectrum is achieved, offering the possibility of visualizing electromagnetic waves in higher bands in the future as well.

7.3 All-optical Control without Electricity

All-optical control becomes necessary in some special cases, and in this study, it is leveraged to minimize the system size. Here, we propose an optical heater utilizing a light absorption and exothermic approach. When the light intended for control is introduced into a waveguide doped with high concentration, it gets absorbed, emitting heat. This generated heat can diffuse from the silicon slab, which possesses high thermal conductivity, to the adjacent waveguide. This causing a change in the phase of the signaling light it transmits. In the actual design, we optimized various parameters such as the shape of the high concentration of doping in the control waveguide, the length of the waveguide slab, the waveguide spacing, etc. We integrated such an optical heater into both MZI-type and MRR-type optical switches to replace the conventional electrical heater. In this study, a 30 μm long triangular doped shape was employed to ensure gradual light absorption and uniform heat emission. Subsequent experiments revealed that for the MZI-type optical switch with the optical heater, the power required to achieve a π phase change was only 17 mW, compared to 22.5 mW for the usual electrical heater. For the MRR-type optical switch, the heating efficiency of both the optical and electrical heaters was measured at 0.19 nm/mW. These findings demonstrate that the heating efficiency of the optical heater can surpass that of the typical electrical heater, ensuring a minimum switching response time of 12 μs, comparable to the usual electrical heating method.

7.4 Optically Controllable MRM Array

Finally, we integrated optical heaters into a 4-channel MRM array to validate the independent optical control of individual MRMs within an MRM array, applicable to an electromagnetic wave imaging system. In this design, the four MRMs share the same modulator design but feature different optical heater designs to achieve a selective impact of the input control light on each MRM. As the control light power increases, the resonance wavelengths of the MRMs gradually separate and successively pass through the wavelength of the laser light source, enabling the sequential modulation of electrical signals. In practical measurements, an MRM with parameters of 8.6 pm/V and $V_\pi L = 2.37$ Vcm was realized, confirming a tuning efficiency of up to 0.07 nm/mW. Optical selection of the four MRMs was achieved by setting the wavelength of the laser light source at the appropriate position. Each MRM in the MRM array can be independently selected and modulated while maintaining low interchannel crosstalk. Consequently, the use of light to control the resonance tuning of individual MRMs in the array is feasible. This lays the groundwork for realizing a more compact MRM imaging system within the 5G band.

Acknowledgements

periodical meetings.

I would like to thank secretaries of Baba Laboratory: Ms. Masako Akaishi, Ms. Makiko Koyanagi, Ms. Makiko Yamada for their clerical support.

Finally, I would like to thank my family for their mental and financial support. I would also like to give a special thanks to my girlfriend, Yujie Ma, who has given me the greatest moral support and has been a great motivator to keep me going.

Publications

Journal Papers

[1] <u>L. Li</u>, H. Arai, and T. Baba, "Imaging of electromagnetic waves using a radio over fiber system including an Si photonics microring modulator array," *Opt. Express*, vol. 30, no. 18, pp. 31530–31538, Aug. 2022, doi: 10.1364/OE.457459.

[2] <u>L. Li</u>, T. Tamanuki, and T. Baba, "All-optic control using a photo-thermal heater in Si photonics," *Opt. Express*, vol. 30, no. 23, pp. 41874–41883, Nov. 2022, doi: 10.1364/OE.469977.

International Conferences

[1] <u>L. Li</u>, H. Arai and T. Baba, "Imaging of electromagnetic-waves using RoF system based on Si photonics microring modulator array", Int. Sympo. Photon. Electron. Convergence, Tokyo, 2021.

[2] <u>L. Li</u>, H. Arai and T. Baba, "Imaging of electromagnetic-waves using RoF system based on Si photonics microring modulator array", Conf. Laser and Electro-Opt. Pacific Rim, Sapporo, no. CWP12A-05, 2022.

[3] <u>L. Li</u>, T. Tamanuki and T. Baba, "All optic control in Si photonics", Optoelectronic and Commun. Conf., Toyama, no. WE2-3 2022.

[4] <u>L. Li</u>, H. Arai, and T. Baba, "Photonic device for electromagnetic wave visualization", Int. Sympo. Photonic and Electromagnetic Crystal Structures, Tokyo, no. P-55, 2023.

[5] <u>L. Li</u>, T. Tamanuki, and T. Baba, "Photo-thermal control in Si photonic devices", Int. Sympo. Photonic and Electromagnetic Crystal Structures, Tokyo, no. P-56, 2023.

[6] <u>L. Li</u> and T. Baba, "Si photonics microring modulators controlled all optically", Optoelectronic and Commun. Conf., Shanghai, no. OECC2023-0322-3, 2023.

[7] <u>L. Li</u> and T. Baba, "Modulation characteristics of microring modulators with self-heating", Int. Sympo. Photon. Electron. Convergence, no. P-36, 2023.

Domestic Conferences

[1] <u>李鎧村</u>, 新井宏之, 馬場俊彦, "Si フォトニクスマイクロリング変調器を用いた電磁波可視化 RoF システム", 応用物理学会秋季講演会, no. 11p-N207-9, 2021.

[2] <u>李鎧村</u>, 馬場俊彦, "電気を一切使わない Si フォトニクス光-光制御デバイス", 応用物理学会春季講演会, no. 16a-Z10-10, 2021.

[3] <u>李鎧村</u>, 新井宏之, 馬場俊彦, "Si フォトニクスマイクロリング変調器アレイを用いた電磁波可視化 RoF システム", 電子情報通信学会無線端末・アンテナシステム測定技術研究会, 2021.

[4] <u>李鎧村</u>, 馬場俊彦, "Si フォトニクスマイクロリング変調器を用いた電磁波可視化 RoF システム", 光集積及びシリコンフォトニクス研究会, 2022.

[5] <u>李鎧村</u>, 新井宏之, 馬場俊彦, "Si フォトニクスマイクロリング変調器 RoF システムによる電磁波可視化実験", 応用物理学会春季講演会, no. 22p-E303-3, 2022.

[6] <u>李鎧村</u>, 玉貫岳正, 馬場俊彦, "電気を一切使わない Si フォトニクス光－光制御デバイス（II）", 応用物理学会春季講演会, no. 22a-E303-6, 2022.

[7] <u>李鎧村</u>, 玉貫岳正, 馬場俊彦, "電気を一切使わない Si フォトニクス光－光制御デバイス（III）", 応用物理学会秋季講演会, no. 21p-A205-21, 2022.

[8] <u>李鎧村</u>, 馬場俊彦, "光ファイバと接続する光インターフェースの設計", JST ムーンショットプロジェクト目標 6 公開シンポジウム, no. 3-19, 2023.

[9] R. Zhang, L. Li, M. Kamata, T. Baba, T. Ozawa, Y. Ota and S. Iwamoto, "Band structure of Quantum Hall Ladder in the synthetic frequency dimensions for a silicon-based coupled two ring resonators", CREST トポロジカル領域セミナー, no. P20, 2023.

[10] 李鎦村，馬場俊彦, "光量子インターフェースのチップ-ファイバ接続の総合設計", 応用物理学会春季講演会, no. 15a-A501-1, 2023.

[11] 李鎦村，馬場俊彦, "自己発熱があるときの Si マイクロリング変調器の変調特性", 応用物理学会秋季講演会, no. 21a-A308-1, 2023.

[12] R. Zhang, L. Li, M. Kamata, T. Baba, T. Ozawa, Y. Ota, S. Iwamoto, "Measurement of band structure in the synthetic frequency dimensions for a silicon-based coupled two ring resonators", 応用物理学会秋季講演会, no. 21a-A308-2, 2023.

[13] 李鎦村，馬場俊彦, "全光制御可能なマイクロリング変調器アレイの実験的検証", 応用物理学会春季講演会, no. 23a-1BJ-2, 2024.